

Author	Xiao Cheng
Title	Controlled solvent vapor annealing of block copolymer films
Language	English
University	Universität Potsdam
Faculty	Mathematisch-Naturwissenschaftlichen Fakultät
Institute	Institut für Chemie
Academic degree	Doctor rerum naturalium
Academic discipline	Polymerchemie
Date of disputation	15.01.2019



Controlled solvent vapor annealing of block copolymer films

Xiao Cheng

Univ.-Diss.

**zur Erlangung des akademischen Grades
"doctor rerum naturalium"
(Dr. rer. nat.)
in der Wissenschaftsdisziplin " Polymerchemie "**

**eingereicht an der
Mathematisch-Naturwissenschaftlichen Fakultät
Institut für Chemie
der Universität Potsdam**

This work is licensed under a Creative Commons License:
Attribution – Noncommercial – Share Alike 4.0 International
To view a copy of this license visit
<https://creativecommons.org/licenses/by-nc-sa/4.0/>

Published online at the
Institutional Repository of the University of Potsdam:
<https://doi.org/10.25932/publishup-42417>
<https://nbn-resolving.org/urn:nbn:de:kobv:517-opus4-424179>

“Only two things are infinite, the universe and human stupidity, and I'm not sure about the former.”

Albert Einstein

志不强者智不达

《墨子·修身》

Erklärung

Ich (Xiao Cheng) versichere, die hier vorliegende schriftliche Arbeit selbständig verfasst und keine anderen als die angegebenen Hilfsmittel benutzt zu haben. Die Stellen der Arbeit, die anderen Werken dem Wortlaut oder dem Sinn nach entstammen, wurden unter Angabe der Quellen kenntlich gemacht. Dies gilt auch für in der Arbeit enthaltenen Zeichnungen und Abbildungen. Ich erkläre hiermit, dass die Dissertation in der vorgelegten oder einer ähnlichen Fassung noch nicht zu einem früheren Zeitpunkt an einer anderen in- oder ausländischen Hochschule als Dissertation eingereicht worden ist.

Berichter:

Prof. Dr. Alexander Böker

PD Dr. Larisa Tsarkova

Contents

Zusammenfassung	1
Summary	3
Motivation.....	5
1 Introduction	9
1.1. Physics and processing of block copolymers.....	9
1.1.1. Basic principles on the micro phase separation of block copolymers	9
1.1.2. Phase behavior of block copolymers in thin films.....	12
1.1.3. Directed self-assembly technology (DSA)	15
1.2. Processing of thin films.....	17
1.2.1. Equilibrium states of polymer blends	17
1.2.2. Equilibration of polymer films by thermal annealing.....	19
1.2.3. Solvent vapor annealing of polymer films.....	20
1.3. Non-solvent induced phase inversion	26
2 Materials and Methods	31
2.1. Materials.....	31
2.2. Film preparation	32
2.2.1. Preparation of the substrates	32
2.2.2. Spin-coating.....	32
2.2.3. Residual solvent elimination.....	34
2.2.4. Drop-casting procedure.....	34
2.2.5. Floating of the films.....	35
2.2.6. Metallization of the microphase separated patterns.....	35
2.3. Film processing via thermo-solvent annealing	35
2.4. Film characterization.....	36
2.4.1. Ellipsometry.....	36
2.4.2. Scanning force microscopy.....	39
2.4.3. Optical Microscopy.....	42
2.4.4. Other imaging techniques	42
3 Scientific and practical aspects of controlled solvent vapor annealing	45

3.1. Description of the annealing setup and discussion of the system relative parameters	45
3.1.1. Reproducibility of the swelling experiments	47
3.1.2. Solvent vapor regulation in the chamber	50
3.2. Swelling behavior of SV ³⁹⁰ films: temperature effects	55
3.2.1. Control over degree of swelling by vapor temperature	55
3.2.2. Combined variation of the temperature of the substrate and temperature of the solvent vapor	56
3.3. Swelling behavior of homopolymer films during annealing process	58
3.3.1. Selectivity of chloroform to PS and P2VP homopolymer in thin films	58
3.3.2. Swelling-dependent properties of PS and P2VP homopolymer films	60
3.4. Swelling behaviors of SV films in vapors of strongly and of slightly selective solvents	63
3.5. Summary	64
4 Tunable morphology in ultrathin films of high molecular weight block copolymer (SV) via thermo-solvent annealing	65
4.1. Swelling behavior of SV ³⁹⁰ films under variation of the vapor flow	65
4.2. Swelling behavior of SV ³⁹⁰ in ~40 nm films under variation of the temperature of the vapor and of the substrate	66
4.3. Morphology of SV ³⁹⁰ in films with thickness under half-layer tuned by the temperature	69
4.4. Challenging of interpretation of the perforated (PL) morphology of SV ³⁹⁰ in thin films	73
4.4.1. Peak force mode characterized morphology of SV ³⁹⁰ in films	73
4.4.2. Characterization of the morphology of SV ³⁹⁰ film/substrate interfaces annealed under slightly selective solvent vapor	74
4.4.3. Metallization of annealed SV ³⁹⁰ template	77
4.4.4. Pattern transfer of SV ³⁹⁰ templates with PL morphology	82
4.5. Time evolution of the structures in SV ³⁹⁰ films with under-half-layer thickness	85
4.6. Summary	89
5 Effects of thickness gradients, surface properties and solvent quality on the microphase separation in block copolymer films¹	91
5.1. Effect of the confinement on the morphological behavior of SV ³⁹⁰	91

5.1.1.	Thickness regime from sub-half layer to above-half layer	92
5.1.2.	Metallization of block copolymer template with gradient thickness	94
5.2.	Effect of confinement and solvent selectivity on the morphological behavior of SV ⁹⁹ in thin films.....	95
5.2.1.	Film thickness dependent microphase separation upon annealing in highly selective solvent vapor	95
5.2.2.	Thickness dependent microphase separation in slightly selective solvent vapor.....	97
5.3.	Substrate-induced morphological behavior.....	99
5.3.1.	Comparison of the swelling behavior of SV ³⁹⁰ in films with the thickness range between under half-layer and over half-layer thickness	99
5.3.2.	Comparison of the microphase separation in SV films on different substrates	100
5.3.3.	Effect of the film thickness in on the phase separation of SV ³⁹⁰ block copolymer on weakly interacting substrates with weak interaction.....	103
5.3.4.	Effect of molecular weight of SV on the efficiency of the solvent annealing on HM supports.....	104
5.4.	Combined effect of film thickness gradients and surface energy at the substrate.....	106
5.4.1.	Phase separation of SV ⁹⁹ in films on patterned photoresist substrates	106
5.4.2.	SV films on wrinkled PDMS substrate.....	107
5.5.	Effect of the starting morphology on the phase separation in SV ³⁹⁰ films	109
5.5.1.	Spin-cast morphology of SV ³⁹⁰ films from various spin-coating solvents.....	109
5.5.2.	Effect of residual solvent on the structures in SV ³⁹⁰ films from DMF spin-coating solution	111
5.6.	Summary	111
6	Preparation of block copolymer-based membranes via orientated vapor flow treatment	113
6.1.	Preparation, treatment and characterization	114
6.2.	Phase separation in SV ⁹⁹ films induced by oriented vapor flow.....	115
6.3.	Phase separation of polystyrene-b-poly(methyl methacrylate) (SM) films induced by oriented vapor flow.....	122
6.4.	Summary	125

7	Acknowledgement	127
8	Bibliography	129
9	Publications and Posters	140
10	Appendix	142
11	Abbreviations	156
12	List of Figures.....	158
13	List of Tables	165

Zusammenfassung

Im Rahmen dieser Arbeit wurde das Phasenverhalten von Poly(styrol)₁₈₇₀₀₀-block-poly(2-Vinylpyridin)₂₀₃₀₀₀ (SV³⁹⁰) hohen Molekulargewichts (390 kg/mol) in dünnen Filmen untersucht, in denen die Selbstassemblierung der Block-Copolymere durch Lösungsmitteltempern erreicht wurde. Das hochentwickelte Verfahren der Behandlung mit Lösungsmitteldampf bietet kontrollierte und stabile Bedingungen.

In **Kapitel 3** werden die Faktoren diskutiert, die den Prozess des Temperns und das Schwellverhalten der dünnen Block-Copolymer Filme beeinflussen. Das Schwellverhalten von Block-Copolymeren in Filmen wird einerseits durch die Temperaturen des Lösungsmitteldampfes und des Substrates sowie andererseits dem Sättigungs-Dampfdruck kontrolliert. Zusätzlich beeinflussen auch Faktoren wie die Geometrie und das Material der Kammer sowie die Art der Strömung in der Kammer die Reproduzierbarkeit und Stabilität der Messungen. Der geringfügig selektive Lösungsmitteldampf von Chloroform führt zu 10% stärkerem Schwellen des P2VP-Blocks im Vergleich zu PS in Filmen mit einer Dicke von ca. 40 nm.

Die variable Morphologie ultradünner Filme eines Block-Copolymers hohen Molekulargewichts (SV³⁹⁰) wurde in **Kapitel 4** untersucht. Das Schwellverhalten kann durch die Temperatur und den Dampfdruck unabhängig voneinander präzise beeinflusst werden. Die Umgebungstemperatur stellt einen limitierenden Faktor für den Bereich der Annealing-Temperatur aufgrund der möglichen Kondensation des Lösungsmitteldampfes dar. Mehrere Methoden, wie zum Beispiel die Charakterisierung mit Rasterkraftmikroskopie, Metallisierung und reaktives Ionenätzen, wurden verwendet, um die Morphologie der Filme als perforierte Lamellen mit PS-Kugeln und P2VP-Matrix zu bestimmen. Eine Analyse der Kinetik der Strukturbildung zeigt, dass sich die ursprüngliche Morphologie von Block-Copolymeren hohen Molekulargewichts sowohl auf Substraten mit schwacher als auch starker Wechselwirkung innerhalb von 5 min ändert und das weitere Tempern zum Ausheilen von Defekten führt.

Die morphologische Veränderung von symmetrischen Block-Copolymeren bei Filmdicken zwischen einer halben Domänendicke und einer ganzen Domänendicke

Zusammenfassung

wurde in **Kapitel 5** in Abhängigkeit von Gradienten der Filmdicke und verschiedenen Oberflächeneigenschaften der Substrate untersucht. SV³⁹⁰ und SV⁹⁹ Filme zeigen eine lamellare Bulk-Morphologie nach Behandlung mit geringfügig selektivem Lösungsmitteldampf (Chloroform). SV⁹⁹ Filme bilden eine zylindrische Morphologie unter Behandlung mit stark selektivem Lösungsmitteldampf (Toluol) aus, weil das SV⁹⁹ Block-Copolymer während des Temperns eine asymmetrische Struktur aufweist (Toluol-Aufnahme ausschließlich im Polystyrol-Block). Beide Morphologien (Lamellen und Zylinder) werden durch die Filmdicke beeinflusst. Die Morphologie von SV³⁹⁰ und SV⁹⁹ nach Tempern ist abhängig von der Filmdicke und den Substrat-Eigenschaften und ähnlich der Morphologie auf flachen Silicium-Wafern.

In **Kapitel 6** wird ein Ansatz zur induzierten orientierten Mikrophasenseparation in dicken Block-Copolymer Filmen durch Behandlung mit orientiertem Dampfdruck unter Verwendung eines Miniextruders vorgestellt, der als Alternative zu existierenden Verfahren wie Nichtlösungsmittel-induzierter Phasenseparation dienen könnte. Die ersten im Rahmen dieser Arbeit durchgeführten Untersuchungen zeigen das Potential der Methode auf, welche die Struktur im gesamten Volumen des Films durchgehend beeinflusst (durch SAXS-Messungen gezeigt). Jedoch sind detailliertere Studien notwendig, um die Prozedur zu optimieren.

Summary

This project was focused on exploring the phase behavior of poly(styrene)₁₈₇₀₀₀-block-poly(2-vinylpyridine)₂₀₃₀₀₀ (SV³⁹⁰) with high molecular weight (390 kg/mol) in thin films, in which the self-assembly of block copolymers (BCPs) was realized via thermo-solvent annealing. The advanced processing technique of solvent vapor treatment provides controlled and stable conditions.

In **Chapter 3**, the factors to influence the annealing process and the swelling behavior of homopolymers are presented and discussed. The swelling behavior of BCP in films is controlled by the temperature of the vapor and of the substrate, on one hand, and variation of the saturation of the solvent vapor atmosphere (different solvents), on the other hand. Additional factors like the geometry and material of the chamber, the type of flow inside the chamber etc. also influence the reproducibility and stability of the processing. The slightly selective solvent vapor of chloroform gives 10% more swelling of P2VP than PS in films with thickness of ~40 nm.

The tunable morphology in ultrathin films of high molecular weight BCP (SV³⁹⁰) was investigated in **Chapter 4**. First, the swelling behavior can be precisely tuned by temperature and/or vapor flow separately, which provided information for exploring the multiple-parameter-influenced segmental chain mobility of polymer films. The equilibrium state of SV³⁹⁰ in thin films influenced by temperature was realized at various temperatures with the same degree of swelling. Various methods including characterization with SFM, metallization and RIE were used to identify the morphology of films as porous half-layer with PS dots and P2VP matrix. The kinetic investigations demonstrate that on substrates with either weak or strong interaction the original morphology of the BCP with high molecular weight is changed very fast within 5 min, and the further annealing serves for annihilation of defects.

The morphological development of symmetric BCP in films with thickness increasing from half-layer to one-layer influenced by confinement factors of gradient film thicknesses and various surface properties of substrates was studied in **Chapter 5**. SV³⁹⁰ and SV⁹⁹ films show bulk lamella-forming morphology after slightly selective solvent

Summary

vapor (chloroform) treatment. SV^{99} films show cylinder-forming morphology under strongly selective solvent vapor (toluene) treatment since the asymmetric structure (caused by toluene uptake in PS blocks only) of SV^{99} block copolymer during annealing. Both kinds of morphology (lamella and cylinder) are influenced by the film thickness. The annealed morphology of SV^{390} and SV^{99} influenced by the combination of confined film and substrate property is similar to the morphology on flat silicon wafers. In this chapter the gradients in the film thickness and surface properties of the substrates with regard to their influence on the morphological development in thin BCP films are presented. Directed self-assembly (graphoepitaxy) of this SV^{390} was also investigated to compare with systematically reported SV^{99} .

In **Chapter 6** an approach to induced oriented microphase separation in thick block copolymer films via treatment with the oriented vapor flow using mini-extruder is envisaged to be an alternative to existing methodologies, e.g. via non-solvent-induced phase separation. The preliminary tests performed in this study confirm potential perspective of this method, which alters the structure through the bulk of the film (as revealed by SAXS measurements), but more detailed studies have to be conducted in order to optimize the preparation.

Motivation

Block copolymers as a kind of self-assembling soft matter have shown a remarkable development since their first synthesis more than 60 years ago [1]. Interest in block polymer thin films has grown considerably with much of the work on thermal dynamics of phase separation, applying the self-assembly of block polymer as advanced approaches to develop nanolithography and generating other functional nanostructures [2–5], since Mansky etc. launched the concept of exploiting block polymer self-assembly for lithographic templates in 1995[6].

The immiscibility on the mesoscale and the miscibility on the microscale make block copolymers an ideal material for emerging nanotechnologies including nanotemplating [7–9], nanoporous membranes [10–12], nanolithography [2; 13–15], anti-reflection coating [16] and storage media [17; 18] etc. Despite these industrial endeavors, each with its own challenges [19], distinct hurdles remain that limit widespread usage of BCP thin films in emerging technologies [20]. These hurdles include precise control over the directed assembly, understanding the influence of nanostructure formation from dynamics and processing protocols, elimination of defects and transformation of ordered templates [19–22]. Another important issue is the effectiveness and reproducibility of the processing of spin-coated block copolymer films towards targeted morphologies and patterns.

Since the film preparation process usually introduces a metastable state of phase separated structure to BCPs, further treatments to drive the BCP to an equilibrium state are necessary. The self-assembly of BCPs is very sensitive to external fields and to experimental conditions. Based on our experience, a tiny fluctuation of environment temperature, humidity, solvent concentration or even solvent quality during the annealing will cause unexpected final morphologies. So a controllable and reproducible annealing process is a very important research topic.

Two popular annealing methods-solvent annealing [3; 23–25] and thermal annealing[26], are widely used processing for inducing phase reorganization and enhancing the long range order of BCPs. The thermal annealing is increasing the temperature higher than T_g

of BCPs and enhancing the chain mobility to achieve equilibrium morphology. When the decomposition temperature is lower than T_g or the window between T_g and the decomposition temperature (usually exists in large BCPs), thermal annealing is not a good choice for this processing [27; 28]. The solvent annealing is introducing solvent vapor molecules as plasticizer [29; 30] to decrease the T_g of BCP down to RT, which is an effective method to reorganize the phase separation. Meanwhile as a cooperated factor, the temperature also influences χ parameter [31], interface energy [32; 33] and chain mobility [34]. The thermo-solvent annealing is used as a finely tuned processing for self-assembly of BCPs through our work. The designation of our annealing system and the factors influencing reproducibility and controllability are discussed in **Chapter 3**.

The use of self-assembly to obtain well-ordered structures is an attractive application of BCPs due to the ease of accessing complex structures with small feature sizes. Since Krausch et al. reported the ordered cylindrical structure of BCP via solvent evaporation in 1999 [35], many preparations of ordered membrane from BCPs are investigated [36–38]. Cyclic solvent vapor treatment is helpful for standing cylindrical structure of asymmetric BCPs in film [39], so the exploration of new designed setup which can provide cyclic solvent vapor and high vapor pressure is developed in **Chapter 6**.

χ , N and f_i , are the three main parameters to control the final structure of diblock copolymers in bulk, which cooperate to systematically influence the phase separation of BCPs, where $\chi - N$ is a product of Flory-Huggins parameter and polymerization of the BCPs, and f_i is a volume fraction of one of the blocks (shown in Figure 2). Besides the phase separation, the high χ value is also a critical parameter to reduce the roughness of the micro domains [40] and to obtain ordered morphology with high dense features [15; 41; 42]. When the BCPs are in a confined geometry of a film, especially with thickness comparable with several domain spacing or below, other factors such as film thickness [43–45], surface properties of substrates [46; 47], and topography [48–51] of substrates will strongly influence the morphology of the BCPs in films [52]. In this work the basic influence of χ is studied in **Chapter 3**. The influence of film thickness increasing from under half-layer to above one-layer, and other factors like substrate properties and solvent quality are discussed in **Chapter 5**.

Block polymer systems usually contain only light molecules (C, H, O, N) leading to small etching contrast between each micro domain. Block copolymers composed of poly (2-vinylpyridine) (P2VP) which contain pyridine moieties as side chains, is a good material to solve this problem. Till now they have been used in many applications [8; 53–56], for presence of an unshared electron pair on the nitrogen atom of the pyridine ring and the resulting pH sensitivity [57–59]. With respect to nanolithography, the convenience of loading metal ions to P2VP block makes this kind of BCPs widely used as etching mask [60].

The phase separation of BCPs with low molecular weight has been well investigated in recent years, but the phase behavior of large BCPs in films is still an empty space to explore. The long molecular weight BCPs with characteristic lengths of larger than 100 nm, have potential applications in desalination technology [61] and in optics industry [62]. Large BCPs have low chain mobility which causes high kinetics barriers for morphology reorganization and unacceptable long time for thermal annealing [63; 64]. Furthermore, larger than 100 nm characteristic length of microdomains can cause more complex phase behavior influenced by the interaction between film thickness and substrates. The phase behavior of high molecular weight BCP with 390 kg/mol in films with under half-layer thickness (~ 40 nm) under varied solvent vapor annealing conditions are explored in **Chapter 4**.

1 Introduction

1.1. Physics and processing of block copolymers

Block copolymers (BCPs) consist of two or more covalently bound immiscible components and construct microscopic liquid-like order and mesoscopic crystal-like order structure. The microscopic structure is provided by the short-range repulsion from the incompatibility of the monomers of different blocks. The macroscopic phase separation is prohibited by the covalent bond between the blocks [65; 66].

The phase behavior of undiluted (bulk) $(A-B)_n$ block copolymers is determined by three experimentally controllable factors: the overall degree of polymerization N , the composition f (overall volume fraction of the A component), and the A-B segment-segment (Flory-Huggins) interaction parameter χ [67].

1.1.1. Basic principles on the micro phase separation of block copolymers

- Polymer-polymer combined interaction parameter χN

Flory-Huggins parameter (χ) also called polymer solvent interaction parameter was first introduced to describe the interaction between solvent and polymer molecules in their lattice model of polymer solutions by Flory and Huggins independently. Liquids with the smallest χ 's are usually the best solvents for a polymer. Negative values of χ often indicate strong polar attractions between polymer and solvent. As χ is relative with Φ_p^{-2} and T^{-1} based on its definition [68–70], during our thermo-solvent annealing χ is not a constant value. So we introduce $\chi_{\text{eff}} = \chi * \Phi_p$ to describe the changing value.

N is the overall degree of polymerization of the block copolymer, which decides the length of the polymer chain. The product χN controls the state of segregation [67]. When the diblock copolymer is symmetric, which means the volume fraction (f) of a block is 0.5, the order and disorder transition occurs at the value of χN around 10.5.

1 Introduction

When $\chi N \ll 10.5$, entropic factors dominate the structure and diblock copolymers exist in a spatially homogeneous state [71]. Increasing N or χ shifts the free energy balance until $\chi N \approx 10$, a delicate balance exists between entropic and energetic effects [70]. Increasing χN further induces the diblock copolymer from disordered state to ordered state by a first-order transition [71; 72]. And the large χN leads to sharper microdomain boundaries as the number of A-B segment-segment contacts decrease at the expense of additional chain stretching [70]. When at the limit situation $\chi N \gg 10$, energetic factors dominate and the ordered microstructures are characterized by narrow interfaces and nearly flat composition profiles [73; 74] (Figure 1).

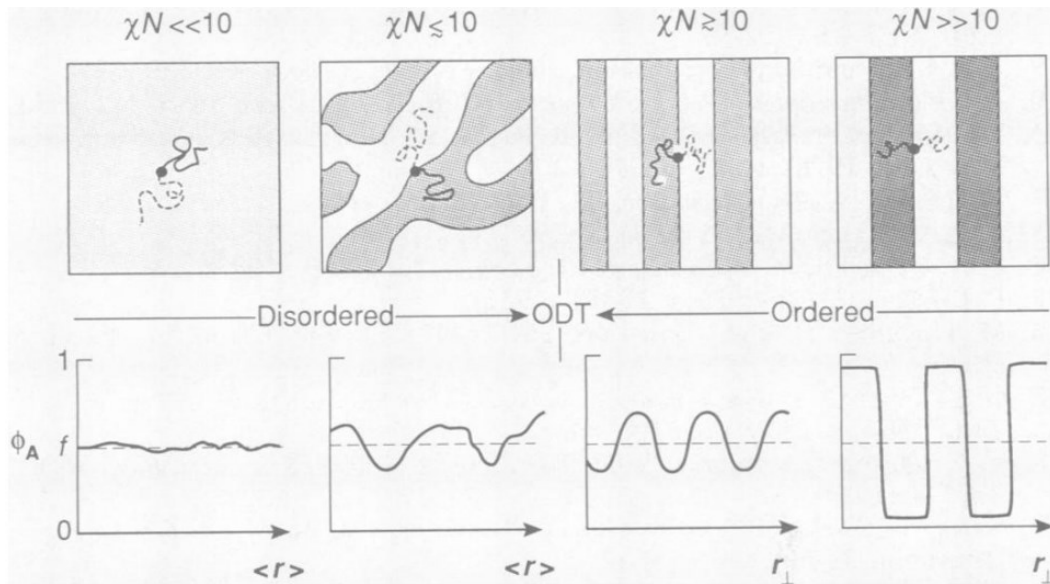


Figure 1 Evolution of structure with the combined parameter χN for a symmetric, diblock copolymer with $f = 0.5$. When $\chi N \sim 10$, small variations in system entropy ($\sim N^{-1}$) or energy ($\sim \chi$) leads to ordered ($\chi N \geq 10$) or disordered ($\chi N \leq 10$) states. A homo-generous composition profile (ϕ_A versus r) results when entropic factors dominate ($\chi N \ll 10$), whereas a strongly microphase segregated pattern characterizes the limit where energetic factors prevail ($\chi N \gg 10$). Reprinted from Reference [70].

- Effect of block copolymer volume composition

Self-consistent mean field theory is developed to predict the behavior of block copolymers. The theoretical phase diagram depending which describes the dependences of the microphase separated structures in a diblock copolymer melt on the volume fraction f of the block A and χN is based on the balancing of the enthalpic interfacial energy between

the blocks and the entropic chain stretching energy of the individual blocks (Figure 2) [75]. As the χN and the volume composition of a diblock copolymer change, the structures including disordered, closely packed spherical (S_{cp}), spherical (S), cylindrical (C), and gyroid (G) and lamellar (L) are displayed in this diagram. The perforated lamellar phase which is not addressed in the picture is believed to be a metastable state between the G and L phases [75].

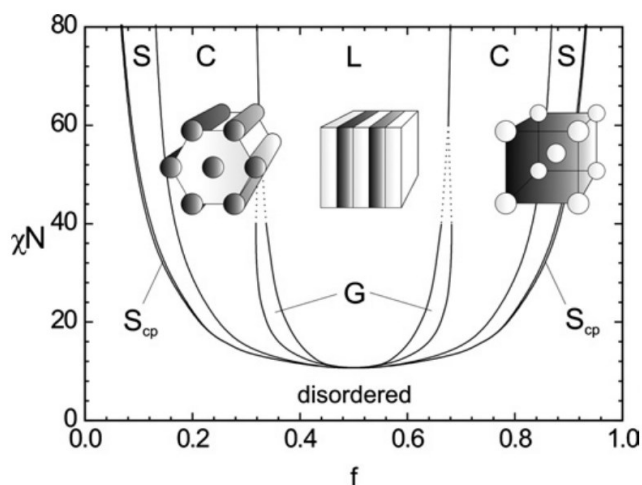


Figure 2 A theoretical phase diagram for a conformationally symmetric diblock copolymer melt. Reproduced from Reference [75] with permission from The Royal Society of Chemistry.

The phase diagram of polyisoprene-polystyrene (PI-b-PS) diblock copolymer with the composition of polyisoprene ranging from 0.24 to 0.82 has been studied near the order-disorder transition point (ODT) by Bates et al. (in Figure 3). Five distinct microstructures including spheres, hexagonally packed cylinders (HEX), lamellae (LAM), hexagonally perforated layers (HPL), and a bicontinuous cubic phase having an $Ia3d$ space group symmetry were observed in this system [76].

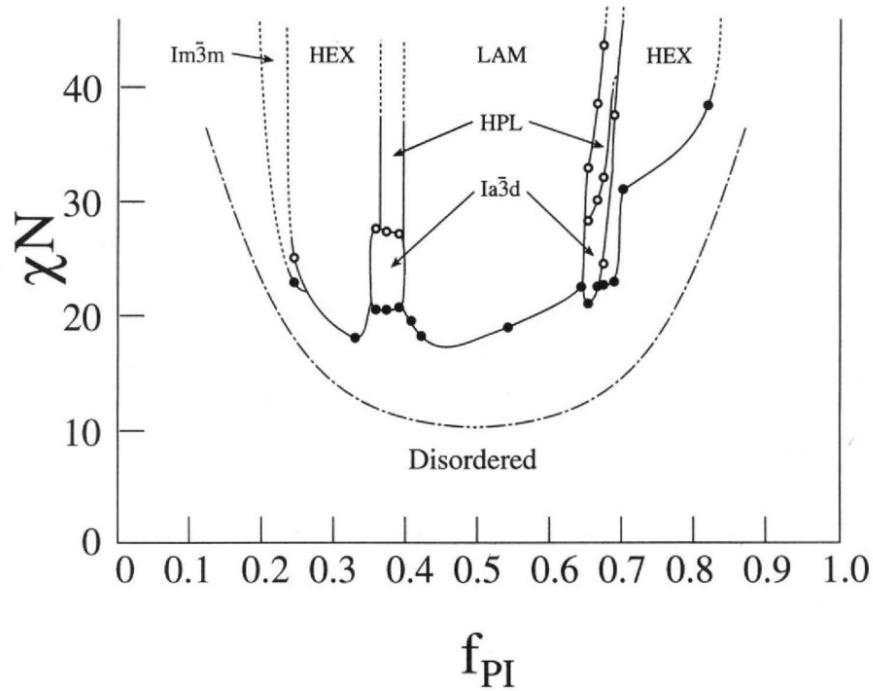


Figure 3 Experimentally determined phase diagram of PI-b-PS. Reprinted from Reference [76].

The feature size of BCPs can be described by equation derived from the mean-field theory: $L_0 \sim N^{2/3} \chi^{1/6}$ for symmetric diblock copolymer in a strong segregation limit ($\chi N \gg 10.5$) [66]. High-molecular-weight (large N) BCP can be used to get large periods close to 100 nm [25; 77; 78]. And the BCPs with high Flory-Huggins interaction parameter (χ) is also used to achieve microphase separation with small interfacial widths ($t \sim \chi^{1/2}$) for minimal line edge roughness [66].

In our case the segregation strength (χN) of the mainly used poly(styrene)-block-poly(2-vinylpyridine) (PS-b-P2VP) ($\chi_{S-2VP} = \sim 0.178$ at $T = 298$ K) [79] with a high molecular weight of 390 kg/mol is ~ 2089 , much higher than the weak-strong transition limit 10.5 [80]. However the low diffusion of BCP with high molecular weight also causes [81] the low chain mobility, which is the challenge to reorganize the phase separation.

1.1.2. Phase behavior of block copolymers in thin films

When the film thickness decreases to the range of domain spacing, the phase separation behavior of films is also influenced by additional energetic factors. Typically, the block with the lowest surface energy collects at the film surface, and the block with the lowest interfacial energy is attracted to the supporting substrate. Furthermore, the wetting conditions of substrates, which confine the film structure relative with its thickness, can cause the thin-film structure to deviate from that of the corresponding bulk material. Figure 4a, b presents the sketches of symmetric block copolymer with surface energy of S_2 and interfacial energy S_1 in the cross-section of a film in equilibrium state. Under symmetric wetting conditions the preferred film thickness is nL_0 , while under asymmetric wetting conditions the preferred thickness is $(n+1/2)L_0$. In Figure 4a, b presents the possibility of morphology of thin films with thickness decreasing from L_0 .

So the phase separation behavior of thin block copolymer in films is more complex and more various than in the bulk [82].

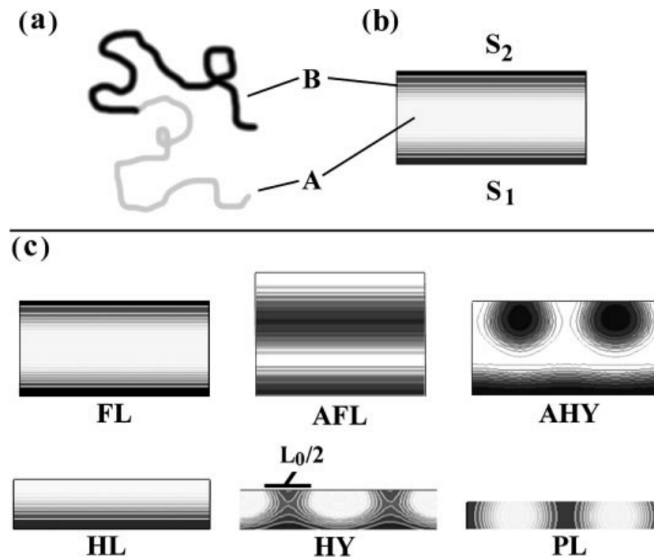


Figure 4 Diblock copolymer thin film morphologies. (a) Schematic representation of volume symmetric diblock with A (light) and B (dark) type segments. (b) Diagram of BCP film system in cross section indicating the bottom (1) and top (2) surfaces, with surface interaction energies S_1 and S_2 , respectively. (c) Summary of diblock thin film morphologies, generally organized by their appearance as film thickness decreases from L_0 . These calculated cross sections indicate the density of B-type segments, i.e., Black=100% B, white=100% A. These structures are referred to in the text with the abbreviations included under each diagram. FL: symmetric surface-parallel full lamella;

1 Introduction

AFL: anti-symmetric surface-parallel lamella; AHY: anti-symmetric hybrid structure; HL: half-lamella; HY: symmetric hybrid structure; PL: surface-perpendicular lamellae.
Reprinted from Reference [83]

- Effect of finite film thickness

The combined confinement allotted by the surface/interfacial energies and film thickness is systematically analyzed by Knoll et al. in elegant experiments [47; 84]. The example in Figure 5 presents various morphologies: featureless wetting layer at the smallest thickness; standing cylinder; parallel-orientated cylinder; perforated lamella etc. of the polystyrene-*b*-polybutadiene (PS-*b*-PB) film present as the film thickness increases.

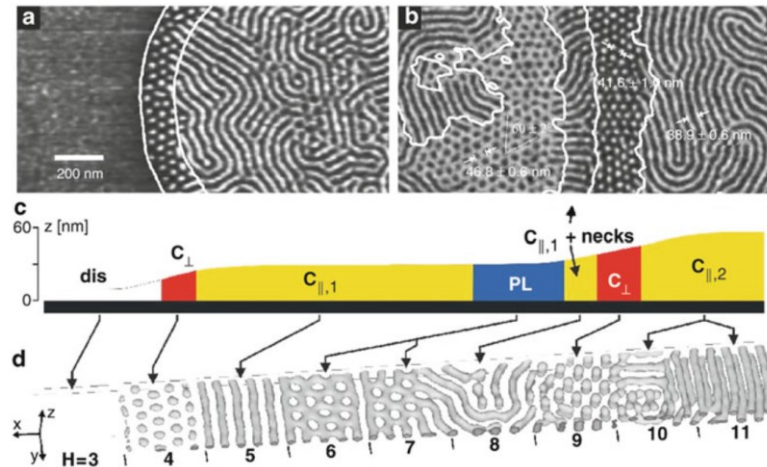


Figure 5 (a) Nanopattern revolution of the block copolymer thin film of PS-*b*-PB and the SFM phase image of SB morphology. The SFM phase images ($1 \times 1 \mu\text{m}$) present examples of the surface structures on carbon-coated (left) and silicon oxide (right) substrates at the indicated film thickness. Reprinted from Reference [84].

- Wetting conditions

The wetting conditions and the energetic/chemical surface also affected the morphology in thin films. A strongly interacting interface attracts one of the blocks selectively; the enriched block at interface affects the morphology as a result. A weakly interacting interface attracts none of the blocks to a significant extent and has been shown to favor the vertical orientation of lamella [47]. Figure 6 presents the morphology of PS-PB thin films on strongly interactive substrates (SiO_x/Si) and weakly interacting substrates (Carbon/ SiO_x/Si).

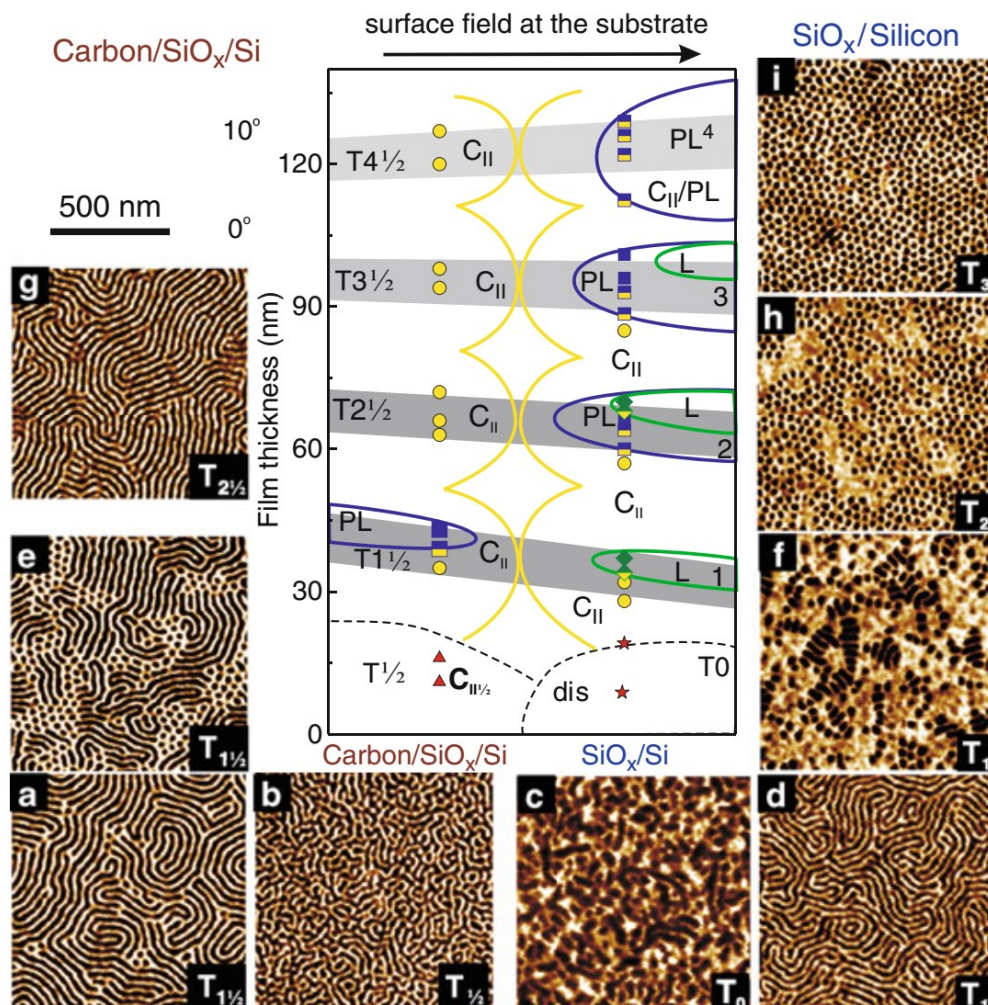


Figure 6 Phase diagram of the surface structures on a weakly interacting surface (carbon coating) under strong surface field with a preference for the majority component (silicon oxide). The SFM phase images ($1 \times 1 \mu\text{m}$) present examples of the surface structures on carbon-coated (left) and silicon oxide (right) substrates at the indicated film thickness. Reprinted from Reference [47].

1.1.3. Directed self-assembly technology (DSA)

Directed self-assembly (DSA) is the process by which external factors, such as physical templates and/or fields, influence the thermodynamic of self-assembly of block copolymers towards defect-free uni-axial orientation [85]. This method can enforce a single preferred orientation along the topographic features at the substrate and have been demonstrated to yield large-scale microphases with lower defect densities [21; 85; 86]

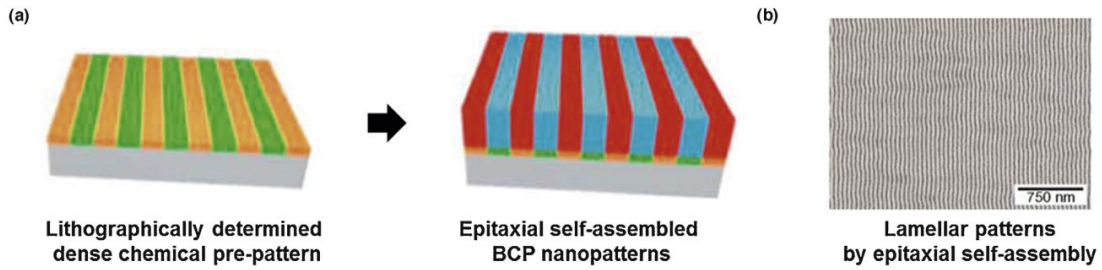
1 Introduction

than other reported strategies towards long-range orientation [87]. Also DSA patterns may achieve smaller features than their lithographic templates through pattern multiplication. This gives a potential possibility to DSA as an effective process to produce sub-10 nm scale templates with highly dense features for semiconductor industry.

DSA mainly uses either chemoepitaxy (chemical patterns) [88; 89] or graphoepitaxy (topographic features) [90] pre-patterning to guide the self-assembly of BCP. The illustration and the corresponding examples are shown in Figure 7. For example in chemoepitaxy the chemical modification of substrates into hydrophilic and hydrophobic patterns can induce the phase separation of BCP into similar patterns [91]. Some previous efforts have demonstrated the generation of periodic patterns of parallel lines (perpendicular lamellae, parallel cylinders) [48; 92; 93] and close-packed dots (perpendicular cylinders, spheres) [94; 41; 95] using topographic guiding patterns [21].

Recently grating substrates have been employed to direct self-assembly of BCP in a facile and low-cost route to fabricate dense, highly ordered thin films [96]. More recent Park and Tsarkova et al. reported using SiCN substrates with 3D sinusoidal surface-relief gratings to induce hierarchical structure of polystyrene-*b*-poly(2-vinylpyridine) [50].

Epitaxial Self-Assembly



Graphoepitaxy

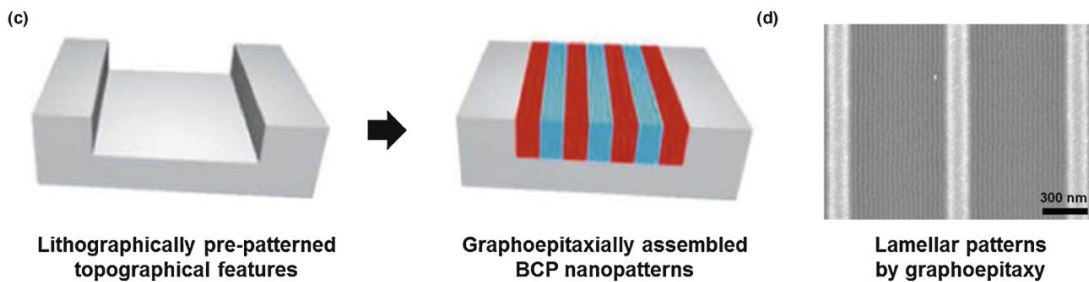


Figure 7 (a) Schematic illustration of epitaxial self-assembly exploiting nanoscopic chemical patterns to direct BCP self-assembly [97]. (b) SEM image showing defect-free lamellar patterns attained by epitaxial self-assembly [97]. (c) Schematic illustration of graphoepitaxy utilizing topographic pattern to direct BCP assembly [98]. (d) SEM image showing highly aligned lamellar patterns prepared by graphoepitaxy [99]. Reprinted from Reference [86] with permission from Elsevier.

1.2. Processing of thin films

1.2.1. Equilibrium states of polymer blends

The thermodynamic equilibrium state is the system with the minimum free energy. The free energy of mixing for a polymer blend is shown in equation:

$$\Delta \bar{F}_{mix} = kT \left[\frac{\phi}{N_A} \ln \phi + \frac{1-\phi}{N_B} \ln(1-\phi) + \chi \phi(1-\phi) \right] \quad (\text{Equation 1})$$

Straight lines connecting the phase two compositions determined the free energy of the phase separated state. So the phase boundary is determined by the common tangent of

1 Introduction

the free energy at the compositions ϕ' and ϕ'' (in the top plot of Figure 8) corresponding to the two equilibrium phases:

$$\left(\frac{\partial \Delta \bar{F}_{mix}}{\partial \phi}\right)_{\phi=\phi'} = \left(\frac{\partial \Delta \bar{F}_{mix}}{\partial \phi}\right)_{\phi=\phi''} \quad (\text{Equation 2})$$

The solution ($\chi(\phi)$) to the above equation is the phase boundary- the bimodal, which coincides with the coexistence curve (green line in bottom plot of Figure 8). Any overall composition at temperature T within the miscibility gap defined by the bimodal has its minimum free energy in a phase-separated state with the compositions given by the two coexistence curve compositions ϕ' and ϕ'' [100].

The inflection points in the plot of free energy $\Delta \bar{F}_{mix}(\phi)$ can be found when the second derivative of the equation is zero. This curve is the boundary between unstable and metastable regions and is called spinodal (blue dash curve in bottom plot of Figure 8). Any small fluctuations in composition will cause free energy lower, thus the phase separation happens spontaneously within the spinodal gap.

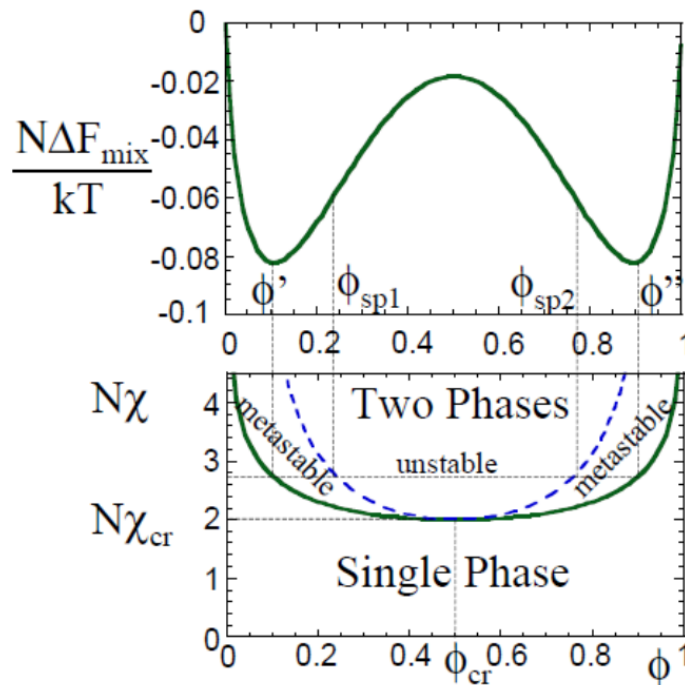


Figure 8 Composition dependence of the free energy of mixing for a symmetric polymer blend with the product $\chi N=2.7$ (top figure) and the corresponding phase diagram

(bottom figure). Binodal (solid curve) and spinodal (dashed curve) are shown on the phase diagram. Reprinted from Reference [100].

1.2.2. Equilibration of polymer films by thermal annealing

In many practical applications, the thin films of block copolymer are prepared by rapid extraction of a solvent, e.g. spin-coating technique in semiconductor industry. Due to the immiscibility of the blocks, block copolymers typically demix during the rapid solvent-casting process [101–103]. The resulting phase separation morphology may be far away from thermodynamic equilibrium, for the process is influenced by many factors like the confinement of two surfaces [104], the casting solution [105; 106], and solvent evaporation rate [107; 108]. The relaxation toward equilibrium may be hindered by kinetic barriers formed by the non-equilibrium morphology [102; 109]. The spontaneously procedure of thermal annealing, solvent annealing at room temperature or solvent annealing at an elevated temperature can increase the mobility of polymer chain allowing for a rearrangement of phase separation and the annihilation of defects [110; 27].

The temperature influences the block copolymer properties related to polymer chain mobility, including diffusivity [111] and viscosity [112], and that, at accessible temperatures, mobility is such that the directed assembly of useful morphologies can occur in minutes or even seconds. Nealey et al. demonstrated that increasing the annealing temperature from 190 °C to 250 °C can decrease the annealing time from 7 days to 15 min within the same system [113]. Thermal annealing is a widely used method to provide additional energy for overcoming the activation barrier for defect annihilation and also increase defect mobility [114]. Raybin and Sibener reported the process of defect annihilation with energetic barrier of 360 ± 80 kJ/mol from 210–230 °C under thermal annealing on chemically patterned substrates[87].

Thermal annealing can be used not only to reduce the kinetic barriers, but also to achieve the non-preferential boundary condition [115]. Gopalan et al. reported that an effectively neutral free surface can be created in the PS-b-PMMA system by annealing

1 Introduction

films between ≈ 170 ° C to 230 ° C, where the block surface tensions are approximately equal (in Figure 9)[116].

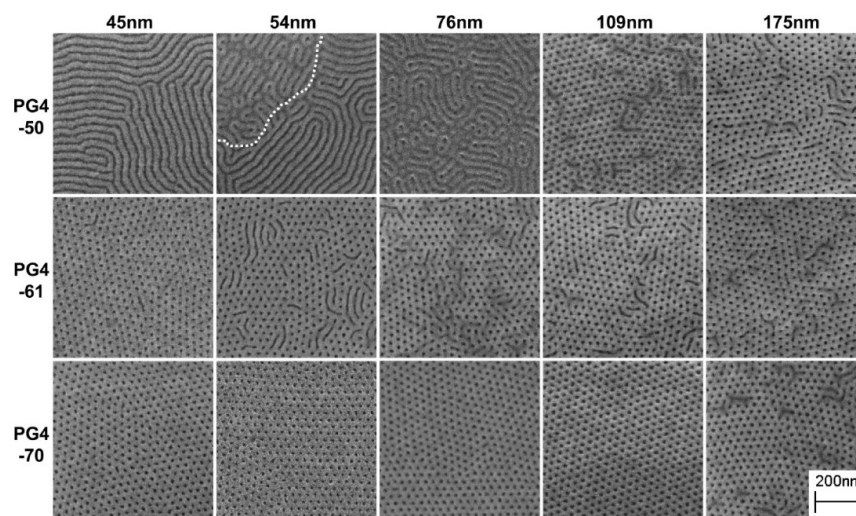


Figure 9 Top view SEM images of assembled BCP films of five different thicknesses on PG4-modified substrates (annealed at 190 °C). Reprinted from Reference [116].

1.2.3. Solvent vapor annealing of polymer films

As it is mentioned above, block copolymer can form at thermal equilibrium state in a variety of ordered microdomain morphologies [117–119]. In some cases the thermal equilibrium can be simply achieved by vacuum annealing the samples above the glass-transition temperature. But in many complex copolymer systems, the temperature gap between T_g of polymers and their thermal decomposition temperatures is very narrow that is not sufficient to achieve thermodynamic equilibrium in reasonable annealing time [120] [121]. Especially for BCP with high χN , the thermal annealing has a drawback of unacceptably long reorganized time even at temperature higher than the glass transition temperature (T_g) [49]. To address this issue, solvent vapor annealing (SVA) is an attractive alternative to thermal annealing [3; 52; 122; 123].

According to the review of Albert et al. [52], exposure of a polymer film to solvent vapors serves multiple purposes during annealing process, including establishing surface preferentiality [124–126], decreasing T_g (increasing polymer chain mobility) [104; 107;

127], changing domain spacing [84; 126; 128], affecting χ_{eff} parameters and the relative volume fractions [104; 123; 129], which may lead to undesirable surface interactions or wetting conditions [122; 130–132].

- Brief review on reported setups for SVA

The simplest setup to carry out solvent annealing is a sealed chamber containing solvent reservoir and the BCP sample is treated in this environment at room temperature without more control (in Figure 10B-a) [102; 133–135]. Park and Choi et al enhanced the kinetics of PS-PDMS by binary solvent annealing in this kind of apparatus [136]. The final degree of swelling and the speed of swelling is critical for the reproducibility of phase separation, and since the solvent vapor pressure is sensitive to humidity and environment temperature, so an *in situ* analysis and the control of solvent vapor are realized by introducing film thickness monitor such as ellipsometry or GISAXS and the control of solvent vapor flow and temperature (in Figure 10B-c) [121; 137–140]. The degree of swelling is very sensitive to the temperature of environment and of the polymer in a film, so the swelling factor is a critical parameter to control the phase separation. Jin et al. improved the setup with automatic controlling of the vapor flow based on the feedback signal of film thickness to remain the degree of swelling at a constant level (in Figure 10B-b) [141]. Evaporation rate of solvent from the film from swollen state to a dry state is also an important factor to influence the final morphology. Nelson et al. controlled the annealing system by computer and pneumatically actuated valves to achieve the precision of annealing time to the range of millisecond [142].

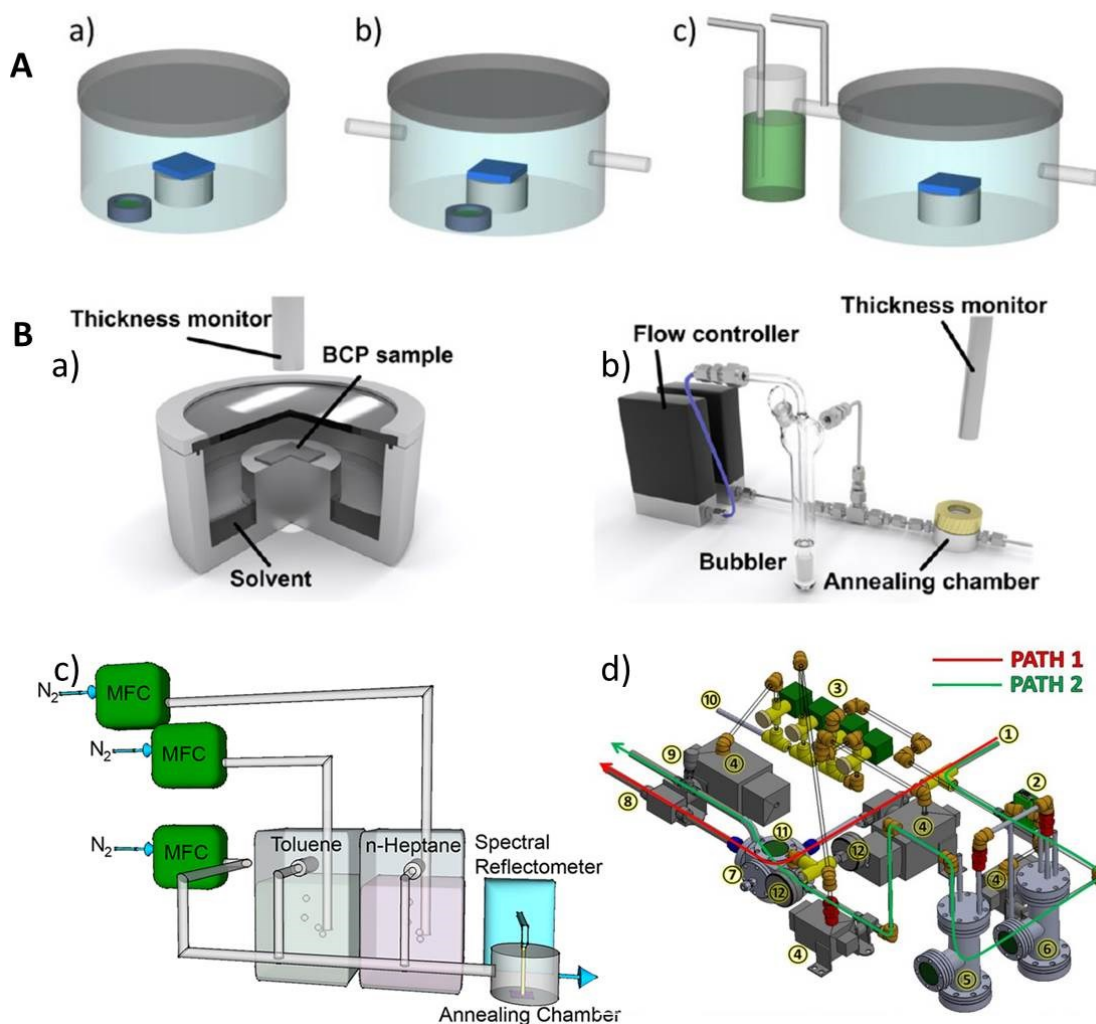


Figure 10 Sketches of primary methods of solvent vapor annealing in **A**, with (a) static annealing, (b) static annealing with gas flow to control swelling and deswelling process, (c) dynamic annealing with controlled solvent vapor flow. Examples of the annealing setups used in current researches in **B**, (a) static annealing with in situ monitor for film thickness, (b) dynamic annealing with controlled feedback loop [141], (c) dynamic annealing with controlled mixture of solvent [138], (d) dynamic annealing with highly precise controlling of annealing time. Reproduced from Reference [138; 141; 142].

- Effect of the nature of the annealing solvent

In SVA the first and foremost factor to consider is the selection of solvent. The most common solvent used for SVA of block polymers is one that is either neutral or only slightly selective for one of the blocks [3]. The selectivity of solvent not only is related to the volume fraction of the bulk mixture of block copolymer and solvent, but also confines the interfacial phenomena of both the solution/vapor and solution/substrate.

Xuan et al. compared the morphologies of ultrathin films of poly(styrene-*b*-methyl methacrylate) (PS-PMMA) annealed by various solvents like acetone and chloroform (selective to PMMA), toluene and carbon disulfide (selective to PS), with changeable surface preference during solvent uptake [125]. Gotrik and Ross reported a framework for predicting the range of morphologies available under different solvent vapor conditions including different proportion of the two-solvent mixture [143].

- Annealing time

Annealing time is a commonly reported factor in researches of phase separation of block copolymers. This factor is related to the swollen state of block copolymer during annealing. If the saturation of the solvent vapor in the atmosphere provides high swelling conditions, so that the block copolymer is in a disordered state due to high solvent concentration in the film, the further annealing should have no influence, the final morphology will be entirely driven by the solvent evaporation step [3]. The annealing time depending morphology is verified by Vayer and Hillmyer et al. [144]. And the ordered swollen state is observed by *in situ* GISAXS for poly(styrene)-*b*-poly(lactide) block polymers by Sinturel and Amenitsch et al [145].

- Degree of swelling of polymer films under SVA

The degree of swelling of block copolymer in films depends on the vapor pressure of the solvent in the annealing chamber, temperatures of the substrate and of the atmosphere, as well as on the solvent selectivity towards block copolymer components. This factor is also very important to affect the swollen morphology of the block copolymer, since it is an indicator of the effective interaction parameter (χ_{eff}) and the chain mobility. To access the morphology in swollen state of block copolymer, *in situ* GISAXS measurements can provide valuable and powerful results allowing the understanding of the whole solvent vapor annealing process. Paik et al. studied SVA process of poly(α -methyl styrene)-*b*-poly(4-hydroxystyrene) block polymer thin films by *in situ* GISAXS allowing assessment of the swollen state [146]. In their study the morphological reorganization (original perpendicular oriented cylinders turn to be parallel) only happened in enough content of solvent with rapid removal of the solvent. And the

1 Introduction

morphology of dry films can be reversibly switched by acetone vapor treatment with higher selectivity (in Figure 11).

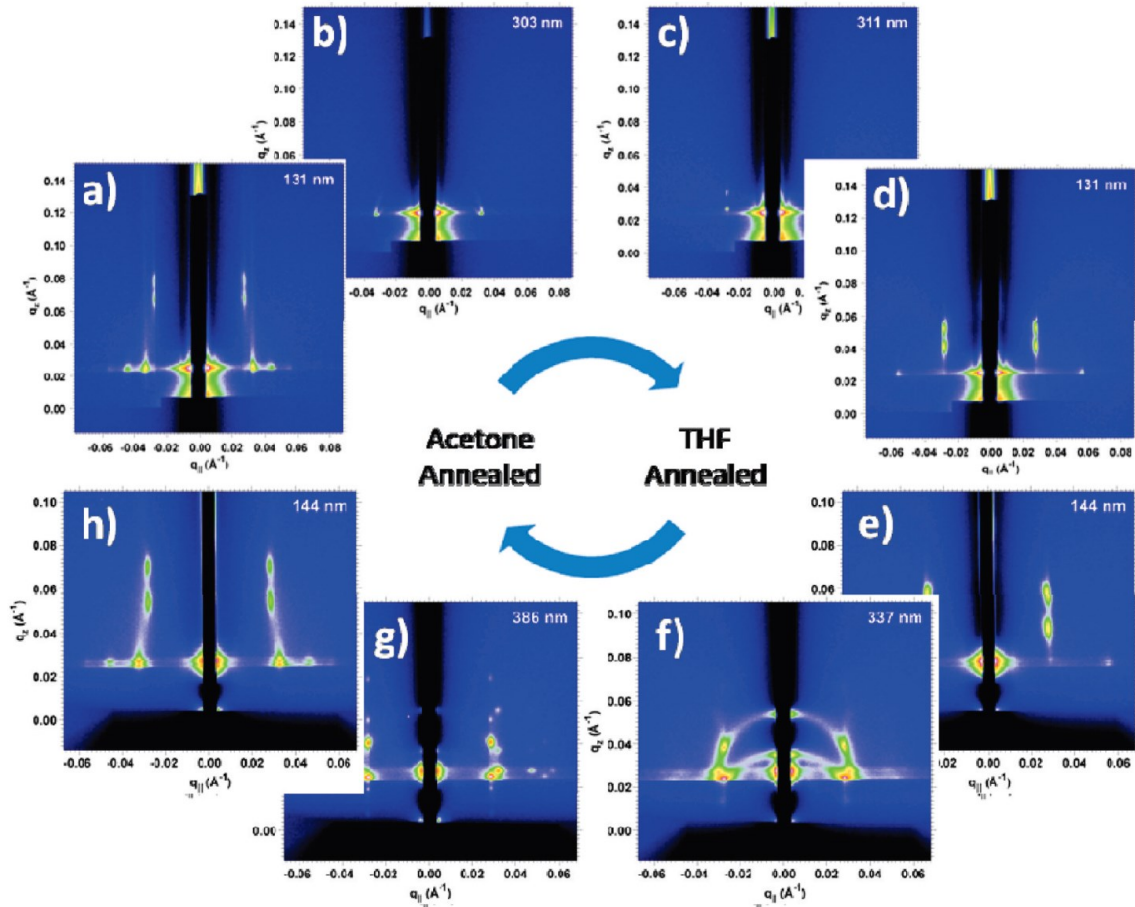


Figure 11 Reversible morphology control through solvent processing as probed *in situ* and in real time with GISAXS. Thin films with spherical morphology obtained through acetone vapor treatment are shown to transition to parallel cylinders upon THF vapor annealing and returned to a spherical morphology upon successive exposure to acetone vapor. Reprinted from Reference [146].

- Effect of the rate of solvent removal on the structure formation

Solvent evaporation is a strong, highly directional field which can induce both the oriented and lateral ordering of the micro domain arrangement such as electric fields [147], shear [148], temperature gradients [149], graphoepitaxy [50; 150; 151], chemically patterned substrates [152; 153], and other external fields. Since Kim and

Libera first found the evaporation rate of solvent can influence the final morphology of block copolymer in films from casting solution [102], the amount of researches about the relative conditions is grown up. Kim et al. first reported that by controlling the rate of solvent evaporation or solvent annealing, ordering of the copolymer is induced at the surface, and this ordering propagates through the entire film (in Figure 12) [107]. Based on this cylinder forming phenomenon Peinemann and Abetz explained the mechanism of the membrane formation from asymmetric block copolymer by non-solvent induced phase separation method (see below) [154].

Also, Albert et al. systematically examined the effect of solvent removal rate on the final thin film morphology of a cylinder-forming ABA triblock copolymer [155]. Through simulation study Hao et al. found that perpendicular cylinder morphology tends to form under weak surface preference, whereas under strong surface preference this morphology is promoted by the fast solvent evaporation rate and the strong solvent selectivity [156]. Making use of the deswelling vapor field, Paradiso et al. performed simulations to investigate a new approach to bias the formation of vertically oriented features in block copolymer thin films by cyclic solvent vapor annealing [157].

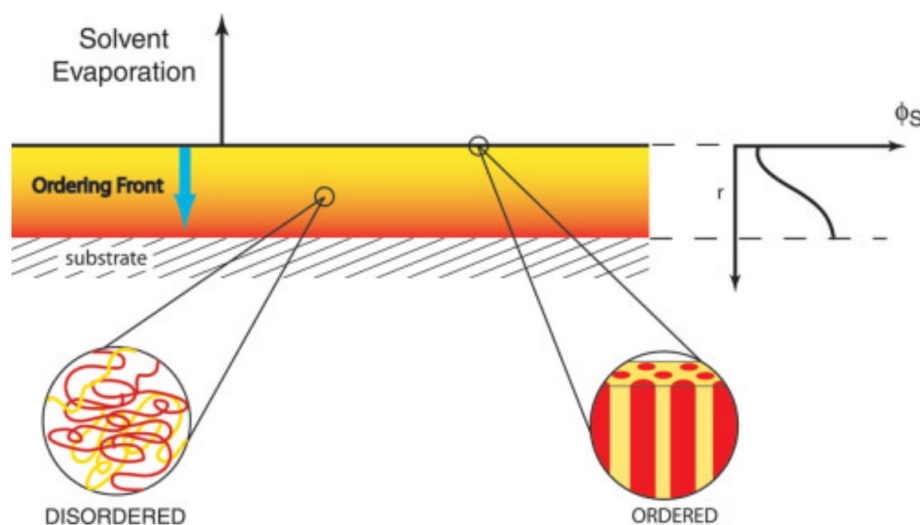


Figure 12 Schematic view of the solvent evaporation in a thin block polymer film illustrating the concept on an ordering front that propagates through the film. Reprinted from Reference [107].

1 Introduction

1.3. Non-solvent induced phase inversion

As a widespread commercial method for preparing membrane, non-solvent induced phase separation has been studied for more than fifty years. Phase inversion techniques are among the most important and commonly used processes for preparing membranes from a large number of polymeric building blocks. The preparation process is usually casting dense polymer solution from a good solvent on a porous mechanical support (e.g. nonwoven), then the wet film and support are immersed into a coagulation bath containing at least a poor solvent. The polymer film solidifies through exchange of solvent and non-solvent, where the solvent and non-solvent system needs to be miscible [158; 159].

The pore structure is generated by phase separation. After immersion into the non-solvent bath, the solvent-nonsolvent exchange (demixing) brings the initial thermodynamically stable system into a condition for which the minimum Gibb's free energy is attained by separating into two coexisting phases [12]. An explanation of macrovoid formation is provided by McKelvey and Koros that the rapidly moving front of non-solvent during the exchange process must be considered (Figure 13). If the non-solvent diffusion rate into the polymer-poor phase being formed exceeds the rate of outward solvent diffusion, the macrovoid formation is favored [160].

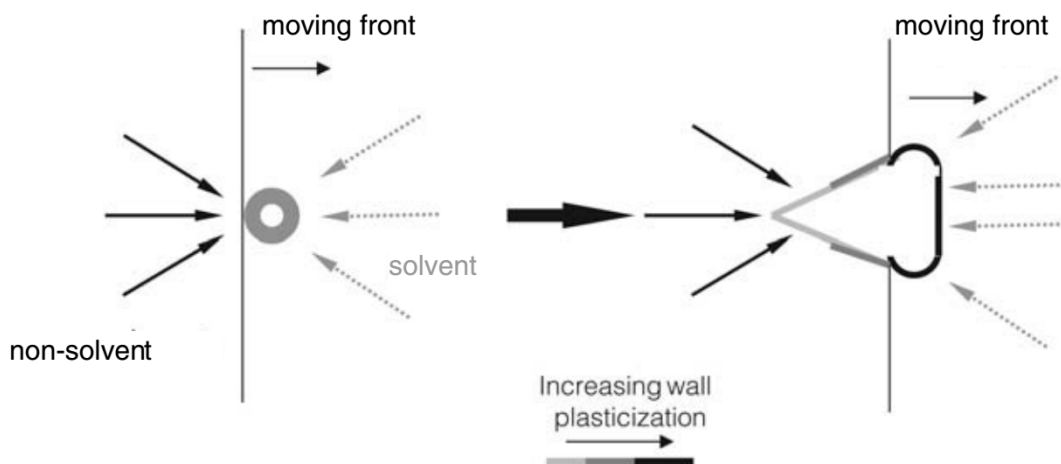


Figure 13 Nonisotropic nucleus growth during macrovoid formation in membranes. Reprinted from Book [161].

In Figure 14 a simple mechanism of pore formation process and respective diagram of phase separation are shown. The critical point of different mechanisms is how the system goes into the unstable region. If it first goes to a metastable condition (Path A), the nucleation and growth mechanism (NG) is favored. If the system crosses the critical point, going directly into the unstable region (Path B), spinodal decomposition (SD) predominates.

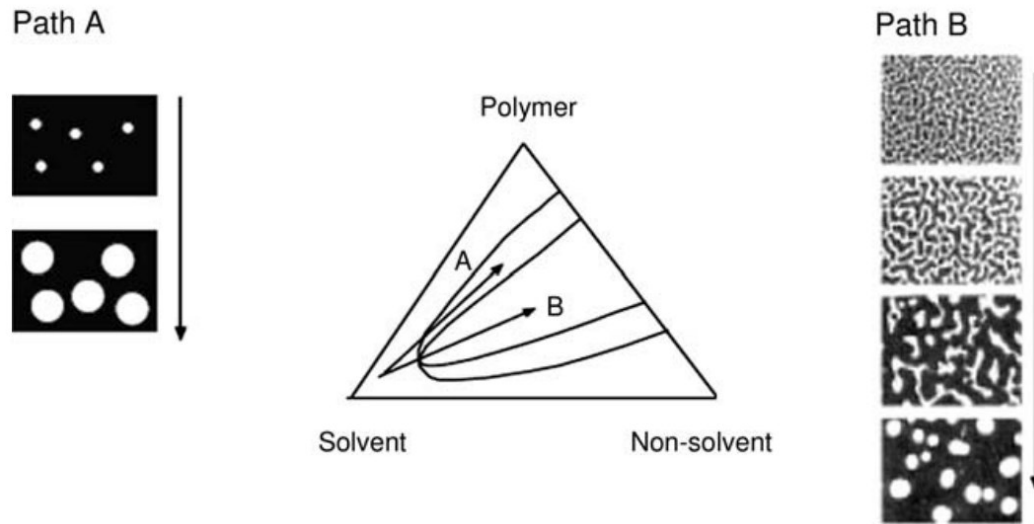


Figure 14 Mechanism of phase separation during membrane formation. Reprinted from Book [161].

As the sketch in Figure 15 shows, the slow solvent-nonsolvent exchange causes the demixing delayed and guides the sponge-like structure. If the demixing happens instantaneously, which means the polymer precipitates and a solid film is formed very rapidly after immersion in the non-solvent bath, finger-like macrovoid will be generated.

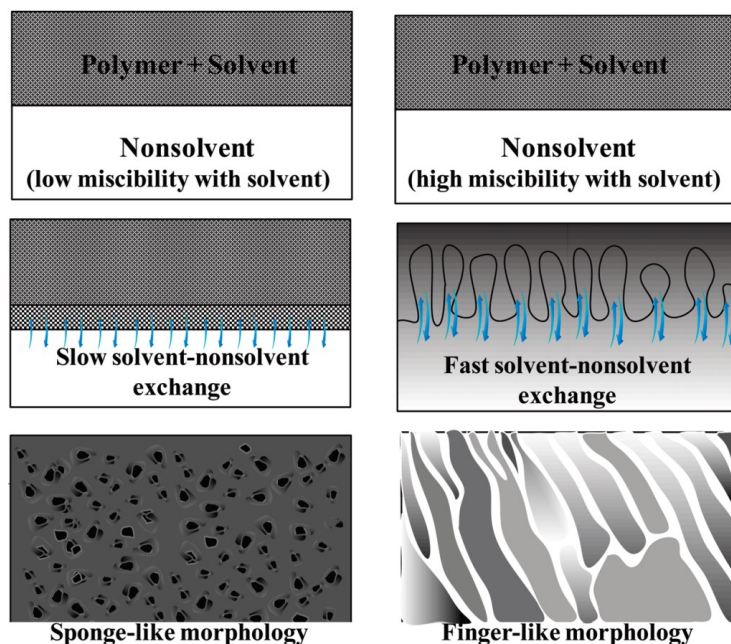


Figure 15 Different membrane morphologies caused of different types of demixing. Reprinted from Reference [162].

The key factors including the solvent type, polymer type and concentration, nonsolvent system type and composition, additives to the polymer solution, and film casting conditions can influence the membrane preparation [162]. More studies in details can be found in reference [162].

The membrane preparation by non-solvent induced phase separation applied on block copolymer in films is firstly realized by Peinemann et al. in 2007 [154]. In their report asymmetric PS-P4VP creates an integral asymmetric membrane with a highly ordered layer on top of a non-ordered sponge-like layer via one-step phase separation. As the two blocks have different hydrophilicity, in the pore formation process the non-solvent (water) first selects and exchanges with solvent in P4VP block and then PS block. The pore formation is guided by the more compatible component (P4VP) to the non-solvent. The solvent from the swollen PS matrix diffuses more easily to the channel walls rather than to the top surface.

The major problem in this process is the lack of sufficient long-range order and the difficulty of up-scaling due to the time-consuming preparation steps. The standing

cylinder structure exists at the surface of solution-cast asymmetric BCP films due to the gradient polymer concentration directly through the film is reported by Russell et al in 2004 [107]. The fast solvent evaporation can induce the cylinder vertically standing to the film surface is demonstrate by Jung and Abetz in 2012 [163].

2 Materials and Methods

2.1. Materials

Poly (styrene-2-vinyl pyridine) (SV⁹⁹) with a total molecular weight of $M_n = 99$ kg/mol and a volume fraction of PS block of 0.56 was synthesized by sequential living anionic polymerization (polydispersity index 1.05). The characteristic lamella spacing L_0 in bulk is about 47.2 nm [137].

Poly (styrene-2-vinyl pyridine) (SV³⁹⁰) with a total molecular weight of $M_n = 390$ kg/mol and a volume fraction of polystyrene block of 0.48 is synthesized by other group. The volume fraction was checked by GPC. The degree of polymerization is 3731 and the interaction parameter (χ) is about 0.178 at room temperature [164], which leads to high segregation strength ($\chi N \approx 664$) with characteristic spacing in bulk of ~ 117 nm. The high segregation strength results a high order-disorder transition temperature, low diffusivity and low kinetics of reorganization [165].

Poly (styrene-block-methyl methacrylate) (SM) with a total molecular weight of $M_n = 50$ kg/mol and a volume fraction of polystyrene block of 0.5 is synthesized by other group.

Polystyrene-block-polybutadiene (SB) with a total molecular weight of $M_n = 47.3$ kg/mol and a volume fraction of polystyrene block of 0.29 is pursued from Polymer Source Inc. and used as received.

Polystyrene (PS) with a molecular weight of $M_n = 184$ kg/mol from Polymer Standards Service Inc. and used as received. Poly (2vinyl pyridine) (P2VP) with a molecular weight of $M_n = 105$ kg/mol synthesized by anionic polymerization.

The solvent including toluene, chloroform, DMF, THF, ethanol with purity of $\geq 99.8\%$ (≤ 50 ppm H₂O) is from Carl Roth GmbH. The boiling point of the solvent like toluene, chloroform and DMF is 110.6 °C, 61.15 °C and 153 °C [166].

2 Materials and Methods

P-type Si wafer was purchased from Crys Tech with ~ 2 nm SiO_x layer in air environment.

$\text{Na}_2\text{PtCl}_4 \cdot x\text{H}_2\text{O}$ for metallization of BCP templates was purchased from Sigma-Aldrich.

2.2. Film preparation

2.2.1. Preparation of the substrates

Si substrates are used as small pieces with $1\text{cm} \times 1\text{cm}$ size after rinsing in toluene solvent for 12 h with further snow-jet treatment and air plasma cleaning. The snow-jet is carbon dioxide crystal from high pressure bottle acting as solid medium to remove dusts from the surface of silicon wafers. In this treatment we put the silicon wafer on the preheated plate with temperature of 200°C , and then blew it with the fast-speed carbon dioxide flow. In this case the crystal evaporates very fast without residual print on substrates. The air plasma was applied using Plasma Flecto 10 (Plasma Technology Company) at a power of 100 W for 60 s with air pressure of 0.2 mbar.

Carbon covered substrates are prepared by PVD of carbon on clean silicon substrates with thickness of ~ 6 nm.

Hard mask (HM) substrates are prepared by spin-coating the solution (HM8006-8) purchased from JSR Micro at 5000 rpm on clean silicon substrates. The coating is then cured on a hot plate at 225°C for 90 s, resulting in ~ 50 nm thick hard mask films [167].

2.2.2. Spin-coating

Polymer films have been prepared by spin-coating from polymer solutions on freshly cleaned substrates. Usually a filtration of the dissolved polymer solution after keeping it still in refrigerator for 12 h is needed for preparation of the polymer solution.

SV^{390} films with varying thickness were prepared from toluene, chloroform and DMF solutions by spin-coating. Film thickness as a function of the solution concentration, also influenced by spin-coating conditions (rotational speed) is presented in Figure 16. The

acceleration of the rotational speed is set as 2k rpm/min in order to arrive at the targeted rotational speed fast.

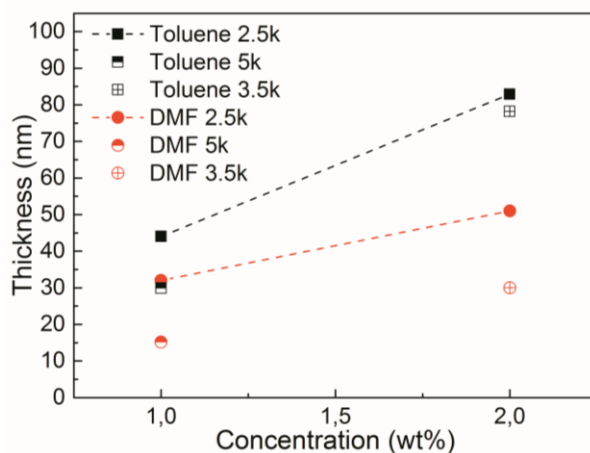


Figure 16 Film thickness of SV^{390} films prepared from solutions in Toluene and DMF as a function of the polymer concentration in spin-cast solution with constant acceleration of 2k rpm/min. The influences to the film thickness from spin-coating condition (rotational speed) are also displayed in the plot, as indicated by symbols. Notation Nk corresponds to N thousands rounds per minute.

BCP films (SV^{390} , SV^{99}) and homopolymer in films (PS^{185} , $P2VP^{105}$) from chloroform solution were prepared with small acceleration of 600 rpm/min which is required to compensate low boiling point of chloroform. The high acceleration will cause un-homogenous spin-cast films with wave-like thickness. The film thicknesses of SV^{390} and SV^{99} studied in this thesis are shown in Figure 17(a) as a function of the polymer concentration in spin-cast solutions. The rotational speed of spin-coating from chloroform solution does not affect the film thickness as much as it does from toluene solution. This difference can be attributed to a slower evaporation rate of toluene as compared to that of chloroform, so that presumably films from chloroform solution get dry before the final rotational speed is reached. The higher molecular weight of BCP causes a thicker film when all the other spin-coating conditions are same, indicating a crucial effect of the viscosity of the solution on this procedure. The spin-coating conditions (polymer concentration and rotational speed) and the prepared film thickness of homopolymer PS^{184} and $P2VP^{105}$ are provided in Figure 17(b).

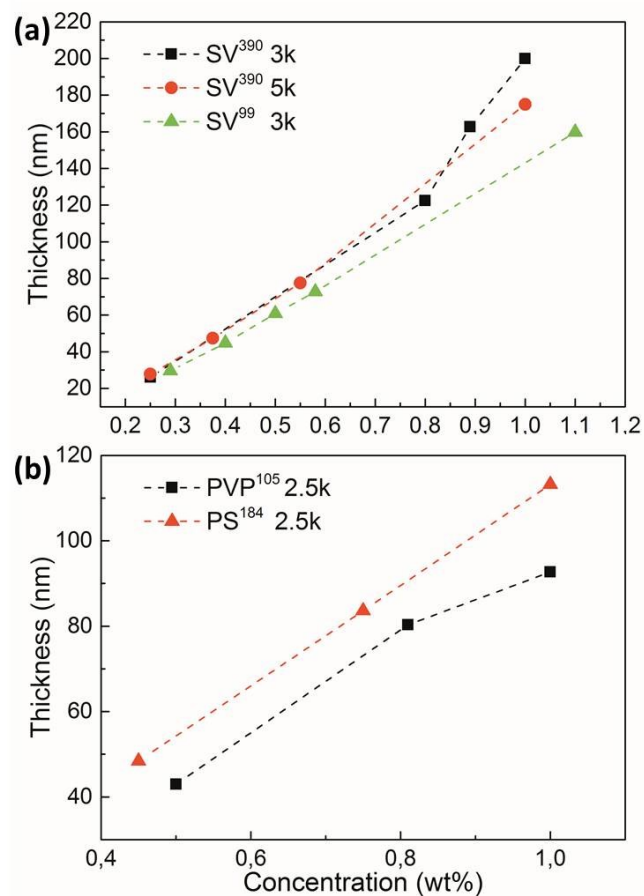


Figure 17 Film thickness of (a) SV³⁹⁰ and SV⁹⁹, (b) PS184, P2VP105 films prepared from chloroform solutions as a function of the spin-cast solution concentration. The comparison between different spin-coating conditions (rotational speeds) is displayed in (a), where notation Nk corresponds to N thousands rounds per minute.

2.2.3. Residual solvent elimination

Then all the films were moved into RT vacuum oven for 12 h to remove residual solution.

2.2.4. Drop-casting procedure

To prepare the polymer in films with thickness of several micrometers the polymer solution is dropped on tilted substrates and the solvent slowly moves out of the solution.

2.2.5. Floating of the films

To check the bottom morphology of BCP films, the films on silicon substrate are floated by inserting the samples in NaOH solution with concentration of 1mM. For the SiO_x layer between the polymer film and the silicon substrate can react with OH⁻, the polymer film will be peeled off from the substrate and float at the solution surface. The film was then caught flipped up by another clean silicon substrate from top of the surface, and then rinsed in deionized water twice.

After preparation the films were moved into RT vacuum oven for 12 h to remove residual solvent.

2.2.6. Metallization of the microphase separated patterns

Pt ions are loaded to P2VP blocks by dropping the Na₂PtCl₄ 1% HCl solution with concentration of 5 mM on SV templates. P2VP blocks become protonated carrying positive charges in acidic environment, so the anions (negatively charged Pt ions) are then attracted to the cationic P2VP blocks and become embedded in these blocks [168]. The polymer is removed by oxygen plasma under 0.2 mbar at 80 W for 90 s leaving Pt nanostructure in the shape of what it was as the P2VP blocks on a substrate [169].

2.3. Film processing via thermo-solvent annealing

Since thermo-solvent annealing is an important part of the research of the present Thesis, all the details of annealing process are presented in Chapter 3

The technical details are the following. The flow controllers were Multi Gas Controller 647C from MKS Instruments, Inc.

The thermostats are from Julabo GmbH in type FH-32. It was established that the temperature of the circulating water is 2 °C lower than the value shown on the screen of the thermostat.

2 Materials and Methods

2.4. Film characterization

Polymer volume fraction in the swollen film Φ_p is calculated as h_d/h_s , where dry and swollen films were measured by in situ ellipsometry as homogeneous film. Polymer volume fraction is a critical parameter for calculating χ_{eff} of BCP during solvent annealing, for the solvent adsorption of BCP will affect χ value a lot and $\chi_{\text{eff}} = \chi * \Phi_p$ is introduced to describe the new interaction between blocks.

Degree of swelling (D) is a reciprocal of Φ_p . In the modulate curve of BCP films, degree of swelling is an important parameter for kinetics analysis of BCP swelling.

2.4.1. Ellipsometry

The incidence angle of ellipsometry (OMT Imaging) was set at 70° and the thickness was simulated by Cauchy model in spectral range from 450 nm to 800 nm with VisuEI software 3.8.

Another single wavelength (632.8 nm) ellipsometry instrument - The Multiskop from Optrel GbR. with program Elli (3.2 version) was also used for film thickness measurement at 70° incidence angles.

- Theory

Ellipsometry is a non-destructive optical technique (the near-UV, visible and near-IR wavelength ranges) relying on the changes in the polarization state of light induced by reflection from the surface of a sample. In a typical ellipsometry system shown in Figure 18, the incident is polarized by passing through a polarizer between the light source and the sample. After reflection the change in polarization state is measured by a second polarizer coupled with a detector, the analyzer.

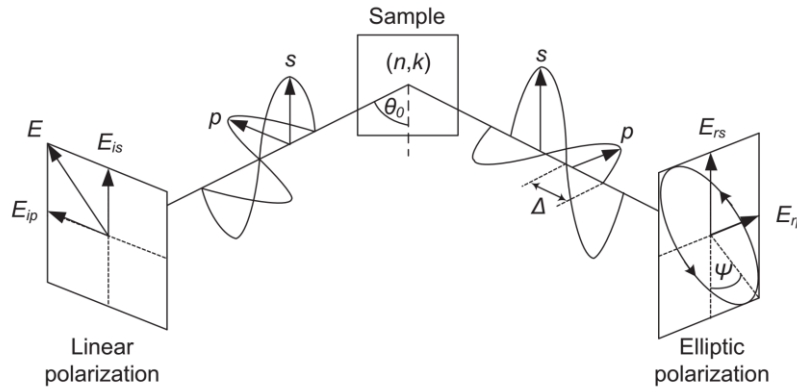


Figure 18 Schematics of ellipsometric measurement principle. Copyright of Reference [170].

The reflected light polarization state can be described in terms of the two angles: psi (Ψ) and delta (Δ), where Ψ represents the angle determined from the amplitude ratio between p- and s-polarizations, while the Δ represents the phase difference the two components. These values are related to the ratio of Fresnel reflection coefficients r_p and r_s for p- and s- polarized light, respectively shown in Equation 3. The polarization state of the reflected light depends on the angle of incidence, θ_0 , the thicknesses of the (m-1) layers, h , and the complex refractive indices ($N = n+ik$) of all of these layers, the ambient (N_0), and the substrate (N_m). This signifies the richness of information contained in the probing light [171].

$$\tan(\Psi) \cdot e^{i\Delta} = \frac{r_p}{r_s} = \rho(N_0, N_1, \dots, N_m, h_1, \dots, h_{m-1}, \theta_0) \quad \text{(Equation 3)}$$

The main three advantages of ellipsometry over simple intensity-based reflection or transmission measurement are precision, sensitivity and information [172]. As the change in polarization state is defined by a ratio, ellipsometry can remain accuracy without measuring ‘absolute’ intensity of the measurement beam. For an optically uniform and transparent polymer film on a polished silicon wafer this translates into a precision [171]. The phase information contained in Δ parameter enhanced sensitivity of ellipsometry to ultra-thin films, even down to the sub- nm thickness level [172]. For single-wavelength ellipsometry, a single pair of Ψ and Δ can be measured at one incident angle, which means at maximum two parameters can be simultaneously

2 Materials and Methods

determined from the measurement. For spectroscopy ellipsometry, a pair of Ψ and Δ can be generated for each employed wavelength, so consequently, the number of sample parameters that can be independently determined increases significantly. The high accuracy, precision and sensitivity of the ellipsometry measurement make it powerful for optical characterization of thin films.

- *In-situ* ellipsometry

In-situ ellipsometry provides a possibility of dynamic measurement to monitor the changes of film properties like thickness and refractive index during the annealing process in our case. The annealing in our work is done in near-atmosphere pressure with an air-tight chamber set to contain samples in ambient of gas or liquid (details and pictures of chamber are presented in Figure 24). The glass windows of the chamber need to be transparent in the range of measurement wavelength and optically isotropic. We choose the incident angle of 70° due to it is close to the Brewster angle of crystalline silicon substrate ($74.9^\circ \sim 78.6^\circ$ depending on the wavelength from 427.5 nm to 774.9 nm [173]) and is not far from the Brewster angle of polymer ($54.5 \sim 58.0$ from refractive index 1.4 ~ 1.6 [174]). The windows of the chamber need to be perpendicular to the incident light.

- Model used to evaluate the ellipsometric data

In this work the samples are mainly polymer material in films with thickness between 20 nm to 200 nm on polished silicon substrates with top oxide layer of ~ 2 nm. When light enters such a sample it reflects and transmits at each of the interfaces, Figure 19. The rays leaving the sample interfere with each other and produce spectral oscillations in Ψ and Δ [171].

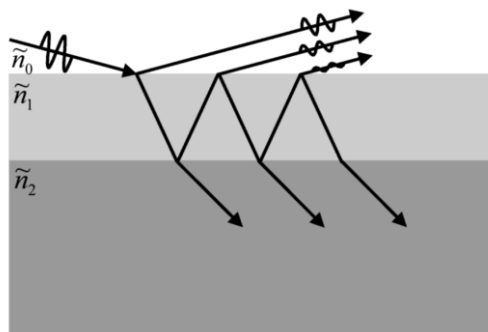


Figure 19 Interference within a transparent thin film. Copyright of Reference [171].

The Cauchy relation (Equation 4) models the optical features like thickness, refractive index and optical dispersion etc. of polymer in films thinner than 500 nm, for polymeric materials are mostly simple transparent dielectrics [175]. For the sample with terraces morphology, the ellipsometry measurement gives the average thickness over the measured area [176].

$$n(\lambda) = A + \frac{B}{\lambda^2} + \frac{C}{\lambda^4} \quad (\text{Equation 4})$$

2.4.2. Scanning force microscopy

Surface images were measured by scanning force microscopy (SFM), Bruker Dimension Icon, in tapping mode and analyzed by Nanoscope Analysis software.

Scanning force Microscopy (SFM) is a branch of Scanning Tunneling Microscopy (STM) whose inventor earned the Nobel Prize for Physics in 1986, was invented by Binnig et al. in 1986 [177]. In contrast to STM, which senses the tunneling current, the SFM senses forces between the tip and the sample [178], which makes the measuring of insulating samples possible. Comparison with other imaging methods like SEM, TEM and Optical Microscopy, the major advantages of SFM is its high resolution (XY direction of 1 nm, Z direction of 0.1 nm) and its non-destructive testing (free of beam irradiation). SFM has been applied in a wide range of disciplines of the natural science including polymer chemistry[179–182], surface chemistry [183; 184], molecular biology [185; 186], cell biology [187], solid-state physics and so on from aspects of force measurement[188], imaging[185; 186; 189–191] and manipulations[192–196]. When it focused on polymer chemistry[197–199], SFM is used for investigating surface topography, surface lattices, conformational and chain order, crystalline order, orientation and morphology and last but not least mechanical properties like elastic modulus and adhesion [200].

2 Materials and Methods

- Setup and Feedback Loop

In SFM the scanning probe is consisted with the cantilever and a sharp tip at the end. The dimension of the tip is typically less than $5\mu\text{m}$ tall and less than 10 nm in diameter. The feedback loop is presented in Figure 20(a). The photodiode detector measures the deflection of a tip which is magnified by the laser light to map the surface topography. The force between a tip and a sample is presented in Figure 20(b) when the tip is brought proximity to the sample surface. This force can be calculated from the deflection of the cantilever based on Hooke's law [201]. Based on this principle, the forces can be measured by SFM including mechanical contact force, van der Waals forces, capillary forces, chemical bonding, electrostatic forces, magnetic forces, etc.

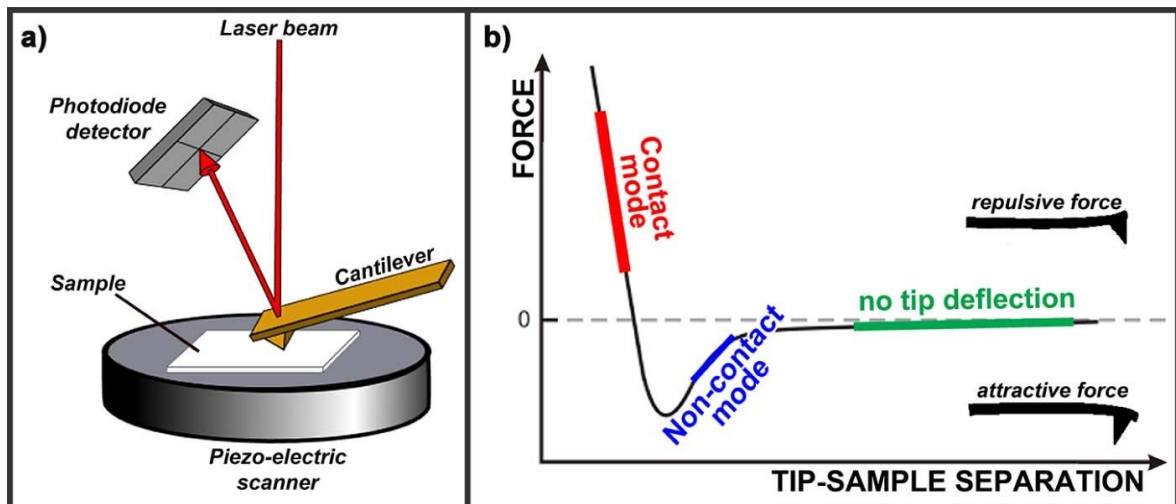


Figure 20 (a) Scheme of depicting feedback loops in XY and Z to create an SFM image. (b)The force related with distance between the approaching tip and the sample. Reprinted from Ref [202]

- Tip issues

The image quality from SFM is influenced by a number of factors and the tip is a critical one as the SFM image is a result of the interaction of the probe tip with the surface topography. In our case the radius of curvature of the tip is a factor should be considered for the details of BCP morphology which is in range of nanometer. As the scheme (in Figure 21) shows, the smaller the radius curvature is the more delicate features can be scanned, especially when the feature has a high aspect ratio of depth and width.

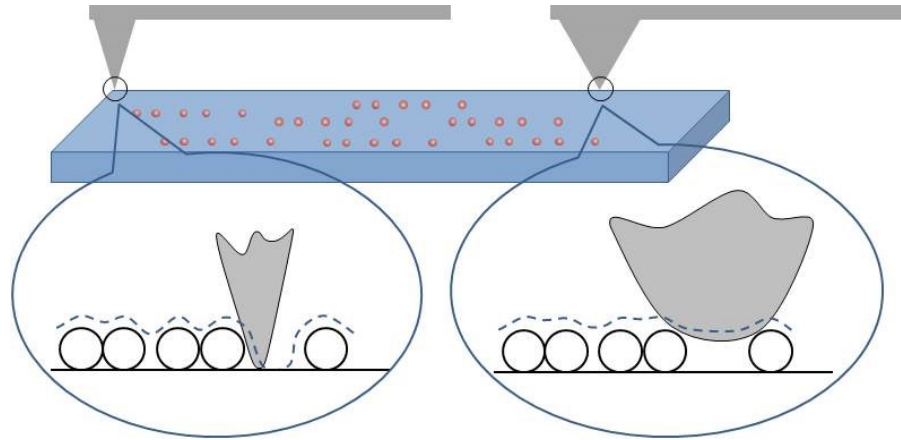


Figure 21 Effect of tip radius.

- Tapping Mode

Tapping mode is the most commonly used SFM mode for its high lateral resolution and minimization of contact and lateral forces between the tip and sample [203], which is important for reproducing images in the study of delicate proteins and polymer.

During measurement the cantilever is driven to oscillate at or a little smaller than its resonance frequency. The oscillation amplitude of cantilever changes as the sample topography changes. The topography image is obtained by monitoring this amplitude change. Phase imaging is a secondary mode of Tapping Mode, which is based on the phase difference between the cantilever oscillation and its drive signal. Phase imaging is usually used in qualitative analysis of surface mechanical properties, for it is very sensitive to both the short and long-range of sample-tip interaction. Sometimes phase imaging can even test the difference of mechanical property under surficial layer.

- Peak Force Mode

PeakForce Tapping operates similarly to Tapping Mode in that it avoids lateral forces by intermittently contacting the sample[204]. But its oscillation is far below the cantilever resonant frequency, the vertical motion of the cantilever using the (main) Z piezo element and relies on peak force for feedback. Peak interaction force and nanoscale material property information is collected for each individual tap[205].

PeakForce Tapping mode can quantitate the mechanical properties. The plot of Force vs. Time is displayed in Figure 22(a) where the blue curve indicates approaching process

2 Materials and Methods

and the red curve indicates withdraw process. Depending on the Z-position this plot is transferred in plot of Force vs. Distance shown in Figure 22(b), which provides information about the peak interaction force for analyzing the mechanical properties of the sample. Deformation usually is not negative and the softer sample has the higher deformation, which is the opposite of modulus.

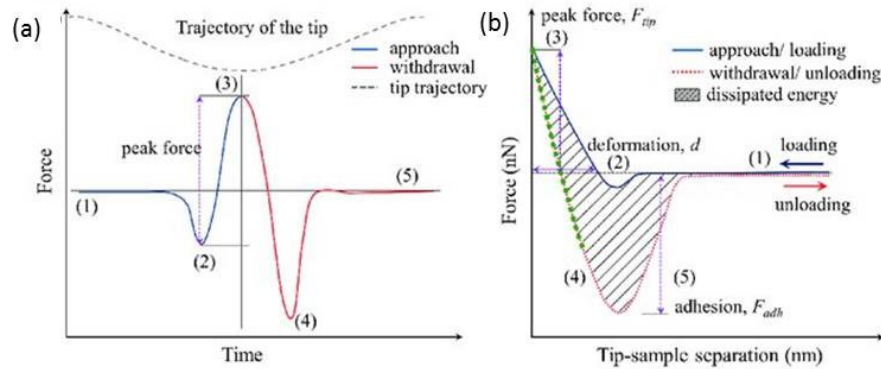


Figure 22 Scheme of Force vs. Tip-sample separation of PeakForce mode and the typical images obtained by this mode. Reprinted from Ref [206].

Dimension FastScan and Dimension Icon from Bruker Corporation are used for SFM measurement in this thesis. Tips in type of OTESPA with spring constant of 42 N/m and initial frequency of 270-349 N/m are used in Tapping Mode. Tips in type ScanAsyst-Air with initial frequency of 70 kHz and small spring constant of 0.4 N/m are used in Peak Force Mode.

2.4.3. Optical Microscopy

Axioplan 2 imaging microscope from Zeiss is used for micrometer range morphologies like terracing and dewetting. These two kinds of morphology usually exist after annealing of long time or high degree of swelling.

2.4.4. Other imaging techniques

Field Emission Scanning Electron Microscopy (FE-SEM) (HITACHI S-4800) at an operating voltage of 3 kV is used for characterizing Pt network after metallization.

Small-angle X-ray scattering (SAXS) (European Synchrotron Radiation Facility) is used to measure bulk structure of SV films.

3 Scientific and practical aspects of controlled solvent vapor annealing

As one of the most widely used methods to equilibrate the microphase separated structures of block copolymers, solvent vapor annealing provides advantages of flexibility and effectiveness in terms of various solvent conditions and time-saving process especially for BCP with high molecular weight. Solvent vapor annealing can also overcome the contradiction of some polymers between their relative low decomposing temperature and high ODT, which has to be solved in thermal annealing. Although this method has been used for decade years, there is still no standard apparatus which can simplify the reproducibility and results comparison [141]. The solvent vapor annealing is sensitive to environment conditions like solvent vapor pressure, temperature of vapor/substrates, and even the orientation of the vapor flow. The self-assembly of block copolymer is decided by the comprehensive effect of the polymer volume fraction, the interaction parameter between two blocks, the interaction of surface/air and film/substrate, the polymer chain mobility and so on, which are also influenced by the annealing conditions.

In this chapter we will first introduce our annealing system from the aspects of technical factors like its design, the flow amount and the flow orientation. Then the temperature influenced swelling behavior of SV is presented. Finally the swelling behavior of homopolymer (PS, P2VP) and the solvent selectivity to SV are studied, which provides important information for the following chapters.

3.1. Description of the annealing setup and discussion of the system relative parameters

The schematic of our annealing system with partial vapor pressure (p/p_0) control system and temperature separate control system (vapor and substrate), which can provide precise annealing conditions, is shown in Figure 23. There are three vapor channels for mixed or pure vapor, flow controllers to quantify the vapor flow, two thermostats to maintain the temperature of vapor and substrate separately, and an in situ ellipsometry to

3 Scientific and practical aspects of controlled solvent vapor annealing

monitor the film thickness during annealing. We tune the partial vapor pressure of solvent in the chamber by mixing the flow of dry nitrogen (Channel 1) with the flow of dry nitrogen purged through a reservoir with the solvent (Channel 2), all immersed in a thermostat bath, at a certain proportion and/or changing the temperature of the vapor and/or the substrate. In this set up not only mono solvent vapor but mixtures of solvent vapors can be realized by adding additional channels (Channel 3 in Figure 23).

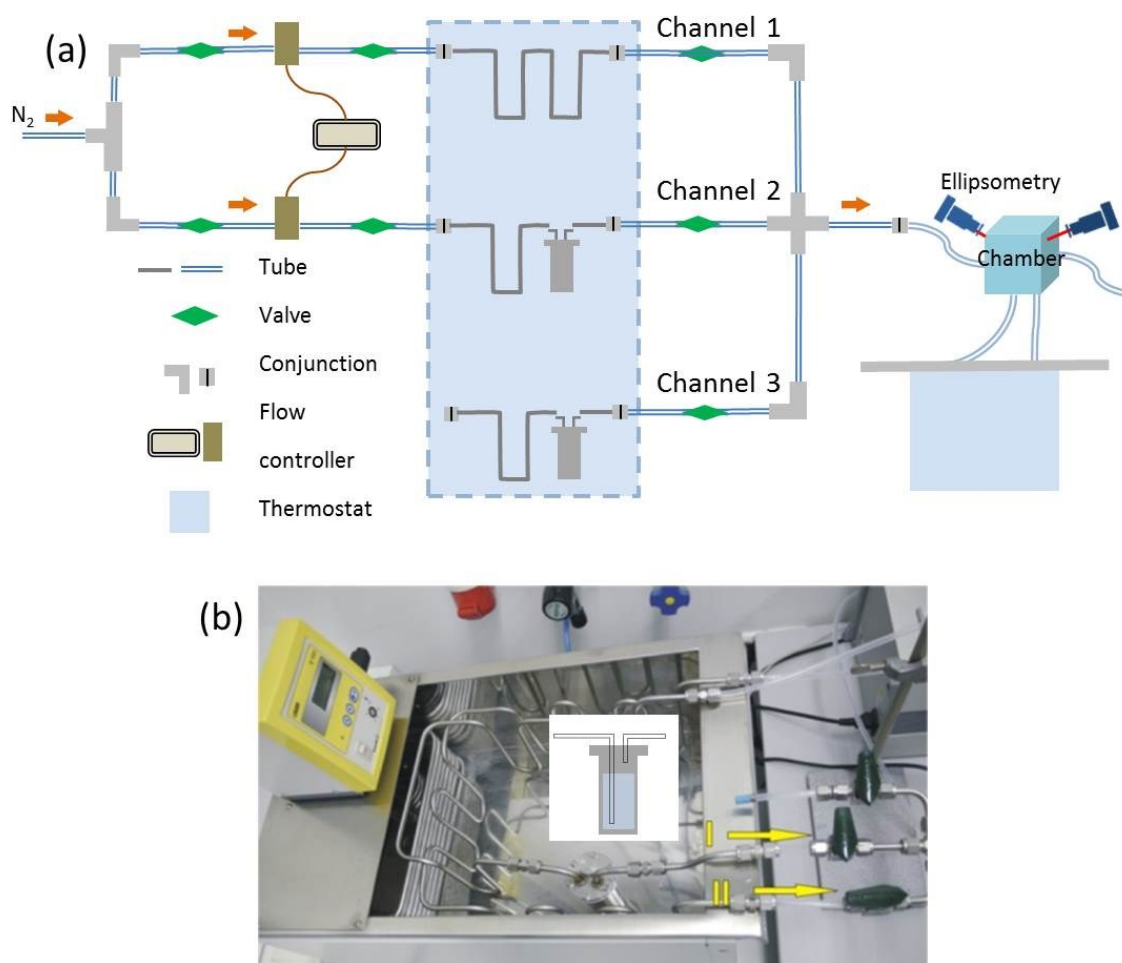


Figure 23 (a)The sketch of the whole annealing system (b) the picture of the solvent vapor controlling reservoir with the sketch of the solvent capsule

The degree of swelling in a swollen film is presented as $\Phi_p = h_d / h_{sw}$, where the h_d is the dry start film thickness and h_{sw} is the swollen film thickness. The polymer volume fraction is the reciprocal of degree of swelling.

3 Scientific and practical aspects of controlled solvent vapor annealing

In the annealing to tune SV self-assembly, films were treated for 200 min to guarantee the re-organization of block copolymer completed. If not stated others, the total flow through the chamber was 100 sccm. To avoid condensation of the solvent at the film surface the temperature of the substrate should be maintained at least 1°C higher than the vapor. The partial vapor pressure of the solvent in a chamber (and consequently the solvent up-take by a polymer film) can be directly adjusted either by mixing the flow of the saturated solvent vapor and the flow of dry nitrogen at a certain proportion, or indirectly by varying the temperature of the vapor in the chamber.

3.1.1. Reproducibility of the swelling experiments

- Assessment of the chamber influenced

Solvent annealing was performed in two kinds of custom-made chambers, as shown in Figure 24, made of Teflon (i) and stainless steel (ii). In the sketches of the chambers (Figure 24 iii and iv) there is the chamber wall (a), transparent window for observation of the film integrity with optical microscopy (b), inlet and outlet connections for vapor tubes (c) and tubing in the bottom of the chamber for the substrate (d). The differences of these two chambers are a) the volume of the chamber and b) the design of vapor tube.

- a) The free volume of the Teflon chamber for solvent vapor is ~1 ml when we use silicon wafer in size of 1*1 cm, which is smaller comparing to the steel chamber of ~60 ml.
- b) As shown in Figure 24, the Teflon chamber in (iii) has an opposite inlet and output design for vapor tubes, while the inlet/outlet tubing is positioned next to each other in the steel chamber. The narrow space and the opposite design of the vapor tube on the Teflon chamber may cause a laminar flow of the solvent vapor above the substrate, while a turbulent flow is expected in the steel chamber.

All these factors can lead a difference in the swelling of the films and indeed we found that the chamber geometry and the chamber material affect the degree of swelling slightly from our results.

3 Scientific and practical aspects of controlled solvent vapor annealing

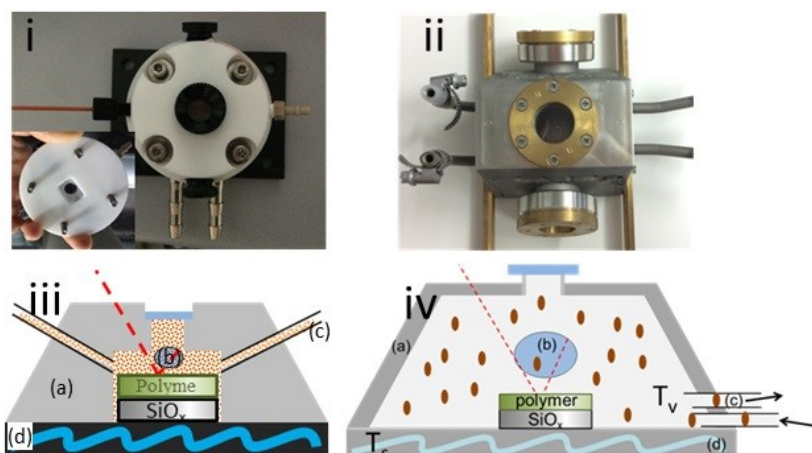


Figure 24 Pictures (i) (ii) and sketches (iii) (iv) of the annealing chamber used in our experiments. T_v and T_s are the temperatures of the vapor and the substrate respectively. (a) The metal wall of the chamber. (b) The transparent window for in situ ellipsometry measurement. (c) The vapor tube connected to the solvent vessels settled in the thermostat reservoir. (d) The cycling water to maintain the substrate at a setting temperature. The Teflon chamber has the vapor tube facing each other, but the steel chamber has them on the same side.

First we compared the film swelling process under the stepwise increasing partial vapor pressure in the two chambers with all the other conditions same in Figure 25. The higher polymer volume fraction in Teflon chamber could be caused by vapor flow characteristics.

As mentioned above, in the Teflon chamber the vapor flow may go through the chamber as laminar flow above the sample. Based on Bernoulli's principle, the flow with high speed has lower pressure. Comparing with the steel chamber with turbulent flow inside, the environment pressure in the Teflon chamber is lower than that in the steel chamber, which causes the smaller swelling.

3 Scientific and practical aspects of controlled solvent vapor annealing

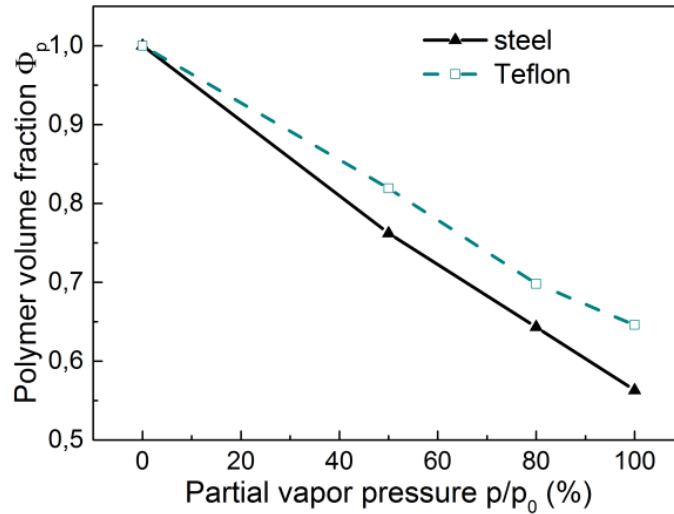


Figure 25 Polymer volume fraction of SV (~40 nm) films as a function of stepwise increasing of the partial vapor pressure (p/p_0) of chloroform at temperature set (T_v/T_s) of 14 °C/20 °C in steel and Teflon chambers.

Table 1 lists the polymer volume fraction displayed in Figure 25 , where the deviation in the two chambers at 100% solvent vapor is 16.1% and 9.9 nm in terms of polymer volume fraction and film thickness, respectively.

Table 1 Polymer volume fraction of SV with thickness of 40 nm in steel and Teflon chamber under increasing partial vapor pressure of chloroform

Chamber	50%	80%	100%
Steel	0.76	0.64	0.56
Teflon	0.82	0.70	0.65

- Influence of the environment on the degree of swelling of polymer films

In Figure 26 we compare the kinetics curves of the SV³⁹⁰ film with thickness of 40 nm in two isotherm systems with different thermostats and tube line cycle, but the same annealing conditions and the steel chamber, denoted as System 1 and System 2. When the partial vapor pressure increases from 0 to 100%, the curve obtained in System 1 increases faster and reaches a higher plateau than the curve obtained in System 2. The factors causing this difference are various including the different environment temperature, different length of vapor circles and even the precision of the thermostat.

3 Scientific and practical aspects of controlled solvent vapor annealing

So the in situ film thickness monitoring during the annealing is very important to control the swelling of the film.

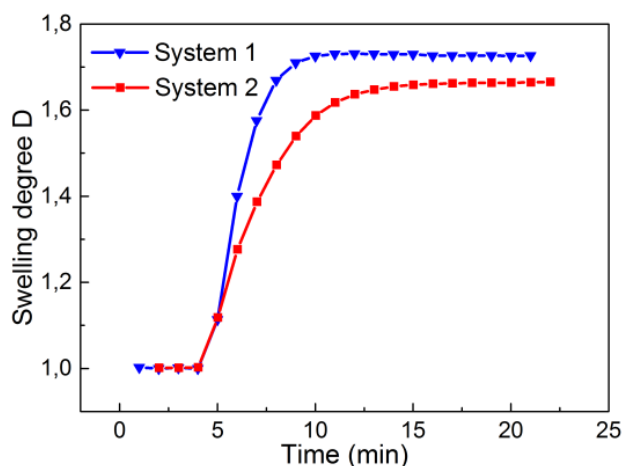


Figure 26 Kinetics curves of ~ 40 nm SV^{390} films under chloroform vapor, when the partial vapor pressure changes from 0 to 100% at 24 °C/30 °C in the steel chamber with two annealing systems as indicated.

Because the reproducibility between different setups is not perfect, meaning that a direct comparison between published results of different groups should account for possible systematic errors, it is important that any comparative experiments are done under exactly the same set up.

3.1.2. Solvent vapor regulation in the chamber

There are two principle methods to adjust the concentration of the solvent vapors in the chamber: (i) by mixing the flows from channels 1 and 2 with constant temperature of the substrate and the vapor, and (ii) by tuning the temperature of the vapor/substrate at constant flows, which is interpreted in part 4.2. While the first approach is more robust with regards to possible fluctuations of the environmental temperature and creates a permanent flow within the chamber, the second approach is promising in a view of developing thermo-solvent annealing method, as will be described below.

- Method (i)

In the experiment we produce solvent vapor using the flow through the vessel with a solvent immersed in the thermostat bath, shown in Figure 23. A flow of dry nitrogen is

3 Scientific and practical aspects of controlled solvent vapor annealing

directed through a short tube immersed in the solvent in the vessel at a fixed temperature in the bath so that the out-coming flow is enriched with the saturated solvent vapor (we assume an air pressure in the closed system and treat the solvent vapor as 100% saturated). Then we mixed the produced mixture of solvent vapor and nitrogen) with a pure nitrogen flow from another channel and calculate the partial vapor pressure p/p_0 based on the proportion of the two channels. The produced concentration of solvent vapor is relative with a) solvent property and is also influenced by b) the total flow of solvent vapor.

a) Effect of the solvent properties on the vapor concentration in the chamber (p/p_0)

The saturated pressure of a solvent increases as the environment temperature does and it depends on the property of solvent, which is shown in Figure 27 with data referred from Dortmund Data Bank (chloroform) and Reference [207] for toluene. As seen in the plot, the saturated pressure of the solvent is sensitive to the temperature especially when it comes to chloroform.

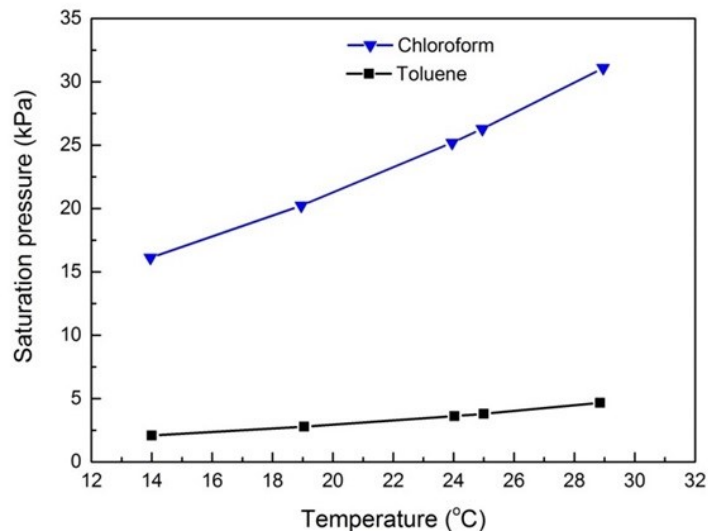


Figure 27 The saturation pressure curves of toluene and chloroform increasing as the temperature does. The blue curve with triangles indicates chloroform and the black curve with squares indicates toluene.

As it mentioned before, we treat the produced vapor from the vessel as 100% partial vapor pressure, but indeed the vapor is mixed with nitrogen. Below we present the data

3 Scientific and practical aspects of controlled solvent vapor annealing

on the consumption of solvent under nitrogen flow with 100 sccm for 3 h and calculate the real partial vapor pressure of solvent at each temperature. As the values shown in table 2, we measured the weight of solvent with the vessel before (m_0) and after (m_1) annealing and calculated the consumed weight (Δm) and their corresponding mole (n). The consumption of chloroform is much higher than that of toluene due to the higher saturated pressure of chloroform.

Table 2 The consumption of solvent during the annealing

	Toluene		Chloroform	
	19 °C	25 °C	19 °C	25 °C
m_0 (g)	558,78	556,55	644,05	646,0
m_1 (g)	556,65	553,6	619,72	612,13
Δm (g)	2,13	2,95	24,33	33,87
n (mol)	0,023	0,032	0,204	0,284

The partial vapor pressure of solvent is calculated by the ideal gas law (Equation 5) and the results are shown in Table 3:

$$PV = nRT \quad (\text{Equation 5})$$

We can find that the real partial vapor pressure of the produced solvent vapor is far from the value of 100% what we use. The real partial vapor pressure is 38.6% for chloroform at room temperature, which is about 9 times more than toluene at the same temperature. The huge difference of the real partial vapor pressure can explain the different degree of swelling under these two solvent vapors from one side. The other side is the interaction parameter between the two blocks, which is interpreted in details below.

These consumption values are useful to approximate the longest time of the annealing can last. These real values do not play an important role in reproducing the swelling between different annealing systems and comparing the swelling at different temperature in a same system.

3 Scientific and practical aspects of controlled solvent vapor annealing

Table 3 The partial vapor pressure calculated from the consumption of solvent

	mole	Temperature (K)	V(ml)	Partial vapor pressure (%)
toluene 19 °C	0,023	292,15	551,38	3,1
toluene 25 °C	0,032	298,15	782,90	4,3
chloroform 19 °C	0,204	292,15	4890,53	27,2
chloroform 25 °C	0,284	298,15	6948,21	38,6

b) Effect of the total flow through the chamber on the degree of swelling of polymer films

To find out if the total flow affects the degree of swelling, we present the annealing curves in Teflon chamber under toluene vapor with temperature control system and varied total flow (Figure 28a).

In Figure 28a, the curves with very unstable plateaus at each partial vapor pressure are obtained under total flows of 20 sccm, 50 sccm, 80 sccm and 100 sccm. After that we found the thermostat for solvent vapor has a problem with the cycling water, so the temperature of solvent capsule fluctuates around the set temperature.

In Figure 28b the swelling curves in chloroform vapor in non-isothermal environment under flow of 20 sccm show slight upwards floating before it arrives at relative stable plateaus at each partial vapor pressure, which is not found in the other vapor-temperature-controlled annealing. The reason of this phenomenon is that the temperature around the annealing system is increasing during annealing because of the heat dissipated from the running devices. Lower heat capacity of the vapor than the substrate makes it is easier to be fluctuated by the change of environment.

But the floating of the swelling curves under 50 sccm and 80 sccm show inversed trend as compared to the case at 20 sccm. Because N₂ flow at standard room temperature blowing into the solvent capsule cools down the vapor temperature. When the total flow is high enough, this cooling-down performance may dominate the film swelling. But for the total flow of 20 sccm, it is not capable to offset the influence from the environment temperature.

3 Scientific and practical aspects of controlled solvent vapor annealing

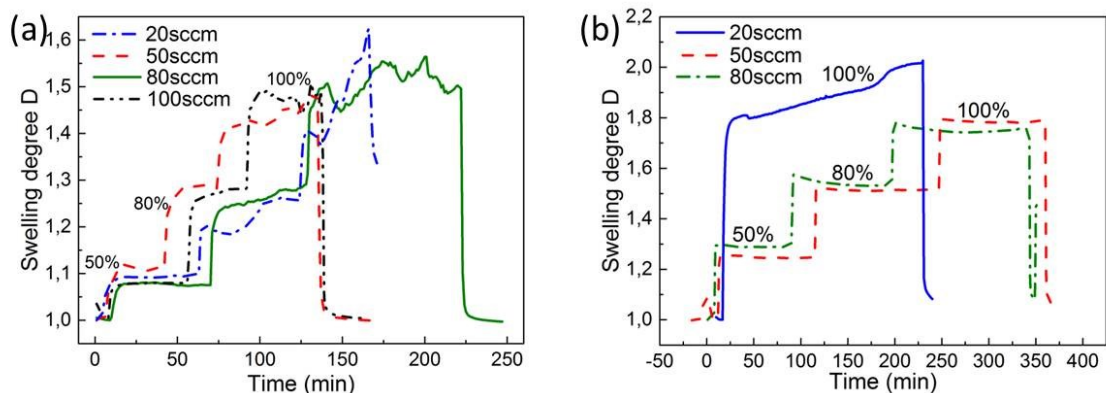


Figure 28 Kinetics curves of ~40 nm SV³⁹⁰ films in (a) Teflon chamber with toluene vapor at 19 °C/20 °C (b) steel chamber with chloroform vapor annealed at room temperature

To find out how big the influence of environment temperature on the partial vapor pressure is, we compared the degree of swelling of a film under different total flow at room temperature and at a strictly controlled temperature of 19 °C/20 °C (Figure 29). All data has been measured under 100% partial vapor pressure of chloroform. We can find the degree of swelling of 20 sccm and 100 sccm at strict control temperature has only 2% deviation. But the swelling at room temperature has 14.6% deviation from 80 sccm to 100 sccm with room temperature changing less than 1 °C.

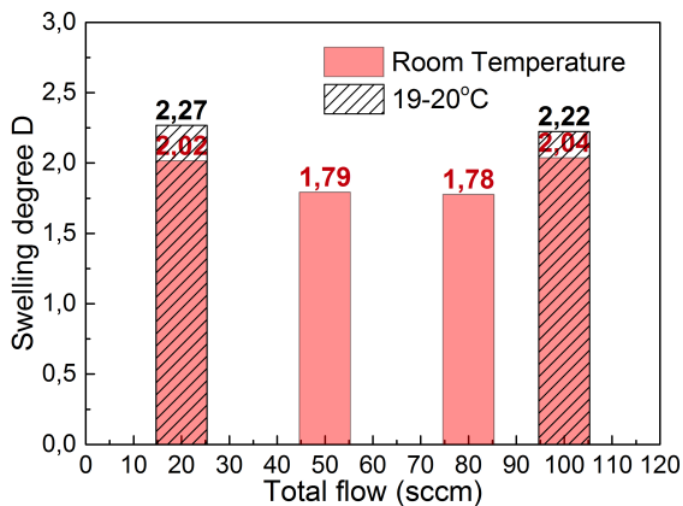


Figure 29 Comparison of the degree of swelling of SV³⁹⁰ ~40 nm thick films between room temperature and maintained at 19 °C/20 °C in chloroform vapor with 100% p/p₀ at total flow of 20 sccm, 50 sccm, 80 sccm and 100 sccm

3 Scientific and practical aspects of controlled solvent vapor annealing

From these two figures we can get that the swelling of the block copolymer film is very sensitive to the environment temperature, so the annealing temperature should be under a strict control.

3.2. Swelling behavior of SV³⁹⁰ films: temperature effects

The temperature control is the most important issue in thermo-solvent annealing, because it is not only an effective method to control the degree of swelling of films but also a critical parameter influencing the surface tension, the interaction parameter and the mobility of the block copolymer in films.

3.2.1. Control over degree of swelling by vapor temperature

In our experiment the partial vapor pressure of the solvent in a chamber (and consequently the solvent up-take by a polymer film) can be directly adjusted by mixing the flow of the solvent vapor and nitrogen with different proportion, or indirectly adjusted by varying the temperature of the vapor and the substrate. We can calculate the partial vapor pressure in chamber according to Clausius-Clapeyron equation:

$$\ln(p_v/p_s) = -\Delta H_{vap}/R * (1/T_v - 1/T_s) \quad (\text{Equation 6})$$

Here R is the ideal gas constant. ΔH_{vap} is the enthalpy of evaporation of the solvent. T_v is the temperature of solvent vapor which is same with the thermostat reservoir which contains the solvent vessel, and T_s indicating the temperature of substrate, p_v/p_s indicating the partial vapor pressure of solvent in chamber.

To evaluate how the vapor temperature affects the degree of swelling of polymer films, we present data obtained at $T_v = 14\text{ }^\circ\text{C}$ $T_s = 20\text{ }^\circ\text{C}$ and $T_v = 19\text{ }^\circ\text{C}$ $T_s = 20\text{ }^\circ\text{C}$ in Figure 30. As expected, the film at $T_v = 14\text{ }^\circ\text{C}$ obviously swells less than that at $T_v = 19\text{ }^\circ\text{C}$. The reason of the decreased swelling is the change of saturated pressure of chloroform. From Equation 2 the saturated pressure of chloroform is 16.04 kPa at $14\text{ }^\circ\text{C}$ and 20.17 kPa at $19\text{ }^\circ\text{C}$. When we decrease the temperature of vapor, the vapor pressure produced by chloroform solvent also decreases. For example when we set the vapor temperature of $14\text{ }^\circ\text{C}$ with the temperature of substrate still at $20\text{ }^\circ\text{C}$, the new partial vapor pressure

3 Scientific and practical aspects of controlled solvent vapor annealing

cannot arrive at what the film needs at 20 °C, although we set the annealing system with 100% chloroform vapor flow. We present the ‘relative partial vapor pressure’ by the ratio of saturated pressure of chloroform at temperature of vapor divided by that at the temperature of substrate. In our example, the ‘relative partial vapor pressure’ is 76.1% under 100% solvent vapor flow, when T_v at 14°C and T_s at 20°C. Using the same idea, we can calculate that the relative pressure of chloroform at 19 °C/20 °C is 95.0% under a same solvent vapor flow.

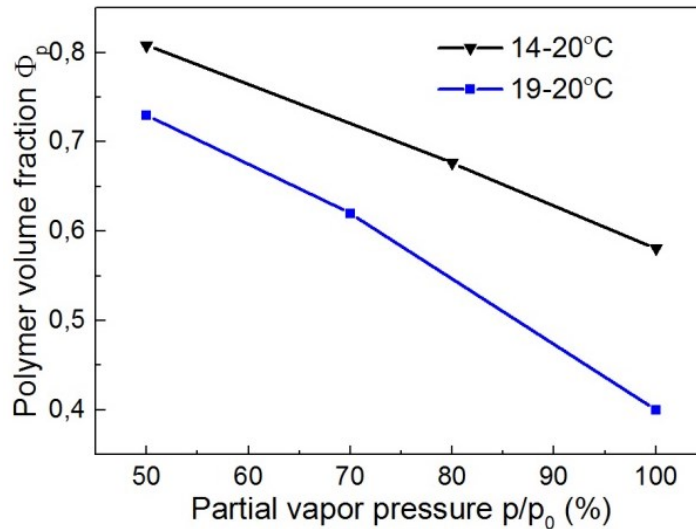


Figure 30 Polymer volume fraction Φ_p of SV film with dry thickness of ~40 nm under stepwise increasing partial vapor pressure of chloroform at $T_v = 14$ °C, $T_s = 20$ °C (black triangle) and $T_v = 19$ °C, $T_s = 20$ °C (blue square)

The effect of the substrate temperature on the degree of swelling is point is presented in details in part 4.2.

3.2.2. Combined variation of the temperature of the substrate and temperature of the solvent vapor

As we presented above, tuning temperature is an effective approach to control the degree of swelling of polymer films. However the temperature influences the mobility, surface tension and interaction parameter consequently. These related effects increase the difficulty in the research of equilibration process of polymer films. Therefore we combine

3 Scientific and practical aspects of controlled solvent vapor annealing

the two tuning approaches (temperature and flow control). And from the analysis of the results we can predict the degree of swelling at various temperatures.

In Figure 31 there are two pairs of polymer volume fraction curves versus the partial vapor pressure for PS and P2VP homopolymer films, at a vapor temperature of 14 °C, 19 °C and a substrate temperature of 20 °C and 25 °C, respectively. We can find that both homopolymer in films are swelling more at higher vapor temperature, although the differences between vapor and substrate temperature are the same. And the second phenomenon is that for each homopolymer the intervals between the two-temperature curves increase as the partial vapor pressure does, where the trend shows in the insert image.

These phenomena can be explained by the deduction below. The relationship between the temperature and the saturated vapor pressure of chloroform can be written as Antoine Equation (Equation 7), which is derivative from Clausius-Clapeyron equation (Equation 6),

$$P(T) = 10^{A - \frac{B}{C+T}} \quad (\text{Equation 7})$$

T denoting the temperature, P denoting the saturated pressure and A of 6.95, B of 1170.97, C of 226.23 are all Antoine Equation Parameters for chloroform when $T \in [-10,60]$. We definite another function (Equation 8) to present the relative partial vapor pressure under 100% total flow when the temperature of vapor is much lower than the substrate,

$$x(T) = \frac{P(T-\Delta T)}{P(T)} = \frac{10^{A - \frac{B}{C+T-\Delta T}}}{10^{A - \frac{B}{C+T}}} = (10^B)^{\frac{-\Delta T}{(C+T)(C+T-\Delta)}} \quad (\text{Equation 8})$$

T denoting the temperature of substrate, ΔT denoting the absolute difference of temperature between vapor and substrate, and ΔT is 6°C in our experiments. Obviously $x(T)$ is a monotonic increasing function at this condition, so when $T_1=20$ °C, $T_2=25$ °C, we can find $x(T_2) > x(T_1)$. Since the relationship between partial vapor pressure and polymer volume fraction of PS and P2VP fits equation 1, a monotonic decreasing function of $\Phi(x)$, where the independent variable x is p/p_0 and the dependent variable is

3 Scientific and practical aspects of controlled solvent vapor annealing

Φ_p , we can get $\Phi[x(T_1)] > \Phi[x(T_2)]$, which is concordant with what we can find on the plot.

The increasing intervals of polymer volume fraction when temperature changes from T_2 to T_1 at 50%, 80% and 100% are essentially caused by the decrease of partial vapor pressure, Δx ($\Delta x = x(T_2) - x(T_1)$), which is associated with the secondary derivative of $y = \Phi(x)$. From the figure of equation 1, we can find $y' < 0$ and $y'' < 0$ for PS, which means if $x_1 < x_2$, then $0 > y'(x_1) > y'(x_2)$. In our case, $\Delta x = 0.00834$ is small enough to approximate $dx \approx \Delta x$ and $dy \approx \Delta y$, then $y' = \frac{dy}{dx} \approx \frac{\Delta y}{\Delta x}$. So we can get $|\Delta y(0.5x_{T_2})| < |\Delta y(0.8x_{T_2})| < |\Delta y(x_{T_2})|$ from $|y'(0.5x_{T_2})| < |y'(0.8x_{T_2})| < |y'(x_{T_2})|$.

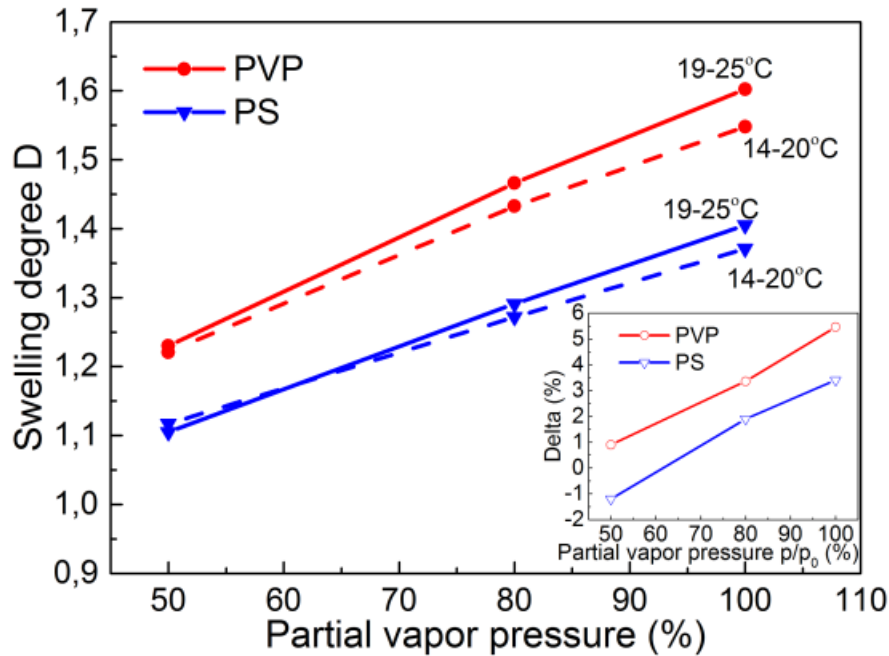


Figure 31 Comparison of the degree of swelling of PS and P2VP films with 40 nm dry thickness upon step-wise increasing partial pressure of chloroform vapor. The dashed lines indicate the film annealing at a vapor temperature of 14 °C and a substrate temperature of 20 °C. The solid lines are 19 °C and 20 °C respectively. The insert is the increase ratio of PS and P2VP films under each partial vapor pressure.

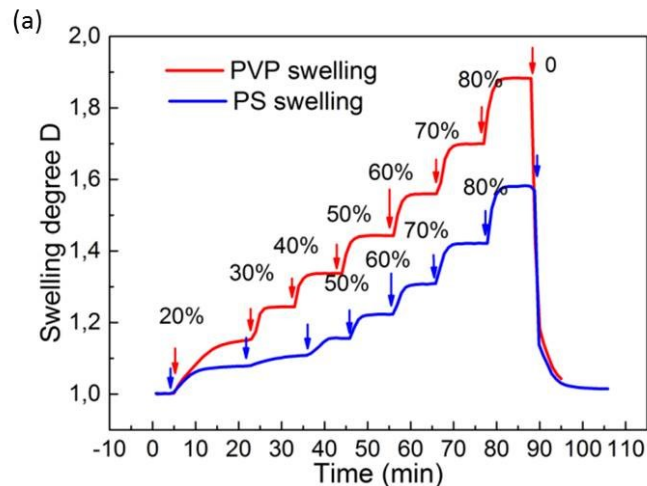
3.3. Swelling behavior of homopolymer films during annealing process

3.3.1. Selectivity of chloroform to PS and P2VP homopolymer in thin films

3 Scientific and practical aspects of controlled solvent vapor annealing

The polymers in our research are PS, P2VP or SV with glass transition temperature around 100 °C, which means at room temperature they are all in a glass state. When they were swelling in the chloroform vapor, the solvent vapor acted as plasticizer to decrease the T_g . In Figure 32(a) (b) we present the step-by-step swelling and deswelling curves of PS and P2VP films with a thickness of ~40 nm. We can find that at low partial vapor pressure the P2VP film swells and deswells obviously faster than PS film, which indicates that after the self-assembly process the P2VP phase reaches the glassy state first when the solvent vapor is quenched with 100% nitrogen, although the PS phase is still swollen and plays plastic behavior. After staying in pure nitrogen atmosphere for longer time, the residual solvent vapor exhausts totally from PS phase. The degree of swelling of polar P2VP in polar chloroform vapor is ~15% larger than that of non-polar PS at each partial vapor pressure. This result gives the information that the selective chloroform can lead the compositionally symmetric SV to act as block copolymer with asymmetric component fraction during the annealing.

The PS film shows more obvious difference than P2VP film in the plot of the polymer volume fraction of the swelling and deswelling process shown in Figure 32 (c). Taking Figure 32 (a) (b) into consideration, we can conclude that the difference is caused by the residual solvent staying in the films.



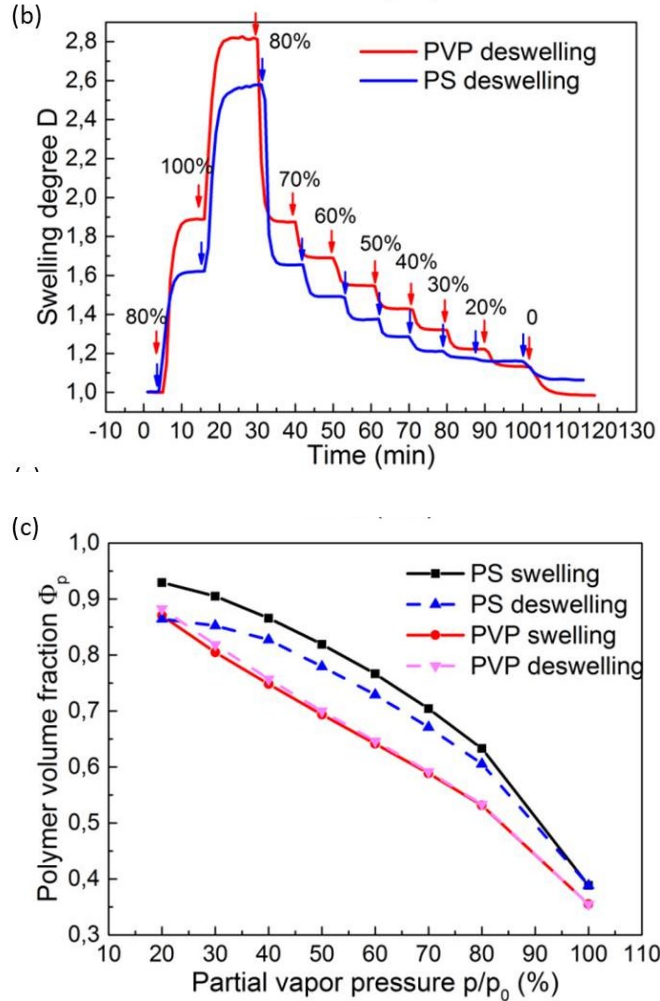


Figure 32 The stepwise swelling (a) and deswelling (b) curves of PS (blue line, ~42 nm thick), P2VP (red line, ~41 nm thick) films as indicated by arrows at 20% 30% 40% 50% 70% 80% 100% of the relative partial vapor pressure of chloroform (p/p_0) at 19 °C/20 °C. (c) polymer volume fraction of the swelling and deswelling of PS and P2VP

3.3.2. Swelling-dependent properties of PS and P2VP homopolymer films

- Variation of the refractive index as a function of swellings

The refractive index (n) is a critical value when we obtain the fitted film thickness from the ellipsometry, and it is a flexible and sensitive factor influenced by the composition of the film and even the thickness of the film. We use the ellipsometry with a single-wavelength laser light, which contributes the possibility to set two factors as depending

3 Scientific and practical aspects of controlled solvent vapor annealing

ones in one measurement. In our measurement the refractive index can be automatically fitted by the software.

In Figure 33 we display the refractive index fitted from the measured data. In deed the refractive index of polymer is usually between 1.4 and 1.6 and the refractive index of dry PS is about 1.58 [208].

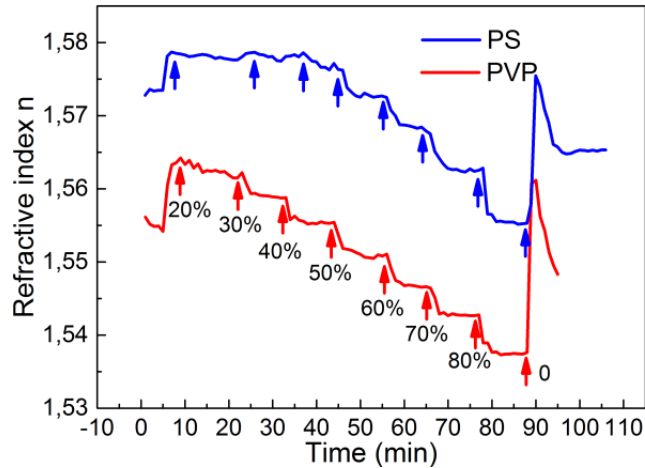


Figure 33 Refractive index as a time-resolving function of PS (42 nm) and P2VP (41 nm) films in chloroform vapor with step-wise increasing of partial vapor pressure at 19 °C/20 °C.

- Variation of the χ parameter

The swelling behavior of films is monitored by an in situ ellipsometry during annealing process, which is sensitive to the partial vapor pressure in the chamber. The polymer volume fraction (Φ_p) is calculated from the initial and swollen film thickness (h_d/h_{sw}). Based on the knowledge of free volume theory in polymers, the volume of polymer under T_g is constituted with constant volume and free volume. The fraction of free volume in glassy state is $\sim 2.5\%$ for most polymers. The dry film thickness of SV³⁹⁰ contains the free volume for T_g of PS (373K) and P2VP (357K) [174] is higher than RT. During the annealing process the free volume is filled up and the polymer chains extend, which means in the swollen film the free volume disappears. So the real Φ_p is a little lower than the value we calculate. As the measurements of the swollen film thickness all by the same method, this deviation will not influence the comparison among different

3 Scientific and practical aspects of controlled solvent vapor annealing

measurements. On the other hand, the obvious swelling of films during annealing means T_g of polymers reducing below the annealing temperature with the solvent vapor functionalized as plasticizer.

According to Flory Huggins theory, χ can be calculated with Equation 9 [209], which is established based on the change of the chemical potential of the solvent in polymer solution.

$$\ln(p/p_0) = \chi_{P,S}\phi_p^2 + \ln(1 - \phi_p) + (1 - 1/N)\phi_p \quad (\text{Equation 9})$$

N is the total degree of polymerization and $\chi_{P,S}$ is the Flory Huggins interaction parameter between the polymer and the solvent. p is the solvent vapor of the solution and p_0 is the solvent vapor of the corresponding pure solvent. ϕ_p is the polymer volume fraction which can be calculated based on film thicknesses.

Krausch et al. reported ellipsometric determined χ between the polymer and the solvent during solvent vapor annealing in 2004 with this formula [210]. They calculated p with Equation 10:

$$p = \hat{p} \exp(-\Delta H_v/RT_{\text{solvent}}) \quad \text{Equation 10}$$

For this equation we still have some confusion:

- a) Is the formula a correction form of Clausius–Clapeyron relation, which provides vapor pressure of polymer solution?
- b) What is \hat{p} in this formula? Taking the material parameters provided in that reference into consideration, it should be the vapor pressure p_0 at boiling point. And we used the material parameters of chloroform in the reference to check this formula. When I chose H_v (25 °C) as ΔH_v , p (25 °C) as p , p_0 of 7.95 GPa as \hat{p} and T_{solvent} of 25 °C, the equation held. Then a new question came.
- c) What is the huge value of 7.95 Gpa? If it is the vapor pressure of pure solvent at boiling point as mentioned in the text, why it is not 1 atm (~101 kPa)? And we did not find it in the reference [211] as the author indicated.

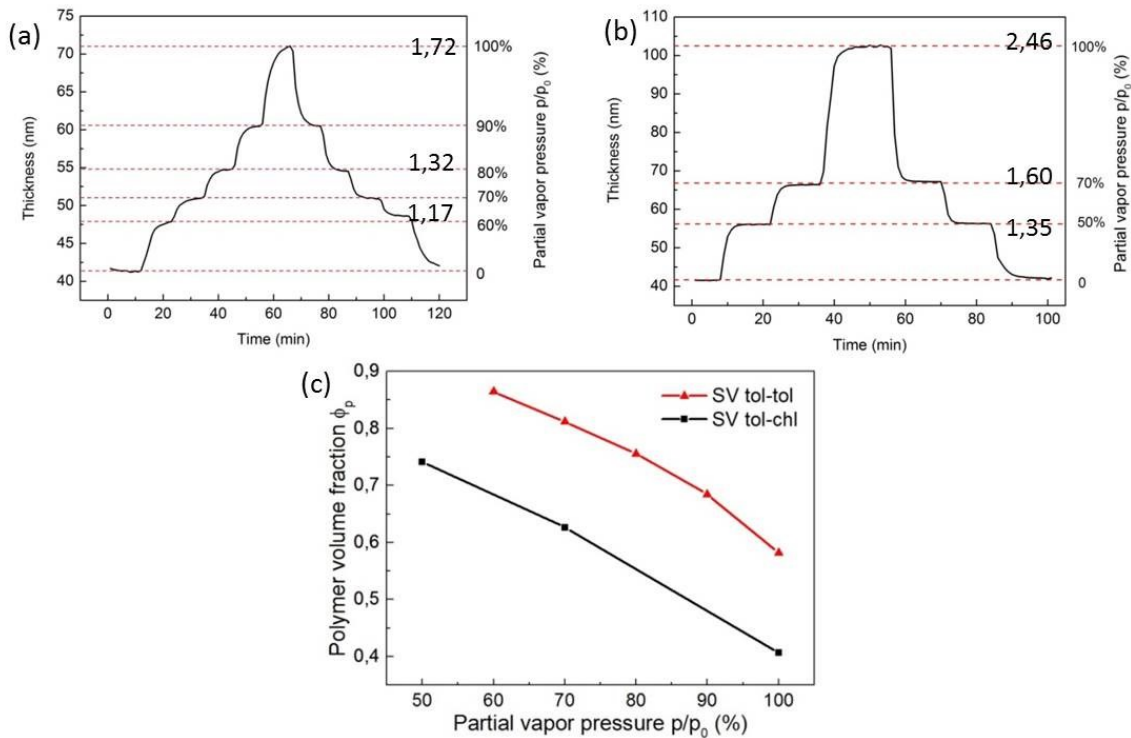
3 Scientific and practical aspects of controlled solvent vapor annealing

So the calculation of χ parameter is temporarily hanging up and next generations may work it out.

3.4. Swelling behaviors of SV films in vapors of strongly and of slightly selective solvents

Figure 34 presents the kinetics curves of SV films under chloroform and toluene vapor with step wise increasing partial vapor pressure. In chloroform vapor the film achieves the equilibrium film thickness as plateau value faster and usually within 10 min at each partial vapor pressure, and the final degree of swelling is $\sim 43\%$ higher than the film in toluene vapor.

Sometimes the speed of the deswelling influences the final morphology of the block copolymer films, i.e. Stahl et al found out that the lower quenching speed provides sufficient time for PEO domains to fully coalesce into cylinders and adopt the expected random fingerprint pattern in PS-b-PEO films [212].



3 Scientific and practical aspects of controlled solvent vapor annealing

Figure 34 The kinetics curve of the ~40 nm SV³⁹⁰ film under stepwise increasing partial vapor pressure of (a) toluene and (b) chloroform with the indicated values in the plots. The separated temperatures of vapor and substrate are 19 °C and 20 °C. (c) The comparison of polymer volume fraction in toluene and chloroform vapor annealing at stepwise increasing partial vapor pressure at 19 °C/20 °C

3.5. Summary

In this chapter the factors to influence the annealing process and the swelling behavior of PS and P2VP homopolymer thin films are presented and discussed.

First, the description of the parameters of the annealing system, including vapor flow, dimension of chamber, solvent property and temperature, are presented. The temperature and the solvent property are the two key factors influencing the swelling behavior of BCP films. We conclude that since the BCP morphologies are sensitive to the swelling process, the analysis of the reproducibility among different annealing systems requires consideration of a number of additional factors, such the geometry of the chamber and its material, the type of the flow inside the chamber, the length and isolation of the tubing connections.

Second, the swelling behavior of BCP in films is controlled by the temperature of the vapor and of the substrate, on one hand and variation of the saturation of the solvent vapor atmosphere, on the other hand. And the exchanging of the two methods are explored which can contribute to the estimation of the swelling behavior at different temperatures. Meanwhile the ‘real’ partial vapor pressure is measured in this part making the comparison of different annealing systems conveniently.

Third, the swelling and deswelling behaviors of PS and P2VP homopolymer in films are researched in slightly selective solvent vapor of chloroform, which gives results of 10% more swelling of P2VP than PS in films with thickness of ~40 nm and the deswelling rate of PS is slower than that of P2VP at low partial vapor pressure. These results provide important information for understanding the PL morphology shown in Chapter 4.

4 Tunable morphology in ultrathin films of high molecular weight block copolymer (SV) via thermo-solvent annealing

4.1. Swelling behavior of SV³⁹⁰ films under variation of the vapor flow

Figure 35a presents the time-resolved swelling and deswelling behavior of a SV block copolymer and respective homopolymer in films when the partial vapor pressure p/p_0 in the chamber was stepwise adjusted by setting a corresponding mixture of a 100% p/p_0 vapor flow with a flow of dry nitrogen, by maintaining the temperature of the sample T_s at a constant level of 20 °C and the temperature of the vapor T_v at 14 °C. The degree of swelling at steady state (typically, achieved after 20 min) has been used to evaluate the polymer volume fraction Φ_p (a ratio of the dry film thickness to the swollen film thickness) as a function of p/p_0 shown in Figure 35(b). The polymer volume fraction (a reverse of the degree of swelling) in the PS film is systematically ~10% higher than that of the P2VP homopolymer, clearly suggesting a selectivity of the chloroform towards more polar polymer. Accordingly, the swelling of the SV block copolymer is defined by the contribution from both blocks, so that the swelling curve of SV lies in between the swelling curves of the homopolymer.

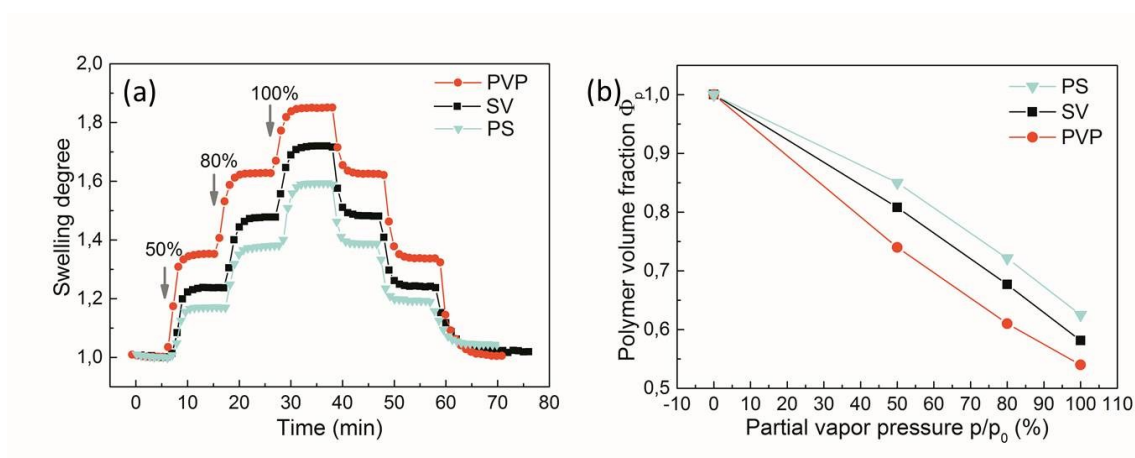


Figure 35 (a) Kinetics curves of the stepwise swelling and deswelling of PS (green triangle, 48 nm thick), P2VP (red circle, 43 nm thick) and SV block copolymer (black square, 39 nm thick) as indicate by arrows at 50% 80% 100% of the relative partial vapor pressure

4 Tunable morphology in ultrathin films of high molecular weight block copolymer (SV) via thermo-solvent annealing

of chloroform (p/p_0) at $T_v=14\text{ }^\circ\text{C}$ and $T_s=20\text{ }^\circ\text{C}$. (b) The polymer volume fraction as a function of p/p_0 based on the curves in (a).

4.2. Swelling behavior of SV³⁹⁰ in ~40 nm films under variation of the temperature of the vapor and of the substrate

At point A (Figure 36a) T_s and T_v are set to $20\text{ }^\circ\text{C}$ and $30\text{ }^\circ\text{C}$. The equilibrium swelling is achieved within 10 min, and corresponds to 100% partial vapor pressure. At point B keeping T_s constant we increase the T_v to $25\text{ }^\circ\text{C}$. The swelling builds up first in a two-step mode: fast stage when 95.7% of the equilibrium thickness (71.5 nm/74.7 nm) is achieved, and a slow mode, when the steady-state swelling was not yet achieved after 50 min. The slow contentious increase in the swollen thickness can be associated with the retarded build-up of the vapor pressure in the chamber, as well as with structural rearrangements in the block copolymer. At point C the temperature of the vapor is further increased up to $29\text{ }^\circ\text{C}$, still being $1\text{ }^\circ\text{C}$ lower than that of the substrate. The vapor and substrate temperature are both above room temperature which caused the heat dissipating from the steel chamber and the tubes. The temperature of solvent vapor is higher than the chamber and the tubes, so the condensation of vapor started in this period. As a result the real partial vapor pressure around the film is lower than what we set on the flow controller. The slight increase of the film thickness can also prove this point. At point D increasing the substrate to $35\text{ }^\circ\text{C}$ with the constant vapor temperature, the film continued increasing slowly instead of descending in an ideal situation. This phenomena can be explained by the compensation of partial vapor pressure came from the evaporation of the condensate vapor adhered on the chamber wall. The condensation on the tube was accumulating, as the disordered film thickness appeared 15 min later. The resulted morphology after this annealing period is shown in Figure 37

4 Tunable morphology in ultrathin films of high molecular weight block copolymer (SV) via thermo-solvent annealing

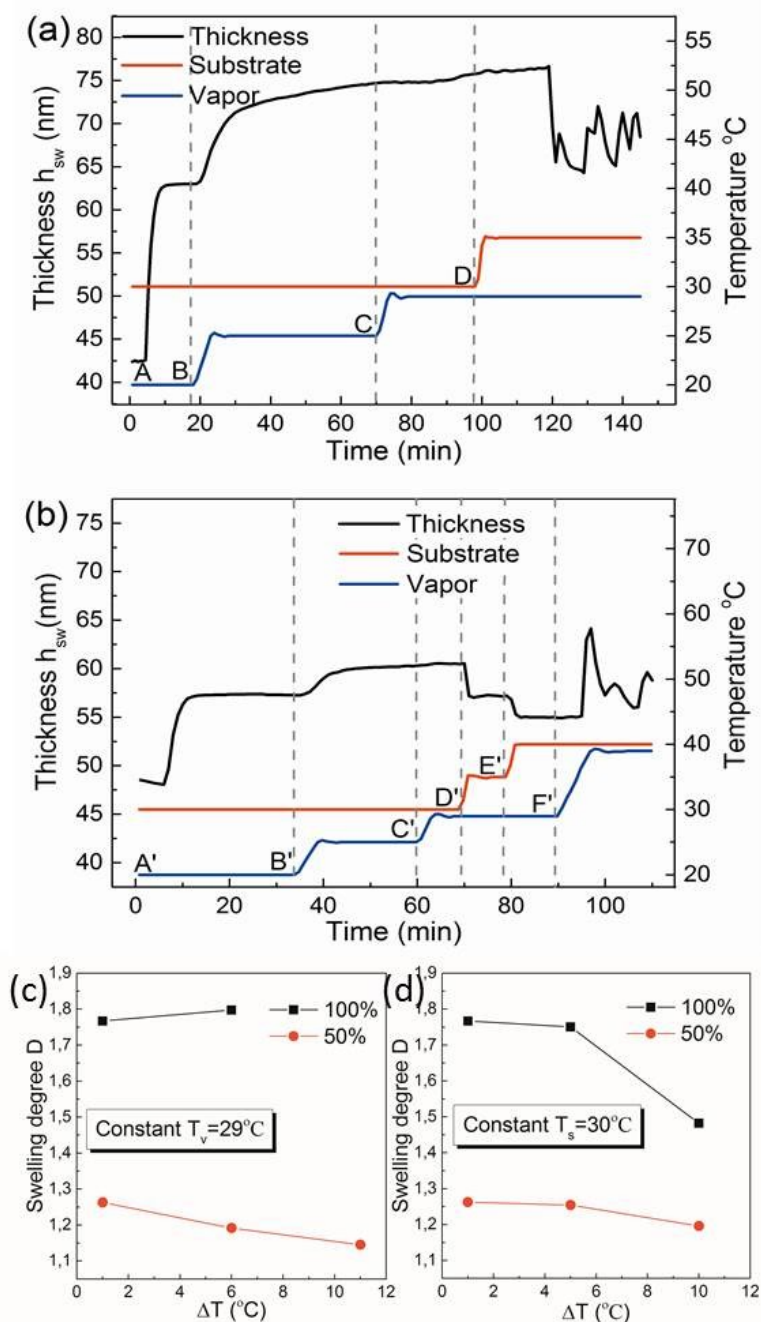


Figure 36 Time-resolved swollen thickness (h_s left axis, solid line) of SV film under variation of (right axis) T_s (dashed line) and T_v (dotted line) in (a) 100% (b) 50% p/p_0 chloroform vapor at temperature of A,A' 20/30 °C, B,B' 25 °C/30 °C, C,C' 29 °C/30 °C, D,D' 29 °C/35 °C, E' 29 °C/40 °C, F' 39/40 °C. Degree of swelling as a function of temperature interval at constant vapor (c) and substrate (d) temperature under 100% and 50% partial vapor pressure of chloroform.

4 Tunable morphology in ultrathin films of high molecular weight block copolymer (SV) via thermo-solvent annealing

In Figure 36b the equilibrium swelling process is achieved under 50% partial vapor pressure. At point A', B', C' the temperature of vapor and substrate are set the same with in Figure 36a. And the swelling builds up as the film does at 100% partial vapor pressure (Figure 36a). Increasing the substrate temperature at point D', E' causes the film thickness decreases stepwise. After point F' the film thickness is out of control, for the vapor temperature is much higher than the room temperature and the condensation affects the partial vapor pressure. The confusion of thickness in Figure 36b appears after point F', at higher temperatures (vapor temperature of 39 °C and substrate of 40 °C) than that appears in Figure 36a after point D (vapor temperature of 29 °C and substrate of 35 °C), for the low partial vapor pressure leads the condensation appearing hardly.

The trends of degree of swelling tuned by temperature interval ($\Delta T = T_s - T_v$) under 100% and 50% p/p_0 at constant temperature of vapor (29 °C) or substrate (30 °C) are presented in Figure 36c, d, respectively. Since the vapor temperature of 29 °C is higher than room temperature of 25 °C, the condensation of solvent vapor exists when the annealing is performed in Figure 36c. The point at temperature interval of 6 °C (indicating the T_s is 35 °C) under 100% p/p_0 is out of correct trend. The error caused by environment temperature under p/p_0 of 50% is not as obvious as under higher partial vapor pressure, because the condensation is not so strong. But this does not mean there is no condensation, which should be always paid attention to during the annealing. In Figure 36d the trend of degree of swelling declining as the temperature interval increasing is clear, although the two points at ΔT of 1 °C ($T_v = 29$ °C) is not as high as expected.

4 Tunable morphology in ultrathin films of high molecular weight block copolymer (SV) via thermo-solvent annealing

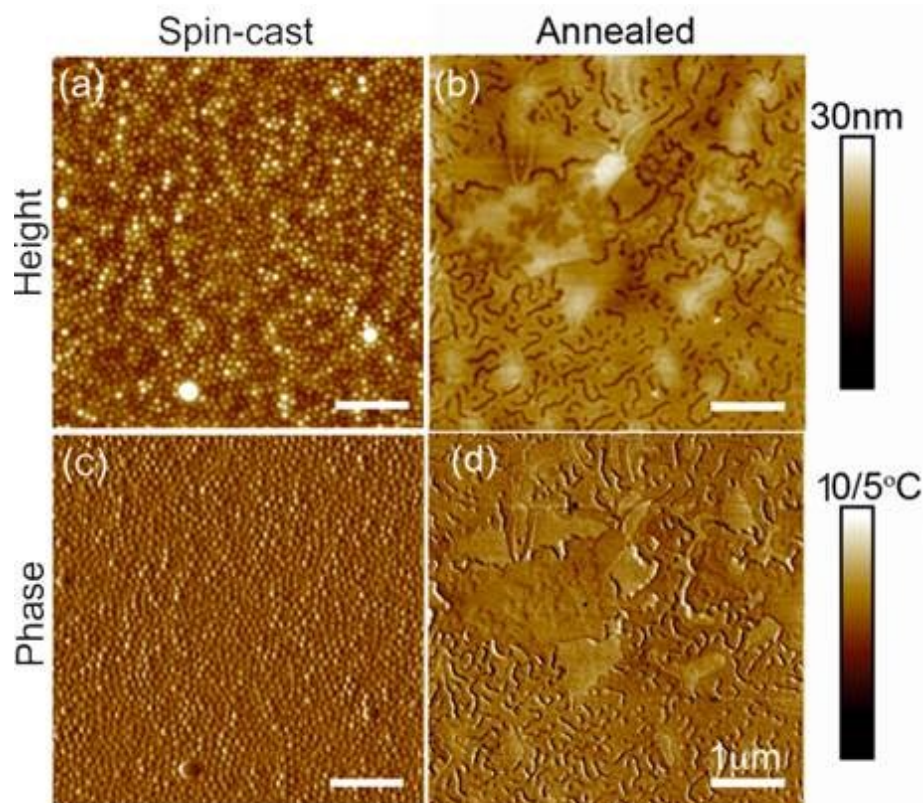


Figure 37 SFM topography (a) (b) and phase (c) (d) images of spin-cast SV³⁹⁰ ~40 nm film (a) (c) and after annealing (b) (d) at $T_v = 29$ °C, $T_s = 30$ °C for 20 min, where the curve is shown in Figure 36 (a).

4.3. Morphology of SV³⁹⁰ in films with thickness under half-layer tuned by the temperature

SFM images of thermo-solvent-annealed films of symmetric SV³⁹⁰ films with initial dry thickness of ~40 nm are shown in Figure 38. The degrees of swelling on two annealing conditions are same of ~1.7 with the same temperature interval of 6 °C indicating the swollen thickness of ~68 nm ($0.58L_0$). The morphology after annealing is perforated lamella with depth of holes being ~6.4 nm and the diameter of the holes being ~32 nm. We chose areas from two samples with few defects for PSD analysis in Figure 38e, f. The domain spacing is calculated by the frequency at the peaks of PSD curves shown in Figure 40. The higher temperature causes the decreasing of the domain spacing from 125 nm at 14 °C/20 °C to 116 nm at 24 °C/30 °C, which shows same trend in ref [213].

4 Tunable morphology in ultrathin films of high molecular weight block copolymer (SV) via thermo-solvent annealing

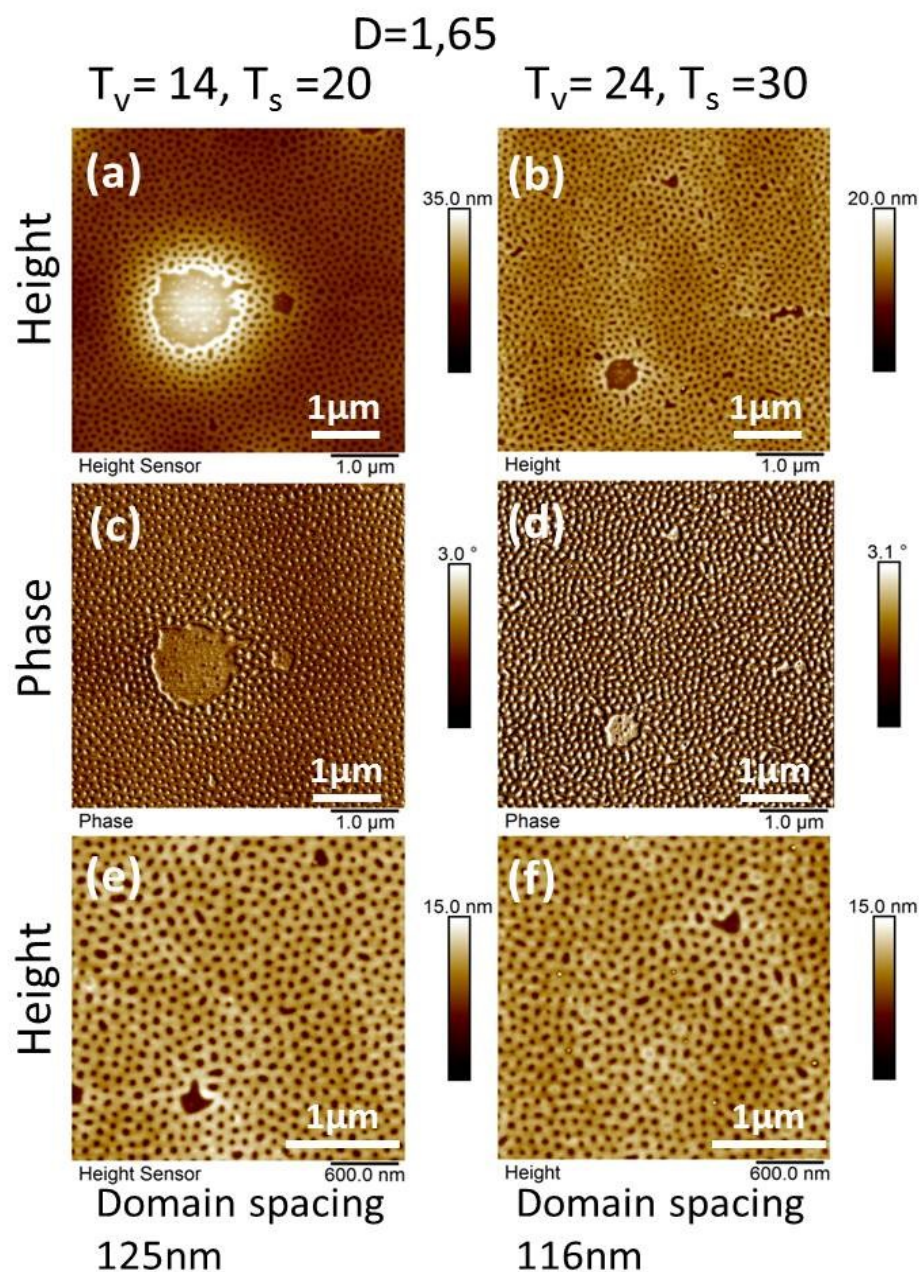


Figure 38 SFM topography images (a) (b), phase images (c) (d) of 40 nm SV³⁹⁰ films annealed by chloroform for 200 min. Area for PSD analysis is shown in (e) (f). The annealing condition and degree of swelling are presented on the top of the image.

In Figure 39 the degree of swelling of films is increased to 2.5 with swollen film thickness of ~ 100 nm ($0.85L_0$). Comparing with the annealed morphology shown in Figure 38, some terracing defects occur in both of the two conditions because the

4 Tunable morphology in ultrathin films of high molecular weight block copolymer (SV) via thermo-solvent annealing

swollen film thickness is higher than the suitable thickness for only perforated lamella. Only in Figure 39b there are stripe-like shapes existing, because the high vapor temperature and high degree of swelling increases the chain mobility and meanwhile their domain spacing from the analysis of Figure 39(e), (f) are 116 nm and 111 nm with further decreasing.

4 Tunable morphology in ultrathin films of high molecular weight block copolymer (SV) via thermo-solvent annealing

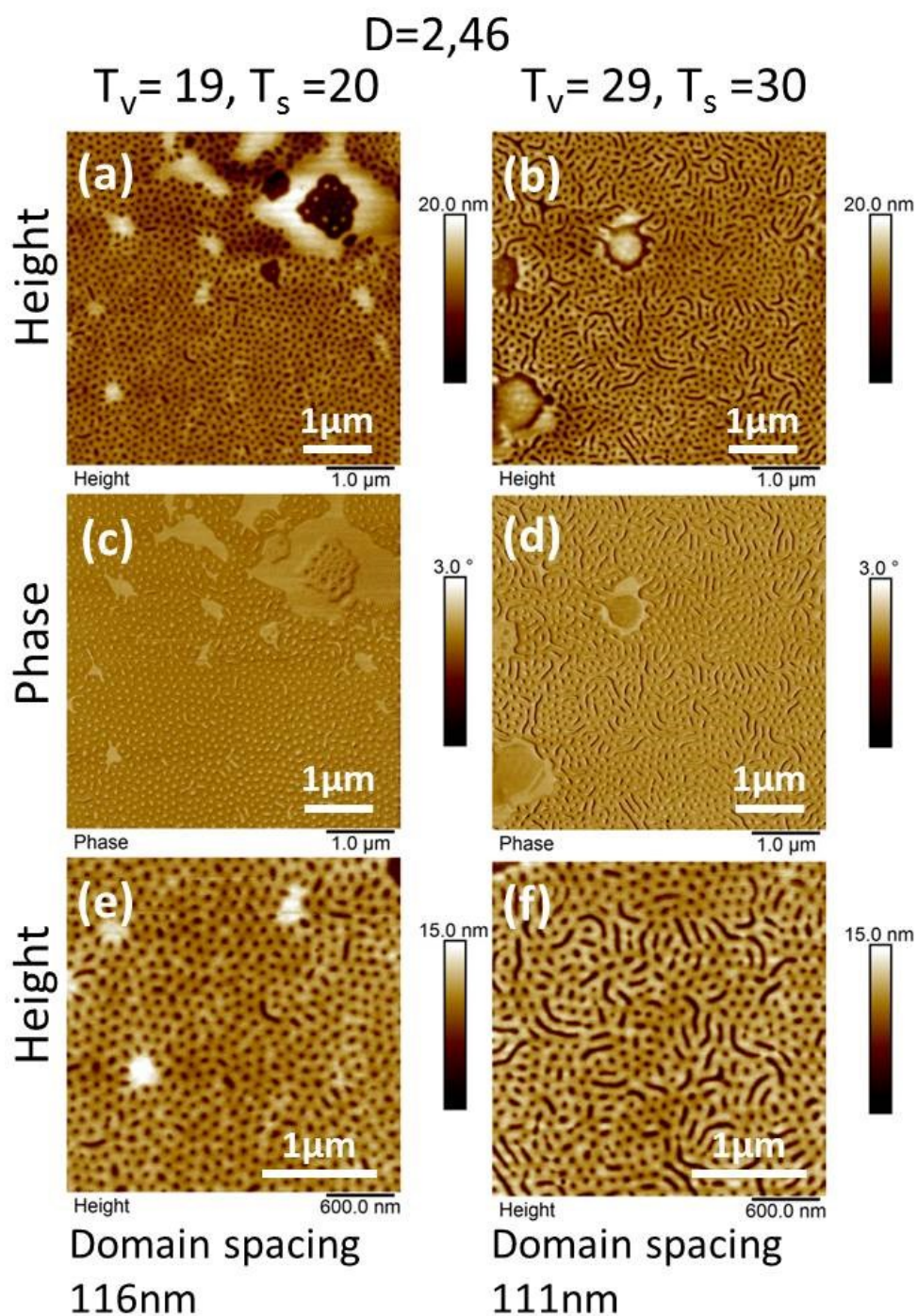


Figure 39 SFM topography images (a) (b), phase images (c) (d) of 40 nm SV³⁹⁰ films annealed by chloroform for 200 min. Area for PSD analysis is shown in (e) (f). The annealing condition and degree of swelling are presented on the top of the image.

4 Tunable morphology in ultrathin films of high molecular weight block copolymer (SV) via thermo-solvent annealing

Figure 40 presents the collection of PSD analysis of the morphology of SV³⁹⁰ films annealed by chloroform with the conditions mentioned above.

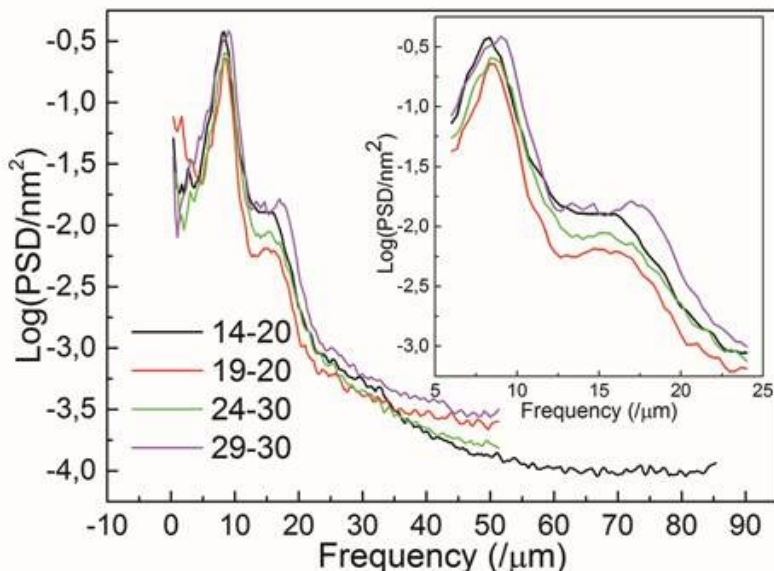


Figure 40 Power spectrum density analysis by Nanoscope Analysis of the annealed ~ 40 nm SV³⁹⁰ films at various temperatures. Their morphologies are shown in Figure 38 and Figure 39.

4.4. Challenging of interpretation of the perforated (PL) morphology of SV³⁹⁰ in thin films

4.4.1. Peak force mode characterized morphology of SV³⁹⁰ in films

To interpret these annealed morphologies of the SV³⁹⁰ ~ 40 nm films, we used the SFM peak force module yielding height, deformation and log Modulus images as shown in Figure 41. From the shape we can tell the high area in (a) corresponds the dark color in the deformation image and the light color in the log modulus image. In the deformation image the dark area is the harder part with less deformation during peak force scanning. Usually the Modulus (Young's Modulus) reflecting the relationship between force and indentation presents a reversed color mapping with the deformation image. In our case, the T_g of PS is 373 K and P2VP is 357 K, which means at room temperature the PS phase is harder than P2VP phase. Taking all the information from the SFM images into

4 Tunable morphology in ultrathin films of high molecular weight block copolymer (SV) via thermo-solvent annealing

consideration, the PS part is the low area in the height image, the dark area in the deformation image and the light area in the modulus image, so the other area in these images are P2VP parts. These distributions of two blocks are also proved by metallization results shown in Figure 44g.

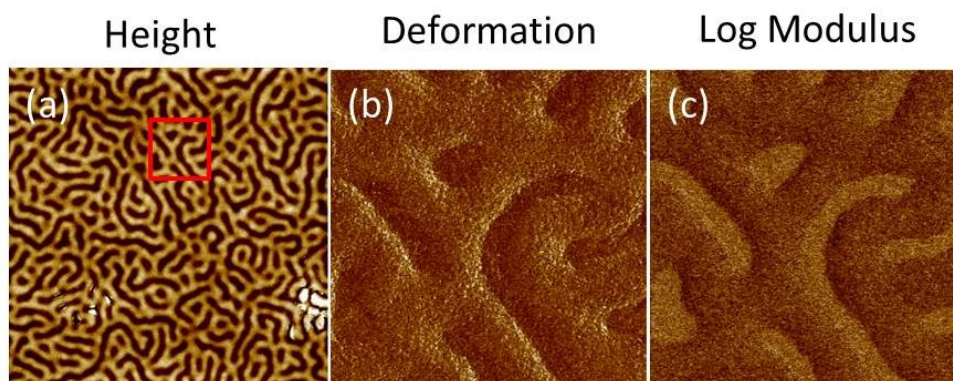


Figure 41 Height image (a), deformation image (b) and log Modulus image (c) from peak force module of SV³⁹⁰ ~40 nm film annealed by chloroform at 25 °C/26 °C. (b), (c) are the area of the red square in (a)

4.4.2. Characterization of the morphology of SV³⁹⁰ film/substrate interfaces annealed under slightly selective solvent vapor

Figure 42 presents the SFM images of the bottom surface of the films with perforated and stipe morphology. These two kinds of templates are prepared in the same procedure with the same SV³⁹⁰. The only difference is the plasma oven we used to clean the silicon wafers before spin casting. We believe that these two kinds of morphologies are caused by the different surface properties of silicon wafers, because the perforated morphology can be reproduced on carbon layer which is homogeneous to both of the blocks shown in Figure 60. The plasma procedures could introduce unexpected surface modification on silicon wafers, for the plasma treatments always sputter some molecules or atoms up in the atmosphere, which will fall back on samples during the next plasma treatment. This episode of reproducibility proves from side that the substrate property strongly influences the phase separation of BCPs, and in thin film a weak surface field is sufficient to form PL.

4 Tunable morphology in ultrathin films of high molecular weight block copolymer (SV) via thermo-solvent annealing

Then we floated the templates to check the bottom morphology of the films. The backs of films also show similar morphology with their top surface in both perforated lamella and stripe-like morphology. But the perforated lamella is less homogeneous at the bottom and the bottom stripes have higher roughness than their tops. Meanwhile the average dots depth of bottom is ~20 nm much higher than that on top surface of ~6 nm. The roughness increasing could be caused by low fluid of the BCP from the stronger interaction of the polymer/substrate than the polymer/air.

4 Tunable morphology in ultrathin films of high molecular weight block copolymer (SV) via thermo-solvent annealing

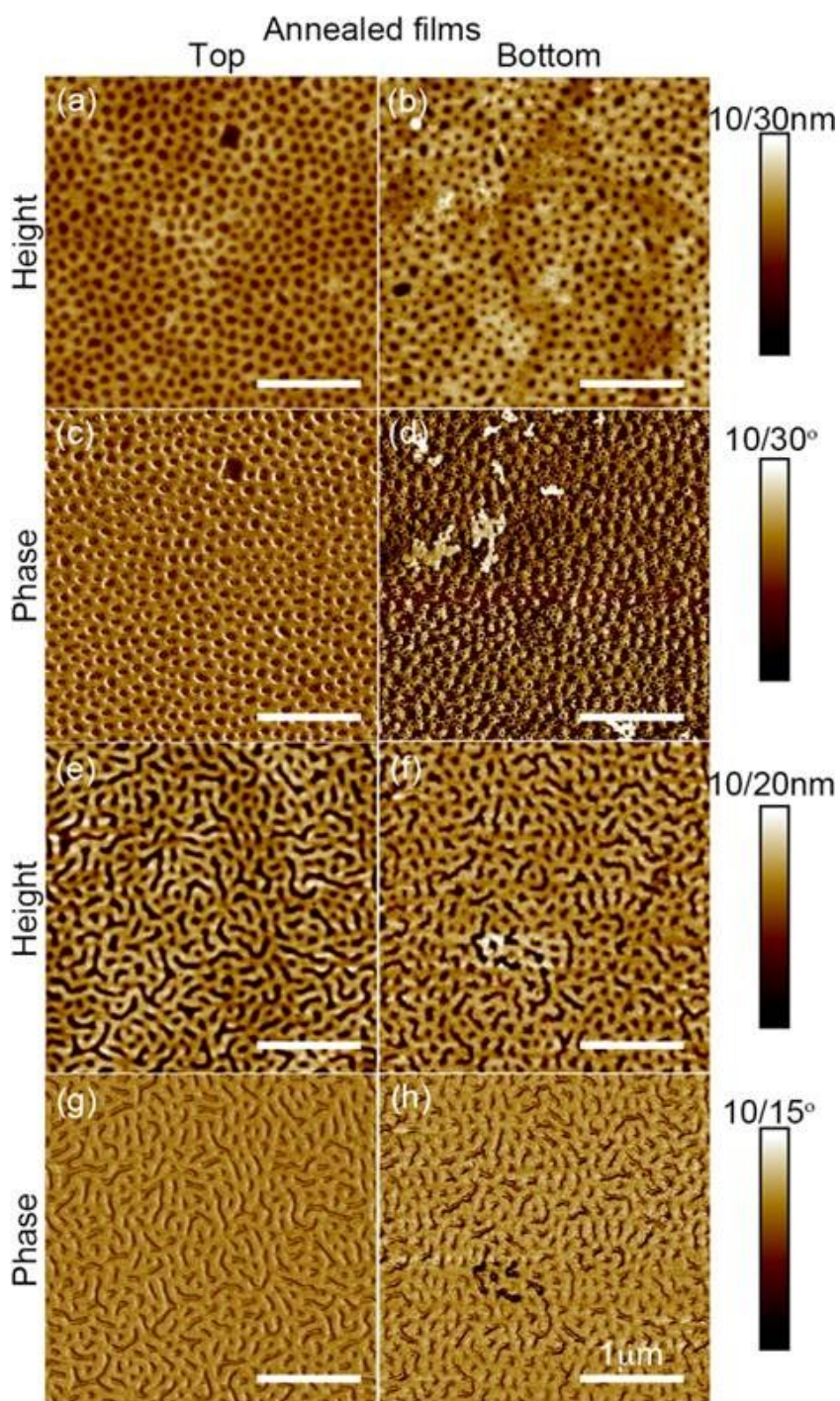


Figure 42 SFM topography images of the free surface (a) (c) of the film and the interface (e) (f) between the film and the substrate from the SV³⁹⁰ film with thickness of ~40 nm annealed by chloroform vapor at 24 °C/30 °C. (c) (d) (g) (h) are their phase images respectively.

4 Tunable morphology in ultrathin films of high molecular weight block copolymer (SV) via thermo-solvent annealing

4.4.3. Metallization of annealed SV³⁹⁰ template

Metallization of the SV templates is an effective method to distinguish the PS and P2VP blocks, for only P2VP blocks containing pyridyl groups can be loaded with metal ions under acid atmosphere. In metallization procedure we immersed the annealed templates in Na₂PtCl₄/HCl solution to load Pt ions on P2VP groups, and then removed the polymer with oxygen plasma. The metallization results of the perforated templates in Figure 43 present that the Pt particles in network morphology indicating the annealed template with the P2VP block as matrix and the PS block as dots. The defects of holes and terraces on the annealed SV³⁹⁰ template shown in Figure 38 and Figure 39 both correspond to empty areas after etching, so the surfaces of the defects are PS. This result shows unexpected morphology from our experience. P2VP has lower surface energy with Si substrates than PS and PS has lower surface energy with air than P2VP, so the PS block prefers to collect at the film surface. To make the reason of this morphology clear, we did more detailed experiments and provided a new explanation in the following part.

4 Tunable morphology in ultrathin films of high molecular weight block copolymer (SV) via thermo-solvent annealing

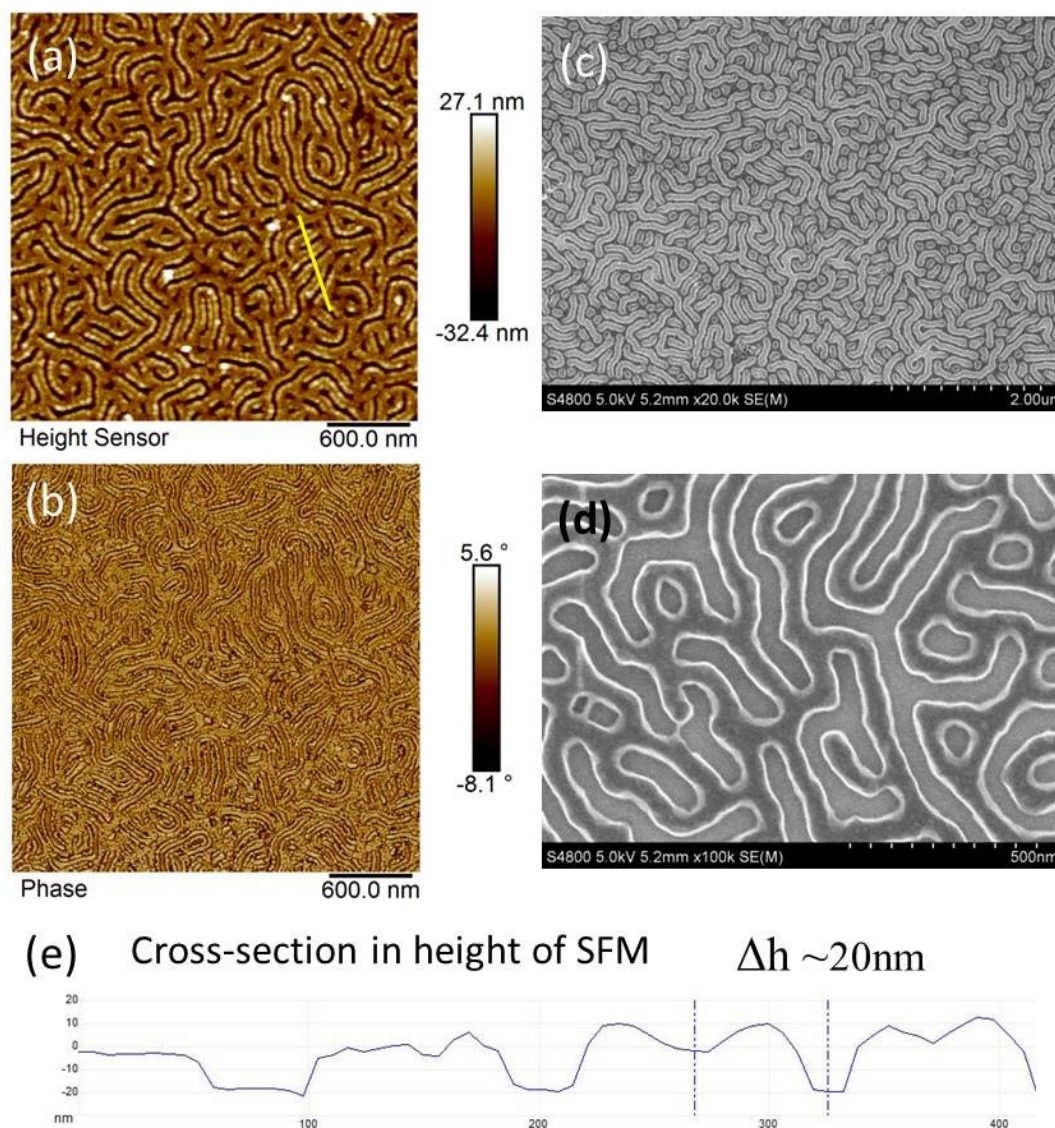


Figure 43 SFM topography (a) and phase (b) images of the metalized stripes from ~ 40 nm template of SV^{390} films annealed by chloroform vapor on silicon wafer. FE-SEM images (c) (d) of the same sample, where the bright wires are Pt. The profile curves (e) of the cross-section line in (a) shows the height of the Pt wires.

Figure 44 presents how the morphology of a SV^{390} film changes from the annealed template (a) (b) to platinum nanowires (g) (h) with its interface (between the film and the silicon wafer) images (c) (d) and the immersed surface images (e) (f) step by step. The interface morphology of the film presents the same stripe-like morphology like its surface with higher edge roughness of the standing stripes. Besides the topography, the distribution of PS and P2VP is also the same, as we can see from the phase images (b)

4 Tunable morphology in ultrathin films of high molecular weight block copolymer (SV) via thermo-solvent annealing

(d). In the images (e) (f) the width of gap between each two stripes shrinks from 50 nm to 20 nm and the depth increases from ~9 nm to ~32 nm, meanwhile the film thickness measured by ellipsometry increases from 45 nm to 49.5 nm. The profile of cross-section (the red line in (e)) shows the depth of the stripe is ~47 nm, slightly thinner than the film thickness. Its corresponding phase image (f) shows the same color contrast like (b) and (d), which means the lower area (in Figure 44e) is not the silicon wafer. The Pt-metallized template shown in (g) (h) proves again that the higher area (in Figure 41a) is P2VP block, because only the pyridine group in acid environment can hold positive metal ions. Based on our results the immersion time, the concentration of the Pt^{2+} and the HCl can all affect the morphology of the nanowire. In Figure 44 (g) the Pt nanowires copy the swollen P2VP stripes from Figure 44 (e) and each nanowire includes many small Pt nanoparticles accumulating at its edge.

4 Tunable morphology in ultrathin films of high molecular weight block copolymer (SV) via thermo-solvent annealing

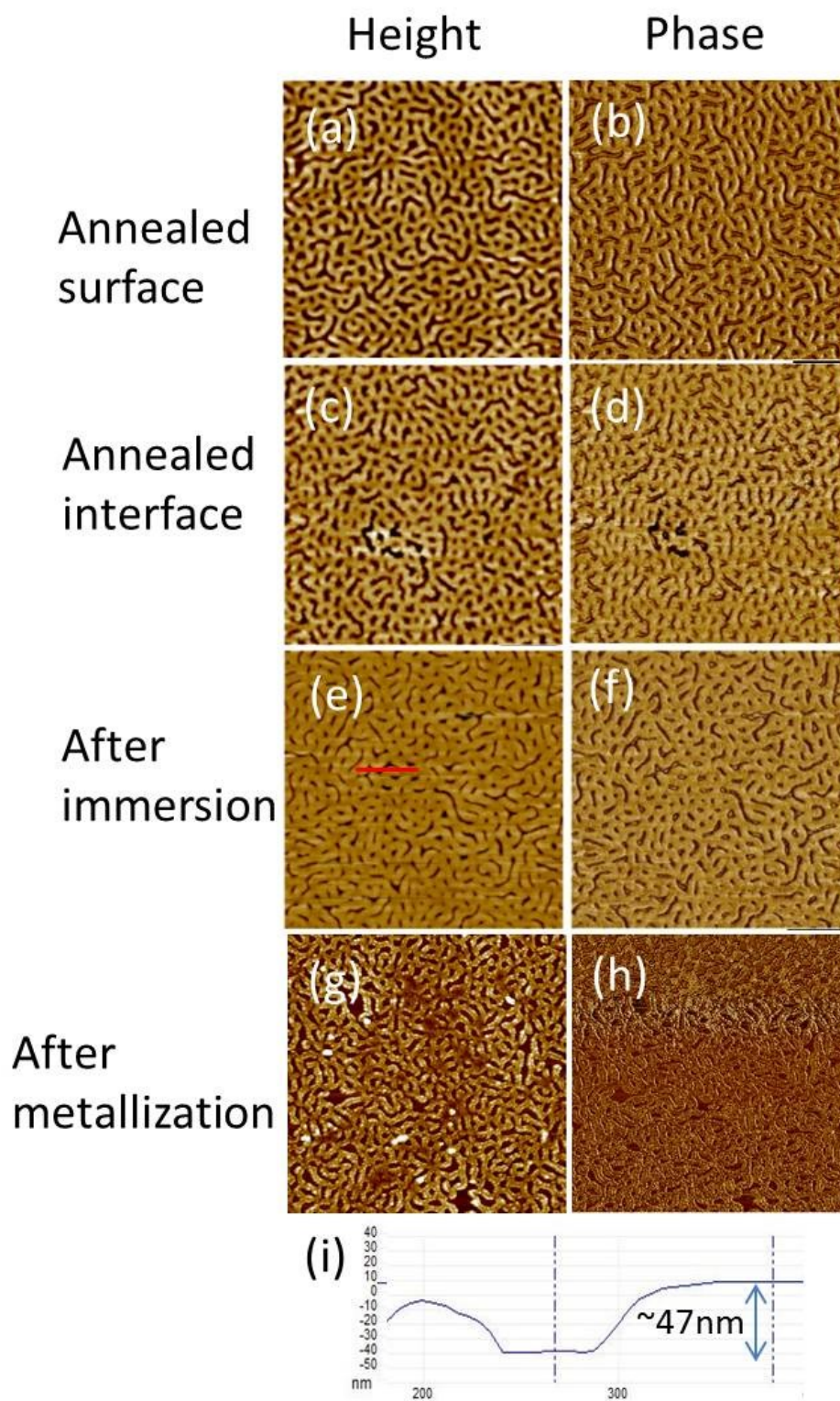


Figure 44 (a) (c) (e) (g) SFM topography images and (b) (d) (f) (h) phase images of SV³⁹⁰ ~45 nm film annealed by chloroform at 24 °C/30 °C (i) profile curve of cross section of the red line on image (e).

4 Tunable morphology in ultrathin films of high molecular weight block copolymer (SV) via thermo-solvent annealing

- Interpretation of the metallized pattern

In Figure 45 we show the annealed SV³⁹⁰ film as template and the corresponding metallized morphology with platinum nanowires and also the profile curves at the two red lines in height images. From the analysis of Figure 41 we know that the light area in (a) is P2VP block, which has period length of ~115 nm. In (c) the platinum particles arranging as nanowires after oxygen plasma treatment has the period length of ~55 nm (almost half of the period in SV³⁹⁰ template (a)). From the insert in (c) with very flat bottom of the curve we know that the bottom is the silicon wafer, which means the polymer phases are cleaned up by plasma treatment. Based on the profile curves in (e), we know that a pair of nanowires split from a stripe in its template with a shallow gap in the middle of the stripe (point B). The reason could lead to this phenomenon is the selectively swelling of P2VP block during the immersing procedure for loading Pt²⁺ in acid environment. This selective swelling of P2VP causes this block collecting at the edges of PS micro domains (also stripe-like).

4 Tunable morphology in ultrathin films of high molecular weight block copolymer (SV) via thermo-solvent annealing

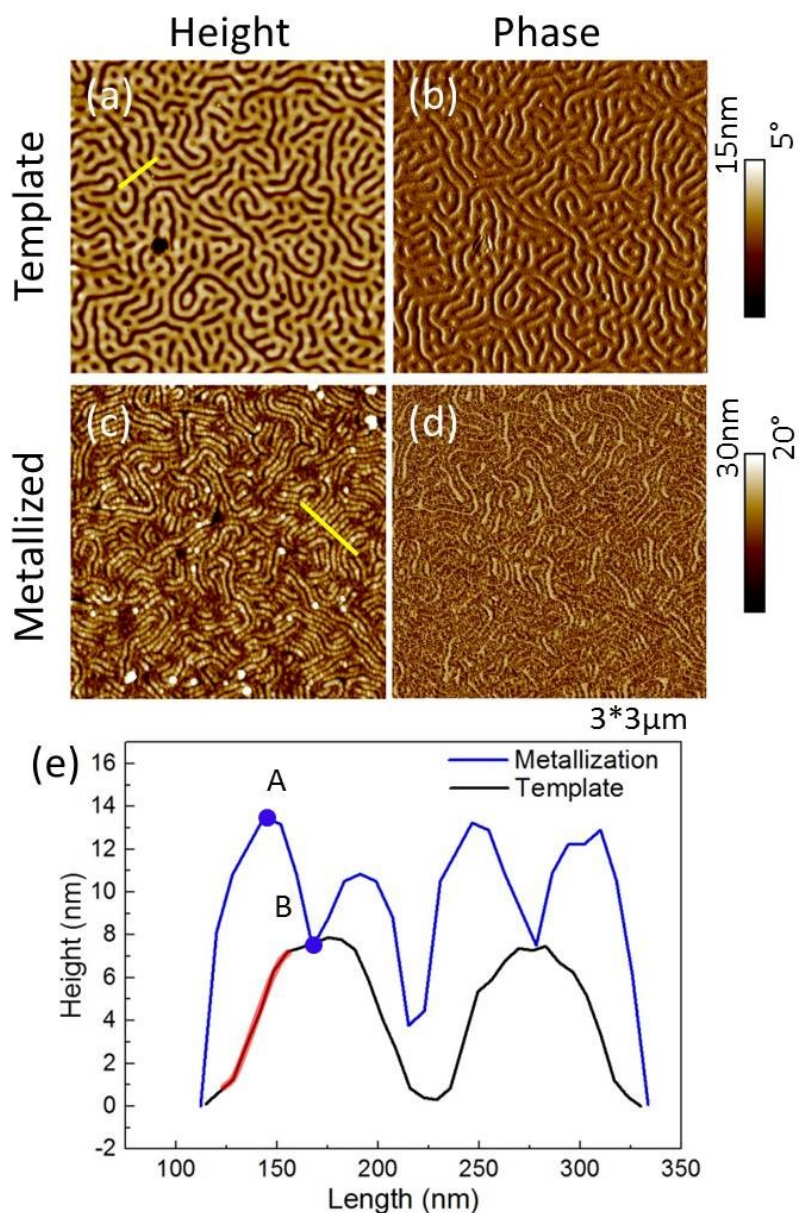


Figure 45 (a) (c) SFM topography images and (b) (d) phase images of SV³⁹⁰ ~40 nm film annealed by chloroform at 24 °C/25°C with degree of swelling of 1.78, (e) the profiles of cross-section at the yellow line in (a) (black) and (c) (blue). In (a) the stripes have height of 7.4 nm in average and width of 51 nm in average. The domain spacing of (a) is ~109 nm and (c) is ~55 nm.

4.4.4. Pattern transfer of SV³⁹⁰ templates with PL morphology

4 Tunable morphology in ultrathin films of high molecular weight block copolymer (SV) via thermo-solvent annealing

The perforated template can act as a mask when we etch the silicon wafer, which is a possible application of ordered block copolymer. Figure 46 presents SV³⁹⁰ films with PL morphology as etching mask for CF₄-etching procedure. A is the BCP template on silicon wafer before and after etching the etched silicon wafer step-by-step using the perforated template as mask and their cross-section profiles. We used the same sample as shown in Figure 38b. The phase images in Figure 46A show that the contrast between the dot-area and the matrix-area is obviously larger in (b) than (d), and the sample in (d) is pure etched silicon wafer. The average depth of the holes before etching, after etching and after removing the polymer residue from the template is 6.4 nm, 5.2 nm and 3.9 nm respectively. From the thickness difference of procedure Figure 46A (b) and (c) the polymer left at the network position is 1.3 nm. In our experiment the etching rate of homopolymer is 13 nm/min and 29 nm/min to PS and P2VP, respectively, and to silicon wafer it is usually 4~6 times greater than PS [60]. The initial film thickness is 40 nm (thickness of P2VP after annealing is estimated to 43.2 nm) and the etched network thickness is 38.7 nm (proved to be P2VP in Figure 43), so the etched thickness of PS is about 18.1 nm. Subtracting the pattern depth at the top of film of 6.4 nm, the dewetting of PS at dot area has depth of ~18.7 nm similar with the pattern depth of ~20 nm on bottom sample shown in Figure 42. From Figure 43 we know that the matrix area is P2VP block. So the sketches of the PL morphology of SV³⁹⁰ and the etching procedure are corresponding shown in Figure 46C. We can find the dewetting area at PS position in the PL morphology.

4 Tunable morphology in ultrathin films of high molecular weight block copolymer (SV) via thermo-solvent annealing

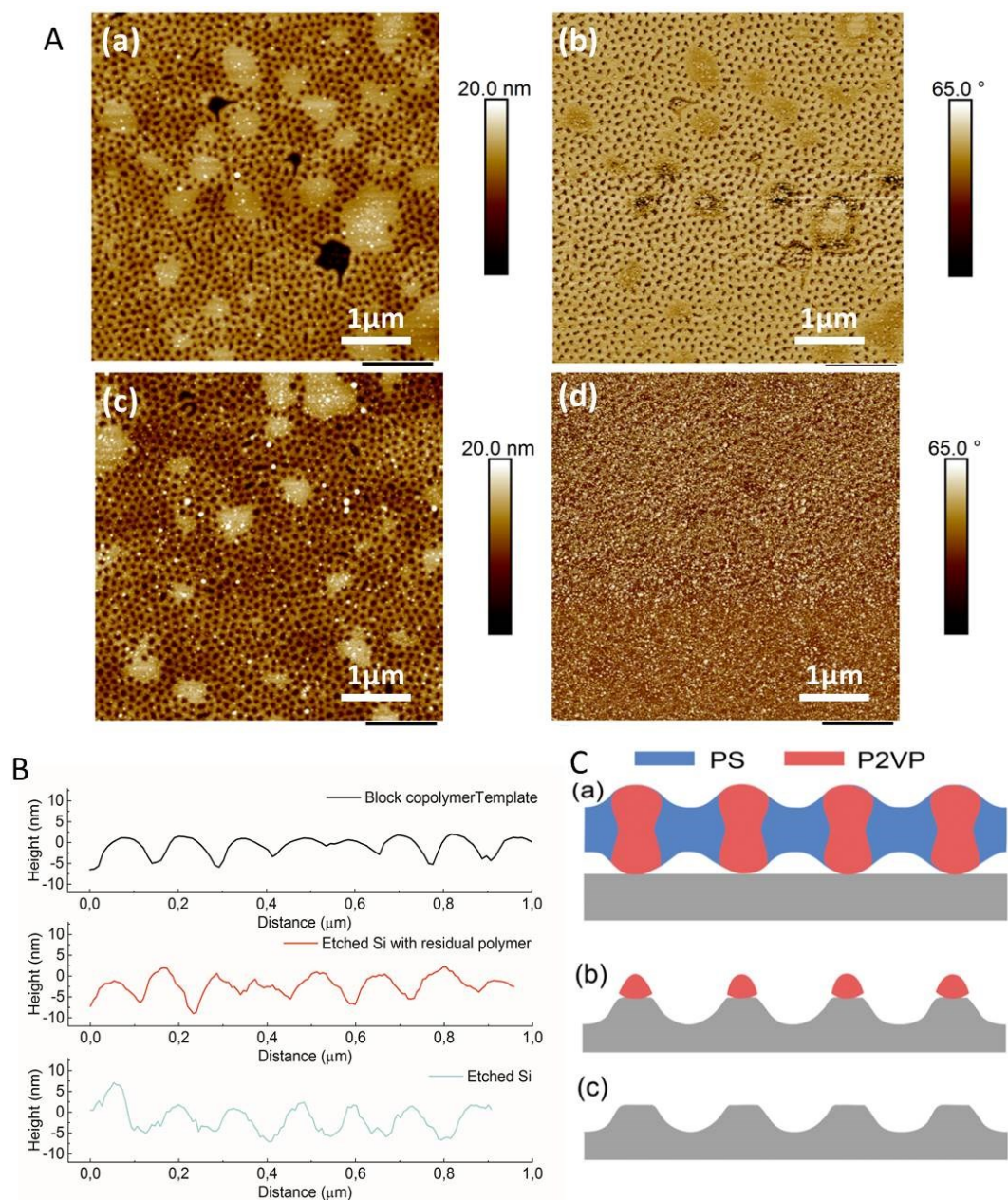


Figure 46 (A) SFM topography images (a) (c) and phase images (b) (d) of etched block copolymer template indicating the procedure of (b) and (c) in (A). (B) The cross-section profile of SV³⁹⁰ template on silicon wafer before (a, black), after (b, red) etching and the etched Si wafer (c, blue). (C) The sketch of etching procedure treated on SV template shown in Figure 38b with (a) before etching (b) after etching with residual polymer (c) after removing the residual polymer.

The dewetting can be explained by the lower deswelling rate of PS than P2VP under chloroform atmosphere. The step wise deswelling curves of PS and P2VP homopolymer

4 Tunable morphology in ultrathin films of high molecular weight block copolymer (SV) via thermo-solvent annealing

in films shown in Figure 47 presents that at low partial vapor pressure of 30% and 20% the degree of swelling of PS is keeping at 1.2 with deswelling rate of 0.013 nm/min and 0.004 nm/min. The film thickness stays at 1.06 times of the initial film thickness even after 100% nitrogen spreading in the chamber. The degree of swelling of P2VP decreases from 1.2 to 1.1 in deswelling rate of 0.03 nm/min when the film is treated with 30% p/p_0 . The film thickness of P2VP easily falls back to the initial value before annealing. This means in the deswelling procedure PS block needs longer time block to solidify than P2VP. So the solidification of P2VP happens first and it roles as anchors with still fluid PS. When PS gets solidified, it shrinks in the confinement of P2VP matrix and the dewetting takes place to compensate the volume reduction of PS.

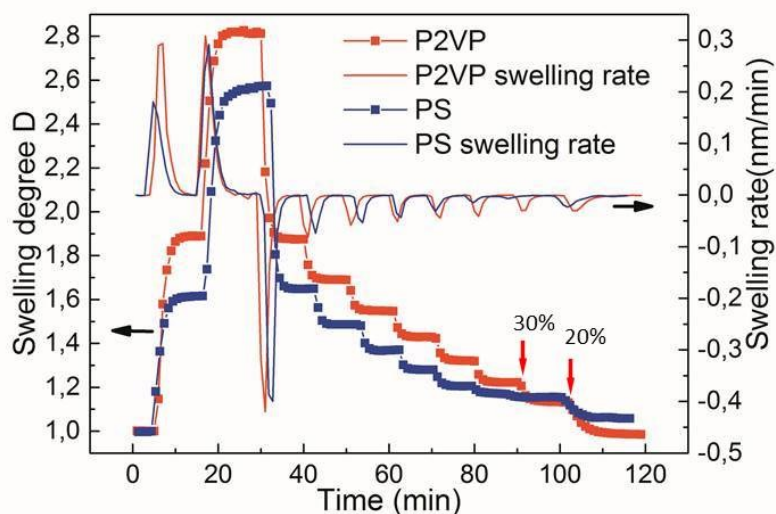


Figure 47 Kinetics curves of stepwise deswelling of ~ 40 nm PS and P2VP films under chloroform vapor with swelling rate. The swelling curves are from Figure 32b.

4.5. Time evolution of the structures in SV^{390} films with under-half-layer thickness

In Figure 48 there are the SFM height images with corresponding optical microscope images below presenting the spin-casted morphology of SV^{390} films from toluene solution by various dissolving method, standing at room temperature for 24h in (a), stirring at room temperature for 24h in (b) and standing at 4 °C for 24h. Method (a) causes a lot of micelles aggregation, which can be observed both on the SFM image as big white dots and on the optical image as black dust. Stirring and low temperature

4 Tunable morphology in ultrathin films of high molecular weight block copolymer (SV) via thermo-solvent annealing

standing can avoid the micelles aggregation in method (b) and method (c) with optical images clean. Comparing (b) and (c) it can be found that the film from standing solution presents more ordered and homogenous spheres than the film from stirred solution.

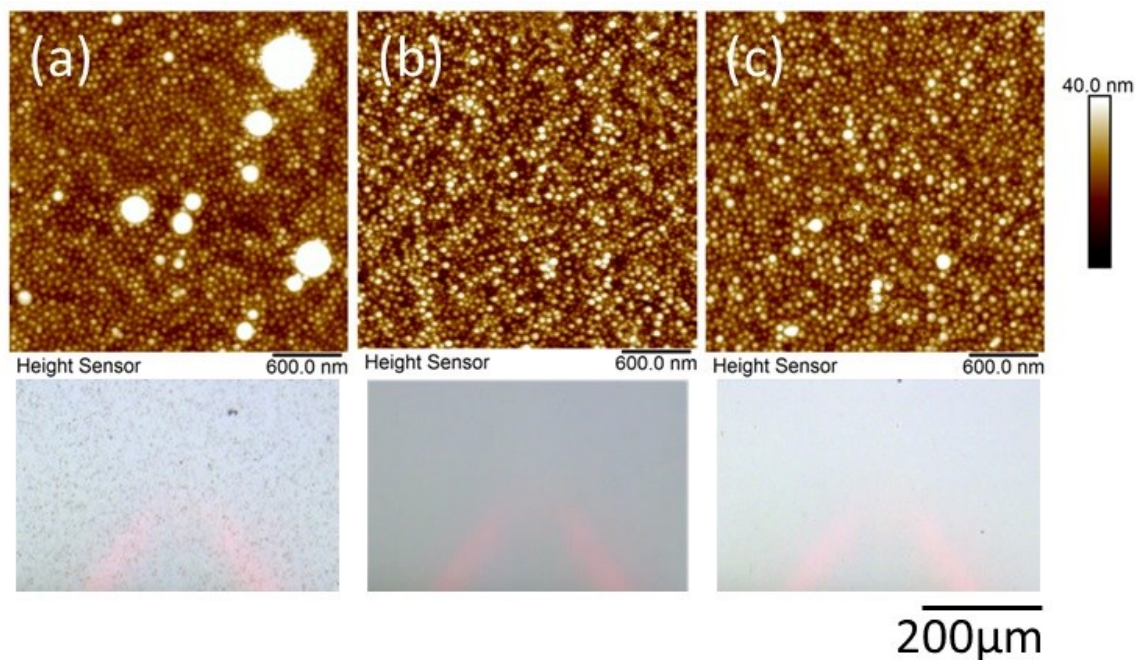


Figure 48 SFM height images of spin-casted SV³⁹⁰ films from toluene by staying at room temperature for 24h (a), stirring at room temperature for 24h (b), staying at 4 °C for 24h with their optical images below respectively.

Figure 49 presents the time-resolving morphology of ~ 40 nm SV³⁹⁰ film on silicon wafer. The initial spin-cast morphology is sphere with periodic length of 70 nm, where the spheres have PS block as shell and P2VP block as core duo to the PS-preferred solvent toluene. Then the slight annealing in chloroform vapor for 80 s induces the micelles turning to be small holes at each position with the periodic length stable. From the phase image we know the dot area is PS and the matrix is P2VP, so we can deduce that every P2VP core spills over the PS shell during annealing and creates the connection to each other. As Figure 35 demonstrated P2VP in ~ 40 nm film swells $\sim 15\%$ more than PS in ~ 40 nm film in chloroform vapor on the same condition, the P2VP block enlarges $\sim 15\%$ more than PS block during this block copolymer annealing.

4 Tunable morphology in ultrathin films of high molecular weight block copolymer (SV) via thermo-solvent annealing

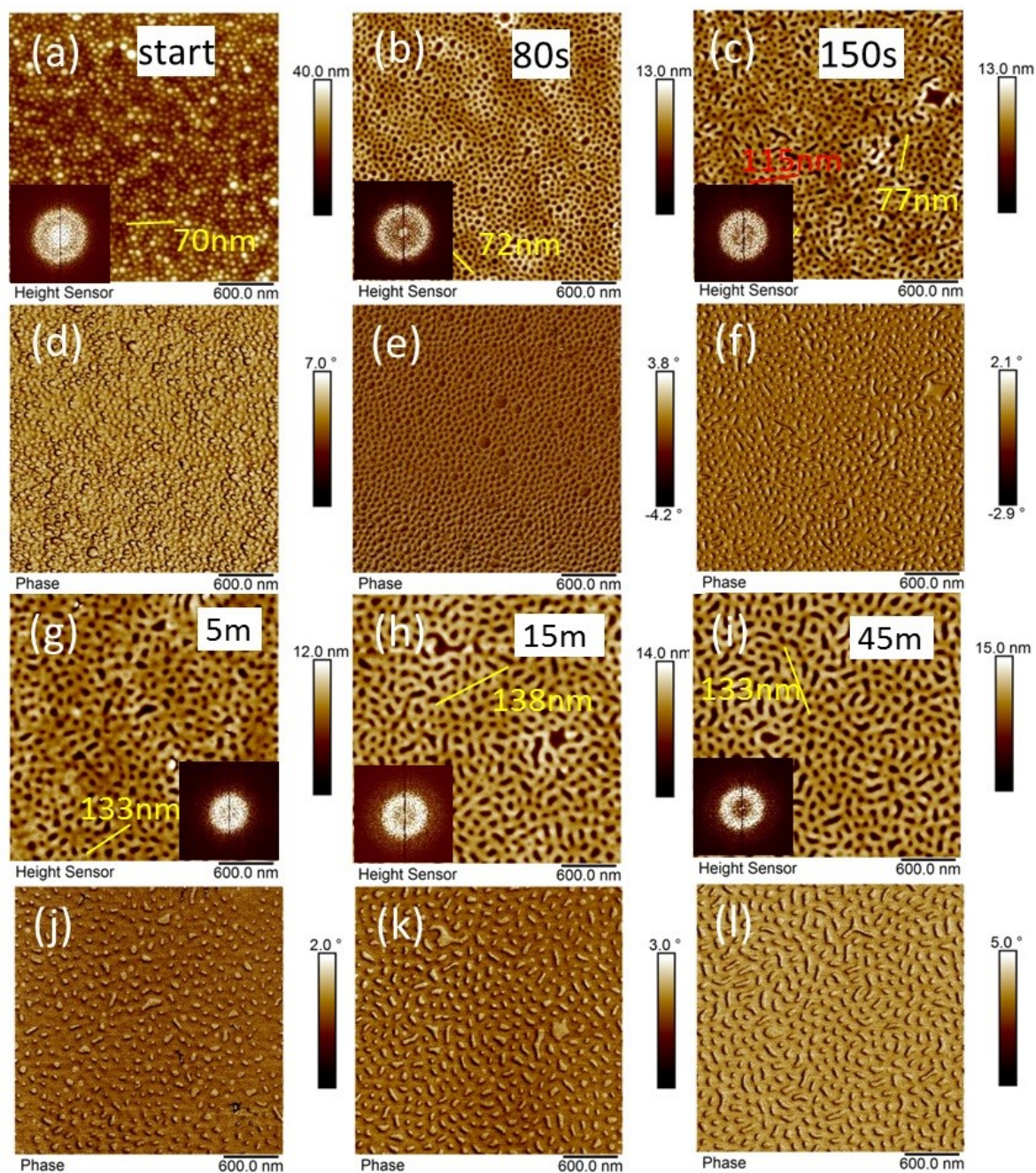


Figure 49 SFM height images (a)-(c) & (g)-(i) and their corresponding phase images (d)-(f) & (j)-(l) of time-resolved morphology of SV³⁹⁰ ~40 nm film on silicon substrate annealed by chloroform at 19 °C/20 °C with their FFT transfer images. The periodic distance and annealing time are labeled on each image.

4 Tunable morphology in ultrathin films of high molecular weight block copolymer (SV) via thermo-solvent annealing

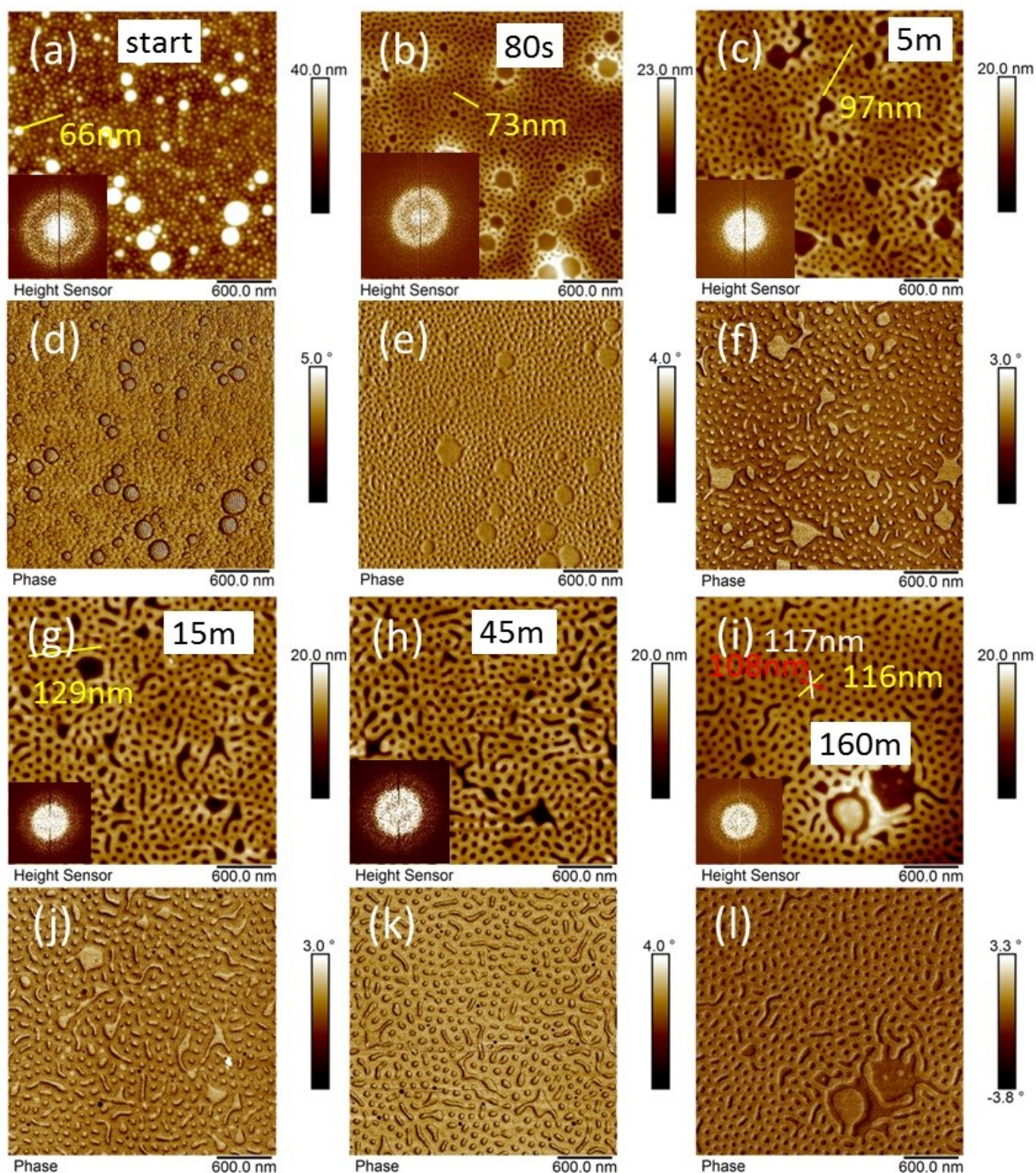


Figure 50 height images (a)-(c) & (g)-(i) and their corresponding phase images (d)-(f) & (j)(k)-(l) of time-resolved morphology of SV³⁹⁰ ~40 nm film on amorphous-carbon-layer covered silicon substrate annealed by chloroform at 19 °C/20 °C with the periodic distance and time on each image.

Figure 51 presents the kinetics curve of a swelling-deswelling cycle finished in 25 min with the morphology images of the SV³⁹⁰ film annealed for 1min, 5 min and 10 min. We

4 Tunable morphology in ultrathin films of high molecular weight block copolymer (SV) via thermo-solvent annealing

scanned not only the middle area with the precise thickness measured by Ellipsometry of each sample, but also the gradient edge which produces in the spin-coating process. The film thickness in the middle of the sample is 43nm and at thicker edge in this plot is below 55 nm.

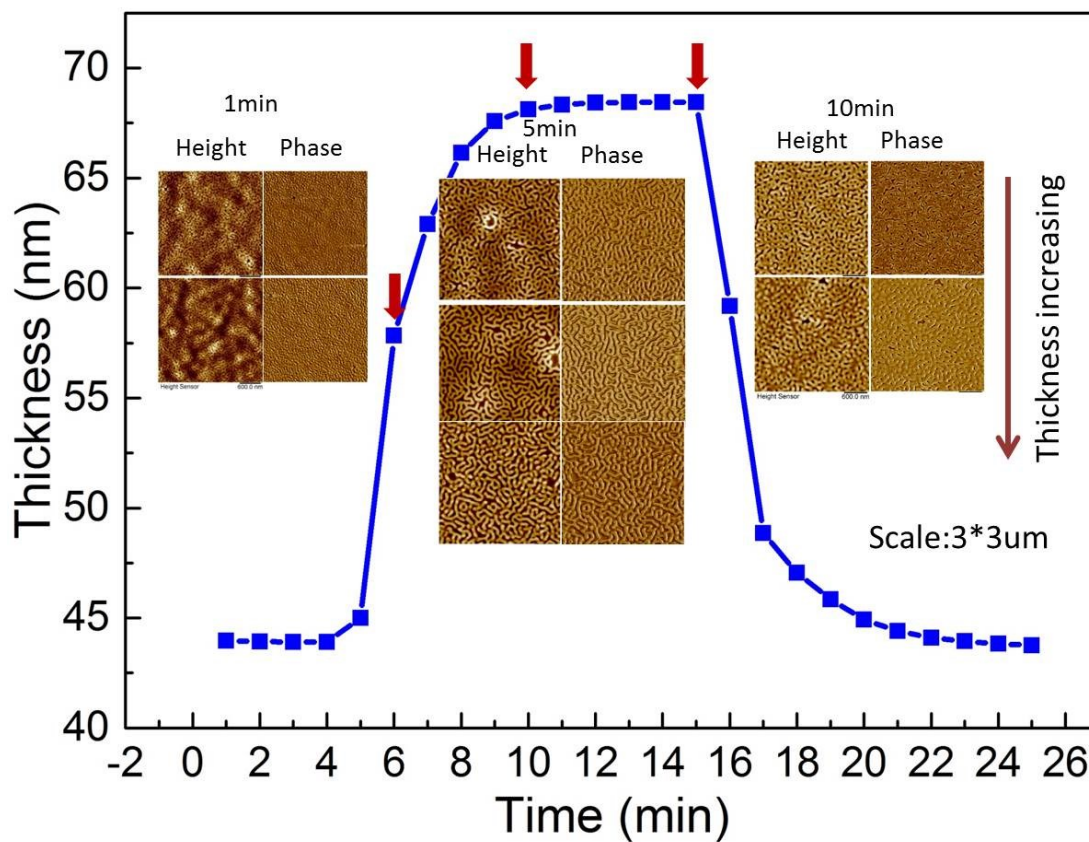


Figure 51 Kinetics curve of ~ 40 nm SV^{390} film annealed in chloroform vapor with its thickness-depending morphology at 1min, 5 min and 10 min.

4.6. Summary

In this chapter the swelling behavior and the morphologies of SV^{390} BCP in films with thickness under half-layer in slightly selective solvent vapor of chloroform are explored. Equilibrium morphology of SV^{390} films is interpreted and the kinetics of this self-assembly is monitored in time.

4 Tunable morphology in ultrathin films of high molecular weight block copolymer (SV) via thermo-solvent annealing

First, the swelling behavior of BCP films can be precisely tuned by temperature and/or vapor flow separately. The temperature is a critical factor, which influences the vapor pressure and limits the sensitivity of films response to various annealing conditions. In this case the factors including degree of swelling, χ and surface tension to influence the equilibration process of BCP films can be explored individually.

Second, the annealing process at higher temperature leads to a faster polymer chain movement even at the same degree of swelling.

Third, the morphology in equilibrium state of ~ 40 nm thick SV³⁹⁰ films constitute with PS dots and P2VP matrix, which is proved by various methods like scanning with Peak Force Mode in SFM, metallization of the SV³⁹⁰ templates and pattern transfer to silicon wafer by CF₄ etching.

Last the kinetics research on the self-assembly of SV³⁹⁰ films demonstrate that the original morphology of the BCP with high molecular weight shows immediately response to the solvent vapor. When the film has strong or weak interaction with the substrate, the equilibration process finishes in 5 min or 15 min respectively. Duo to these results the initial morphology of BCP films from spin-coating solution has no influence to their final morphology.

5 Effects of thickness gradients, surface properties and solvent quality on the microphase separation in block copolymer films¹

In the previous chapter we discussed the influence of the degree of swelling and the temperature conditions on the phase separation in films of high molecular weight SV block copolymer. In this chapter we consider a number of further factors which affect the structure formation of block copolymer in films and can be used to guide the structure into desired patterns. In particular, we focus on the confinement and thickness gradient effects, nature and properties of the substrate, as well as the possibility to tune the starting morphology by utilizing solvents of varied quality. To study the confinement effects which arise when the film thickness is compatible with the intrinsic domain spacing, we compared two lamella-forming SV block copolymers with 4-fold difference in the molecular weight. High molecular weight, SV³⁹⁰ block copolymer has low chain mobility and therefore a very slow ordering dynamics. Also it experiences a strong confinement effects since its domain spacing (117 nm) is much below or comparable with the studied film thicknesses. The shorter SV⁹⁹, block copolymer with a domain spacing of ~47 nm has been intensively studied before [137], and was used in this work as a reference system.

In the experiments the film thickness was varied between sub half-layer to one-layer. Film thickness gradients have been prepared by spin-coating block copolymer solutions on patterned substrates. The various initial morphologies have been obtained by dissolving SV³⁹⁰ in a number of solvents with different selectivity to each block and with different physical properties.

5.1. Effect of the confinement on the morphological behavior of SV³⁹⁰

As substrates cleaned Si wafers with ~2 nm thick SiO₂ layer at surface have been used. For SV block copolymer this substrate implies asymmetric wetting conditions, since the substrate prefers polar P2VP block, while PS segregates to the free surface due to its

¹ The patterned photoresist substrates we used in this chapter are provided by Sascha Brose from Fraunhofer-Institut für Lasertechnik (ILT) in Aachen.

5 Effects of thickness gradients, surface properties and solvent quality on the microphase separation in block copolymer films

lower surface tension than that of P2VP. All ~ 40 nm films have been spin-coated from toluene solutions and thicker films from chloroform solutions. They all are annealed under solvent vapor at indicated conditions.

5.1.1. Thickness regime from sub-half layer to above-half layer

In this regime the block copolymer is under strong confinement conditions. The SV³⁹⁰ films with thickness from 36 nm to 61 nm were prepared at varied spin-coating conditions from toluene solution. Then they were treated by solvent vapor annealing under the same conditions of $T_v = 14$ °C, $T_s = 20$ °C and the partial vapor pressure of 100% for 200 min. Their (quasi)equilibrium morphologies after annealing and quench with dry nitrogen are shown in Figure 52. We note that the starting morphology is represented by micelles (shown in Figure 67) since toluene is a strongly selective solvent for the PS block. In all cases the initial spherical pattern vanished and developed into stripe-like patterns with different dimensions and different degree of regularity. With increase of the starting thickness, and corresponding, the swollen film thickness from $\sim 0.5L_0$ to $0.85L_0$, (in Figure 52) the morphology changes from disordered arrangement to ordered standing lamella.

5 Effects of thickness gradients, surface properties and solvent quality on the microphase separation in block copolymer films

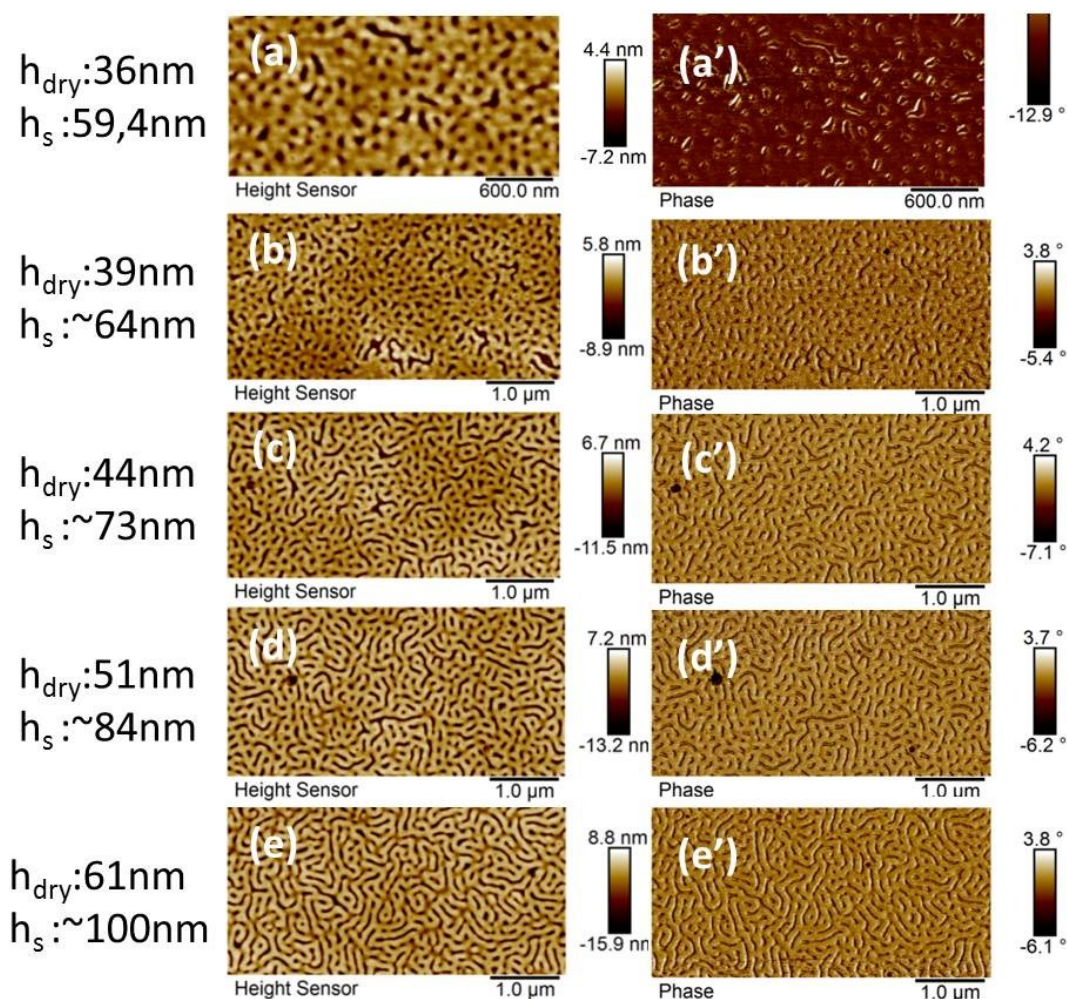


Figure 52 SFM height and phase images of SV^{390} films with dry thickness from 36 nm to 61 nm annealed by chloroform with degree of swelling of 1.65.

Shown in Figure 53 are the surface structures of SV^{390} films with the dry thicknesses increasing from 41 nm to 134 nm after annealing at a degree of swelling of 2.5. The morphology is stripe-like lamella when the swollen film thickness is 100.9 nm ($\sim 0.85L_0$). As film thickness increases to 175 nm ($\sim 1.5L_0$), the lying lamella co-exists with striped pattern. The step height between the featureless flat areas of in-plane lamella and striped pattern of up-standing lamella is ~ 8 nm. The height difference between the top and the bottom of up-standing lamella is ~ 15 nm.

When the swollen thickness achieves ~ 255 nm ($\sim 2.2L_0$), the morphology transforms to lying lamella almost all over the sample. There are also some hole-like terraces with

5 Effects of thickness gradients, surface properties and solvent quality on the microphase separation in block copolymer films

depth of ~ 30 nm due to the deviation of film thickness from the equilibrium value, which for asymmetric wetting conditions should be $(n+1/2)L_0$.

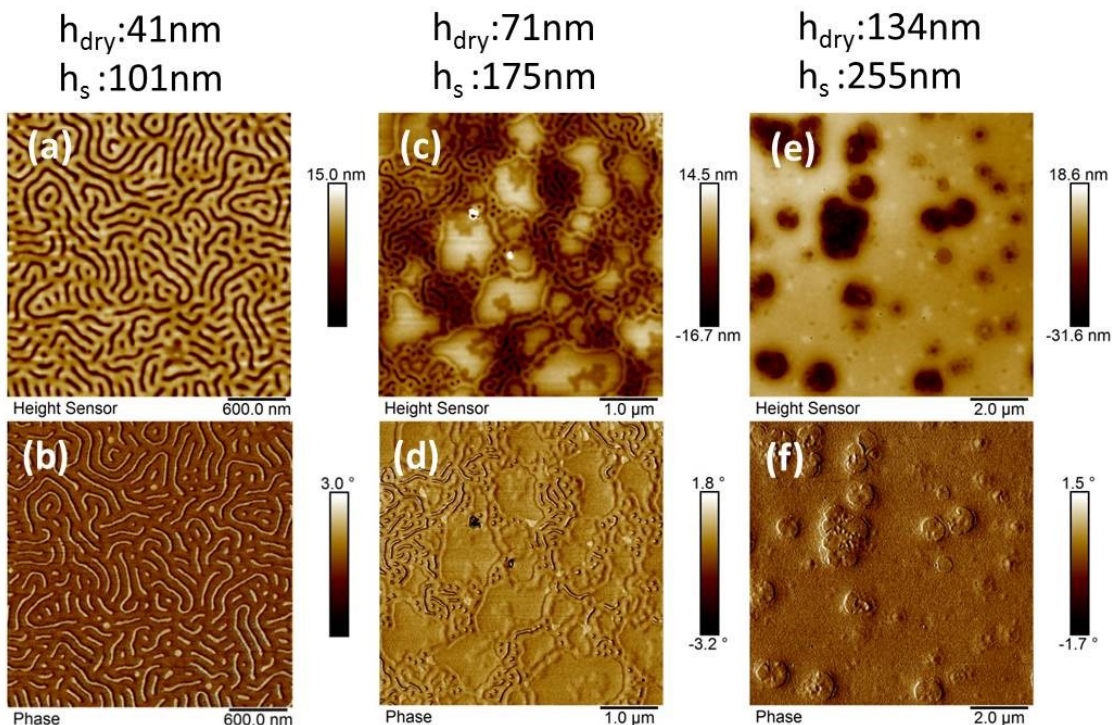


Figure 53 SFM (a) (c) (e) height and (b) (d) (f) phase images of SV^{390} annealed under chloroform vapor on SiO_2 substrate at 19 °C/20 °C for 200 min with a degree of swelling of 2.5.

5.1.2. Metallization of block copolymer template with gradient thickness

To distinguish these two kinds of morphologies (perforated lamella as shown in Figure 38 in Chapter 4 and standing lamella), we metallized the templates with Pt^{2+} solution. The SFM images of these templates before and after metallization with their cross-section profiles are shown in Figure 54. As expected, the metallization of the perforated template in Figure 54a shows Pt perforated membrane, and the Pt from the template in Figure 54d shows metal stripes. In the cross-section profiles we found the distance between each stripes in Figure 54c is obviously larger than that in Figure 54f, which could be a cue for different types of morphology. But more stable and direct evidence to distinguish the cylinder and lamella morphology is still needed.

5 Effects of thickness gradients, surface properties and solvent quality on the microphase separation in block copolymer films

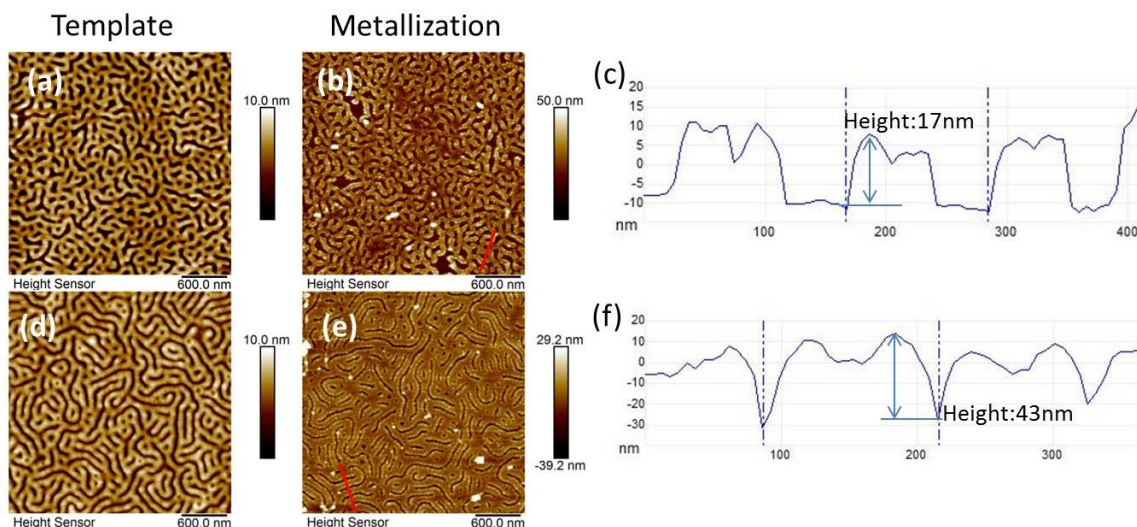


Figure 54 SFM (a) (b) (d) (e) height images of SV^{390} template(a) (d) and metallization(b) (e) and their cross-section profiles (c) (f). The templates are prepared by annealing ~ 40 nm SV^{390} films under chloroform vapor to swollen thickness of (a) 64 nm (d) 100 nm.

5.2. Effect of confinement and solvent selectivity on the morphological behavior of SV^{99} in thin films

Symmetric SV^{99} block copolymer in films with $f_{PS} = 0.54$, which show lamella morphology under neutral solvent vapor, are annealed under strongly selective solvent to PS block. The films show cylinder-forming morphological behaviors as block copolymer with asymmetric volume fraction.

5.2.1. Film thickness dependent microphase separation upon annealing in highly selective solvent vapor

SV^{99} thin films with domain spacing of 47.2 nm in bulk [137] were prepared from chloroform solution on silicon wafers in various thicknesses ranging from 14 nm to 35 nm. The thickness gradient from the center to the edges of the film was created by spin-coating on small-size substrates. After annealing in toluene vapor for 60 min with a degree of swelling of 1.8, the morphology shows obvious trend: standing cylinder of P2VP ($h_{sw} = \sim 0.5L_0$), mixture of standing cylinder and parallel cylinder ($h_{sw} = \sim L_0$) and perforated lamella of PS ($h_{sw} = \sim 1.3L_0$).

5 Effects of thickness gradients, surface properties and solvent quality on the microphase separation in block copolymer films

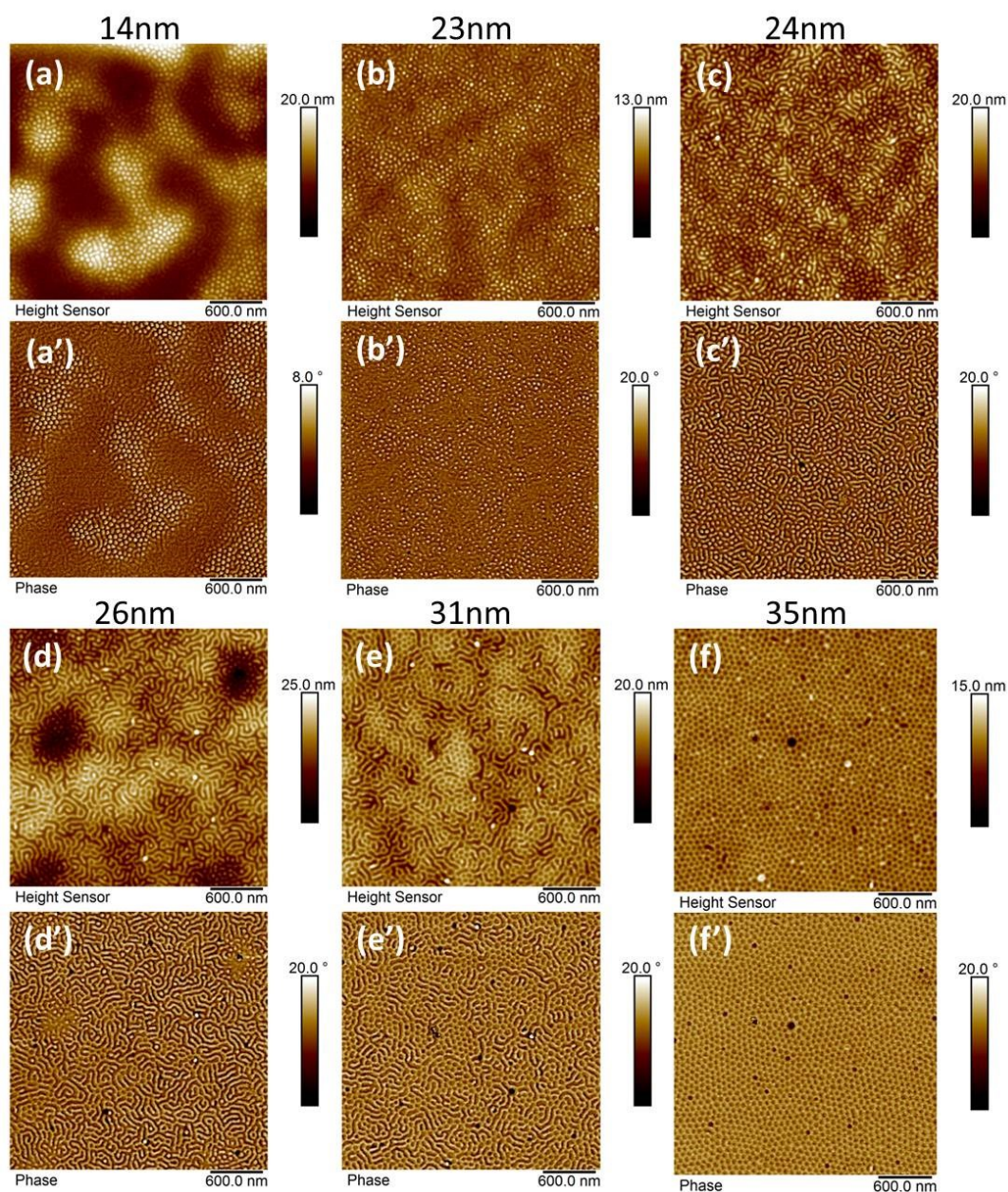


Figure 55 SFM height (a)-(f) and phase (a')-(f') images of SV⁹⁹ annealed by selective solvent vapor toluene at 19 °C/20 °C for 60 min with initial thickness increasing from 14 nm to 35 nm. The degree of swelling is 1.8 during annealing.

Figure 56 presents the power spectral density (PSD) analysis of each morphology shown in Figure 55. The peak of every curve reveals the periodic feature on each image indicating the characteristic spacing (d_0) is a 56.6 nm, b 55.6 nm, c 58.8 nm, d 60.0 nm,

5 Effects of thickness gradients, surface properties and solvent quality on the microphase separation in block copolymer films

e 62.5 nm and f 65 nm. The characteristic lamella spacing (L_0) of SV⁹⁹ is $\sqrt{3}/2$ times of d_0 in Figure 55a.

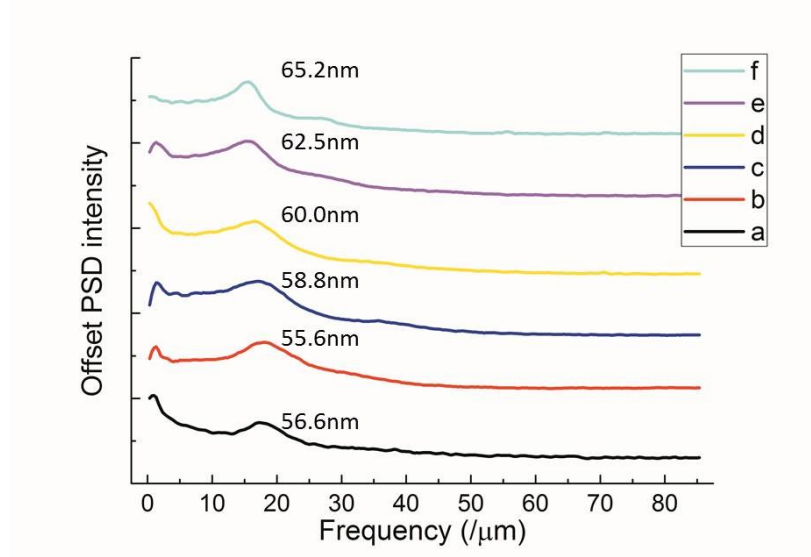


Figure 56 PSD analysis of SV³⁹⁰ morphology shown in Figure 55 to obtain their domain spacing. Line a-f indicates the corresponding images in Figure 55.

5.2.2. Thickness dependent microphase separation in slightly selective solvent vapor

The combined interaction parameter $\chi_{AB}N$ plays an important role in phase separation of BCPs. For the films under annealing $\chi_{eff} = \chi_{AB} * \Phi_p$, where Φ_p is the polymer volume fraction, so the degree of swelling influences this parameter directly. Here we annealed two SV⁹⁹ films with different initial thicknesses to a same swollen thickness at the same temperature conditions to evaluate the effect of the degree of swelling separately. Figure 57 presents the morphologies in two SV⁹⁹ films upon annealing with initial thicknesses of 46 nm and 52 nm. The swollen thickness of both films was 94 nm ($1.7L_0$) with degree of swelling of 2.1 and 1.8 respectively. The film with a higher degree of swelling shows a mixture of lying lamella and standing lamella with a trend of terracing, so that the in-plane lamella develops in the thicker areas of the film, and up-standing lamella – in the lower terrace. The film swelling to degree of 1.8 (Figure 57b, d) displays only standing

5 Effects of thickness gradients, surface properties and solvent quality on the microphase separation in block copolymer films

lamella. These results prove that the larger degree of swelling gives the film obviously higher kinetics since the solvent decrease the viscosity of the film.

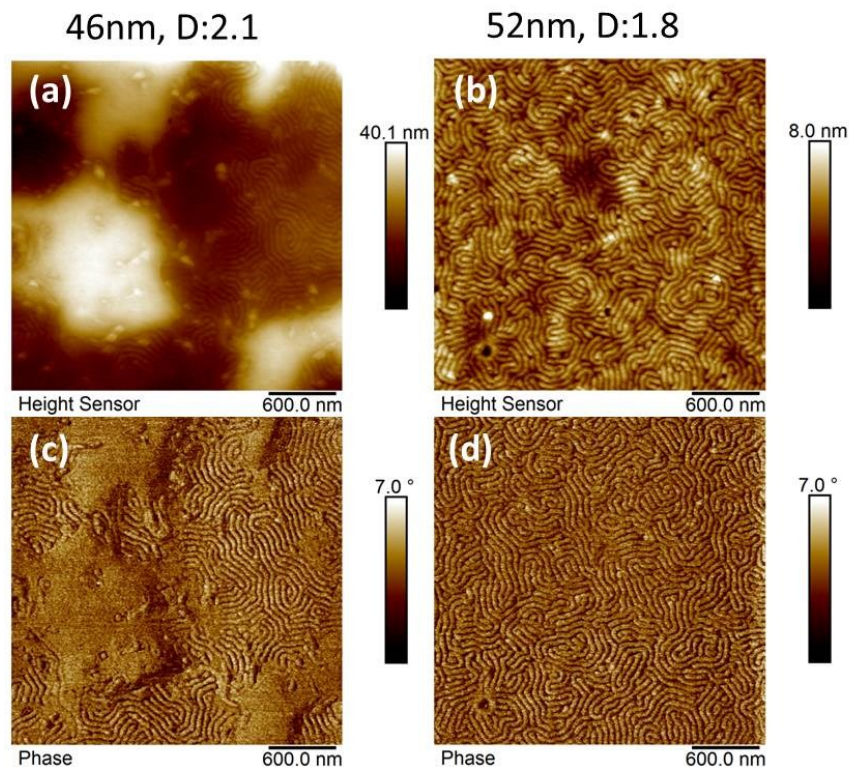


Figure 57 SFM (a) (b) height and (c) (d) phase images of SV⁹⁹ films with initial film thickness of (a) (c) 46 nm (b) (d) 52 nm, annealed by chloroform vapor at 19 °C/20 °C for 60 min. Their swollen thicknesses are both 94 nm ($1.7L_0$).

To find out how film thickness influences the phase behavior of compositionally symmetric BCPs under slightly selective solvent, the SV⁹⁹ film with initial thickness of 39 nm, 42 nm and 52 nm (measured at different places of the same sample) was annealed under chloroform vapor at T_v/T_s 14 °C/20 °C for 120 min. With increasing film thickness the annealed morphologies develop from lying lamella ($h_{sw} = \sim 1.3L_0$) in Figure 58a, d to standing lamella ($h_{sw} = \sim 1.7L_0$) in Figure 58c, f.

5 Effects of thickness gradients, surface properties and solvent quality on the microphase separation in block copolymer films

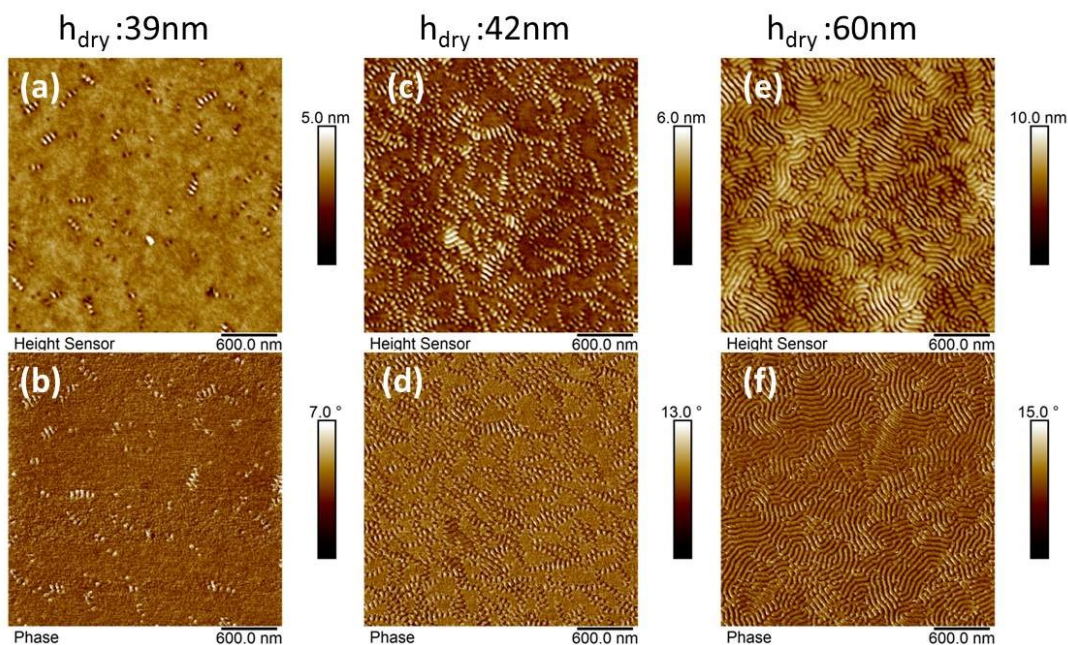


Figure 58 SFM (a) (c) (e) height and (b) (d) (f) phase images of SV^{99} with initial film thickness of 39 nm, 42 nm and 60 nm, annealed by chloroform at 14 °C/20 °C for 120 min. The degree of swelling is 1.53 controlled by partial vapor pressure.

5.3. Substrate-induced morphological behavior

Substrate property shows strong influence on the phase separation of BCP films when the film thickness is in the range of its domain spacing. In substrate-supported films the question of the range of the propagation of the surface field at the substrate to the free surface, i.e. throughout the film – is still an important issue to study.

5.3.1. Comparison of the swelling behavior of SV^{390} in films with the thickness range between under half-layer and over half-layer thickness

In Figure 59 we present kinetics curves of PS, P2VP and SV^{390} films with the thickness of ~80 nm under chloroform vapor and also the data of polymer volume fraction comparing ~40 nm thick and ~80 nm thick films. The volume fraction of thicker films is systematically higher as compared to thin films of homopolymer samples, while for the block copolymer the difference is negligible. From the mathematic point of view this phenomenon is not logical, but in our measurement the ellipsometry detects the change

5 Effects of thickness gradients, surface properties and solvent quality on the microphase separation in block copolymer films

of polarization of light and calculates the film thickness based on the refractive index of the film. It is a very sensitive test method influenced by the film structure and solvent adsorption capacity, which could lead to the measurement error. From current curves in (b) we can infer the thicker films swell less than thinner films at the same partial vapor pressure.

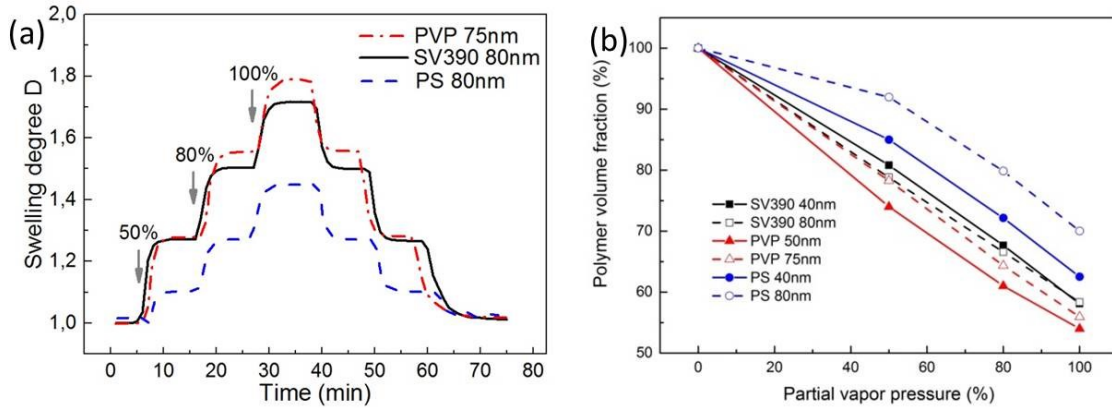


Figure 59 (a) Kinetics of the stepwise swelling and deswelling of PS (dashed line, 48 nm thick), P2VP (dash-dot line, 43 nm thick) and SV block copolymer (solid line, 39 nm thick) as indicated by arrows at 50% 80% 100% of the relative partial vapor pressure of chloroform (p/p_0). (b) Polymer volume fraction Φ_p as a function of the relative partial vapor pressure of chloroform (p/p_0) in swollen films of PS (blue triangles, 48 nm thick), P2VP (red circles, 43 nm thick) homopolymer and SV block copolymer (black squares, 39 nm thick). The swelling has been done at $T_v = 14^\circ\text{C}$ and $T_s = 20^\circ\text{C}$

The annealed morphologies of ~ 40 nm and ~ 80 nm films of SV³⁹⁰ on the same condition is shown in Figure 39a and Figure 62c.

5.3.2. Comparison of the microphase separation in SV films on different substrates

Shown in Figure 60 are ~ 40 nm thick SV³⁹⁰ films which have been annealed on SiO₂, carbon and hard mask (HM) substrate under identical conditions (chloroform vapor at 19 °C/20 °C with swollen film thickness of ~ 102 nm on Si for 200 min). SiO₂ substrate is about a 2 nm-thick amorphous layer on Si wafer prepared by air plasma treatment. Carbon substrate is prepared by carbon sputtering on Si wafer, which is usually used as weakly interacting substrate with both blocks of SV block copolymer.

5 Effects of thickness gradients, surface properties and solvent quality on the microphase separation in block copolymer films

HM is a ~50 nm-thick highly cross-linked glassy polymer network with high carbon content prepared by spin-coating the solution (HM8006-8) on silicon wafer with thermal treatment at 225°C for 90 s [137]. The films show standing lamella, perforated lamella with stripe and island defects, and perforated lamella with island defects on each substrate. The terraces in Figure 60e, f, the film on HM substrate, contain both PS and P2VP block based on the analysis of the height and phase images together. The color contrast of the phase image d is inverted with b and f. When the physical properties (like stiffness, adhesion) of two blocks are very different, phase channel provides reliable information to distinguish them (e.g. SB). However phase data can also be influenced by various parameters during the measurement, so that their interpretation is not straightforward. The physical properties of PS and P2VP show no obvious difference. So in this case the phase channel is not a reliable tool to distinguish between the two blocks.

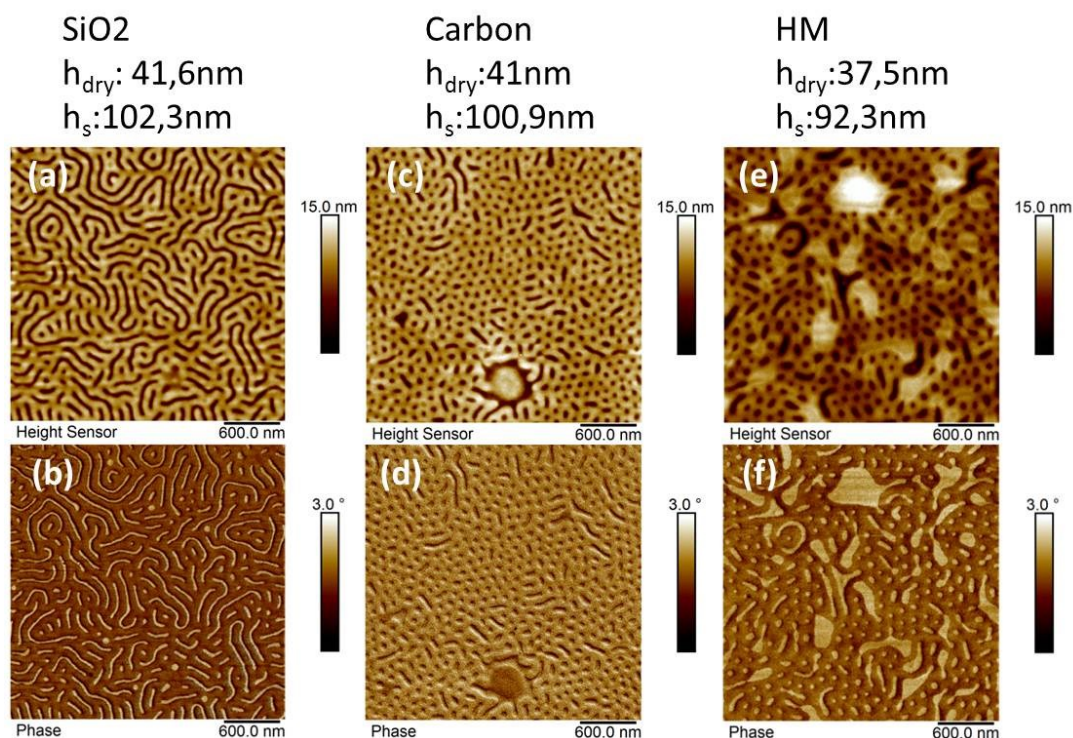


Figure 60 SFM height (a) (c) (e) and phase (b) (d) (f) images of SV390 films annealed in chloroform vapor at 19 °C/20 °C on (a) (b) SiO₂ (c) (d) carbon (e) (f) HM substrate for 200 min. The swollen film thickness of films on carbon and HM is estimated to be 101 nm and 92 nm respectively, based on the degree of swelling of film on silicon substrate.

5 Effects of thickness gradients, surface properties and solvent quality on the microphase separation in block copolymer films

Half-layer thick SV³⁹⁰ films on various substrates including SiO₂, carbon and HM were annealed under chloroform vapor at 19 °C/20 °C to 1.3L₀ swollen film thicknesses (Figure 61). The swollen thickness on SiO₂ substrates is measured by *in situ* ellipsometry, but the other two swollen thicknesses on carbon and HM substrates are estimated from the similar degree of swelling on the same annealing conditions. Due to the different substrate/film interaction, the degree of swelling may have a little deviation. The annealing time here was set for 30 min to catch the morphology changing route. The ~80 nm SV³⁹⁰ films are from chloroform solution and their original morphologies are similar with the ~40 nm film in Figure 67c, d. Taking the ~80 nm SV³⁹⁰ annealed for long time on Si substrates (Figure 62) into consideration, the morphology could first turn to be mixture of lying lamella and micelles, and then stripes come out from the micelles. But to confirm this, more experiments are still needed.

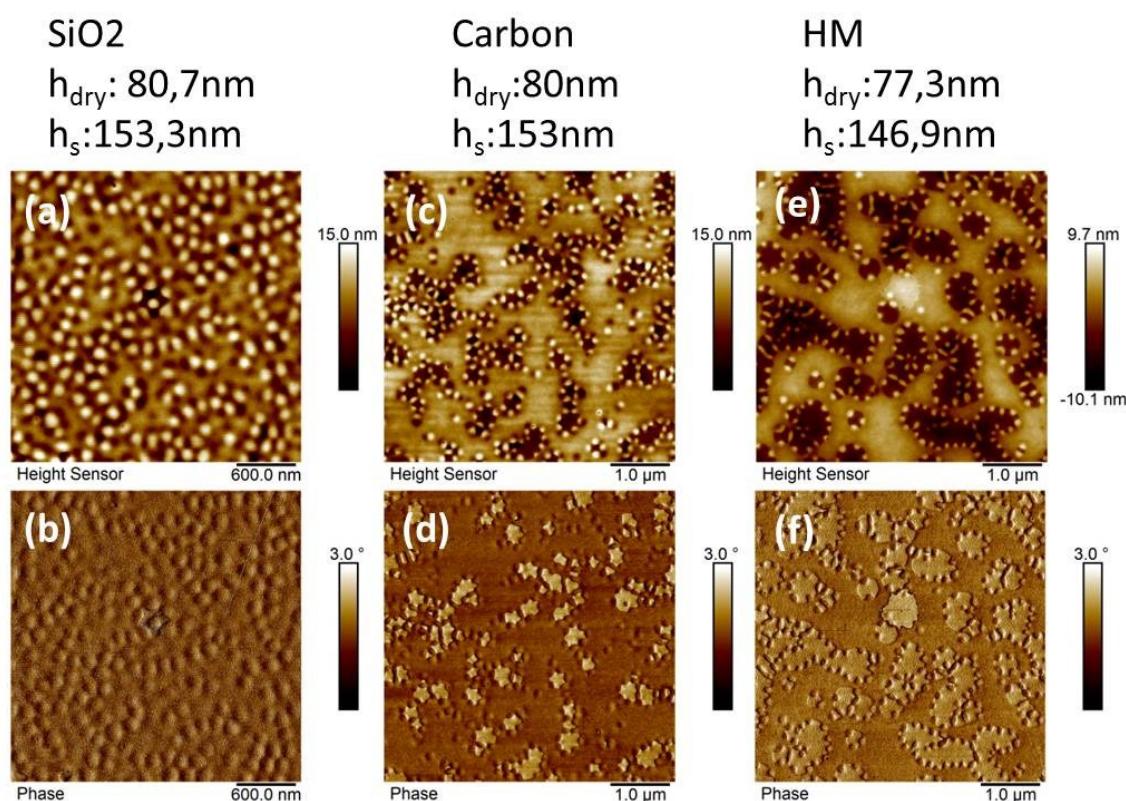


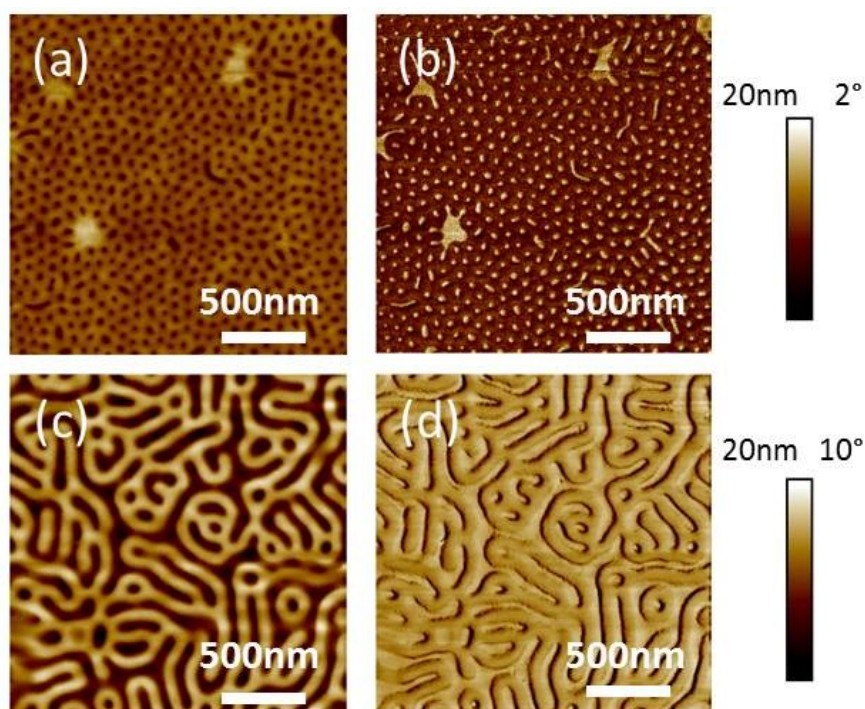
Figure 61 SFM height (a) (c) (e) and phase (b) (d) (f) images of SV³⁹⁰ films with dry thickness of ~80 nm annealed in chloroform vapor of 90% p/p₀ at 19 °C/20 °C with degree of swelling of 1.9 (based on the film on the SiO₂ substrate) for 30 min. The

5 Effects of thickness gradients, surface properties and solvent quality on the microphase separation in block copolymer films

swollen thickness of the film on SiO₂ substrate is measured by *in situ* ellipsometry, while the swollen thicknesses of those on carbon and HM substrates are approximately estimated by the same degree of swelling on silicon wafers [137].

5.3.3. Effect of the film thickness in on the phase separation of SV³⁹⁰ block copolymer on weakly interacting substrates with weak interaction

Figure 62 shows the change of the annealed morphology of SV³⁹⁰ films depending on film thickness. Under chloroform vapor the film with dry thickness of 42 nm swells to 75,4 nm (0,58L₀), the thicker one with 78 nm swells to 106,6 nm (0.82L₀). The morphology changes from perforated lamella in 42 nm thick SV³⁹⁰ film to the mixture of perforated and stripe-like lamella in 78 nm thick film, then to standing lamella in 150 nm thick film. Here we find the effect on morphology to decrease as the film thickness increases. When the film thickness is above one layer, the effect disappears completely and the SV film shows bulk phase behavior.



5 Effects of thickness gradients, surface properties and solvent quality on the microphase separation in block copolymer films

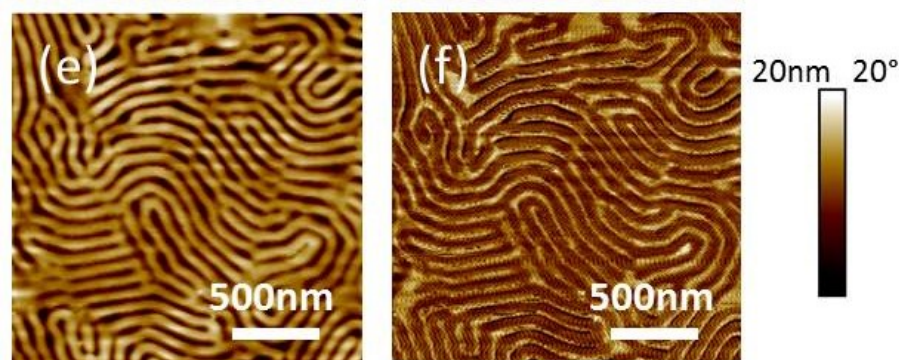


Figure 62 (a) (c) (e) SFM topography and (b) (d) (f) phase images of PS-*b*-P2VP films with dry thicknesses of (a) (b) ≈ 42 nm, (c), (d) ≈ 78 nm and (e) (f) ≈ 150 nm after annealed in chloroform vapor at vapor temperature of 19 °C and substrate temperature of 20 °C. The center-to-center distance of period pattern is 132.3 nm in a) 127 nm in (c) and 128 nm in (e). The lamella height is 4.7 nm in (a), 13 nm in c) and 6.8 nm in (e). The dot radius is 23.4 nm in (a) and the lamella width (light area) is 66 nm in (c), 80 nm in (e).

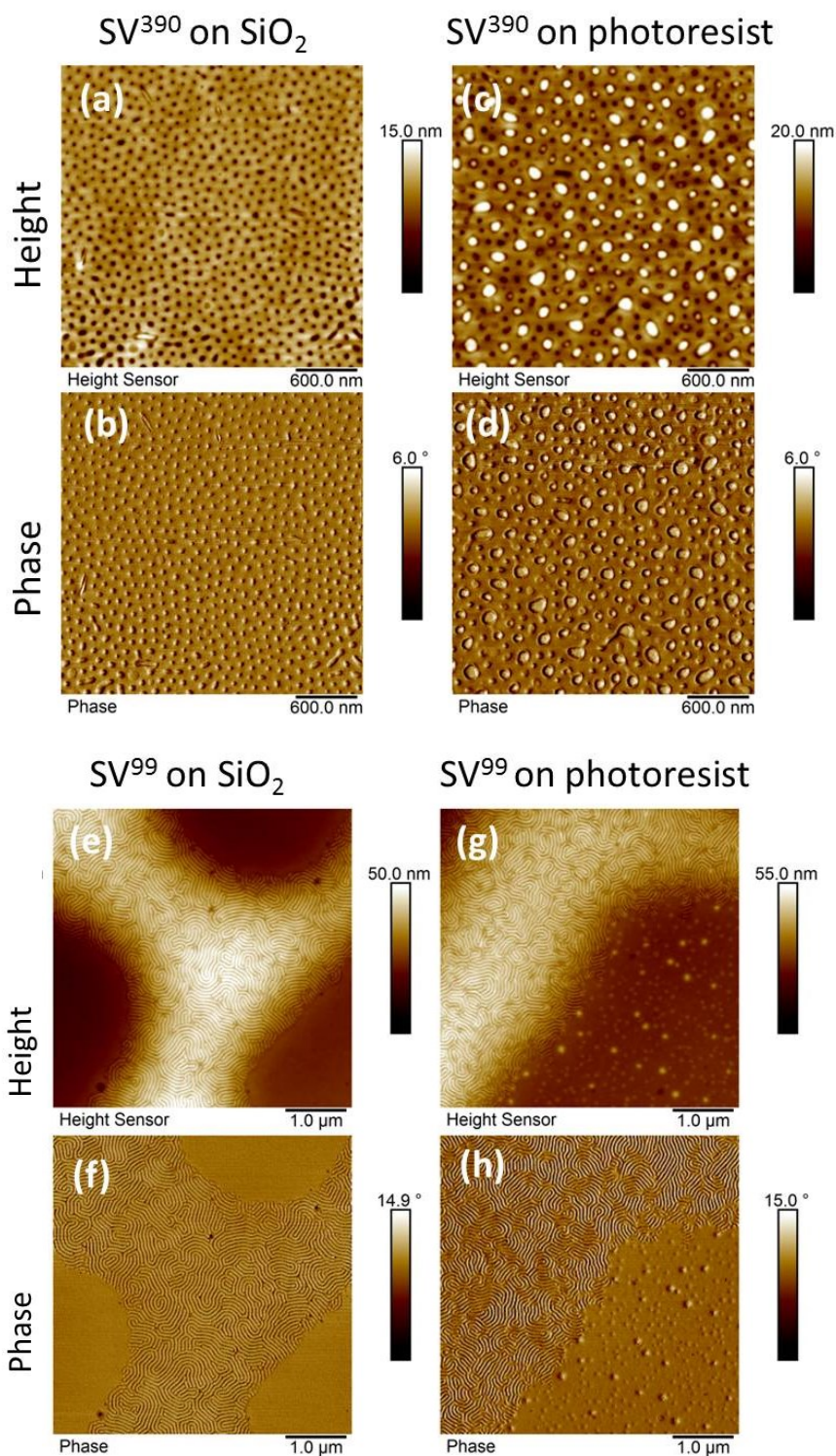
5.3.4. Effect of molecular weight of SV on the efficiency of the solvent annealing on HM supports

BCPs templates can be used for facile and reproducible transfer of topographic patterns into photoresist masks. At the same time, as has been shown earlier [137], the swelling of HM supports affects the microphase separation in block copolymer film. Here we compared the morphologies in SV³⁹⁰ and SV⁹⁹ films on photoresist substrates and on silicon wafers after annealing under chloroform vapor 100% p/p₀, (Figure 63). The basic morphologies can be reproduced, but many unexpected micelles exist in Figure 63(c), (d) (observed from the phase image). It is known, that after annealing of the HM film its surface is covered by spherical structures which are presumably formed by collapsed dangled end of the non-crosslinked chains. These spherical features may serve as nucleation centers for the development of novel structures in the block copolymer film. These micelles are also found in the lying lamella area in Figure 63g, h.

The analysis of the data for SV⁹⁹ block copolymer in Figure 63 suggests that at 100%-saturated chloroform atmosphere and at long annealing time of 200 min the HM support

5 Effects of thickness gradients, surface properties and solvent quality on the microphase separation in block copolymer films

does not bring any difference in the structure development: both films show coexistence of the first terrace with in-plane lamella and the second terrace of up-standing lamella.



5 Effects of thickness gradients, surface properties and solvent quality on the microphase separation in block copolymer films

Figure 63 SFM (a) (c) (e) (g) height and (b) (d) (f) (h) phase images of SV³⁹⁰ and SV⁹⁹ films on SiO₂ and photoresist substrate as indication annealed by chloroform vapor at 14 °C/20 °C for 120 min.

5.4. Combined effect of film thickness gradients and surface energy at the substrate

As the combined interaction of film thickness and substrate confines the phase separation of thin BCP films, we chose some patterned substrates of photoresist and PDMS to induce ordered morphology in this part.

5.4.1. Phase separation of SV⁹⁹ in films on patterned photoresist substrates

The patterned substrate containing hexagonal arranged pins, as well as spin-coated and annealed SV⁹⁹ films with their cross-section profiles are shown in Figure 64. The original patterned substrate contains pins with features of 41 nm height, 56 nm distance 1 and 660 nm distance 2, where the distance 1, 2 is the shortest and longest distance between every two pins. And the pins have curved side walls. After spin-coating the BCP accumulates more at the flat area, especially at the small gap (Distance 1), and stays relatively thin at the top of the pins. This is proved in Figure 64b, e, comparing with the original substrate. So the film has gradient thickness with patterned arrangement base on the position of pins. From the values shown in Figure 64e, we can figure out the thickness difference between the top of pins and the flat substrates are ~20 nm. Since the pins are not grown straightly on the substrate, the distance between every two pins are also increased. The morphology after spin-cast of SV⁹⁹ is represented by a striped pattern, which is not influenced by the gradient in the film thickness. After annealing in 90% toluene vapor at 14 °C/20 °C with the degree of swelling of 1.3, the changes of the morphology and film thickness are shown in Figure 64c, f. The striped pattern presents parallel arrangement at the middle of every 6 hexagonal pins and perforated trend at the gap between two pins with the short distance. The distance 1 increases but the distance 2 decreases in the cross-section profile indicating the BCP film at the tops and side walls of the pins moving down to the flat substrate. In this result the gradient film thickness is successfully obtained and the annealed morphology is

5 Effects of thickness gradients, surface properties and solvent quality on the microphase separation in block copolymer films

induced by the change of film thickness, which provides an effective method for tuning morphology of BCP template on photoresist substrates. More details to the dependence of the microphase separation on the annealing process and the geometry of the pattern are summarized in Appendix 10.

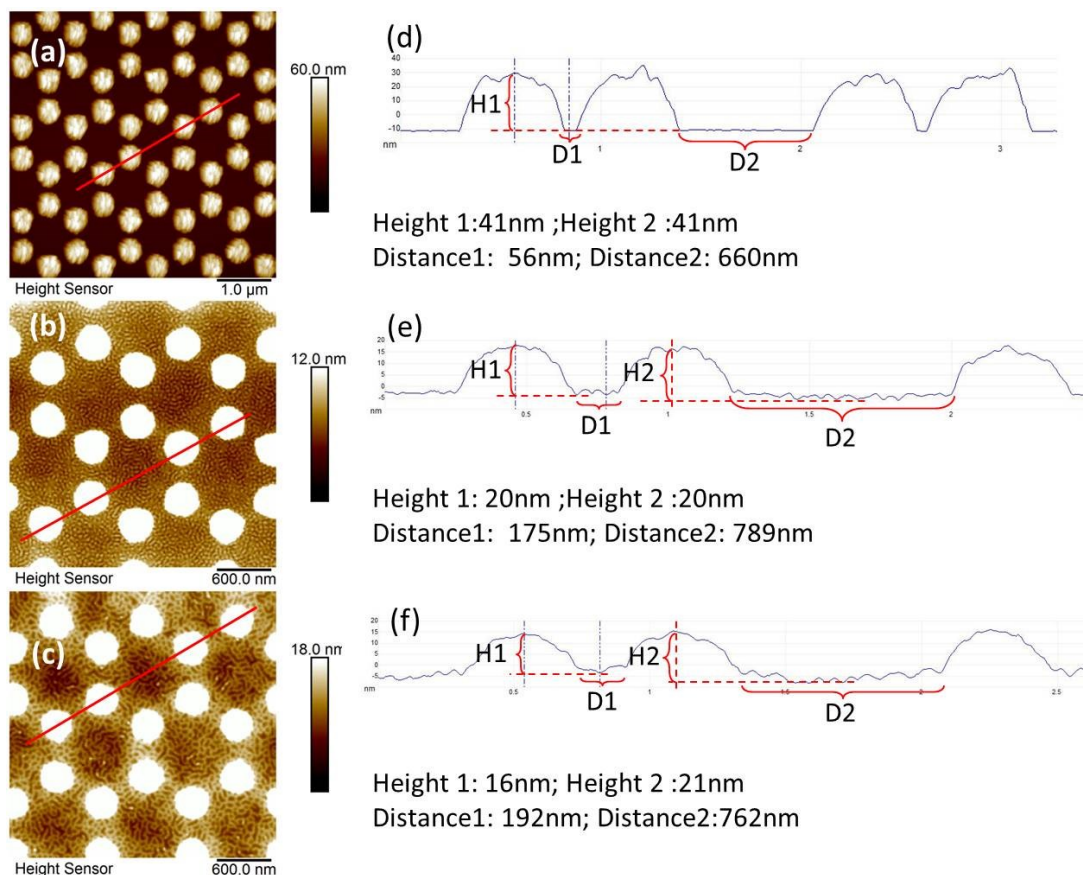


Figure 64 SFM height images of (a) patterned photoresist substrate, a SV^{99} film from chloroform on patterned substrate (b) before and (c) after annealing by toluene vapor at 19 °C/20 °C for 60 min.

5.4.2. SV films on wrinkled PDMS substrate

Wrinkled PDMS substrates after oxygen plasma treatment contain SiO_2 at the surface, which can also induce the gradient film thickness. Figure 65 presents the SV^{390} films (b, e) on wrinkled PDMS (a, d) after annealing in chloroform vapor (c, f). We spin-cast the SV^{390} film on the wrinkled PDMS substrate with the same conditions for 175 nm film on flat silicon wafer, where the film is thinner at the top and thicker at the bottom than

5 Effects of thickness gradients, surface properties and solvent quality on the microphase separation in block copolymer films

expected. After annealing the film shows same morphology with the chloroform annealed SV³⁹⁰ films from chloroform solution on flat silicon wafer, meanwhile the wrinkles of PDMS release after annealing.

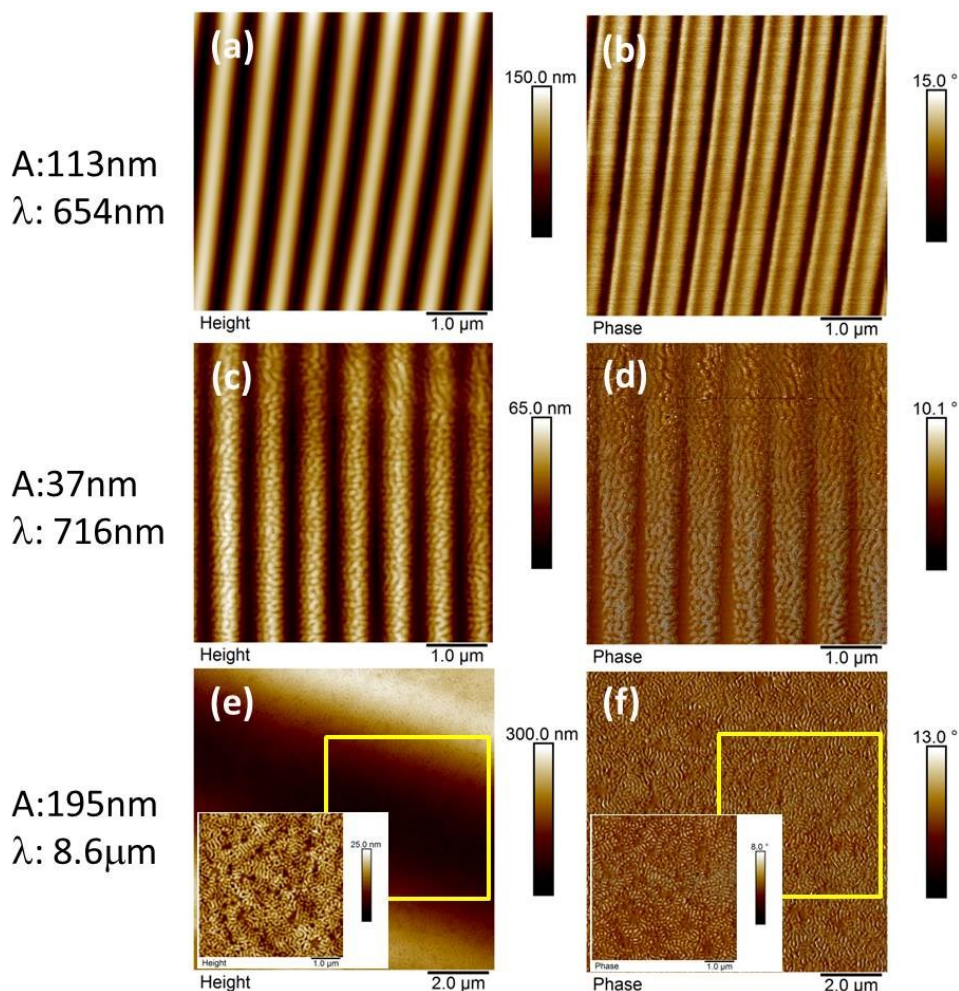


Figure 65 SFM (a) (b) (c) height and (d) (e) (f) phase images of (a) (d) pure wrinkled PDMS substrate, (b) (e) SV³⁹⁰ spin-cast on wrinkled PDMS and (c) (f) annealed SV³⁹⁰ by chloroform vapor for 200 min. The insets are the small areas in the yellow square with flatten treatment in the software Nanoscope Analysis. If the films are spin-coated on flat silicon wafers with the same spin-coating parameters, the film thickness will be 175 nm.

To reduce the deformation of PDMS substrate during the vapor annealing, we chose SV⁹⁹ which can restructure in short-time annealing. The spin-cast films from chloroform solution on flat SiO₂/Si (a, e), wrinkled PDMS (c, g) and chloroform annealed films on SiO₂/Si (b, f), wrinkled PDMS (d, h) are shown in Figure 66. The morphology on

5 Effects of thickness gradients, surface properties and solvent quality on the microphase separation in block copolymer films

SiO₂/Si changes from lying cylinder to standing lamella after chloroform annealing. The film on wrinkled PDMS substrate presents lying lamella at the thick position (bottom of the wrinkle) and lying lamella at the thin position (top of the wrinkle). But from the inserted images, this short annealing time cannot prevent PDMS wrinkles from deformation everywhere.

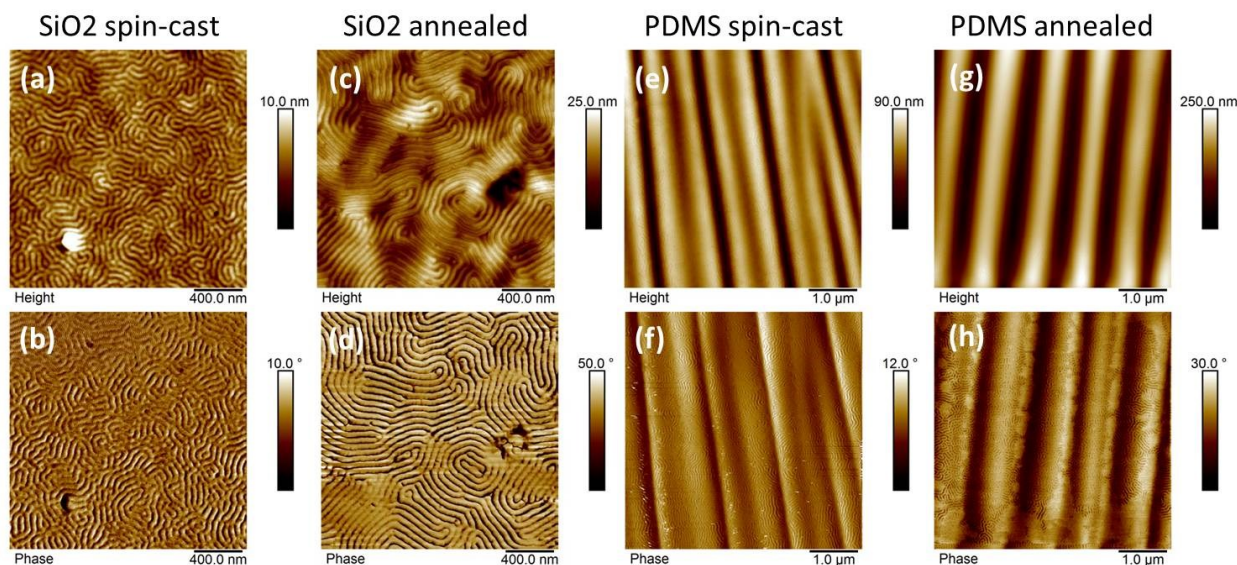


Figure 66 SFM (a) (c) (e) (g) height and (b) (d) (f) (h) phase images of 160 nm-thick SV⁹⁹ films on SiO₂ substrates (a) (b) before and (c) (d) after, on wrinkled PDMS substrate (e) (f) before and (g) (h) after, annealing by chloroform vapor at 14 °C/20 °C. The films were prepared on wrinkled PDMS and flat silicon substrates with same conditions.

5.5. Effect of the starting morphology on the phase separation in SV³⁹⁰ films

5.5.1. Spin-cast morphology of SV³⁹⁰ films from various spin-coating solvents

SV³⁹⁰ films from toluene, chloroform and DMF solution were spin-cast on silicon wafers. Figure 67 demonstrates that the starting morphology can be tuned between dot-like (spheres), striped (in-plane cylinder or up-standing lamella) and disordered pattern, respectively, due to the differences in the solvent selectivity to each block. Toluene is a good solvent only for PS, so the morphology shows sphere with P2VP core and PS shell. Chloroform can dissolve both PS and P2VP with slight selectivity to P2VP. When we

5 Effects of thickness gradients, surface properties and solvent quality on the microphase separation in block copolymer films

annealed the homo polymer thin films (~ 40 nm) PS and P2VP, the degree of swelling of P2VP films is about 10% more than PS films on the same conditions (Chapter3). The domain spacing of sphere and cylinder from toluene and chloroform solutions are 57 nm and 107 nm, respectively. The phase image in Figure 67d shows that the arrangement of PS and P2VP is not ordered. DMF is a highly miscible solvent for the PS and P2VP blocks, so the spin-cast morphology from DMF solution is disordered.

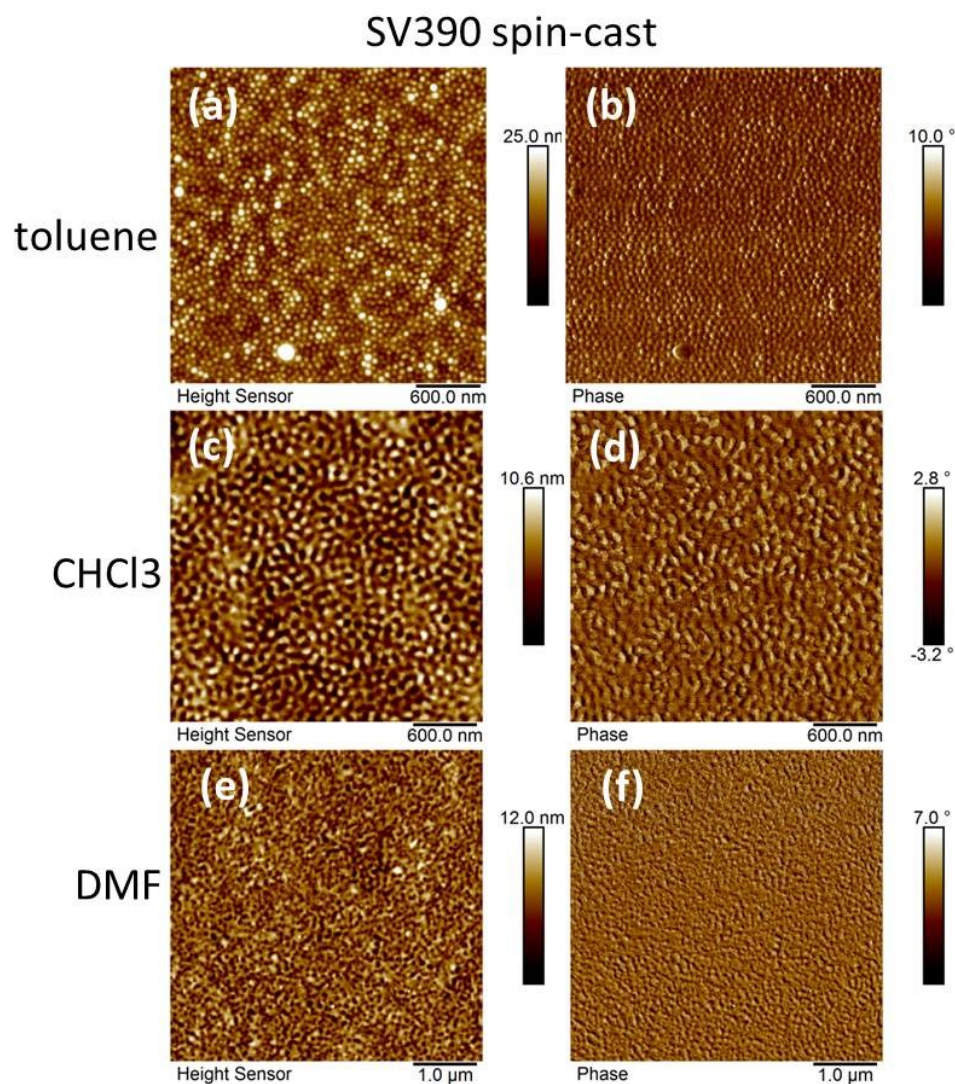


Figure 67 SFM (a) (c) (e) height and (b) (d) (f) phase images of SV³⁹⁰ from (a) (b) toluene (c) (d) chloroform and (e) (f) DMF solution spin-cast on SiO₂ substrate with thickness of ~ 40 nm.

5 Effects of thickness gradients, surface properties and solvent quality on the microphase separation in block copolymer films

5.5.2. Effect of residual solvent on the structures in SV³⁹⁰ films from DMF spin-coating solution

Not only DMF provided good miscibility to PS and P2VP, both blocks appear to have quite good mobility when the film is swollen in DMF vapor [214]. We annealed the SV⁹⁹ films at thickness of 15 nm, 27 nm and 46 nm under chloroform vapor, where the annealed morphologies are quite different from the films from chloroform or toluene solution. The annealed results in Figure 68 present the perforated lamella when film is very thin (~15 nm) and the disordered morphologies when film thickness increases to 27 nm and 46 nm. The reason causing this phenomenon could be the residual DMF in the initial dry films influence the χ parameter between PS and P2VP blocks or the surface tension of them.

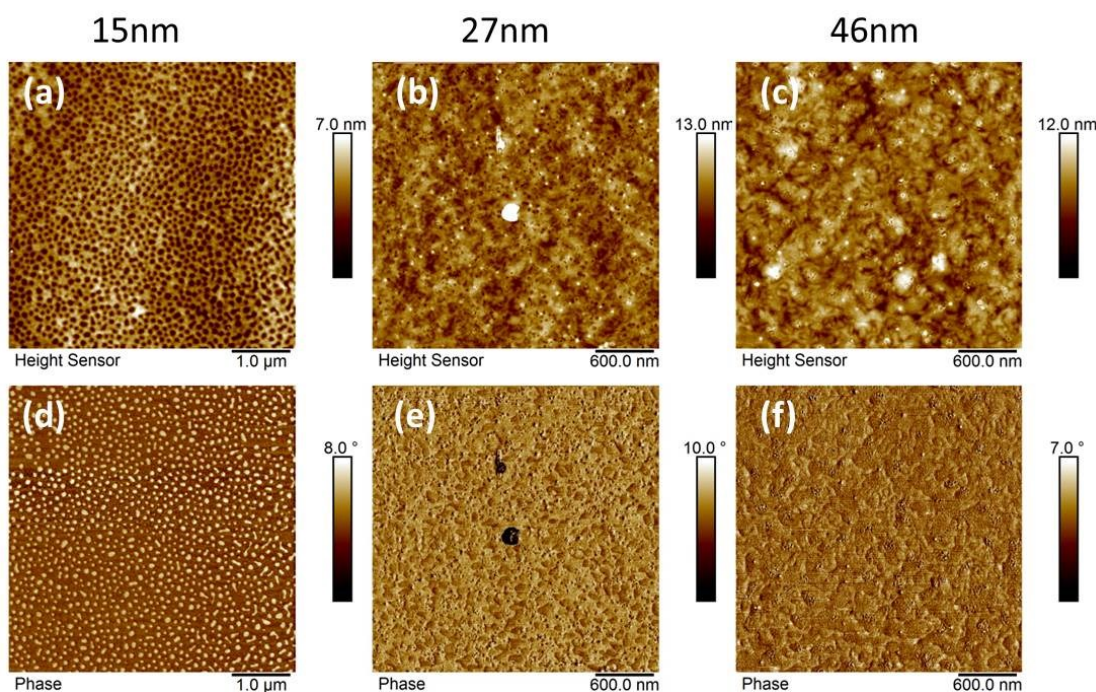


Figure 68 SFM (a) (b) (c) height images and (d) (e) (f) phase images of SV³⁹⁰ films from DMF spin-coating solution annealed by chloroform vapor at 29 °C/30 °C for 200 min with degree of swelling of 2.5. The film thicknesses are shown at the top of each image.

5.6. Summary

5 Effects of thickness gradients, surface properties and solvent quality on the microphase separation in block copolymer films

In this chapter, the gradients in the film thickness and surface properties of the substrates with regards to their influence on the morphological development in BCP thin films are presented.

First, the films of symmetric lamella-forming SV³⁹⁰ and SV⁹⁹ block copolymers on silicon wafers with thickness increasing from half-layer to one-layer are annealed in the vapors of slightly selective solvent (chloroform) and of highly selective solvent (toluene). SV³⁹⁰ and SV⁹⁹ films show bulk lamella-forming morphology after chloroform treatment, which is typical for symmetric BCPs. SV⁹⁹ films shows cylinder-forming morphology since the toluene uptake effectively enlarges the volume fractions of the PS block only. This causes the structural asymmetry of SV⁹⁹ block copolymer during annealing. Both kinds of morphology (lamella and cylinder) are influenced by the film thickness.

Second, the influence of the substrate nature on the annealing behavior of SV³⁹⁰ films was explored. Carbon-coating, hard mask and photoresist supports are used as substrates in a view of potential of such films as BCP templates in the area of semiconductor industry.

Third, the combination of confined film and substrate property are realized by preparing the films on patterned photoresist (hydrogen silsesquioxane) and wrinkled PDMS (with SiO₂ surface-layer). In these cases the annealed morphology of SV³⁹⁰ and SV⁹⁹ induced by gradient film thickness is similar to the morphology on flat silicon wafers.

Last, the morphology in SV³⁹⁰ films annealed in chloroform vapors from various initial microphase separated structures is compared. The initial morphology affect the kinetics of the phase reorganization and the residual solvent from spin-coating is supposed to contribute to the structure development in thin films.

6 Preparation of block copolymer-based membranes via orientated vapor flow treatment

Formation of isoporous membranes is an attractive application of block copolymer materials. A combination of industrially well-established membrane formation method by non-solvent-induced phase separation with the self-assembly of a block copolymer was demonstrated by the group of Abetz in 2007 [154]. In their case, an integral asymmetric BCP membrane with ordered cylindrical porous as top layer and sponge-like porous as support layer was formed. The formation of cylindrical porous formation in BCP films proceeds by two steps: first, the BCP self-assembles to form standing cylinder structure at the shallow area of the cast swollen BCP film; second, the non-solvent induced phase separation is guided through the pores by the more compile component.

Here we introduce a new approach to produce membranes with oriented structure of nanoscale porosity via oriented solvent vapor flow field, which directs uni-axial orientation of microdomain in BCP films along the flow direction. The apparatus used in this chapter is mini-extruder (Avanti Lipids) with syringes for accelerating the air flow to speed up the solvent evaporation rate (air-solvent exchange rate) in swollen BCP films. Three kinds of BCPs (SV⁹⁹, SV³⁹⁰ and SM⁵⁰) including blocks of PS, P2VP and PMMA, and several organic solvents (ethanol, chloroform, toluene and THF) covering solvents with good and bad properties are used in this chapter. Ethanol is a non-solvent for all blocks, and toluene, chloroform and THF is solvent for all blocks, where toluene strongly prefers PS than P2VP. The morphology and the cross-section of the films are measured by SFM and FE-SEM, where the cross-section samples are prepared by Cryo-cutting. The SAXS investigation of the inner structure of SV³⁹⁰ films was performed at European Synchrotron Radiation Facility (ESRF) in Grenoble.

6 Preparation of block copolymer-based membranes via orientated vapor flow treatment

6.1. Preparation, treatment and characterization

PDMS support layers were prepared using SYLGARD kit by mixing the base and agent in weight ratio of 10:1, locating the mixture in a horizontal polystyrene dish for still staying for 12 h to exhaust the air bubbles from the mixture. Then the PDMS support was thermally treated at 80 °C for 2 h. In this chapter PDMS supports with thickness of 5 mm and 1 mm, depending on the evaporation rate, have been used.

μm -thick block copolymer films on PDMS substrates were prepared by solvent casting of chloroform solutions with a concentration of 0.35wt% and 0.6wt% for SV³⁹⁰ and SV⁹⁹, respectively. When the film thickness increases to $\sim 4 \mu\text{m}$, it is easy to directly peel the films off the substrate.

The T_g of PS, P2VP and PDMS ($\sim 99 \text{ }^\circ\text{C}$, $\sim 83^\circ\text{C}$ and $\sim 123^\circ\text{C}$ [174], respectively) makes the film-breaking in liquid nitrogen for the preparation of cross-sectional profiles for the measurements in FE-SEM possible, since all polymers stay in a glassy state.

- Processing with the orientated vapor flow

The picture and the sketches in Figure 69 present the oriented vapor flow apparatus and the assumed evolution of the structure in block copolymer films. The two syringes are connected by the steel conjunction with PTFE cylinders (the circled write stuff in Figure 69a) inside, which contain a permeable structure to allow for solvent flow. The BCP films are located between the two cylinders and the steel conjunctions are fixed during treatment to make the system air-tight.

The sketch of the mini-extruder is shown in details in Figure 69b, where the BCP films, PDMS films and the PE supports are indicated by the yellow layer, dot-pattern layers and the cross-line pattern layers, respectively. When the treatment is in progress, the liquid non-solvent (ethanol) in the syringes (e.g. left) is forced to saturate (oversaturate) the film, thus decreasing the T_g of BCP components and enabling the forced re-organization. In a next step, the other syringe (right) is pulled out fast to suck the solvent out of the films, which is expected to accelerate the evaporation rate of solvent. The following cycles are reciprocated by running the syringes in turns in opposite direction.

6 Preparation of block copolymer-based membranes via orientated vapor flow treatment

As the treatment circles are repeated many times, the film structure is expected to form a uni-axial-oriented cylinder or lamella structure extending through the interior of the film with macrovoids by the flow field according to schematic in Figure 69c.

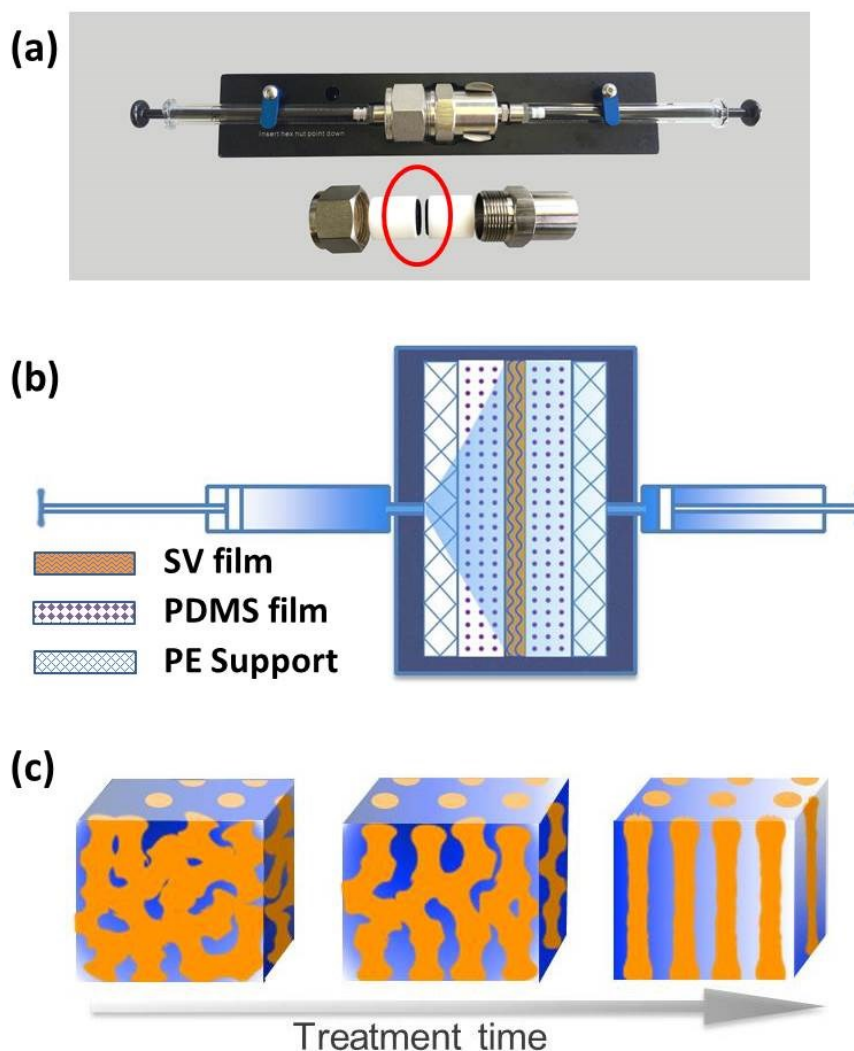


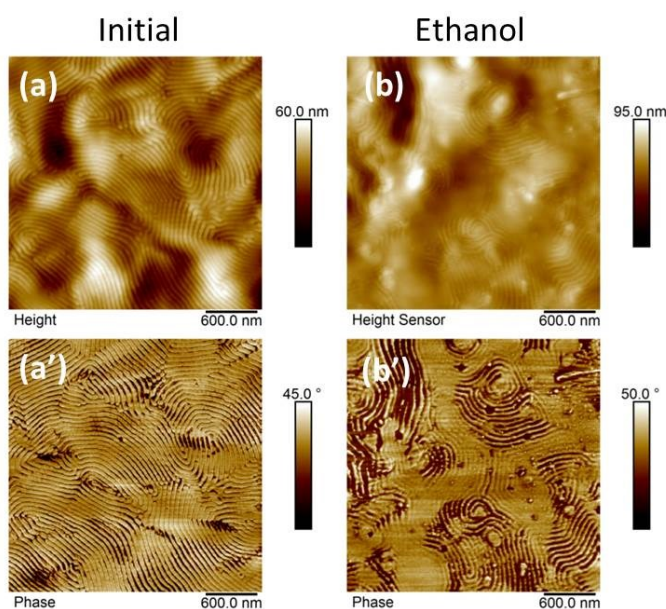
Figure 69 The image (a) and the sketch (b) of the vapor flow treatment apparatus used in this chapter. (c) The sketch of the expected membrane changing procedure.

6.2. Phase separation in SV⁹⁹ films induced by oriented vapor flow

First we chose symmetric SV⁹⁹ films to be treated for its relative small molecular weight and the amphiphilic property. The selected solvent including ethanol (non-solvent), chloroform (solvent) and THF (solvent and high evaporation rate) is used to treat the

6 Preparation of block copolymer-based membranes via orientated vapor flow treatment

films. The surface structures of as solvent-cast and of flow-treated films are presented in Figure 70. The film after solvent-casting shows standing lamella morphology with 3~4 nm depth. After ethanol treatment the standing lamella structure turns to be shallow with depth less than 2 nm, and a small amount of standing lamella turns to be lying lamella, but the lamella is relatively competed. After chloroform treatment the morphology of the film shown in Figure 70c, c' turns to be mixed lying lamella and standing lamella with defects in the middle of the standing lamella, where the depth of the holes and standing lamella is ~6 nm. The images in Figure 70d, d' present the similar morphology with the ethanol-treated films in Figure 70b, b' with some defects of micelles. The thermal treatment under ethanol/THF induces the standing lamella showing lying orientation. The reason could be THF in the solvent mixture improves the evaporation rate and its better solubility to the both blocks enhances the mobility of the SV⁹⁹ film.



6 Preparation of block copolymer-based membranes via orientated vapor flow treatment

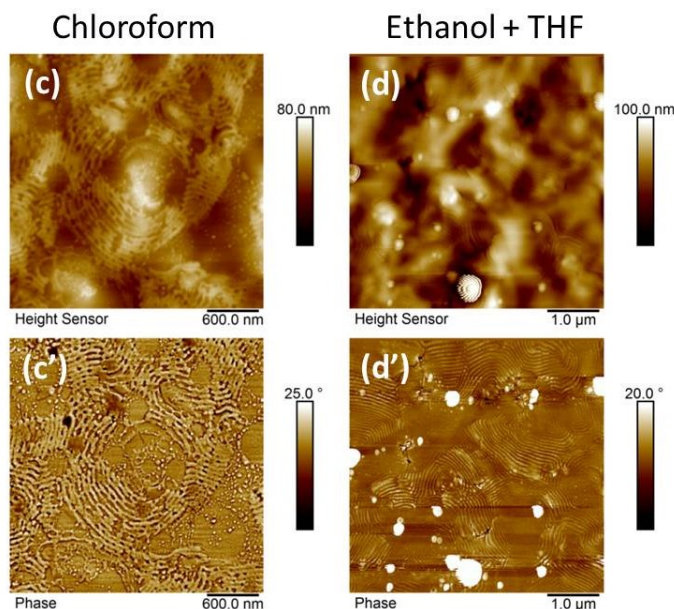


Figure 70 SFM images of the solvent-cast (a) (a'), ethanol treated (b) (b'), chloroform treated (c) (c') and ethanol: THF=1:1 treated (d) (d') SV⁹⁹ films with thickness of 1µm between PDMS supports. Except for (d) (d') was treated at 50 °C, all the other treatments were finished at room temperature.

To explore how the bulk structure changes in these films, we compare the cross-section profiles of SV⁹⁹ films in Figure 71 of (a) the solvent-cast film, (b) the chamber annealed film by ethanol, and the vapor flow induced films by (c) ethanol, (d) chloroform, (e) mixed ethanol and THF, (f) mixed ethanol and chloroform. The distinct lying cylinder structure shows only in (a) the solvent-cast film. The structure of SV⁹⁹ film annealed in chamber by ethanol shows similar structure as the initial film, which means the ethanol vapor with normal pressure is not effective to the phase re-organization of SV⁹⁹. The porous structure exists in the ethanol and ethanol/THF treated films in Figure 71(c), (e) with finger-like and sponge-like structure, respectively. The mixed solvent consists of both a good solvent (THF) and non-solvent (ethanol) to the BCP, where the SV⁹⁹ film absorbs THF [215] during the pulling process and ethanol exchanges with THF during pushing process. In the chloroform and the mixed ethanol and chloroform treated films there is no porous existing shown in Figure 71(d) and (f). But the mixed ethanol and chloroform treated SV⁹⁹ film shows approximate separated lamella structure. These two

6 Preparation of block copolymer-based membranes via orientated vapor flow treatment

kinds of mixed solvent, ethanol/THF and ethanol/chloroform, have the same proportion of the non-solvent and the solvent (1:1).

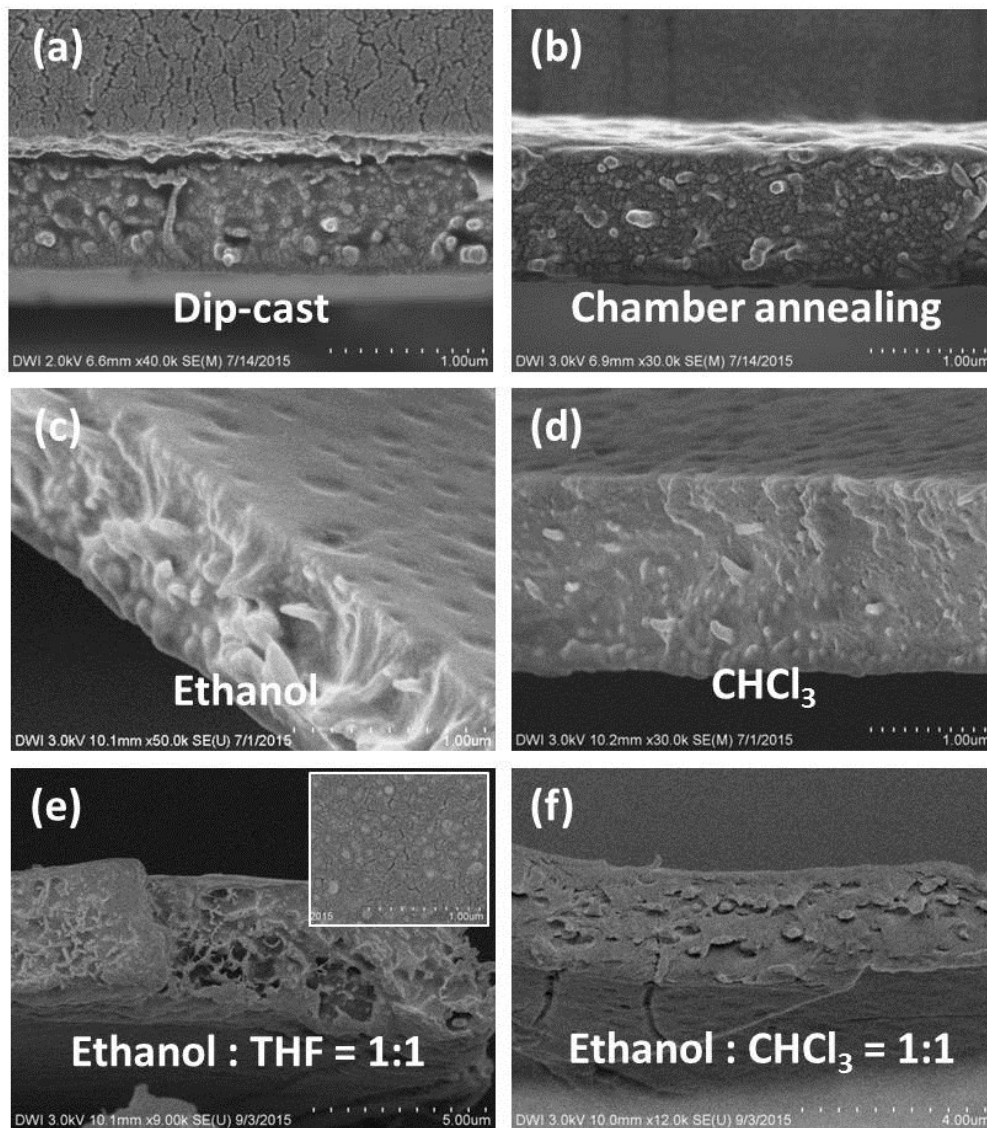


Figure 71 FE-SEM images of the cross-section profiles of SV⁹⁹ films which are (a) solvent-cast, (b) annealed in chamber by ethanol for 200 min and flow treated by (c) ethanol, (d) chloroform, (e) ethanol: THF=1:1 and (f) ethanol: chloroform=1:1 for 15 min.

Single chloroform treatment has no effect to the phase inversion of SV⁹⁹ films, but the treatments by non-solvent of ethanol, and the mixed solvents of ethanol/THF and ethanol/chloroform show trend to produce SV⁹⁹ membrane with porous structure.

6 Preparation of block copolymer-based membranes via orientated vapor flow treatment

The drop-casting of $\sim 1 \mu\text{m}$ SV^{390} film on PDMS substrates presents a mixture of standing and lying lamella in Figure 72. The depth of stripes is about 19 nm and the domain spacing of the standing lamella is about 139 nm.

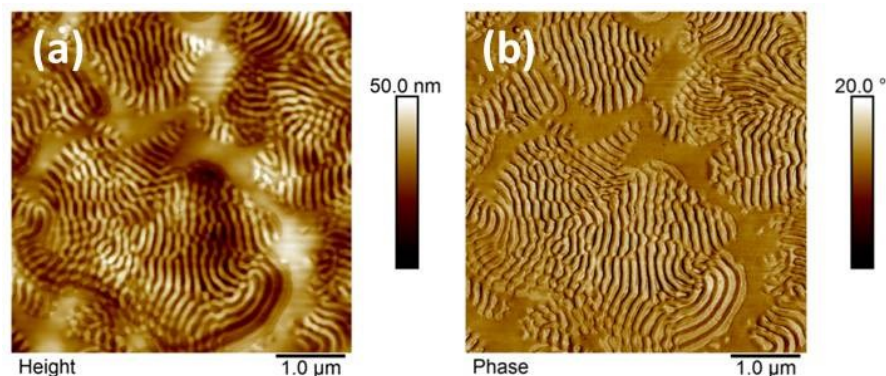


Figure 72 SFM height (a) and phase (b) images of the drop-cast SV^{99} film on the PDMS substrate.

The surface structure of SV^{390} film with thickness of $\sim 80 \text{ nm}$ which is prepared by spin-coating on PDMS substrate and then is treated by oriented ethanol flow between PDMS layers was measured by SFM (Figure 73). The lamella depth at the cross-section with a yellow line is $\sim 120 \text{ nm}$ more than the film thickness indicating the vapor flow forces the voids between lamella sheets. Since this film is so thin that it is hard to keep the film entire during the process of peeling the PDMS supports off it, unfortunately, we cannot check the cross-section profile of this film by FE-SEM.

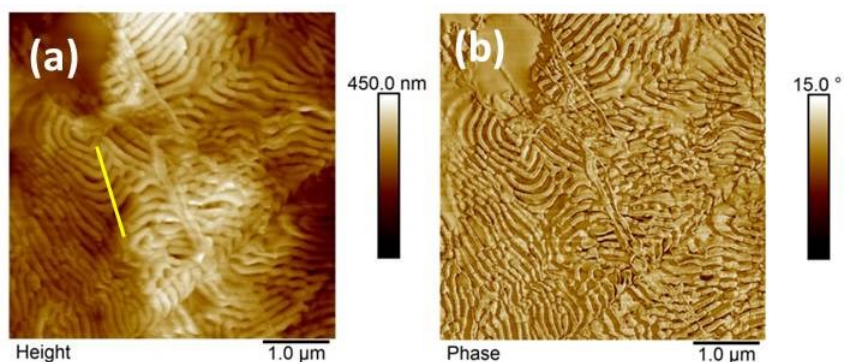


Figure 73 SFM (a) height and (b) phase images of the $\sim 80 \text{ nm}$ thick SV^{390} film treated by oriented flow of ethanol.

6 Preparation of block copolymer-based membranes via orientated vapor flow treatment

~1 μm thick SV^{390} films treated by ethanol, chloroform and toluene oriented flow at 50 °C are presented in Figure 74. The morphologies after ethanol and toluene treatment present very similar standing lamella with small area of lying lamella, where the depth of the lamella is 10 nm-20 nm. The film after treatment of chloroform shows standing lamella with the same depth of 10 nm-20 nm, and there are connections existing between two lamellas next to each other.

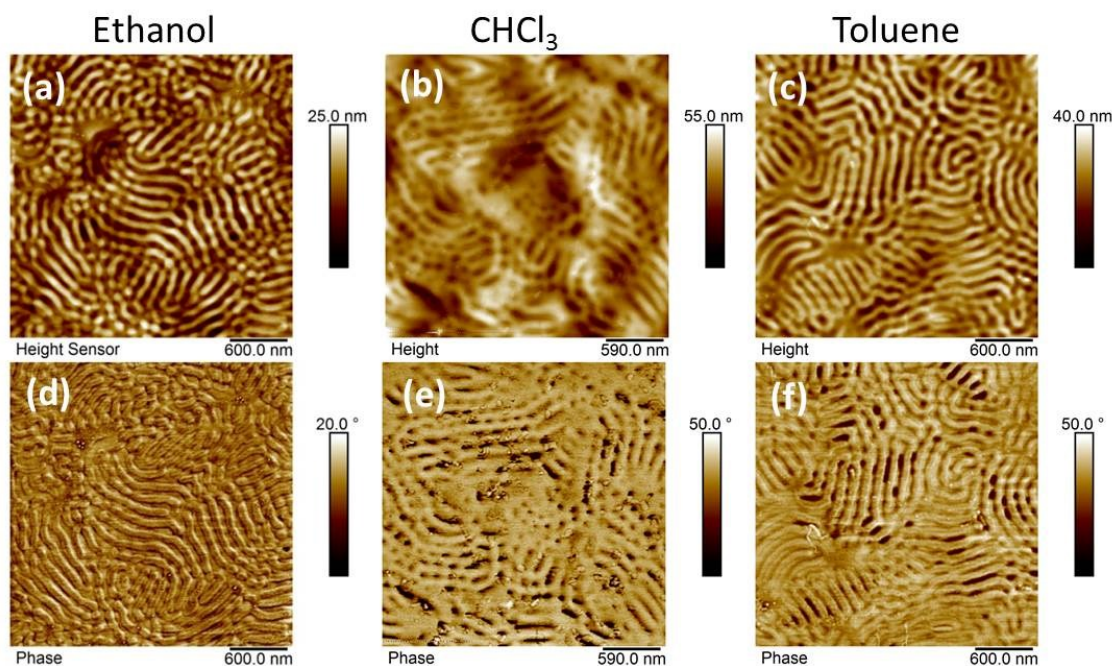


Figure 74 SFM height (a)-(c) and phase (d)-(f) images of SV^{390} films supported by PDMS substrates with thickness ~ 1 μm , after treatment of (a) (d) ethanol, (b) (e) chloroform and (c) (f) toluene at 50 °C for 15 min.

The cross-section profiles of SV^{390} films were measured by FE-SEM and are presented in Figure 75. The initial solvent-cast film reveals a disordered structure, while the films treated with ethanol and chloroform flow display a lying cylinder-forming structure, but neither of them presents standing cylinders at the edge area of the films.

6 Preparation of block copolymer-based membranes via orientated vapor flow treatment

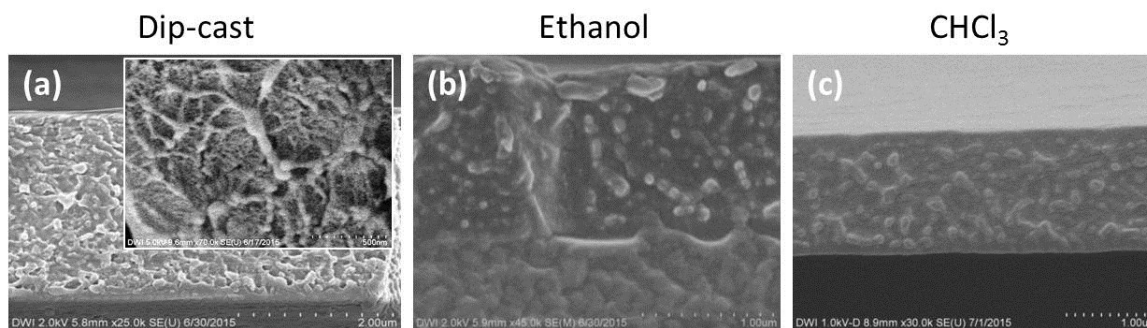
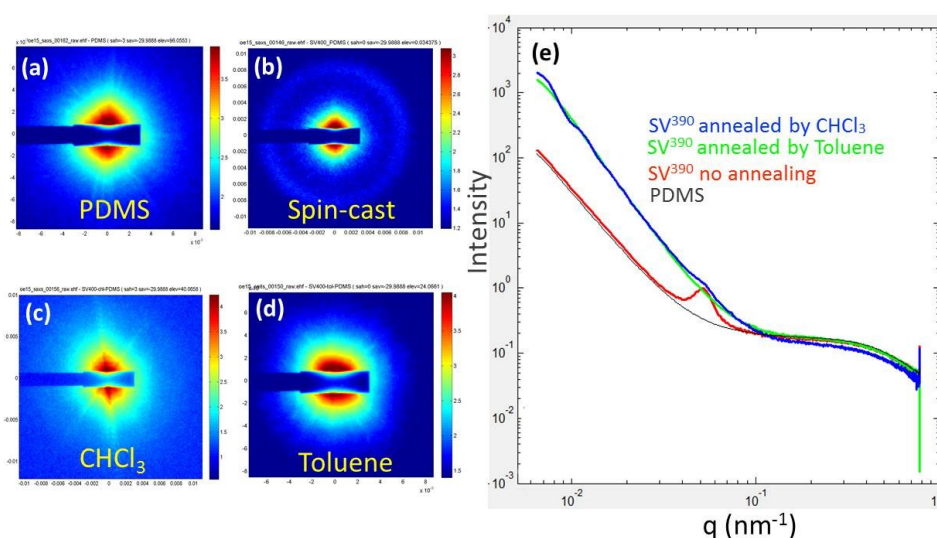


Figure 75 FE-SEM images of the cross-section profiles of (a) drop-cast, (b) ethanol and (c) chloroform treated $\sim 1\mu\text{m}$ SV^{390} films on PDMS supports.

The SAXS measurements of the bulk structure in thick films of PDMS substrate, the solvent-cast film and the vapor treated films are shown in Figure 76. As expected, the PDMS substrate shows disordered structure and there is no scattering ring or peak in Figure 76a, e. The SV^{390} film after drop-casting shows domain spacing of $\sim 116\text{ nm}$ calculated from the peak position at q of 0.0541 nm^{-1} . But the films after treatment with chloroform and toluene present no scattering period around this position even with the same sample shown in Figure 75c. However, a closer inspection of the radial scattering pattern reveals specific signal in the treated films. The data still has to be evaluated taking into account the residual solvent left in the films during the treatment which decreases the contrast between the PS and P2VP blocks.



6 Preparation of block copolymer-based membranes via orientated vapor flow treatment

Figure 76 2D SAXS profiles from (a) empty PDMS substrate and the (b) solvent-cast, (c) chloroform-treated and (d) toluene-treated SV³⁹⁰ films with thickness of $\sim 1\mu\text{m}$. (e) the in-plane plots of the same samples from the 2D results.

6.3. Phase separation of polystyrene-b-poly(methyl methacrylate) (SM) films induced by oriented vapor flow

The SFM images of SM⁵⁰ after treatment by mixed vapor of ethanol and THF display lying lamella morphology in Figure 77. The treatment was done at 50 °C for 15 min and the proportion of these two solvent is 1: 1.

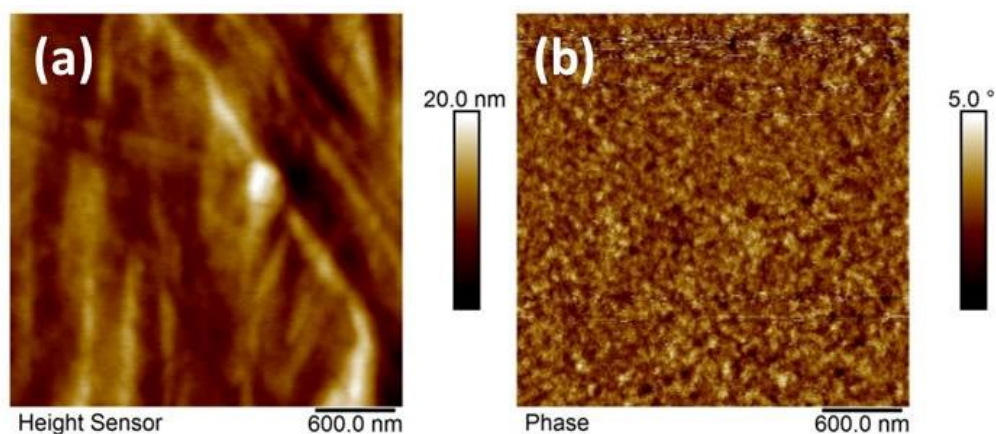


Figure 77 SFM height (a) and phase (b) images of the $\sim 1\mu\text{m}$ SM film treated by ethanol: THF=1:1 at 50 °C for 15 min.

The cross-section profiles of $\sim 1\mu\text{m}$ SM⁵⁰ before and after treatment by ethanol, mixed vapor of ethanol and chloroform and the mixed vapor of ethanol and THF are shown in Figure 78. The film before solvent treatment shows no obvious cylinder-forming structure in (a). The structure of the treated films is all lying cylinder presented with cylinders collecting in the middle of the ethanol treated film, disspreading homogeneously in the ethanol: chloroform=1:1 treated film and existing not obvious in the ethanol: THF=1:1 treated film. They all do not present channel or macrovoid structure in the films.

6 Preparation of block copolymer-based membranes via orientated vapor flow treatment

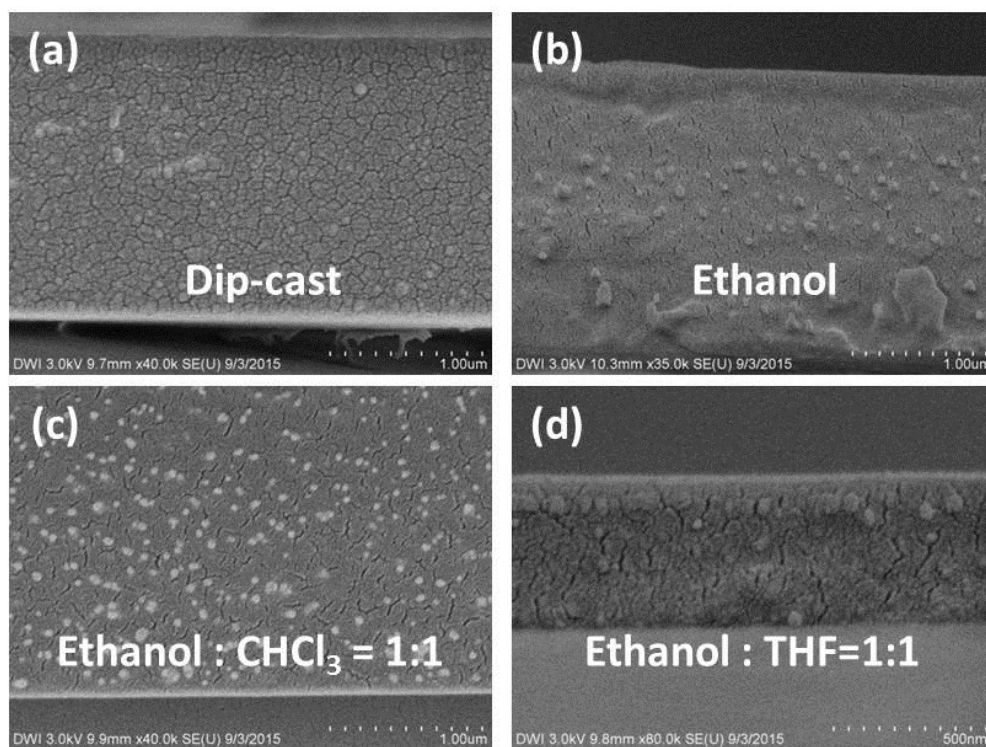


Figure 78 FE-SEM images of the cross-section profiles of (a) drop-cast (b) ethanol, (c) ethanol: chloroform=1:1 and (d) ethanol: THF=1:1 treated SM⁵⁰ films. The films are all ~1 μm , except for the film in (d) is ~500 nm.

In this part we improved our treatment of the films by using flow orientation via only one syringe containing solvent and the other one being empty with the plug always being extracted. Since the volume of the syringe is limited, we re-fixed the syringe with its plug at the start position when its plug arrives at the end. To speed up the solvent evaporation, the thickness of PDMS supports is reduced to 1 mm from 5 mm which is used in the experiments described above.

Figure 80 compares FE-SEM images of the cross-sections of flow-treated SV⁹⁹ SM⁵⁰ and SV³⁹⁰ films with indicated thickness and treatment conditions. The SV⁹⁹ film still shows disordered porous structure after treatment by ethanol (Figure 80a), similar to the film under slow evaporation (Figure 79a). The other samples here were treated under fast evaporation like Figure 79b. The SV³⁹⁰ film shows sponge-like structure after ethanol/THF treatment (Figure 80b), but this structure is not evenly distributed. The ~3 μm -thick SM⁵⁰ film contains both bottom-to-up channel structure in scale of several

6 Preparation of block copolymer-based membranes via orientated vapor flow treatment

micrometers and non-porous structure (magnified in the inserted image) after ethanol treatment, shown in Figure 80c. When the film thickness increases to $\sim 5 \mu\text{m}$, the channel structure only exists at the shallow edge of the film shown in Figure 80d. Based on the knowledge of non-solvent induced phase separation in membrane preparation, (1) high polymer concentration of the cast solution, (2) high viscosity of the polymer and (3) mixing solvent in the non-solvent – all these factors could be the reason for the sponge-like structure rather than finger-like structure formation [161].

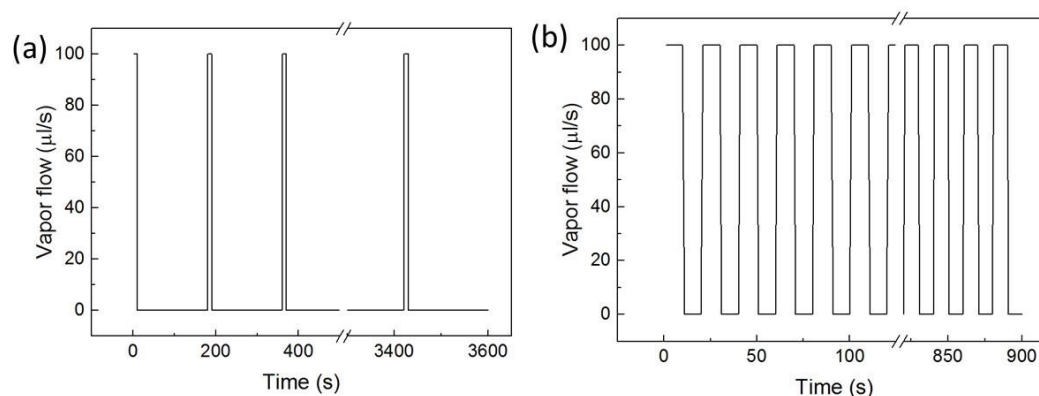


Figure 79 The record of the cycled vapor flows as a function of time in ethanol treatments.
(a) 6 min/cycling 60 min at 50 °C (b) 0.5 min/cycling 15 min at 50 °C

6 Preparation of block copolymer-based membranes via orientated vapor flow treatment

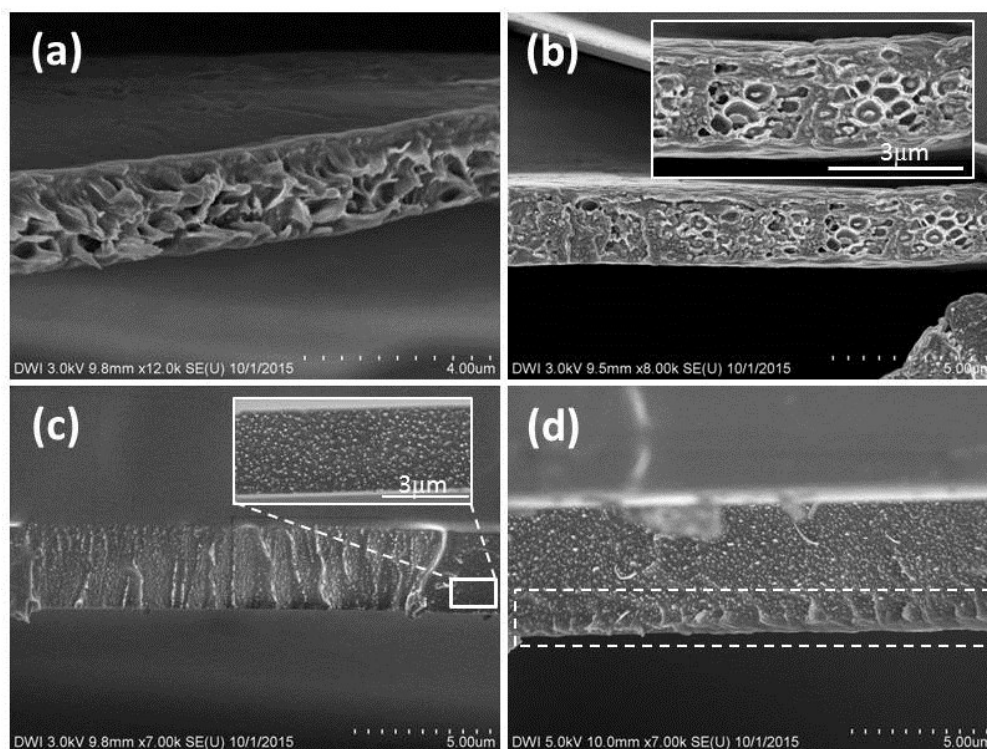


Figure 80 FE-SEM images of the cross-section profiles of (a) ethanol treated $\sim 2 \mu\text{m}$ SV⁹⁹, (b) ethanol:THF=1:1 treated $\sim 3 \mu\text{m}$ SV³⁹⁰ (c) ethanol treated $\sim 3 \mu\text{m}$ SM⁵⁰ and (d) ethanol treated $\sim 5 \mu\text{m}$ SM⁵⁰ with single orientated flow between 1 mm thick PDMS supports.

6.4. Summary

In this chapter an approach to induced oriented microphase separation in thick block copolymer films via treatment with the oriented vapor flow using mini-extruder is envisaged to be an alternative to existing methodologies, e.g. via non-solvent-induced phase separation.

The preliminary tests performed in this study confirm potential perspective of this method, which alters the structure through the bulk of the film (as revealed by SAXS measurements), but more detailed studies have to be conducted in order to optimize following parameters:

- The amount of solvent/vapor purged through the film might not be sufficient to induce reorganization of the microdomains

6 Preparation of block copolymer-based membranes via orientated vapor flow treatment

- Alternatively, the time of the cycled flow has to be adjusted with regards to the intrinsic relaxation times of polymer chains
- The homogeneity of the solvent distribution, affected both by the concentration and by the cycling time, has to be assessed
- Introducing further technical means to enhance the solvent flow through the film, e.g. switchable vacuum pump is considered as an optimization option.
- Finally, a proper solvent mixture which can provide the critical concentration for phase re-separation of BCP films and simultaneously can evaporate fast enough to drive the macro structure formation has to be optimized.

7 Acknowledgement

It is a pleasure to show my gratitude to all the people who have accompanied and supported me throughout my PhD.

First, I would like to sincerely thank my supervisor Prof. Dr. Alexander Böker for providing me opportunities twice to work in his group on this interesting and theoretical topic. I also thank him for always showing interests and confidence in my research.

I show the largest appreciation to my daily supervisor Dr. Larisa Tsarkova who influenced me deeply in my PhD project. Her comments on work criticized me. Her pursuit of truth inspired me. And her accompaniment in life supported me. Both high quality of work she insisted and the patience in supervising me she paid impressed me. All the details in her work will be memorized by me and influence me in the future, for which I shall like to be ever grateful to her.

I cheerfully thank my friends here, in Aachen and abroad for constantly standing by me. I feel grateful to Dr. Ulrich Glebe and Xiaolin Dai for a lot help in life, to Xiaorui Zhang, Zhi Chen for bringing me joyful and wonderful time in Germany.

I thank all the past and present colleagues from DWI, Aachen and Fraunhofer IAP, Potsdam. I also thank my office colleagues for the friendly and positive atmosphere to conduct work.

I thank to Shengliang Zheng for always caring my feeling and standing in my side. He is the best distant boyfriend for me.

Most importantly I thank my parents, without their selfless love I can never have finished my work.

7 Acknowledgement

8 Bibliography

- 1 Bates, Christopher M.; Bates, Frank S. *Macromolecules*. 2016. 50. 3–22.
- 2 Park, M.; Harrison, C.; Chaikin, P. M.; Register, R. A.; Adamson, D. H. *Science*. 1997. 276. 1401.
- 3 Sinturel, Christophe; Vayer, Marylène; Morris, Michael; Hillmyer, Marc A. *Macromolecules*. 2013. 46. 5399–5415.
- 4 Mansky, P.; Harrison, C. K.; Chaikin, P. M.; Register, R. A.; Yao, N. *Applied Physics Letters*. 1996. 68. 2586–2588.
- 5 Nunns, Adam; Gwyther, Jessica; Manners, Ian. *Polymer*. 2013. 54. 1269–1284.
- 6 Mansky, P.; haikin, P.; Thomas, E. L. *Journal of Materials Science*. 1995. 30. 1987–1992.
- 7 Urade, Vikrant N.; Wei, Ta-Chen; Tate, Michael P.; Kowalski, Jonathan D.; Hillhouse, Hugh W. *Chemistry of Materials*. 2007. 19. 768–777.
- 8 Hayward, Ryan C.; Chmelka, Bradley F.; Kramer, Edward J. *Advanced Materials (Weinheim, Germany)*. 2005. 17. 2591–2595.
- 9 Pai, Rajaram A.; Humayun, Raashina; Schulberg, Michelle T.; Sengupta, Archita; Sun, Jia-Ning; Watkins, James J. *Science (Washington, DC, United States)*. 2004. 303. 507–511.
- 10 Yang, Seung Y.; Ryu, Incheol; Kim, Hwang Y.; Kim, Jin K.; Jang, Sung K.; Russell, Thomas P. *Advanced Materials (Weinheim, Germany)*. 2006. 18. 709–712.
- 11 Zhang, Xiaoyan; Tanner, Pascal; Graff, Alexandra; Palivan, Cornelia G.; Meier, Wolfgang. *Journal of Polymer Science Part A: Polymer Chemistry*. 2012. 50. 2293–2318.
- 12 Jung, Jun Tae; Kim, Jeong F.; Wang, Ho Hyun; Di Nicolo, Emanuele; Drioli, Enrico; Lee, Young Moo. *Journal of Membrane Science*. 2016. 514. 250–263.
- 13 [Cannot display reference #314, because the template "Bibliography - Journal Article - (Default template)" contains only fields that are empty in this reference.]
- 14 Stoykovich, Mark P.; Nealey, Paul F. *Materials Today (Oxford, United Kingdom)*. 2006. 9. 20–29.
- 15 Kwak, Jongheon; Mishra, Avnish Kumar; Lee, Jaeyong; Lee, Kyu Seong; Choi, Chungryong; Maiti, Sandip; Kim, Mooseong; Kim, Jin Kon. *Macromolecules*. 2017. 50. 6813–6818.
- 16 Joo, Wonchul; Park, Min Soo; Kim, Jin Kon. *Langmuir*. 2006. 22. 7960–7963.
- 17 Thurn-Albrecht, T.; Schotter, J.; Kastle, G. A.; Emley, N.; Shibauchi, T.; Krusin-Elbaum, L.; Guarini, K.; Black, C. T.; Tuominen, M. T.; Russell, T. P. *Science*. 2000. 290. 2126.
- 18 Cheng, J. Y.; Ross, C. A.; Chan, V.Z.-H.; Thomas, E. L.; Lammertink, R.G.H.; Vancso, G. J. *Advanced Materials*. 2001. 13. 1174–1178.

8 Bibliography

- 19 Bates, Christopher M.; Maher, Michael J.; Janes, Dustin W.; Ellison, Christopher J.; Willson, C. Grant. *Macromolecules*. 2013. 47. 2–12.
- 20 Thomas H. Epps, III; O'Reilly, Rachel K. *Chemical Science*. 2016. 7. 1674–1689.
- 21 Luo, Ming; Epps, Thomas H. *Macromolecules*. 2013. 46. 7567–7579.
- 22 Choi, Jonathan W.; Kim, Myungwoong; Safron, Nathaniel S.; Arnold, Michael S.; Gopalan, Padma. *ACS applied materials & interfaces*. 2014. 6. 9442–9448.
- 23 Kim, Kyunginn; Park, Sungmin; Kim, Yeongsik; Bang, Joon; Park, Cheolmin; Du Ryu, Yeol. *Macromolecules*. 2016. 49. 1722–1730.
- 24 Gu, Xiaodan. *Self-Assembly of Block Copolymers by Solvent Vapor Annealing, Mechanism and Lithographic Applications*.
- 25 Choi, Eunyoung; Park, Sungmin; Ahn, Hyungju; Lee, Moongyu; Bang, Joon; Lee, Byeongdu; Du Ryu, Yeol. *Macromolecules*. 2014. 47. 3969–3977.
- 26 Ferrarese Lupi, Federico; Giammaria, Tommaso Jacopo; Seguni, Gabriele; Vita, Francesco; Francescangeli, Oriano; Sparnacci, Katia; Antonioli, Diego; Gianotti, Valentina; Laus, Michele; Perego, Michele. *ACS applied materials & interfaces*. 2014. 6. 7180–7188.
- 27 Gu, Xiaodan; Gunkel, Ilja; Hexemer, Alexander; Russell, Thomas P. *Macromolecules*. 2016. 49. 3373–3381.
- 28 Louis M. Leung and Jeffrey T. Koberstein.
- 29 Arias-Zapata, Javier; Böhme, Sophie; Garnier, Jérôme; Girardot, Cécile; Legrain, Antoine; Zelsmann, Marc. *Advanced Functional Materials*. 2016. 26. 5690–5700.
- 30 Kim, Jong Min; Kim, YongJoo; Park, Woon Ik; Hur, Yoon Hyung; Jeong, Jae Won; Sim, Dong Min; Baek, Kwang Min; Lee, Jung Hye; Kim, Mi-Jeong; Jung, Yeon Sik. *Advanced Functional Materials*. 2015. 25. 306–315.
- 31 Emerson, Jillian A.; Toolan, Daniel T. W.; Howse, Jonathan R.; Furst, Eric M.; Epps, Thomas H. *Macromolecules*. 2013. 46. 6533–6540.
- 32 Kim, Yoojin; Pyun, Jeffrey; Fréchet, Jean M. J.; Hawker, Craig J.; Frank, Curtis W. *Langmuir : the ACS journal of surfaces and colloids*. 2005. 21. 10444–10458.
- 33 Helfand, Eugene; Tagami, Yukiko. *J. Chem. Phys.* 1972. 56. 3592.
- 34 Roth, Connie B.; McNerny, Katie L.; Jager, Wolter F.; Torkelson, John M. *Macromolecules*. 2007. 40. 2568–2574.
- 35 Elbs, Hubert; Fukunaga, Kenji; Stadler, Reimund; Sauer, Gustav; Magerle, Robert; Krausch, Georg. *Macromolecules (Washington, DC, United States)*. 1999. 32. 1204–1211.
- 36 Abetz, Volker. *Macromolecular Rapid Communications*. 2015. 36. 10–22.
- 37 Yin, Jun; Yao, Xueping; Liou, Jiun-You; Sun, Wei; Sun, Ya-Sen; Wang, Yong. *ACS NANO*. 2013. 7. 9961–9974.
- 38 Wang, Zhaogen; Yao, Xueping; Wang, Yong. *Journal of Materials Chemistry*. 2012. 22. 20542.

- 39 Paradiso, Sean P.; Delaney, Kris T.; García-Cervera, Carlos J.; Cenicerros, Hector D.; Fredrickson, Glenn H. *Macromolecules*. 2016. 49. 1743–1751.
- 40 Durand, William J.; Blachut, Gregory; Maher, Michael J.; Sirard, Stephen; Tein, Summer; Carlson, Matthew C.; Asano, Yusuke; Zhou, Sunshine X.; Lane, Austin P.; Bates, Christopher M.; Ellison, Christopher J.; Willson, C. Grant. *Journal of Polymer Science Part A: Polymer Chemistry*. 2015. 53. 344–352.
- 41 Fitzgerald, Thomas G.; Borsetto, Francesca; O'Callaghan, John M.; Kosmala, Barbara; Holmes, Justin D.; Morris, Michael A. *Soft Matter*. 2007. 3. 916–921.
- 42 Park, Soojin; Lee, Dong Hyun; Xu, Ji; Kim, Bokyoung; Hong, Sung Woo; Jeong, Unyong; Xu, Ting; Russell, Thomas P. *Science (New York, N.Y.)*. 2009. 323. 1030–1033.
- 43 Basutkar, M. N.; Samant, S.; Strzalka, J.; Yager, K. G.; Singh, G.; Karim, A. *Nano Lett.* 2017. 17. 7814–7823.
- 44 Mishra, Vindhya; Fredrickson, Glenn H.; Kramer, Edward J. *ACS NANO*. 2012. 6. 2629–2641.
- 45 Jung, Jueun; Park, Hae-Woong; Lee, Sekyung; Lee, Hyojoon; Chang, Taihyun; Matsunaga, Kazuyuki; Jinnai, Hiroshi. *ACS NANO*. 2010. 4. 3109–3116.
- 46 Joachim P. Spatz, Martin Moeller. *Adv Mater.* 1996. 8.
- 47 Tsarkova, Larisa; Knoll, Armin; Krausch, Georg; Magerle, Robert. *Macromolecules*. 2006. 39. 3608.
- 48 Park, Sang-Min; Stoykovich, Mark P.; Ruiz, Ricardo; Zhang, Ying; Black, Charles T.; Nealey, Paul F. *Advanced Materials (Weinheim, Germany)*. 2007. 19. 607–611.
- 49 Park, Cheolmin; Cheng, Joy Y.; Fasolka, Michael J.; Mayes, Anne M.; Ross, C. A.; Thomas, Edwin L.; Rosa, Claudio de. *Applied Physics Letters*. 2001. 79. 848.
- 50 Park, Sungjune; Cheng, Xiao; Böker, Alexander; Tsarkova, Larisa. *Adv. Mater.* 2016. 28. 6900–6905.
- 51 Lee, Seung-Heon; Kang, Huiman; Kim, Youn Sang; Char, Kookheon. *Macromolecules*. 2003. 36. 4907.
- 52 Albert, Julie N.L.; Epps, Thomas H. *Materials Today*. 2010. 13. 24–33.
- 53 Gurmessa, Bekele; Croll, Andrew B. *Macromolecules*. 2015. 48. 5670–5676.
- 54 Ludwigs, Sabine; Böker, Alexander; Abetz, Volker; Muller, Axel H. E.; Krausch, Georg. *Polymer*. 2003. 44. 6815.
- 55 Han, Sung Hyun; Lee, Dong Hyun; Kim, Jin Kon. *Macromolecules*. 2007. 40. 7416–7419.
- 56 Lee, Jaeyong; Kwak, Jongheon; Choi, Chungryong; Han, Sung Hyun; Kim, Jin Kon. *Macromolecules*. 2017. 50. 9373–9379.
- 57 Hashimoto, Takeji; Harada, Masafumi; Sakamoto, Naoki. *Macromolecules*. 1999. 32. 6867–6870.
- 58 Kang, Nam-Goo; Changez, Mohammad; Lee, Jae-Suk. *Macromolecules*. 2007. 40. 8553–8559.

8 Bibliography

- 59 Zhao, Hanying; Douglas, Elliot P.; Harrison, Benjamin S.; Schanze, Kirk S. *Langmuir*. 2001. 17. 8428–8433.
- 60 Asakawa, Koji; Hiraoka, Toshiro. *Japanese Journal of Applied Physics*. 2002. 41. 6112.
- 61 Werber, Jay R.; Osuji, Chinedum O.; Elimelech, Menachem. *Nature Reviews Materials*. 2016. 1. 41683.
- 62 Mokarian-Tabari, Parvaneh; Senthamaraikannan, Ramsankar; Glynn, Colm; Collins, Timothy W.; Cummins, Cian; Nugent, David; O'Dwyer, Colm; Morris, Michael A. *Nano Letters*. 2017. 17. 2973–2978.
- 63 Kim, Eunhye; Ahn, Hyungju; Park, Sungmin; Lee, Hoyeon; Lee, Moongyu; Lee, Sumi; Kim, Taewoo; Kwak, Eun-Ae; Lee, Jun Han; Lei, Xie; Huh, June; Bang, Joona; Lee, Byeongdu; Du Ryu, Yeol. *ACS NANO*. 2013. 7. 1952–1960.
- 64 Eunhye Kim, Du Yeol Ryu. *ACS NANO*. 2013. 7. 1952–1960.
- 65 Tsarkova, Larisa; Sevink, G. J. A.; Krausch, Georg; Sevink, G. J. Agur. *Advances in Polymer Science*. 2010. 227. 33–73.
- 66 Bates, F. S.; Fredrickson, G. H. *Annual Review of Physical Chemistry*. 1990. 41. 525.
- 67 Bates, Frank S. *Annual Review of Physical Chemistry*. 1990. 41. 525–557.
- 68 Polymer–Solvent Interaction Parameter χ .
- 69 Kim, Jin Kon. *Macromolecular Research*. 2008. 16. 267–292.
- 70 Bates, Frank S. *Science*. 1991. 251.
- 71 Fredrickson, Glenn H.; Helfand, Eugene. *The Journal of chemical physics*. 1987. 87. 697–705.
- 72 Leibler, Ludwik.
- 73 Goodman, Isaac. *Developments in block copolymers--2*. Elsevier Applied Science Publishers. 1985.
- 74 A. N. Semenov. *Sov. Phys.* 1985. 61.
- 75 van Zoelen, Wendy; Brinke, Gerrit ten. *Soft Matter*. 2009. 5. 1568.
- 76 Ashish K. Khandpur; Stephan Foerster; Frank S. Bates; Ian W. Hamley; Anthony J. Ryan; Wim Bras; Kristoffer Almdal; Kell Mortensen. *Macromolecules*. 1995. 28. 8796.
- 77 Urbas, A.; Sharp, R.; Fink, Y.; Thomas, E. L.; Xenidou, M.; Fetters, L. J. *Advanced Materials*. 2000. 12. 812–814.
- 78 Kang, Youngjong; Walish, Joseph J.; Gorishnyy, Taras; Thomas, Edwin L. *Nature Materials*. 2007. 6. 957–960.
- 79 Gu, Xiaodan; Gunkel, Ilja; Russell, Thomas P. *Philosophical transactions. Series A, Mathematical, physical, and engineering sciences*. 2013. 371. 20120306.
- 80 Leibler, Ludwik. *Macromolecules*. 1980. 13. 1602.
- 81 *Materials Science and Engineering: R: Reports*. 2006. 53. 199–248.
- 82 Krausch, G.; Magerle, R. *Advanced Materials*. 2002. 14. 1579–1583.

- 83 Michael J Fasolka, Anne M Mayes. *Annual Review of Materials Research*. 2001. 31. 323–355.
- 84 Knoll, A.; Horvat, A.; Lyakhova, K. S.; Krausch, G.; Sevink, G. J. A.; Zvelindovsky, A. V.; Magerle, R. *Physical Review Letters*. 2002. 89. 35501.
- 85 Herr, Daniel J.C. *Journal of Materials Research*. 2011. 26. 122–139.
- 86 Jeong, Seong-Jun; Kim, Ju Young; Kim, Bong Hoon; Moon, Hyoung-Seok; Kim, Sang Ouk. *Materials Today*. 2013. 16. 468–476.
- 87 Raybin, Jonathan; Ren, Jiaxing; Chen, Xuanxuan; Gronheid, Roel; Nealey, Paul F.; Sibener, S. J. *Nano Letters*. 2017. 17. 7717–7723.
- 88 Liu, Chi-Chun; Ramírez-Hernández, Abelardo; Han, Eungnak; Craig, Gordon S. W.; Tada, Yasuhiko; Yoshida, Hiroshi; Kang, Huiman; Ji, Shengxiang; Gopalan, Padma; Pablo, Juan J. de; Nealey, Paul F. *Macromolecules*. 2013. 46. 1415–1424.
- 89 Kim, Sang Ouk; Solak, Harun H.; Stoykovich, Mark P.; Ferrier, Nicola J.; Pablo, Juan J. de; Nealey, Paul F. *Nature*. 2003. 424. 411.
- 90 Sundrani, Deepak; Darling, S. B.; Sibener, S. J. *Nano Letters*. 2004. 4. 273–276.
- 91 Kim, Ho-Cheol; Park, Sang-Min; Hinsberg, William D. *Chemical reviews*. 2010. 110. 146–177.
- 92 Sundrani, Deepak; Darling, S. B.; Sibener, S. J. *Nano Letters*. 2004. 4. 273.
- 93 Sundrani, Deepak; Darling, S. B.; Sibener, S. J. *Langmuir*. 2004. 20. 5091–5099.
- 94 Cheng, Joy Y.; Mayes, Anne M.; Ross, Caroline A. *Nature Materials*. 2004. 3. 823–828.
- 95 Stein, G. E.; Kramer, E. J.; Li, X.; Wang, J. *Physical Review Letters*. 2007. 98. 86101.
- 96 Aissou, Karim; Shaver, Jonah; Fleury, Guillaume; Pécastaings, Gilles; Brochon, Cyril; Navarro, Christophe; Grauby, Stéphane; Rampnoux, Jean-Michel; Dilhaire, Stefan; Hadziioannou, Georges. *Advanced materials (Deerfield Beach, Fla.)*. 2013. 25. 213–217.
- 97 Kim, Sung J.o; Park, Sang Eun; Lee, Chan; Lee, Sun Young; Kim, I.n H.o; An, Hee Jung; Oh, Y.u-Kyoung. *Gynecologic Oncology*. 2003. 88. 411–418.
- 98 Segalman, R. A.; Yokoyama, H.; Kramer, E. J. *Advanced Materials*. 2001. 13. 1152–1155.
- 99 “Defect Free” DSA Patterning Spin-on Coat & Anneal Track. 2012.
- 100 Rubinstein, Michael; Colby, Ralph H. *Polymer physics*. Oxford University Press. 2003.
- 101 Walheim, Stefan; Böltau, Martin; Mlynek, Jürgen; Krausch, Georg; Steiner, Ullrich. *Macromolecules*. 1997. 30. 4995–5003.
- 102 Kim, G.; Libera, M. *Macromolecules*. 1998. 31. 2569–2577.
- 103 Li, Z.; Zhao, W.; Liu, Y.; Rafailovich, M. H.; Sokolov, J.; Khougaz, K.; Eisenberg, A.; Lennox, R. B.; Krausch, G. *Journal of the American Chemical Society*. 1996. 118. 10892–10893.

8 Bibliography

- 104 Zettl, Ute; Knoll, Armin; Tsarkova, Larisa. *Langmuir*. 2010. 26. 6610–6617.
- 105 Huang, Haiying; Hu, Zhijun; Chen, Yongzhong; Zhang, Fajun; Gong, Yumei; He, Tianbai; Wu, Chi. *Macromolecules*. 2004. 37. 6523–6530.
- 106 Karpitschka, Stefan; Weber, Constans M.; Riegler, Hans. *Chemical Engineering Science*. 2015. 129. 243–248.
- 107 Kim, S. H.; Misner, M. J.; Xu, T.; Kimura, M.; Russell, T. P. *Advanced Materials*. 2004. 16. 226–231.
- 108 Spatz, Joachim P.; Sheiko, Sergei; Möller, Martin. *Advanced Materials*. 1996. 8. 513–517.
- 109 Gu, Xiaodan; Gunkel, Ilja; Hexemer, Alexander; Russell, Thomas P. *Colloid and Polymer Science*. 2014. 292. 1795–1802.
- 110 Hamley, I. W. *Progress in Polymer Science*. 2009. 34. 1161–1210.
- 111 Dalvi, M. C.; Eastman, C. E.; Lodge, T. P. *Physical Review Letters*. 1993. 71. 2591.
- 112 Chapman, Bryan R.; Hamersky, Mark W.; Milhaupt, Jodi M.; Kostecky, Clayton; Lodge, Timothy P.; Meerwall, Ernst D. von; Smith, Steven D. *Macromolecules*. 1998. 31. 4562–4573.
- 113 Welander, Adam M.; Kang, Huiman; Stuenkel, Karl O.; Solak, Harun H.; Müller, Marcus; Pablo, Juan J. de; Nealey, Paul F. *Macromolecules*. 2008. 41. 2759–2761.
- 114 Campbell, Ian P.; Hirokawa, Soichi; Stoykovich, Mark P. *Macromolecules*. 2013. 46. 9599–9608.
- 115 P. Mansky, T. P. Russell, C. J. Hawker, J. Mays, D. C. Cook, and S. K. Satija. *Physical Review Letters*. 1997. 79. 237–240.
- 116 Han, Eungnak; Stuenkel, Karl O.; Leolukman, Melvina; Liu, Chi-Chun; Nealey, Paul F.; Gopalan, Padma. *Macromolecules*. 2009. 42. 4896–4901.
- 117 Bates, Frank S.; Fredrickson, Glenn H. *Physics Today*. 1999. 52. 32–38.
- 118 Matsen, M. W. *Macromolecules*. 1995. 28.
- 119 Hamley, Ian W. *The physics of block copolymers*. Oxford University Press. 1998.
- 120 Fukunaga, Kenji; Elbs, Hubert; Magerle, Robert; Krausch, Georg. *Macromolecules*. 2000. 33. 947–953.
- 121 Lundy, R.; Flynn, S. P.; Cummins, C.; Kelleher, S. M.; Collins, M. N.; Dalton, E.; Daniels, S.; Morris, M. A.; Enright, R. *Phys Chem Chem Phys*. 2017. 19. 2805–2815.
- 122 Kim, S. H.; Misner, M. J.; Russell, T. P. *Advanced Materials*. 2004. 16. 2119–2123.
- 123 Jung, Yeon Sik; Ross, Caroline A. *Adv. Mater.* 2009. 21. 2540–2545.
- 124 Lin, Zhiquan; Kim, Dong Ha; Wu, Xiaodong; Boosahda, Laurie; Stone, Daria; LaRose, Luanne; Russell, Thomas P.; Lin, Z. Q.; Kim, D. H.; Wu, X. D.; Boosahda, L.; Stone, D.; LaRose, L.; Russell, T. P. *Adv. Mater.* 2002. 14. 1373–1376.

- 125 Xuan, Yu; Peng, Juan; Cui, Liang; Wang, Hanfu; Li, Binyao; Han, Yanchun. *Macromolecules*. 2004. 37. 7301–7307.
- 126 Knoll, Armin; Magerle, Robert; Krausch, Georg. *Journal of Chemical Physics*. 2004. 120. 1105.
- 127 Di, Zhenyu; Posselt, Dorthé; Smilgies, Detlef-M; Papadakis, Christine M. *Macromolecules*. 2010. 43. 418–427.
- 128 Knoll, Armin; Tsarkova, Larisa; Krausch, Georg. *Nano Letters*. 2007. 7. 843–846.
- 129 Li, Yuhu; Huang, Haiying; He, Tianbai; Gong, Yumei. *The Journal of Physical Chemistry B*. 2010. 114. 1264–1270.
- 130 Cavicchi, Kevin A.; Russell, Thomas P. *Macromolecules (Washington, DC, United States)*. 2007. 40. 1181–1186.
- 131 Thomas H. Epps, III, Dean M. DeLongchamp, and Michael J. Fasolka. *Langmuir*. 2007. 23. 3355–3362.
- 132 Park, Soojin; Wang, Jia-Yu; Kim, Bokyoung; Chen, Wei; Russell, Thomas P. *Macromolecules*. 2007. 40. 9059–9063.
- 133 Wan, Lei; Ji, Shengxiang; Liu, Chi-Chun; Craig, Gordon S. W.; Nealey, Paul F. *Soft Matter*. 2016. 12. 2914–2922.
- 134 Bai, Wubin; Hannon, Adam F.; Gotrik, Kevin W.; Choi, Hong Kyoong; Aissou, Karim; Liontos, George; Ntetsikas, Konstantinos; Alexander-Katz, Alfredo; Avgeropoulos, Apostolos; Ross, Caroline A. *Macromolecules*. 2014. 47. 6000–6008.
- 135 Sinturel, Christophe; Grosso, David; Boudot, Mickael; Amenitsch, Heinz; Hillmyer, Marc A.; Pineau, Alain; Vayer, Marylène. *ACS applied materials & interfaces*. 2014. 6. 12146–12152.
- 136 Park, Woon Ik; Choi, Young Joong; Yun, Je Moon; Hong, Suck Won; Jung, Yeon Sik; Kim, Kwang Ho. *ACS applied materials & interfaces*. 2015. 7. 25843–25850.
- 137 Stenbock-Fermor, A.; Knoll, Armin W.; Böker, Alexander; Tsarkova, L.; Stenbock-Fermor, Anja; Böker, Alexander; Tsarkova, Larisa. *Macromolecules*. 2014. 47. 3059–3067.
- 138 Gotrik, Kevin W.; Hannon, Adam F.; Son, Jeong Gon; Keller, Brent; Alexander-Katz, Alfredo; Ross, Caroline A. *ACS NANO*. 2012. 6. 8052–8059.
- 139 Shelton, Cameron K.; Jones, Ronald L.; Dura, Joseph A.; Epps, Thomas H. *Macromolecules*. 2016. 49. 7525–7534.
- 140 Gu, Xiaodan; Gunkel, Ilja; Hexemer, Alexander; Gu, Weiyin; Russell, Thomas P. *Advanced materials (Deerfield Beach, Fla.)*. 2014. 26. 273–281.
- 141 Jin, Cong; Olsen, Brian C.; Luber, Erik J.; Buriak, Jillian M. *Chemistry of Materials*. 2016. 29. 176–188.
- 142 Nelson, Gunnar; Drapes, Chloe; Grant, Meagan; Gnabasik, Ryan; Wong, Jeffrey; Baruth, Andrew. *Micromachines*. 2018. 9. 271.
- 143 Gotrik, Kevin W.; Ross, C. A. *Nano Letters*. 2013. 13. 5117–5122.

8 Bibliography

- 144 Vayer, Marylène; Hillmyer, Marc A.; Dirany, Mohammed; Thevenin, Guillaume; Erre, René; Sinturel, Christophe. *Thin Solid Films*. 2010. 518. 3710–3715.
- 145 Sinturel, C.; Vayer, M.; Grosso, D.; Amenitsch, H. 2011.
- 146 Paik, Marvin Y.; Bosworth, Joan K.; Smilges, Detlef-M; Schwartz, Evan L.; Andre, Xavier; Ober, Christopher K. *Macromolecules*. 2010. 43. 4253–4260.
- 147 Olszowka, V.; Hund, M.; Kuntermann, V.; Scherdel, S.; Tsarkova, L.; Boker, A.; Krausch, G. *Soft Matter*. 2006. 2. 1089.
- 148 Marencic, Andrew P.; Wu, Mingshaw W.; Register, Richard A.; Chaikin, Paul M. *Macromolecules (Washington, DC, United States)*. 2007. 40. 7299–7305.
- 149 Hashimoto, Takeji; Bodycomb, Jeffrey; Funaki, Yoshinori; Kimishima, Kohtaro. *Macromolecules*. 1999. 32. 952.
- 150 Bitá, Ion; Yang, Joel K. W.; Jung, Yeon Sik; Ross, Caroline A.; Thomas, Edwin L.; Berggren, Karl K. *Science*. 2008. 321. 939–943.
- 151 Segalman, Rachel A.; Yokoyama, Hideaki; Kramer, Edward J. *Advanced Materials*. 2001. 13. 1152.
- 152 Yang, G. W.; Wu, G. P.; Chen, X.; Xiong, S.; Arges, C. G.; Ji, S.; Nealey, P. F.; Lu, X. B.; Darensbourg, D. J.; Xu, Z. K. *Nano Lett.* 2017. 17. 1233–1239.
- 153 Pandav, Gunja; Durand, William J.; Ellison, Christopher J.; Willson, C. Grant; Ganesan, Venkat. *Soft Matter*. 2015. 11. 9107–9114.
- 154 Peinemann, Klaus-Viktor; Abetz, Volker; Simon, Peter F. W. *Nature Materials*. 2007. 6. 992–996.
- 155 Albert, Julie N. L.; Young, Wen-Shiue; Lewis, Ronald L.; Bogart, Timothy D.; Smith, Jasmine R.; Epps, Thomas H. *ACS NANO*. 2012. 6. 459–466.
- 156 Hao, Jinlong; Wang, Zhan; Wang, Zheng; Yin, Yuhua; Jiang, Run; Li, Baohui; Wang, Qiang. *Macromolecules*. 2017. 50. 4384–4396.
- 157 Paradiso, Sean P.; Delaney, Kris T.; García-Cervera, Carlos J.; Ceniceros, Hector D.; Fredrickson, Glenn H. *ACS Macro Letters*. 2014. 3. 16–20.
- 158 Koenhen, D. M.; Mulder, M. H. V.; Smolders, C. A. *Journal of Applied Polymer Science*. 1977. 21. 199–215.
- 159 Vinit, J.; Noel, C.; Monnerie, L. *Desalination*. 1974. 15. 267–278.
- 160 McKelvey, S. *Journal of Membrane Science*. 1996. 112. 29–39.
- 161 Sammells, Anthony F.; Mundschau, Michael V. *Membrane Technology*. Wiley-VCH Verlag GmbH & Co. KGaA. 2006.
- 162 Guillen, Gregory R.; Pan, Yinjin; Li, Minghua; Hoek, Eric M. V. *Industrial & Engineering Chemistry Research*. 2011. 50. 3798–3817.
- 163 Jung, Adina; Rangou, Sofia; Abetz, Clarissa; Filiz, Volkan; Abetz, Volker. *Macromolecular Materials and Engineering*. 2012. 297. 790–798.
- 164 DAI, K. *Polymer*. 1994. 35. 157–161.
- 165 Cheng, L. C.; Bai, W.; Fernandez Martin, E.; Tu, K. H.; Ntetsikas, K.; Lontos, G.; Avgeropoulos, A.; Ross, C. A. *Nanotechnology*. 2017. 28. 145301.

- 166 Ian M. Smallwood. *Handbook of Organic Solvent Properties*. Elsevier. 1996.
- 167 Cheong, Lin Lee; Paul, Philip; Holzner, Felix; Despont, Michel; Coady, Daniel J.; Hedrick, James L.; Allen, Robert; Knoll, Armin W.; Duerig, Urs. *Nano Letters*. 2013. 13. 4485–4491.
- 168 Cui, Z. *Nanofabrication*. Springer US. 2009.
- 169 Chai, J.; Wang, D.; Fan, X.; Buriak, J. M. *Nat Nanotechnol*. 2007. 2. 500–506.
- 170 *Spectroscopic ellipsometry*. Wiley. 2007.
- 171 Ogieglo, Wojciech; Wormeester, Herbert; Eichhorn, Klaus-Jochen; Wessling, Matthias; Benes, Nieck E. *Progress in Polymer Science*. 2015. 42. 42–78.
- 172 J.A. Woollam Co., Inc.
- 173 Aspnes, D. E.; Studna, A. A. *Physical Review B*. 1983. 27. 985–1009.
- 174 *Polymer Data Handbook*. Oxford Univ. Press. 1999.
- 175 Jenkins, Francis Arthur; White, Harvey Elliott. *Fundamentals of optics*. McGraw-Hill. 1976.
- 176 Zettl, Ute; Knoll, A.; Tsarkova, L. *Langmuir*. 2010. 26(9). 6610–6617.
- 177 Binnig, G.; Quate, C. F.; Gerber, C. *Physical Review Letters*. 1986. 56. 930.
- 178 *Scanning Tunneling Microscopy II*. Springer Berlin Heidelberg. 1995.
- 179 Olszowka, Violetta; Tsarkova, Larisa; Böker, Alexander. *Soft Matter*. 2009. 5. 812–819.
- 180 Niihara, Ken-ichi; Sugimori, Hidekazu; Matsuwaki, Ukyo; Hirato, Fumio; Morita, Hiroshi; Doi, Masao; Masunaga, Hiroyasu; Sasaki, Sono; Jinnai, Hiroshi. *Macromolecules (Washington, DC, United States)*. 2008. 41. 9318–9325.
- 181 Komura, Motonori; Iyoda, Tomokazu. *Macromolecules (Washington, DC, United States)*. 2007. 40. 4106–4108.
- 182 Fasolka, Michael J.; Mayes, Anne M. *Annual Review of Materials Research*. 2001. 31. 323–355.
- 183 Maurice, Patricia A. *Colloids and Surfaces, A: Physicochemical and Engineering Aspects*. 1996. 107. 57–75.
- 184 Smith, D. A.; Connell, S. D.; Robinson, C.; Kirkham, J. *Analytica Chimica Acta*. 2003. 479. 39–57.
- 185 Bustamante, Carlos; Vesenka, James; Tang, Chun Lin; Rees, William; Guthold, Martin; Keller, Rebecca. *Biochemistry*. 1992. 31. 22–26.
- 186 Rees, William A.; Keller, Rebecca W.; Vesenka, James P.; Yang, Guoliang; Bustamante, Carlos. *Science*. 1993. 260. 1646–1649.
- 187 Takano, Hajime; Kenseth, Jeremy R.; Wong, Sze-Shun; O'Brie, Janese C.; Porter, Marc D. *Chemical Reviews*. 1999. 99. 2845–2890.
- 188 Chada, Nagaraju; Sigdel, Krishna P.; Gari, Raghavendar Reddy Sanganna; Matin, Tina Rezaie; Randall, Linda L.; King, Gavin M. *Scientific Reports*. 5. 12550.
- 189 Tamayo, J.; Garcia, R. *Langmuir*. 1996. 12. 4430.

8 Bibliography

- 190 Gruverman, Alexei; Auciello, Orlando; Tokumoto, Hiroshi. *Annual review of materials science*. 1998. 28. 101–123.
- 191 van der Vegte, Eric W.; Hadziioannou, Georges. *Langmuir*. 1997. 13. 4357–4368.
- 192 Müller, Daniel J.; Dufrêne, Yves F. *Nature nanotechnology*. 2008. 3. 261–269.
- 193 Junno, T.; Keeppert, K.; Montelius, L.; Samuelson, L. *Applied Physics Letters*. 1995. 66. 3627–3629.
- 194 Hertel, Tobias; Martel, Richard; Avouris, Phaedon. *Journal of Physical Chemistry B*. 1998. 102. 910–915.
- 195 Rief, Matthias; Oesterhelt, Philipp; Heymann, Berthold; Gaub, Hermann E. *Science* (Washington, DC, United States). 1997. 275. 1295–1297.
- 196 Kong, Jing; Soh, Hyongsok T.; Cassell, Alan M.; Quate, Calvin F.; Dai, Hongjie. *Nature* (London). 1998. 395. 878–881.
- 197 Sheiko, Sergei S.; Sumerlin, Brent S.; Matyjaszewski, Krzysztof. *Progress in Polymer Science*. 2008. 33. 759–785.
- 198 Raghavan, D.; Gu, X.; Nguyen, T.; VanLandingham, M.; Karim, A. *Macromolecules* (Washington, DC, United States). 2000. 33. 2573–2583.
- 199 Goddard, J. M.; Hotchkiss, J. H. *Progress in Polymer Science*. 2007. 32. 698–725.
- 200 Magonov, Sergei N.; Reneker, Darrell H. *Annual Review of Materials Science*. 1997. 27. 175–222.
- 201 Cappella, B.; Dietler, G. *Surface Science Reports*. 1999. 34. 1–104.
- 202 Maver, Uroš; Velnar, Tomaž; Gaberšček, Miran; Planinšek, Odon; Finšgar, Matjaž. *TrAC Trends in Analytical Chemistry*. 2016. 80. 96–111.
- 203 Zhong, Q.; Inness, D.; Kjoller, K.; Elings, V. B. *Surface Science Letters*. 1993. 290. L688-L692.
- 204 Corporation, Bruker.
- 205 *PeakForce QNM User Guide*. Veeco Instruments Inc. 2010.
- 206 Nahar, S. N. *Phase-Separation Characteristics of Bitumen and their Relation to Damage-Healing*. Delft University of Technology.
- 207 Goodwin, Robert D. *Journal of Physical and Chemical Reference Data*. 1989. 18. 1565–1636.
- 208 Hu, Xuesong; Shin, Kwanwoo; Rafailovich, Miriam; Sokolov, Jonathan; Stein, Richard; Chan, Yee; Wlwu, Kurt Williams; Wu, W. L.; Kolb, Rainer. *High Performance Polymers*. 2016. 12. 621–629.
- 209 Flory, Paul J. *Science*. 1953. 72. 393–394.
- 210 Elbs, Hubert; Krausch, Georg. *Polymer*. 2004. 45. 7935–7942.
- 211 EBOOKS, L. R.N.
- 212 Stahl, Brian C.; Kramer, Edward J.; Hawker, Craig J.; Lynd, Nathaniel A. *Journal of Polymer Science Part B: Polymer Physics*. 2017. 55. 1125–1130.
- 213 Hashimoto, Takeji; Shibayama, Mitsuhiro; Kawai, Hiromichi. *Macromolecules*. 1983. 16. 1093–1101.

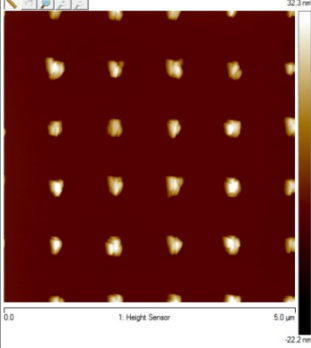
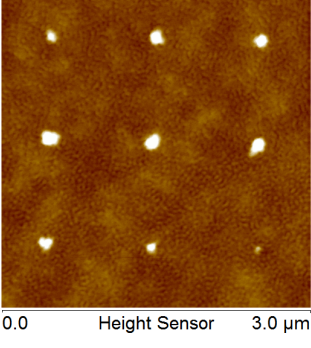
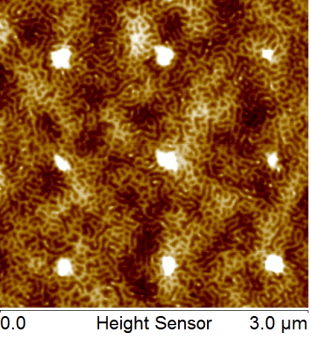
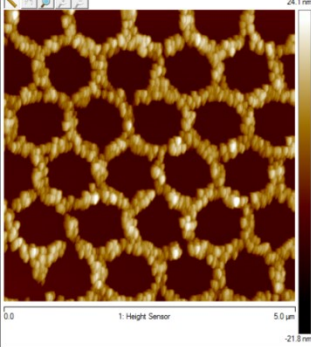
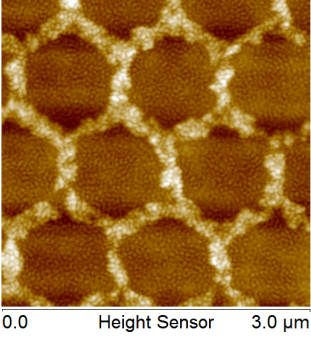
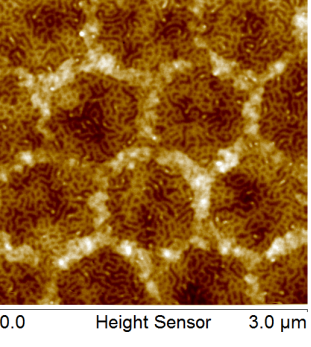
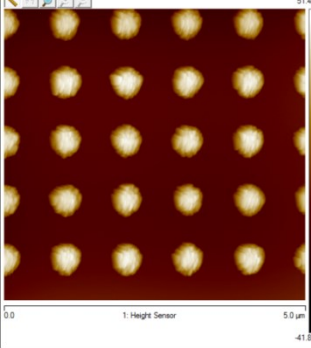
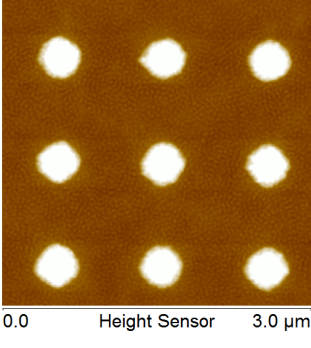
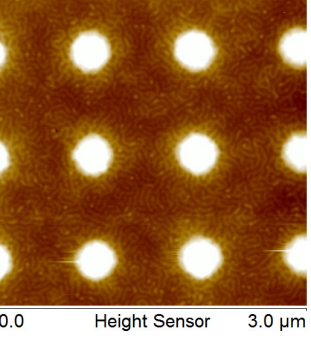
- 214 Liang, Chengdu; Hong, Kunlun; Guiochon, Georges A.; Mays, Jimmy W.; Dai, Sheng. *Angewandte Chemie (International ed. in English)*. 2004. 43. 5785–5789.
- 215 Termonia, Yves. *Journal of Polymer Science Part B: Polymer Physics*. 1999. 37. 2782–2787.

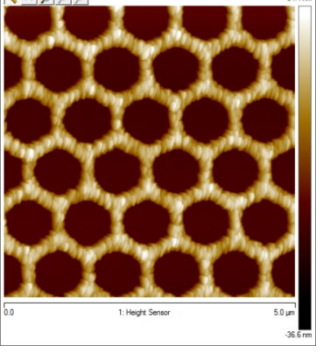
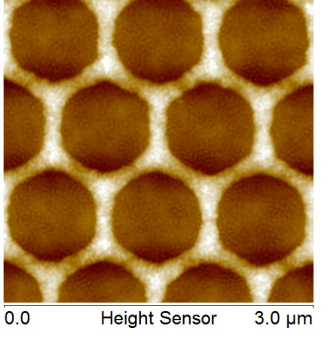
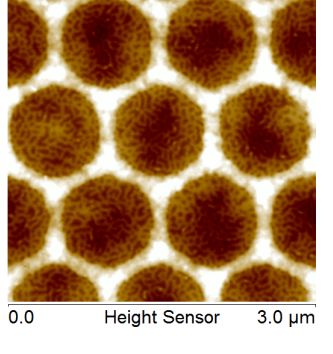
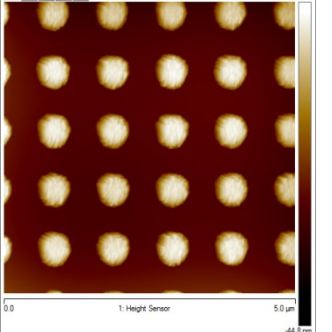
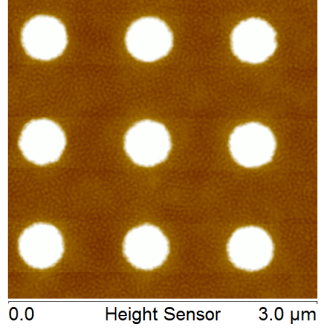
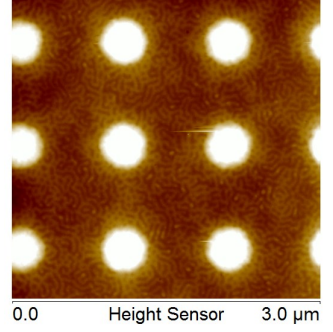
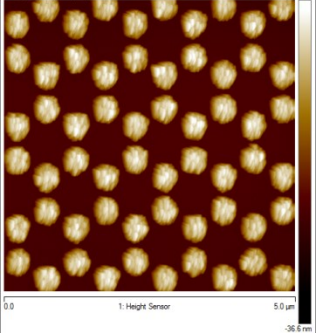
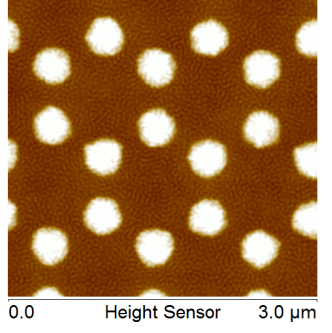
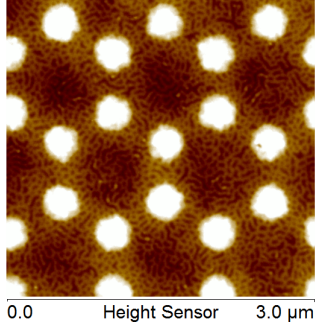
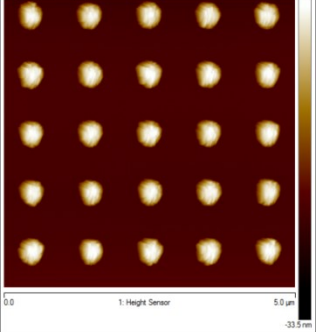
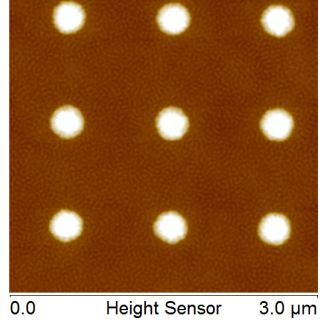
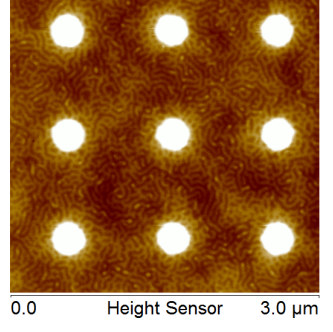
9 Publications and Posters

- Publications
 - “Hierarchical Manipulation of Block Copolymer Patterns on 3D Topographic Substrates” Park, Sungjune; Cheng, Xiao; Böker, Alexander; Tsarkova, Larisa. *Advanced materials*. 2016. 28. 6900–6905.
 - X. Cheng, J. Tempeler, S. Danylyuk, A. Böker and L. Tsarkova Tunable Templates from High Molecular Weight Block copolymers by Controlled Solvo-thermal Annealing, [in preparation]
 - X. Cheng, JA. Böker¹ and L. Tsarkova, Scientific and practical aspects of controlled solvent vapor annealing, [in preparation]
- In non peer-reviewed books
 - “High Molecular Weight Block Copolymer as Tunable Templates for Pattern Transfer” X. Cheng, J. Tempeter, S. Danylyuk, L. Tsarkova, JARA-FIT Annual Report 2015
- Conference Posters
 - “Plasma etch resistivity of high molecular weight microphase separated PS-b-P2VP block copolymers” Xiao Cheng, Christian Lewin, Anja Stenbock, Larisa Tsarkova, Jenny Tempeler, Sascha Brose, Serhiy Danylyuk
1st International Symposium on Directed Self-Assembly, Leuven, 26.Oct.2015

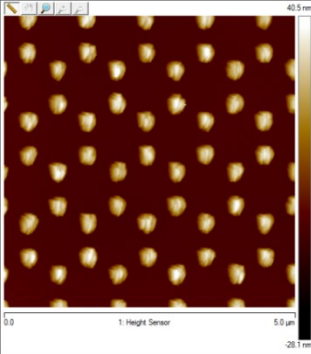
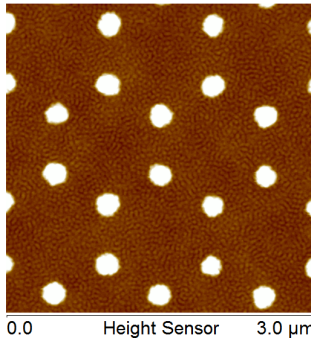
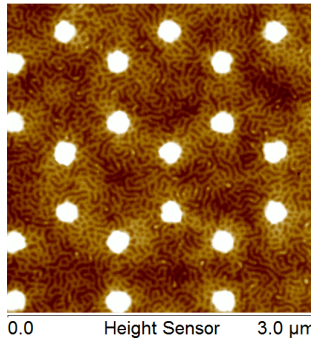
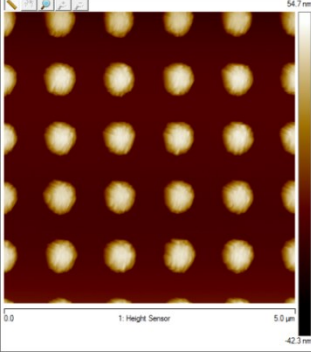
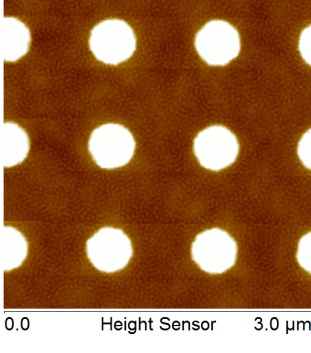
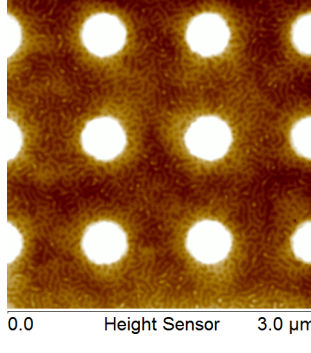
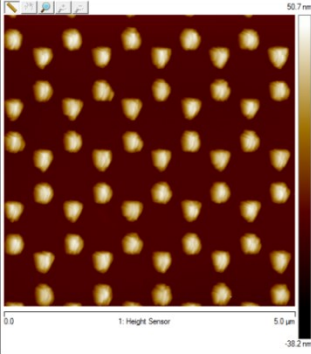
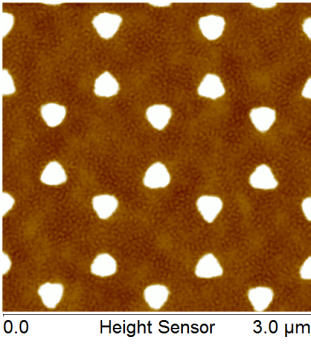
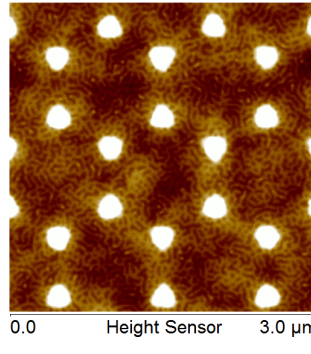
10 Appendix

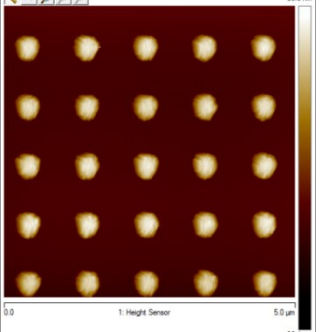
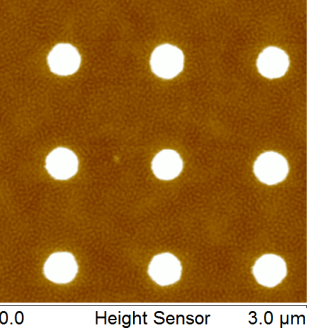
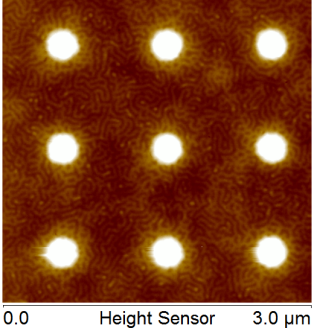
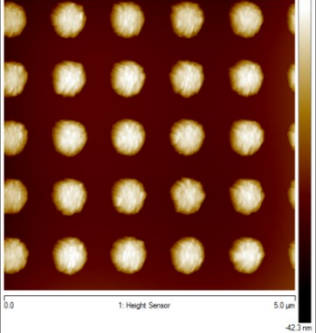
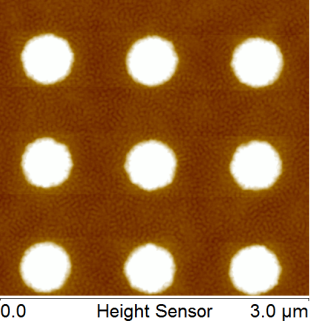
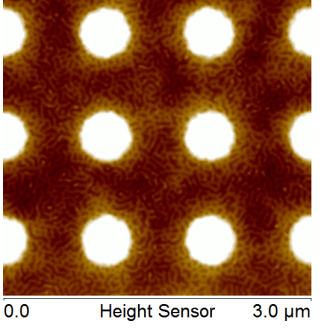
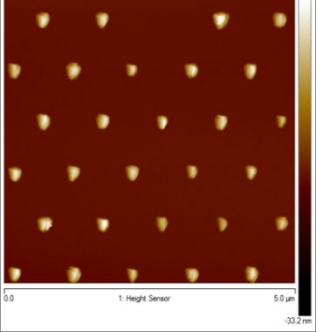
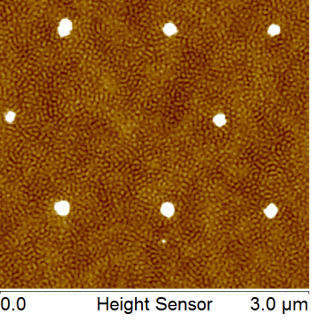
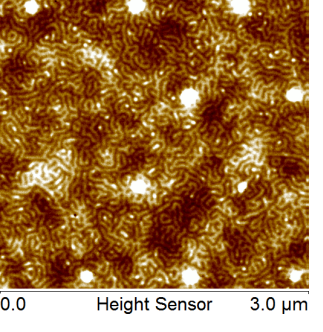
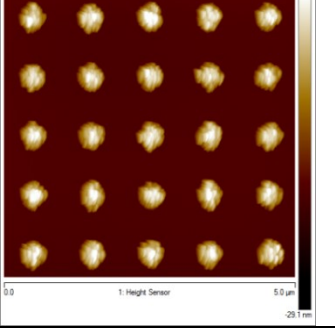
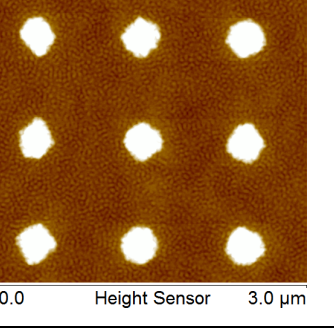
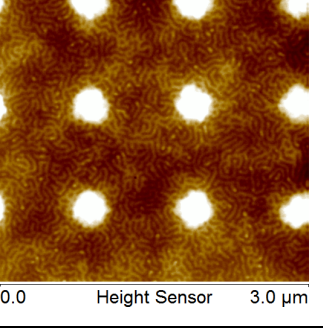
Table 4 SFM height images of original patterned substrates, spin-cast SV⁹⁹ films and annealed SV⁹⁹ films on patterned substrates. The annealing is in toluene vapor with degree of swelling of ~1.3 at 14 °C/20 °C for 45 min.

No.	Original	SV ⁹⁹ spin-cast	Annealed by toluene
000			
	H:31 nm D:750 nm	H: 11 nm D:758*829 nm	
001			
	H:22 nm D:700 nm	H: 10 nm D: 763 nm	
002			
	H:52 nm D: 450 nm	H: 34 nm D: 510 nm	

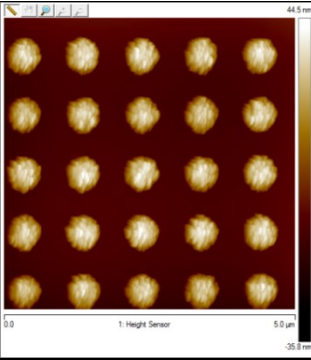
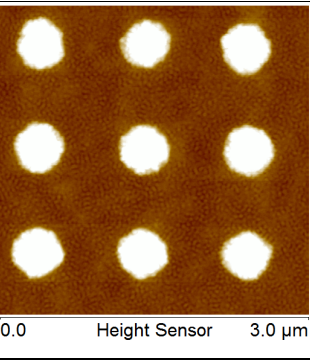
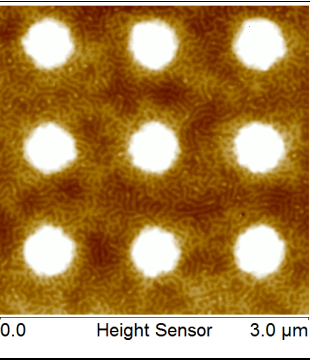
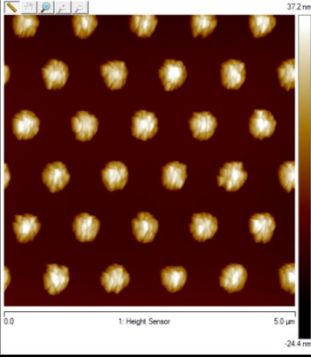
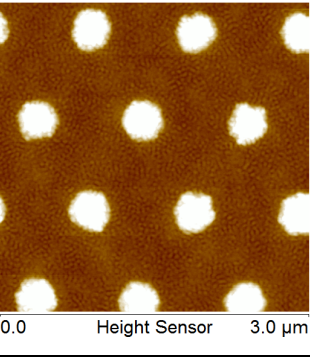
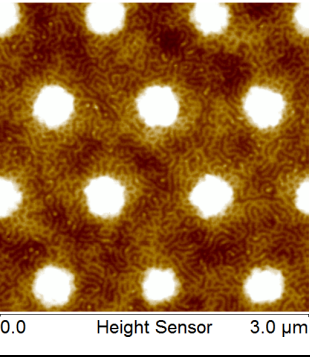
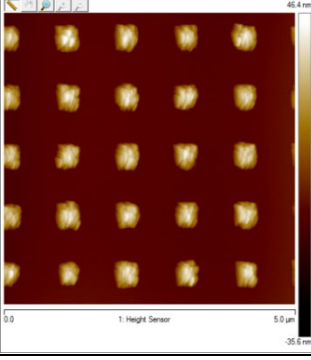
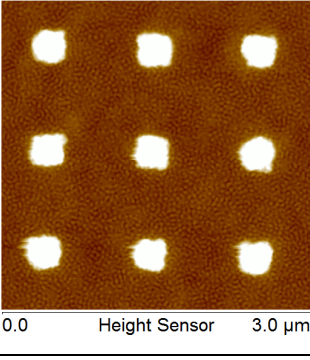
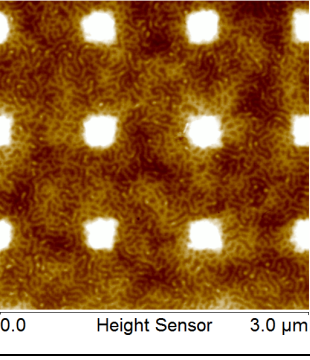
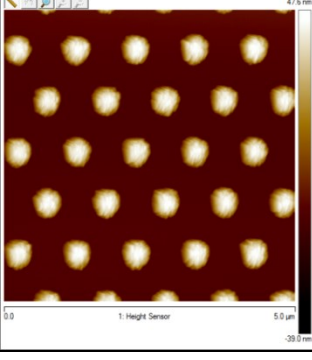
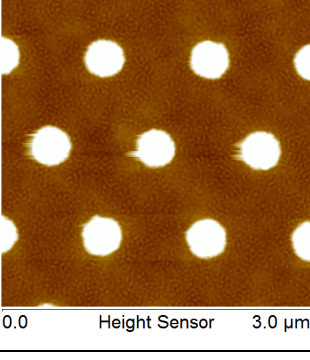
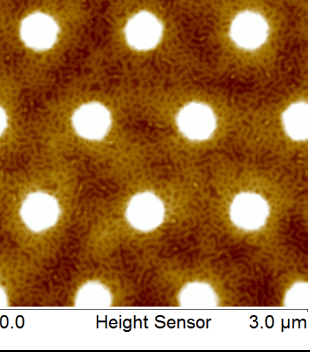
003			
	<p>H:34 nm D:750 nm</p>	<p>H: 15 nm D: 822 nm</p>	
004			
	<p>H: 53 nm D: 400 nm</p>	<p>H: 35 nm D: 540*520 nm</p>	
005			
	<p>H:40 nm D1:68 nm</p>	<p>H: 20 nm D: 190 nm</p>	
006			

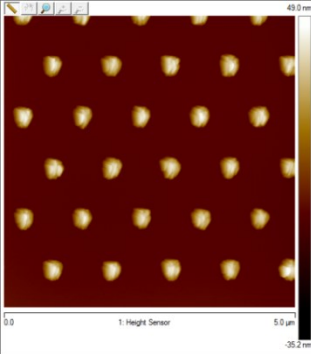
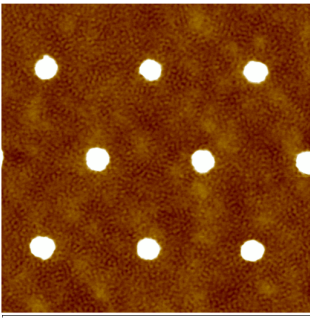
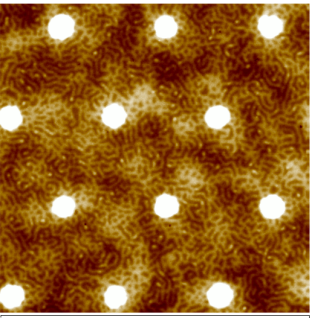
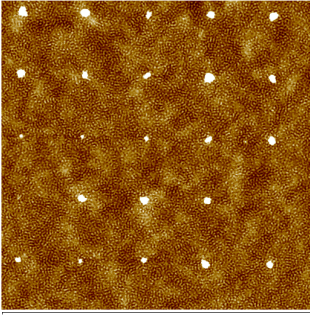
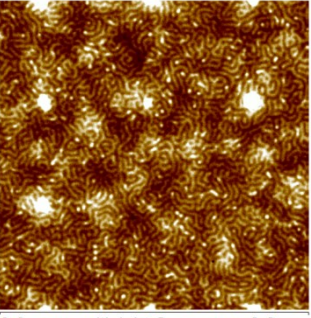
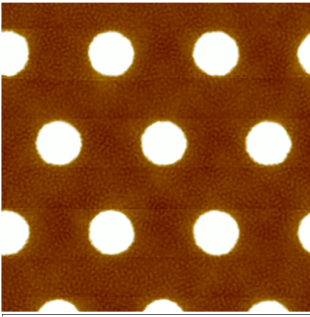
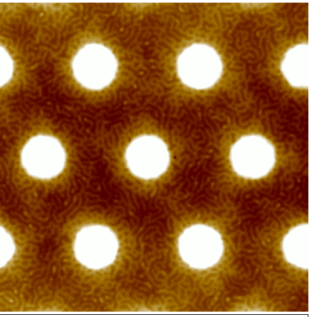
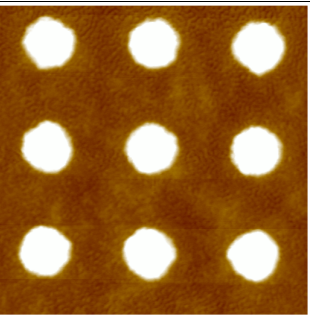
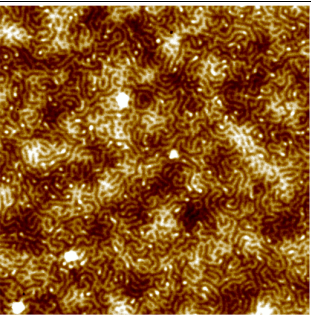
10 Appendix

007	H:53 nm D:538 nm	H:31 nm D: 620*640 nm	
			
008	H:39 nm D:203 nm	H:18 nm D:330 nm	
			
009	H:55 nm D:428 nm	H: 35 nm D: 550 nm	
			
	H:48 nm D1:150 nm	H: 26 nm D: 922 nm; 276 nm	

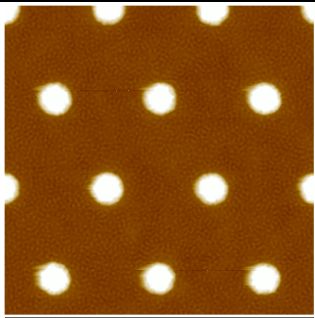
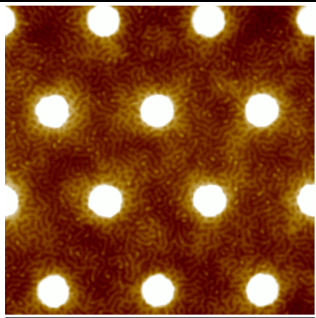
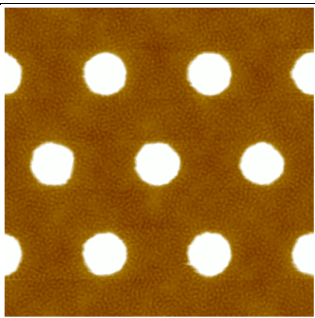
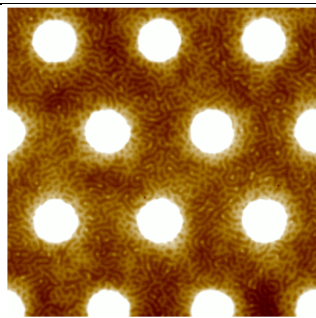
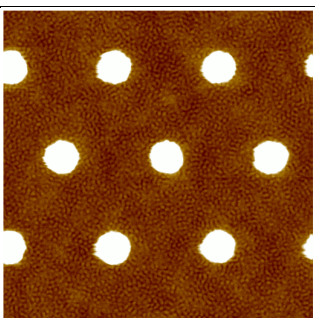
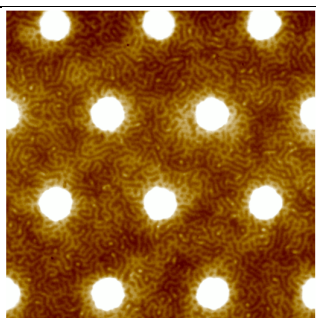
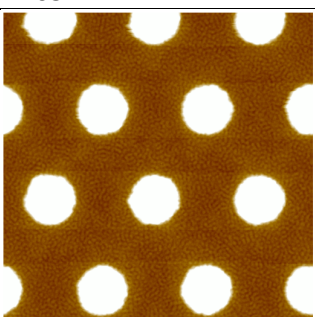
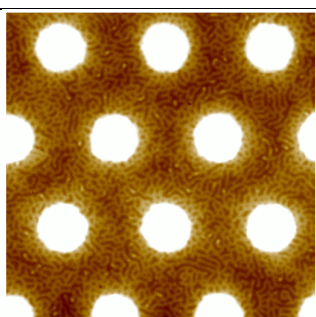
010			
	<p>H:54 nm D:529 nm</p>	<p>H: 35 nm D: 640*655 nm</p>	
011			
	<p>H:54 nm D:382 nm</p>	<p>H: 33 nm D: 500 nm</p>	
012			
	<p>H:33 nm D:723 nm</p>	<p>H: 11 nm D: 850 nm*1.6μm</p>	
013			
	<p>H:40 nm</p>	<p>H: 20 nm</p>	

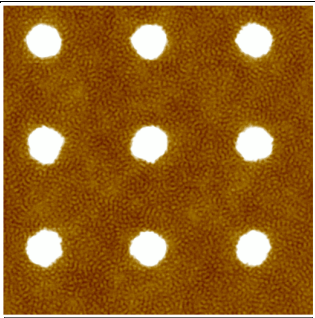
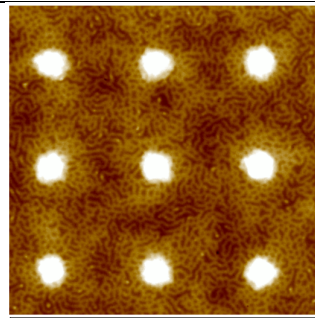
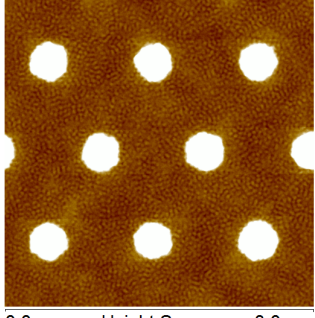
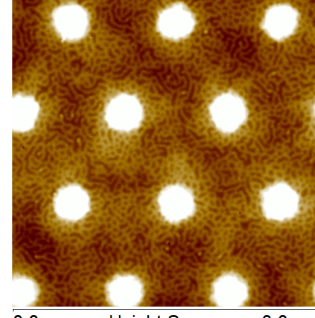
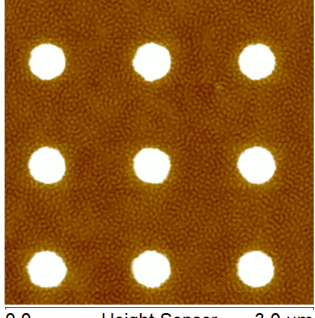
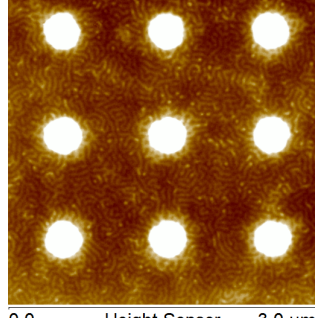
10 Appendix

014	D:484 nm	D: 615*615 nm	
			
	H:46 nm D:369 nm	H: 24 nm D: 500 nm	
015			
		H:42 nm D:490 nm	H: 21 nm D: 580 nm*1.3μm
016			
		H:43 nm D:570 nm	H: 21 nm D: 680 nm
017			

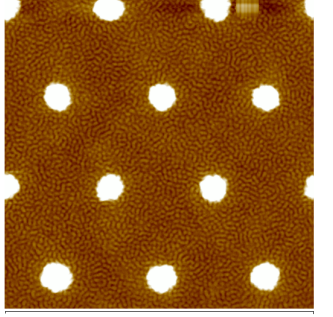
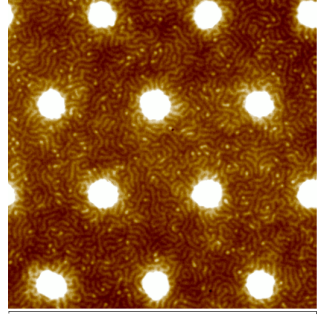
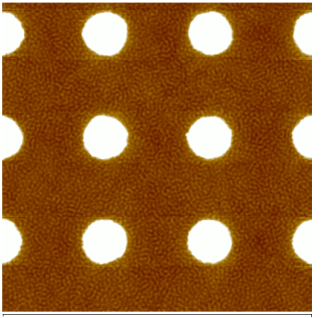
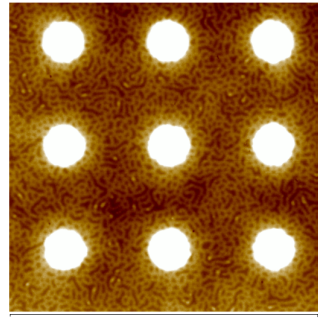
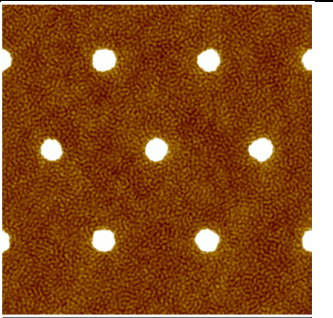
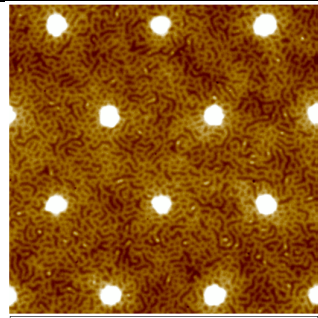
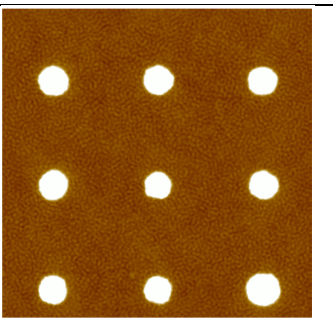
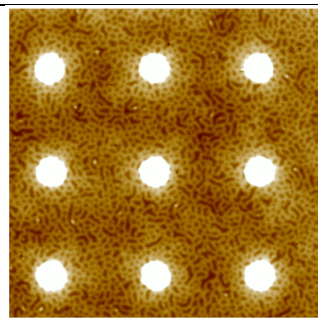
	H:53 nm D:487 nm	H: 32 nm D: 590 nm	
018			
	H:46 nm D:640 nm	H: 21 nm D: 775 nm	
019			
		H: 10 nm D: 890 nm	
020			
		H: 33 nm D: 555 nm	
021			

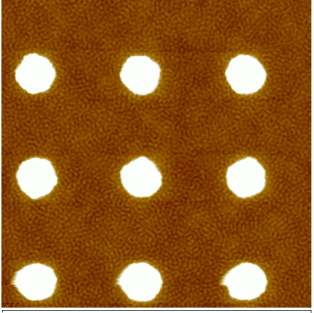
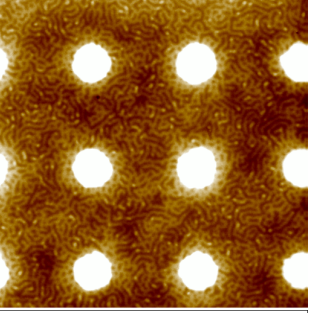
10 Appendix

		H: 24 nm D: 487 nm	
022			
		H: 31 nm D: 652 nm	
023			
		H: 34 nm D: 575 nm	
024			
		H: 26 nm D: 652 nm	
025			
		H: 29 nm	

026		D: 493 nm  0.0 Height Sensor 3.0 μm	 0.0 Height Sensor 3.0 μm
		H: 20 nm D: 634 nm	
027		 0.0 Height Sensor 3.0 μm	 0.0 Height Sensor 3.0 μm
		H: 25 nm D: 620 nm	
028		 0.0 Height Sensor 3.0 μm	 0.0 Height Sensor 3.0 μm
		H: 32 nm D: 634 nm	

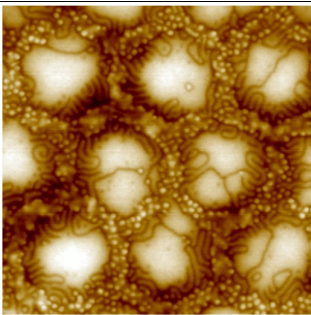
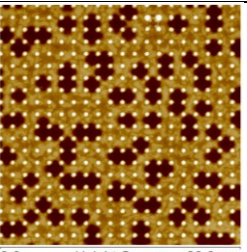
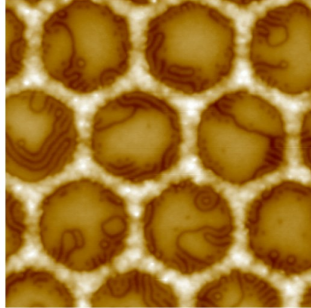
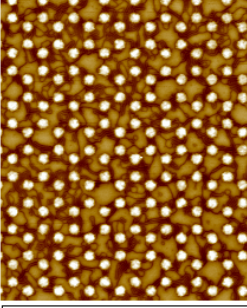
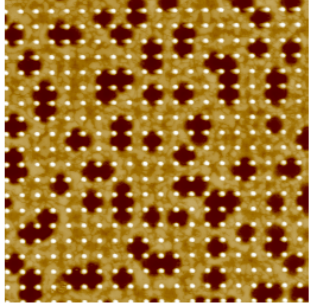
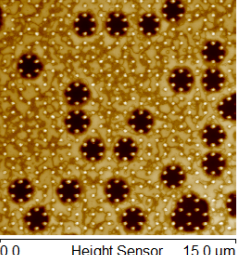
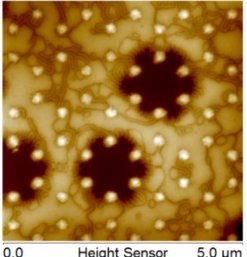
10 Appendix

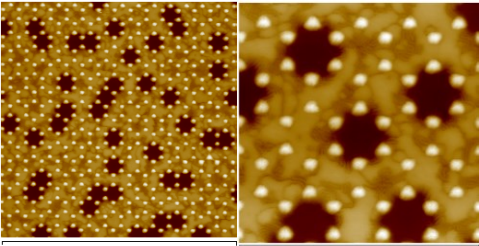
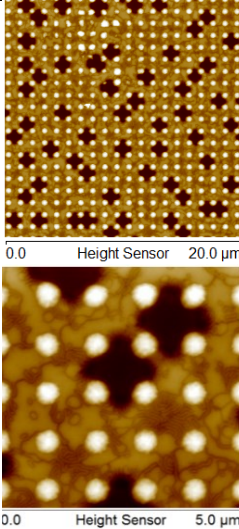
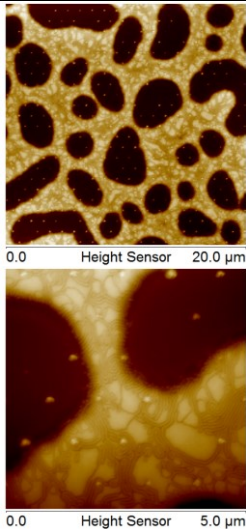
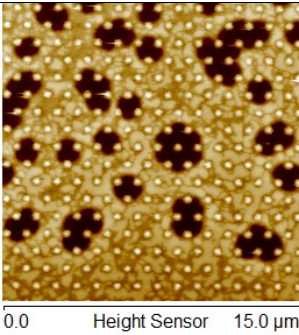
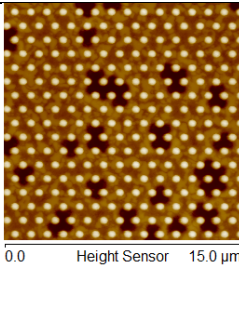
029		 <p>0.0 Height Sensor 3.0 μm</p>	 <p>0.0 Height Sensor 3.0 μm</p>
		<p>H: 21 nm D: 716 nm</p>	
030		 <p>0.0 Height Sensor 3.0 μm</p>	 <p>0.0 Height Sensor 3.0 μm</p>
		<p>H: 32 nm D: 552 nm</p>	
031		 <p>0.0 Height Sensor 3.0 μm</p>	 <p>0.0 Height Sensor 3.0 μm</p>
		<p>H: 19 nm D: 787 nm</p>	
032		 <p>0.0 Height Sensor 3.0 μm</p>	 <p>0.0 Height Sensor 3.0 μm</p>
		<p>H: 30 nm D: 722 nm</p>	

033		 <p>0.0 Height Sensor 3.0 μm</p>	 <p>0.0 Height Sensor 3.0 μm</p>
		<p>H: 30 nm D: 600 nm</p>	

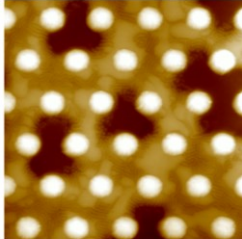
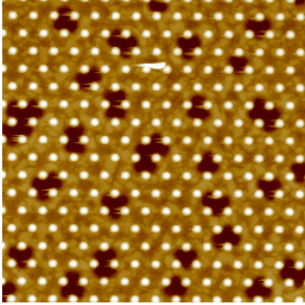
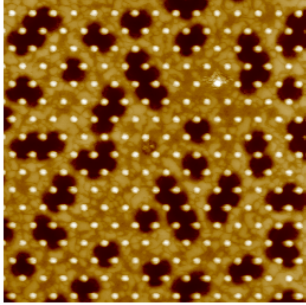
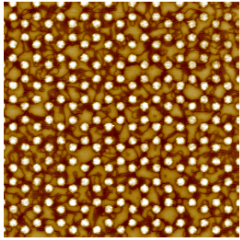
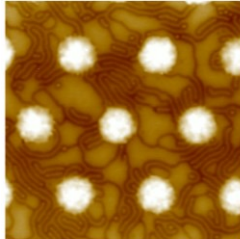
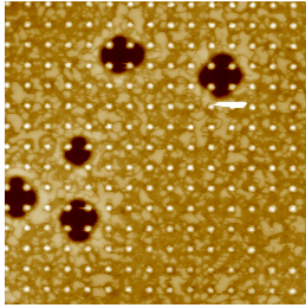
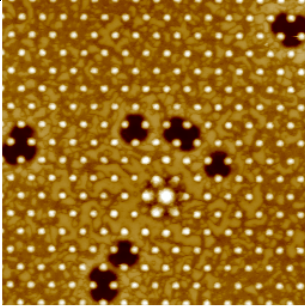
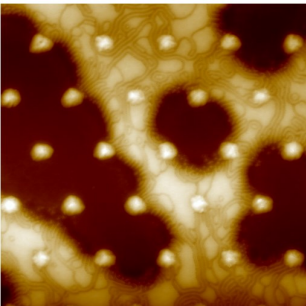
10 Appendix

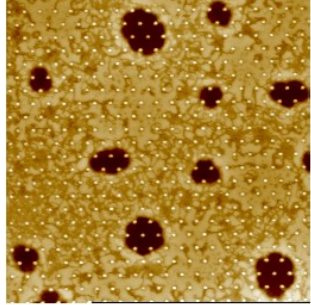
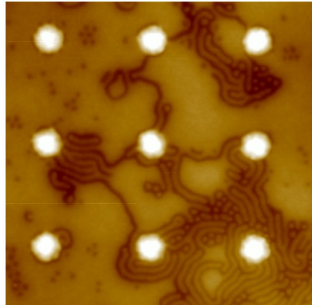
Table 5 SFM height images of SV⁹⁹ films on patterned substrates annealed in toluene vapor with over pressure at 25 °C/30 °C

001		002	
H:22 nm D:700 nm		H:52 nm D: 450 nm	
003		005	
H:34 nm D:750 nm		H:40 nm D1:68 nm	
006		007	
			

	<p>H:53 nm D:538 nm</p>	<p>H:39 nm D1:203 nm</p>
009	 <p>0.0 Height Sensor 15.0 μm 0.0 Height Sensor 5.0 μm</p>	 <p>0.0 Height Sensor 20.0 μm 0.0 Height Sensor 5.0 μm</p>
	<p>H:48 nm D1:150 nm, D2:619 nm, D3:795 nm</p>	<p>H:54 nm D:382 nm</p>
012	 <p>0.0 Height Sensor 20.0 μm 0.0 Height Sensor 5.0 μm</p>	014
	<p>H:33 nm D1:723 nm, D2:776 nm</p>	<p>H:46 nm D:369 nm</p>
015	 <p>0.0 Height Sensor 15.0 μm</p>	020
		 <p>0.0 Height Sensor 15.0 μm</p>

10 Appendix

			 <p>0.0 Height Sensor 5.0 μm</p>
	<p>H:42 nm D:490 nm</p>		
023	 <p>0.0 Height Sensor 15.0 μm</p>	024	 <p>0.0 Height Sensor 15.0 μm</p>
025	 <p>0.0 Height Sensor 10.0 μm</p>  <p>0.0 Height Sensor 3.0 μm</p>	026	 <p>0.0 Height Sensor 15.0 μm</p>
027	 <p>0.0 Height Sensor 15.0 μm</p>	029	 <p>0.0 Height Sensor 5.0 μm</p>

031	 <p data-bbox="332 499 641 529">0.0 Height Sensor 20.0 μm</p>	032	 <p data-bbox="917 499 1226 529">0.0 Height Sensor 3.0 μm</p>
-----	--	-----	---

11 Abbreviations

BCP	Block copolymer
C	Cylinder
D	Degree of swelling
DSA	Directed self-assembly
FE-SEM	Field emission scanning electron microscopy
f_i	Volume fraction of block i
GISAXS	Grazing-incidence small-angle scattering
GPC	Gel permeation chromatography
h_{dr}	Dry film thickness
h_{sw}	Swollen film thickness
HM	Hard mask
n	Mole
N_i	Polymerization of composition i
ODT	Order-disorder transition
p/p_0	Partial vapor pressure
p_0	Saturated vapor pressure
P2VP	Poly(2vinyl pyridine)
PB	Polybutadiene
PE	Polyethylene
PEO	Poly(ethylene oxide)
PDMS	Polydimethylsiloxane
PL	Perforated lamella
PMMA	Poly(methyl methacrylate)
PS	Polystyrene
p_s	Saturated vapor pressure
PSD	Power-spectral-density
PTFE	Polytetrafluoroethylene
PVD	Physical vapor deposition
PVP	Poly(2vinyl pyridine)

RIE	Reactive-ion etching
RT	Room temperature
SAXS	Small-angle X-ray scattering
SEM	Scanning electron microscopy
SFM	Scanning force microscopy
STM	Scanning tunneling microscopy
SB	PS ₂₉ -b-PB ₇₁
sccm	Standard cubic centimeter per minute
SV	Polystyrene-block-poly(2-vinylpyridine)
SV ³⁹⁰	Polystyrene-block-poly(2-vinylpyridine) with molecular weight of 390 kg/mol
SV ⁹⁹	Polystyrene-block-poly(2-vinylpyridine) with molecular weight of 99 kg/mol
SVA	Solvent vapor annealing
T _g	Temperature of glass transition
T _s	Temperature of substrates
T _v	Temperature of vapor
digit 1 °C / digit 2°C	Temperature set (T _v /T _s)
χ	Flory-Huggins interaction parameter
χ _{eff}	Effective Flory-Huggins interaction parameter
Φ _p	Polymer volume fraction
Φ _{eff}	Effective polymer volume fraction

12 List of Figures

- Figure 1 Evolution of structure with the combined parameter χN for a symmetric, di-block copolymer with $f = 0.5$. When $\chi N \sim 10$, small variations in system entropy ($\sim N^{-1}$) or energy ($\sim \chi$) leads to ordered ($\chi N \geq 10$) or disordered ($\chi N \leq 10$) states. A homo-generous composition profile (4A versus r) results when entropic factors dominate ($\chi N \ll 10$), whereas a strongly microphase segregated pattern characterizes the limit where energetic factors prevail ($\chi N > 10$). Reprinted from Reference [70]. 10
- Figure 2 A theoretical phase diagram for a conformationally symmetric diblock copolymer melt. Reproduced from Reference [75] with permission from The Royal Society of Chemistry. 11
- Figure 3 Experimentally determined phase diagram of PI-b-PS. Reprinted from Reference [76]. 12
- Figure 4 Diblock copolymer thin film morphologies. (a) Schematic representation of volume symmetric diblock with A (light) and B (dark) type segments. (b) Diagram of BCP film system in cross section indicating the bottom (1) and top (2) surfaces, with surface interaction energies S_1 and S_2 , respectively. (c) Summary of diblock thin film morphologies, generally organized by their appearance as film thickness decreases from L_0 . These calculated cross sections indicate the density of B-type segments, i.e., Black=100% B, white=100% A. These structures are referred to in the text with the abbreviations included under each diagram. FL: symmetric surface-parallel full lamella; AFL: anti-symmetric surface-parallel lamella; AHY: anti-symmetric hybrid structure; HL: half-lamella; HY: symmetric hybrid structure; PL: surface-perpendicular lamellae. Reprinted from Reference [83] 13
- Figure 5 (a) Nanopattern revolution of the block copolymer thin film of PS-b-PB and the SFM phase image of SB morphology. The SFM phase images ($1 \times 1 \mu\text{m}$) present examples of the surface structures on carbon-coated (left) and silicon oxide (right) substrates at the indicated film thickness. Reprinted from Reference [84]. 14
- Figure 6 Phase diagram of the surface structures on a weakly interacting surface (carbon coating) under strong surface field with a preference for the majority component (silicon oxide). The SFM phase images ($1 \times 1 \mu\text{m}$) present examples of the surface structures on carbon-coated (left) and silicon oxide (right) substrates at the indicated film thickness. Reprinted from Reference [47]. 15
- Figure 7 (a) Schematic illustration of epitaxial self-assembly exploiting nanoscopic chemical patterns to direct BCP self-assembly [97]. (b) SEM image showing defect-free lamellar patterns attained by epitaxial self-assembly [97]. (c) Schematic illustration of graphoepitaxy utilizing topographic pattern to direct BCP assembly [98]. (d) SEM image showing highly aligned lamellar patterns prepared by graphoepitaxy [99]. Reprinted from Reference [86] with permission from Elsevier. 17
- Figure 8 Composition dependence of the free energy of mixing for a symmetric polymer blend with the product $\chi N = 2.7$ (top figure) and the corresponding phase diagram (bottom figure). Binodal (solid curve) and spinodal (dashed curve) are shown on the phase diagram. Reprinted from Reference [100]. 18
- Figure 9 Top view SEM images of assembled BCP films of five different thicknesses on PG4-modified substrates (annealed at $190 \text{ }^\circ\text{C}$). Reprinted from Reference [116]. 20

Figure 10	Sketches of primary methods of solvent vapor annealing in A , with (a) static annealing, (b) static annealing with gas flow to control swelling and deswelling process, (c) dynamic annealing with controlled solvent vapor flow. Examples of the annealing setups used in current researches in B , (a) static annealing with in situ monitor for film thickness, (b) dynamic annealing with controlled feedback loop [141], (c) dynamic annealing with controlled mixture of solvent [138], (d) dynamic annealing with highly precise controlling of annealing time. Reproduced from Reference [138; 141; 142].	22
Figure 11	Reversible morphology control through solvent processing as probed <i>in situ</i> and in real time with GISAXS. Thin films with spherical morphology obtained through acetone vapor treatment are shown to transition to parallel cylinders upon THF vapor annealing and returned to a spherical morphology upon successive exposure to acetone vapor. Reprinted from Reference [146].	24
Figure 12	Schematic view of the solvent evaporation in a thin block polymer film illustrating the concept on an ordering front that propagates through the film. Reprinted from Reference [107].	25
Figure 13	Nonisotropic nucleus growth during macrovoid formation in membranes. Reprinted from Book [161].	26
Figure 14	Mechanism of phase separation during membrane formation. Reprinted from Book [161].	27
Figure 15	Different membrane morphologies caused of different types of demixing. Reprinted from Reference [162].	28
Figure 16	Film thickness of SV ³⁹⁰ films prepared from solutions in Toluene and DMF as a function of the polymer concentration in spin-cast solution with constant acceleration of 2k rpm/min. The influences to the film thickness from spin-coating condition (rotational speed) are also displayed in the plot, as indicated by symbols. Notation Nk corresponds to N thousands rounds per minute.	33
Figure 17	Film thickness of (a) SV ³⁹⁰ and SV ⁹⁹ , (b) PS184, P2VP105 films prepared from chloroform solutions as a function of the spin-cast solution concentration. The comparison between different spin-coating conditions (rotational speeds) is displayed in (a), where notation Nk corresponds to N thousands rounds per minute.	34
Figure 18	Schematics of ellipsometric measurement principle. Copyright of Reference [170].	37
Figure 19	Interference within a transparent thin film. Copyright of Reference [171].	39
Figure 20	(a) Scheme of depicting feedback loops in XY and Z to create an SFM image. (b) The force related with distance between the approaching tip and the sample. Reprinted from Ref [202]	40
Figure 21	Effect of tip radius.	41
Figure 22	Scheme of Force vs. Tip-sample separation of PeakForce mode and the typical images obtained by this mode. Reprinted from Ref [206].	42
Figure 23	(a) The sketch of the whole annealing system (b) the picture of the solvent vapor controlling reservoir with the sketch of the solvent capsule.	46

12 List of Figures

- Figure 24 Picture and sketch of the annealing chamber used in our experiments. T_v and T_s are the temperatures of the vapor and the substrate respectively. (a) The metal wall of the chamber. (b) is the transparent window for in situ ellipsometry measurement. (c) The vapor tube connected to the solvent vessels settled in the thermostat reservoir. (d) The cycling water to maintain the substrate at a setting temperature. The Teflon chamber has the vapor tube facing each other, but the steel chamber has them on the same side. 48
- Figure 25 Polymer volume fraction of SV (~ 40 nm) films as a function of stepwise increasing of the partial vapor pressure (p/p_0) of chloroform at temperature set (T_v/T_s) of 14 °C/20 °C in steel and Teflon chambers..... 49
- Figure 26 Kinetics curves of ~ 40 nm SV³⁹⁰ films under chloroform vapor, when the partial vapor pressure changes from 0 to 100% at 24 °C/30 °C in the steel chamber with two annealing systems as indicated. 50
- Figure 27 The saturation pressure curves of toluene and chloroform increasing as the temperature does. The blue curve with triangles indicates chloroform and the black curve with squares indicates toluene. 51
- Figure 28 Kinetics curves of ~ 40 nm SV³⁹⁰ films in (a) Teflon chamber with toluene vapor at 19 °C/20 °C (b) steel chamber with chloroform vapor annealed at room temperature 54
- Figure 29 Comparison of the degree of swelling of SV³⁹⁰ ~ 40 nm thick films between room temperature and maintained at 19 °C/20 °C in chloroform vapor with 100% p/p_0 at total flow of 20 sccm, 50 sccm, 80 sccm and 100 sccm..... 54
- Figure 30 Polymer volume fraction Φ_p of SV film with dry thickness of ~ 40 nm under stepwise increasing partial vapor pressure of chloroform at $T_v = 14$ °C, $T_s = 20$ °C (black triangle) and $T_v = 19$ °C, $T_s = 20$ °C (blue square)..... 56
- Figure 31 Comparison of the degree of swelling of PS and P2VP films with 40 nm dry thickness upon step-wise increasing partial pressure of chloroform vapor. The dashed lines indicate the film annealing at a vapor temperature of 14 °C and a substrate temperature of 20 °C. The solid lines are 19 °C and 20 °C respectively. The insert is the increase ratio of PS and P2VP films under each partial vapor pressure..... 58
- Figure 32 The stepwise swelling (a) and deswelling (b) curves of PS (blue line, ~ 42 nm thick), P2VP (red line, ~ 41 nm thick) films as indicated by arrows at 20% 30% 40% 50% 70% 80% 100% of the relative partial vapor pressure of chloroform (p/p_0) at 19 °C/20 °C. (c) polymer volume fraction of the swelling and deswelling of PS and P2VP 60
- Figure 33 Refractive index as a time-resolving function of PS (42 nm) and P2VP (41 nm) films in chloroform vapor with step-wise increasing of partial vapor pressure at 19 °C/20 °C. 61
- Figure 34 The kinetics curve of the ~ 40 nm SV³⁹⁰ film under stepwise increasing partial vapor pressure of (a) toluene and (b) chloroform with the indicated values in the plots. The separated temperatures of vapor and substrate are 19 °C and 20 °C. (c) The comparison of polymer volume fraction in toluene and chloroform vapor annealing at stepwise increasing partial vapor pressure at 19 °C/20 °C 64
- Figure 35 (a) Kinetics curves of the stepwise swelling and deswelling of PS (green triangle, 48 nm thick), P2VP (red circle, 43 nm thick) and SV block copolymer (black square, 39 nm thick) as indicated by arrows at 50% 80% 100% of the relative partial vapor pressure of chloroform (p/p_0)

at $T_v = 14\text{ }^\circ\text{C}$ and $T_s = 20\text{ }^\circ\text{C}$. (b) The polymer volume fraction as a function of p/p_0 based on the curves in (a)..... 65

Figure 36 Time-resolved swollen thickness (h_s left axis, solid line) of SV film under variation of (right axis) T_s (dashed line) and T_v (dotted line) in (a) 100% (b)50% p/p_0 chloroform vapor at temperature of A,A' 20/30 $^\circ\text{C}$, B,B' 25 $^\circ\text{C}/30\text{ }^\circ\text{C}$, C,C' 29 $^\circ\text{C}/30\text{ }^\circ\text{C}$, D,D' 29 $^\circ\text{C}/35\text{ }^\circ\text{C}$, E' 29 $^\circ\text{C}/40\text{ }^\circ\text{C}$, F' 39/40 $^\circ\text{C}$. Degree of swelling as a function of temperature interval at constant vapor (c) and substrate (d) temperature under 100% and 50% partial vapor pressure of chloroform. 67

Figure 37 SFM topography (a) (b) and phase (c) (d) images of spin-cast $SV^{390} \sim 40\text{ nm}$ film (a) (c) and after annealing (b) (d) at $T_v = 29\text{ }^\circ\text{C}$, $T_s = 30\text{ }^\circ\text{C}$ for 20 min, where the curve is shown in Figure 36(a). 69

Figure 38 SFM topography images (a) (b), phase images (c) (d) of 40 nm SV^{390} films annealed by chloroform for 200 min. Area for PSD analysis is shown in (e) (f). The annealing condition and degree of swelling are presented on the top of the image. 70

Figure 39 SFM topography images (a) (b), phase images (c) (d) of 40 nm SV^{390} films annealed by chloroform for 200 min. Area for PSD analysis is shown in (e) (f). The annealing condition and degree of swelling are presented on the top of the image. 72

Figure 40 Power spectrum density analysis by Nanoscope Analysis of the annealed $\sim 40\text{ nm}$ SV^{390} films at various temperatures. Their morphologies are shown in Figure 38 and Figure 39. 73

Figure 41 Height image (a), deformation image (b) and log Modulus image (c) from peak force module of $SV^{390} \sim 40\text{ nm}$ film annealed by chloroform at 25 $^\circ\text{C}/26\text{ }^\circ\text{C}$. (b), (c) are the area of the red square in (a) 74

Figure 42 SFM topography images of the free surface (a) (c) of the film and the interface (e) (f) between the film and the substrate from the SV^{390} film with thickness of $\sim 40\text{ nm}$ annealed by chloroform vapor at 24 $^\circ\text{C}/30\text{ }^\circ\text{C}$. (c) (d) (g) (h) are their phase images respectively. 76

Figure 43 SFM topography (a) and phase (b) images of the metalized stripes from $\sim 40\text{ nm}$ template of SV^{390} films annealed by chloroform vapor on silicon wafer. FE-SEM images (c) (d) of the same sample, where the bright wires are Pt. The profile curves (e) of the cross-section line in (a) shows the height of the Pt wires. 78

Figure 44 (a) (c) (e) (g) SFM topography images and (b) (d) (f) (h) phase images of $SV^{390} \sim 45\text{ nm}$ film annealed by chloroform at 24 $^\circ\text{C}/30\text{ }^\circ\text{C}$ (i) profile curve of cross section of the red line on image (e). 80

Figure 45 (a) (c) SFM topography images and (b) (d) phase images of $SV^{390} \sim 40\text{ nm}$ film annealed by chloroform at 24 $^\circ\text{C}/25\text{ }^\circ\text{C}$ with degree of swelling of 1.78, (e) the profiles of cross-section at the yellow line in (a) (black) and (c) (blue). In (a) the stripes have height of 7.4 nm in average and width of 51 nm in average. The domain spacing of (a) is $\sim 109\text{ nm}$ and (c) is $\sim 55\text{ nm}$. 82

Figure 46 (A) SFM topography images (a) (c) and phase images (b) (d) of etched block copolymer template indicating the procedure of (b) and (c) in (A). (B) The cross-section profile of SV^{390} template on silicon wafer before (a, black), after (b, red) etching and the etched Si wafer (c, blue). (C) The sketch of etching procedure treated on SV template shown in Figure 38b with (a) before etching (b) after etching with residual polymer (c) after removing the residual polymer. 84

12 List of Figures

- Figure 47 Kinetics curves of stepwise deswelling of ~ 40 nm PS and P2VP films under chloroform vapor with swelling rate. The swelling curves are from Figure 32b. 85
- Figure 48 SFM height images of spin-casted SV^{390} films from toluene by staying at room temperature for 24h (a), stirring at room temperature for 24h (b), staying at 4 °C for 24h with their optical images below respectively. 86
- Figure 49 SFM height images (a)-(c) & (g)-(i) and their corresponding phase images (d)-(f) & (j)-(l) of time-resolved morphology of SV^{390} ~ 40 nm film on silicon substrate annealed by chloroform at 19 °C/20 °C with their FFT transfer images. The periodic distance and annealing time are labeled on each image..... 87
- Figure 50 height images (a)-(c) & (g)-(i) and their corresponding phase images (d)-(f) & (j)(k)-(l) of time-resolved morphology of SV^{390} ~ 40 nm film on amorphous-carbon-layer covered silicon substrate annealed by chloroform at 19 °C/20 °C with the periodic distance and time on each image. 88
- Figure 51 Kinetics curve of ~ 40 nm SV^{390} film annealed in chloroform vapor with its thickness-depending morphology at 1min, 5 min and 10 min. 89
- Figure 52 SFM height and phase images of SV^{390} films with dry thickness from 36 nm to 61 nm annealed by chloroform with degree of swelling of 1.65..... 93
- Figure 53 SFM (a) (c) (e) height and (b) (d) (f) phase images of SV^{390} annealed under chloroform vapor on SiO_2 substrate at 19 °C/20 °C for 200 min with a degree of swelling of 2.5. 94
- Figure 54 SFM (a) (b) (d) (e) height images of SV^{390} template(a) (d) and metallization(b) (e) and their cross-section profiles (c) (f). The templates are prepared by annealing ~ 40 nm SV^{390} films under chloroform vapor to swollen thickness of (a) 64 nm (d) 100 nm. 95
- Figure 55 SFM height (a)-(f) and phase (a')-(f') images of SV^{99} annealed by selective solvent vapor toluene at 19 °C/20 °C for 60 min with initial thickness increasing from 14 nm to 35 nm. The degree of swelling is 1.8 during annealing..... 96
- Figure 56 PSD analysis of SV^{390} morphology shown in Figure 55 to obtain their domain spacing. Line a-f indicates the corresponding images in Figure 55. 97
- Figure 57 SFM (a) (b) height and (c) (d) phase images of SV^{99} films with initial film thickness of (a) (c) 46 nm (b) (d) 52 nm, annealed by chloroform vapor at 19 °C/20 °C for 60 min. Their swollen thicknesses are both 94 nm ($1.7L_0$)..... 98
- Figure 58 SFM (a) (c) (e) height and (b) (d) (f) phase images of SV^{99} with initial film thickness of 39 nm, 42 nm and 60 nm, annealed by chloroform at 14 °C/20 °C for 120 min. The degree of swelling is 1.53 controlled by partial vapor pressure. 99
- Figure 59 (a) Kinetics of the stepwise swelling and deswelling of PS (dashed line, 48 nm thick), P2VP (dash-dot line, 43 nm thick) and SV block copolymer (solid line, 39 nm thick) as indicate by arrows at 50% 80% 100% of the relative partial vapor pressure of chloroform (p/p_0). (b) Polymer volume fraction Φ_p as a function of the relative partial vapor pressure of chloroform (p/p_0) in swollen films of PS (blue triangles, 48 nm thick), P2VP (red circles, 43 nm thick) homopolymer and SV block copolymer (black squared, 39 nm thick). The swelling has been done at $T_v = 14$ °C and $T_s = 20$ °C..... 100

- Figure 60 SFM height (a) (c) (e) and phase (b) (d) (f) images of SV390 films annealed in chloroform vapor at 19 °C/20 °C on (a) (b) SiO₂ (c) (d) carbon (e) (f) HM substrate for 200 min. The swollen film thickness of films on carbon and HM is estimated to be 101 nm and 92 nm respectively, based on the degree of swelling of film on silicon substrate. 101
- Figure 61 SFM height (a) (c) (e) and phase (b) (d) (f) images of SV³⁹⁰ films with dry thickness of ~80 nm annealed in chloroform vapor of 90% p/p₀ at 19 °C/20 °C with degree of swelling of 1.9 (based on the film on the SiO₂ substrate) for 30 min. The swollen thickness of the film on SiO₂ substrate is measured by *in situ* ellipsometry, while the swollen thicknesses of those on carbon and HM substrates are approximately estimated by the same degree of swelling on silicon wafers [137]. 102
- Figure 62 (a) (c) (e) SFM topography and (b) (d) (f) phase images of PS-*b*-P2VP films with dry thicknesses of (a) (b) ≈42 nm, (c), (d) ≈78 nm and (e) (f) ≈ 150 nm after annealed in chloroform vapor at vapor temperature of 19 °C and substrate temperature of 20 °C. The center-to-center distance of period pattern is 132.3 nm in (a) 127 nm in (c) and 128 nm in (e). The lamella height is 4.7 nm in (a), 13 nm in (c) and 6.8 nm in (e). The dot radius is 23.4 nm in (a) and the lamella width (light area) is 66 nm in (c), 80 nm in (e). 104
- Figure 63 SFM (a) (c) (e) (g) height and (b) (d) (f) (h) phase images of SV³⁹⁰ and SV⁹⁹ films on SiO₂ and photoresist substrate as indication annealed by chloroform vapor at 14 °C/20 °C for 120 min. 106
- Figure 64 SFM height images of (a) patterned photoresist substrate, a SV⁹⁹ film from chloroform on patterned substrate (b) before and (c) after annealing by toluene vapor at 19 °C/20 °C for 60 min. 107
- Figure 65 SFM (a) (b) (c) height and (d) (e) (f) phase images of (a) (d) pure wrinkled PDMS substrate, (b) (e) SV³⁹⁰ spin-cast on wrinkled PDMS and (c) (f) annealed SV³⁹⁰ by chloroform vapor for 200 min. The insets are the small areas in the yellow square with flatten treatment in the software Nanoscope Analysis. If the films are spin-coated on flat silicon wafers with the same spin-coating parameters, the film thickness will be 175 nm. 108
- Figure 66 SFM (a) (c) (e) (g) height and (b) (d) (f) (h) phase images of 160 nm-thick SV⁹⁹ films on SiO₂ substrates (a) (b) before and (c) (d) after, on wrinkled PDMS substrate (e) (f) before and (g) (h) after, annealing by chloroform vapor at 14 °C/20 °C. The films were prepared on wrinkled PDMS and flat silicon substrates with same conditions. 109
- Figure 67 SFM (a) (c) (e) height and (b) (d) (f) phase images of SV³⁹⁰ from (a) (b) toluene (c) (d) chloroform and (e) (f) DMF solution spin-cast on SiO₂ substrate with thickness of ~40 nm. ... 110
- Figure 68 SFM (a) (b) (c) height images and (d) (e) (f) phase images of SV³⁹⁰ films from DMF spin-coating solution annealed by chloroform vapor at 29 °C/30 °C for 200 min with degree of swelling of 2.5. The film thicknesses are shown at the top of each image. 111
- Figure 69 The image (a) and the sketch (b) of the vapor flow treatment apparatus used in this chapter. (c) The sketch of the expected membrane changing procedure. 115
- Figure 70 SFM images of the solvent-cast (a) (a'), ethanol treated (b) (b'), chloroform treated (c) (c') and ethanol: THF=1:1 treated (d) (d') SV⁹⁹ films with thickness of 1 μm between PDMS supports. Except for (d) (d') was treated at 50 °C, all the other treatments were finished at room temperature. 117

12 List of Figures

- Figure 71 FE-SEM images of the cross-section profiles of SV⁹⁹ films which are (a) solvent-cast, (b) annealed in chamber by ethanol for 200 min and flow treated by (c) ethanol, (d) chloroform, (e) ethanol: THF=1:1 and (f) ethanol: chloroform=1:1 for 15 min..... 118
- Figure 72 SFM height (a) and phase (b) images of the drop-cast SV⁹⁹ film on the PDMS substrate. 119
- Figure 73 SFM (a) height and (b) phase images of the ~80 nm thick SV³⁹⁰ film treated by oriented flow of ethanol. 119
- Figure 74 SFM height (a)-(c) and phase (d)-(f) images of SV³⁹⁰ films supported by PDMS substrates with thickness ~ 1 μ m, after treatment of (a) (d) ethanol, (b) (e)chloroform and (c) (f) toluene at 50 °C for 15 min. 120
- Figure 75 FE-SEM images of the cross-section profiles of (a) drop-cast, (b) ethanol and (c) chloroform treated ~1 μ m SV³⁹⁰ films on PDMS supports. 121
- Figure 76 2D SAXS profiles from (a) empty PDMS substrate and the (b) solvent-cast, (c) chloroform-treated and (d) toluene-treated SV³⁹⁰ films with thickness of ~1 μ m. (e) the in-plane plots of the same samples from the 2D results. 122
- Figure 77 SFM height (a) and phase (b) images of the ~1 μ m SM film treated by ethanol: THF=1:1 at 50 °C for 15 min. 122
- Figure 78 FE-SEM images of the cross-section profiles of (a) drop-cast (b) ethanol, (c) ethanol: chloroform=1:1 and (d) ethanol: THF=1:1 treated SM⁵⁰ films. The films are all ~1 μ m, except for the film in (d) is ~500 nm. 123
- Figure 79 The record of the cycled vapor flows as a function of time in ethanol treatments. (a) 6 min/cycling 60 min at 50 °C (b) 0.5 min/cycling 15 min at 50 °C..... 124
- Figure 80 FE-SEM images of the cross-section profiles of (a) ethanol treated ~2 μ m SV⁹⁹, (b) ethanol:THF=1:1 treated ~3 μ m SV³⁹⁰ (c) ethanol treated ~3 μ m SM⁵⁰ and (d) ethanol treated ~5 μ m SM⁵⁰ with single orientated flow between 1 mm thick PDMS supports. 125

13 List of Tables

Table 1	Polymer volume fraction of SV with thickness of 40 nm in steel and Teflon chamber under increasing partial vapor pressure of chloroform.....	49
Table 2	The consumption of solvent during the annealing	52
Table 3	The partial vapor pressure calculated from the consumption of solvent	53
Table 4	SFM height images of original patterned substrates, spin-cast SV ⁹⁹ films and annealed SV ⁹⁹ films on patterned substrates. The annealing is in toluene vapor with degree of swelling of ~1.3 at 14 °C/20 °C for 45 min.	142
Table 5	SFM height images of SV ⁹⁹ films on patterned substrates annealed in toluene vapor with over pressure at 25 °C/30 °C.....	152

Suporvisors: Prof. Dr. Alexander Böker

PD Dr. Larisa Tsarkova

Reviewers: Prof. Dr. Alexander Böker

PD Dr. Larisa Tsarkova

Prof. Dr. Michael Gradzielski